Fabrication and Characterization of Nanowire Arrays on InP (100) Surfaces

Thesis Submitted for the Degree of

Doctor of Philosophy

By

Guiping Zhao

INEX-Innovation in Nanotechnology Exploitation

School of Chemical Engineering and Advanced Materials

University of Newcastle upon Tyne

April 2007

Abstract

This work investigates the technique of mass fabrication of nanowires on semiconductor InP (100) surfaces by low energy Ar^+ ion beam bombardment. Systematic investigation shows that under some crucial experimental parameters, nanowire arrays of regular periodicity can be produced.

An ambient Atomic Force Microscope was used in contact mode to examine the morphology of the irradiated InP surfaces. The chemical composition of the irradiated samples was characterized by X-ray Photoelectron Spectroscopy (XPS). The electronic structure of the fabricated nanowire arrays was jointly explored by Scanning Tunnelling Spectroscopy and XPS.

The research shows that In enriched ripples and nanowires form under prolonged irradiation by Ar^+ ions due to preferential sputtering of P from InP under grazing ion incident angle above some crucial irradiation ion dose. A model of mergence from tailed cones is proposed to account for the formation of these ripples and nanowires. The drive to the formation of periodic ripples and nanowires is believed to be stress-field induced self-organisation of strained cones. The cone-mergence model is a combination of the model of stress-field induced self-organization and the model of ripple topography by Bradley and Harper (BH). The research proposes that the mobility of atoms on the corresponding solid surfaces under ion bombardment decides whether the surface morphology is generated by the stress-field, the BH, or a combination of the two models.

Monte-Carlo simulation was used to evaluate the effect of surface damage and preferential sputtering of P from InP and N from Si_3N_4. The calculations predict that P and N can be preferentially sputtered from InP and Si_3N_4 surfaces.

Acknowledgement

The author is greatly indebted to Professor Ken Snowdon, who supervised this project. Valuable discussions with Dr. Graeme Hill, Dr. Sofian Muhammad Daud and Dr. Abdal Khamim Ismail on the experimental results and computer related problems are greatly appreciated.

XPS data acquisition and have been made in collaboration with Dr. Richard Cutting and Dr. Zhidong Xiang under the consent of Professor Psantu Datta of the University of Northumbria at Newcastle; STS data acquisition was made by Mr. Adam Busiakiewicz under consent of Professor Psantu Datta, and analyzed by Professor Zbigniew Klusek form University of Northumbria at Newcastle. The author here extends great thanks to these scientists.

The author appreciates Dr. Neal Fairley from Casa Software Ltd. for his donation of and instruction in the demo version Casa XPS analysis software.

The author would like to acknowledge Dr. Darren Bagnall and Dr. Graham Ensellfor from the University of Southampton for donation of LPCVD Si_3N_4 samples. Acknowledgement is also paid to European Science Fellowship program for funding the experiment on Si_3N_4 at the University of Genova in Italy, through collaboration with Professor Ugo Valbusa. Great thanks are extended to Professor Ugo Valbusa, Professor Corrado Boragno, Dr. Renato Buzio, Dr. Francisco Buotier and Mr. Anderea Toma from Genova University for their generous help and valuable discussion.

This work was supported by the UK Department of Trade and Industry, through the University Innovation Centre for Nanotechnology, European Structural Funds, and the North-East of England Regional Development Agency ONE North-East.

Great thanks are extended to Dr. Michael Hunt from Durham University and Professor Steve Bull from Newcastle University for their valuable instruction on modification of the thesis, and to Dr. Bill King and Dr. Jonathon West for their help with proofreading.

Table of Contents

Introduction 1

Chapter 1 Review of Current Techniques for Nanowire Fabrication 3

1.1 The Top-down Approach 3

1.1.1 Nanolithography 3

1.1.2 SPM Nanostructuring 7

1.1.3 Soft Lithography 11

1.1.4 Nanofabrication by Energetic Particles 13

1.2 The Bottom-up Approach 29

1.2.1 Vapour Phase Growth of Nanowires 29

1.2.2 Nanowire Formation using Templates 30

1.2.3 Nanowire Fabrication by Electrodeposition 33

1.2.4 Nanowire Growth by Molecular Beam Epitaxy 34

1.3 Combination of Top-down and Bottom-up Approach 36

1.4 Potential Applications of Nanowires 38

Chapter 2 Characterization of Nanowires 44

2.1 Universal Tools for Nanowire Characterization 44

2.1.1 Scanning and Transmission Electron Microscopy 44

2.1.2 Scanning Tunnelling Microscopy 47

2.1.3 Atomic Force Microscopy 51

2.2 Characterization of Electronic Transport Properties of Nanowires 62

2.2.1 Conventional Two-terminal Method for the Measurement of I-V Curves of Nanowires 62

2.2.2 The Four-probe Method 65

2.3 Non-destructive Characterization of Chemical Composition of Nanowires 66

2.3.1 X-Ray Photoelectron Spectroscopy 67

2.3.2 Auger Electron Spectroscopy 76

2.3.3 Ion Scattering Techniques 77

2.4 Characterization of Photonic Properties of Nanowires 79

Chapter 3 Theory of Ion Beam Induced Topography on Solid Surfaces 82

3.1 A Brief Introduction to the Physics of Ion Beam Interaction with Solid Surfaces 82

3.2 Quantification of Ion Bombardment—Mote Carlo Simulation of Ion Beam Interaction with Solid Surfaces using Trim 2000 87

3.3 Models of Ion Beam Induced Morphology on Solid Surfaces 89

3.3.1 Some Basic Concepts in Surface Physics 89

3.3.2 Theory of Ripple Formation by Bradley and Harper (B-H) 91

3.3.3 Kardar-Parisi-Zhang Model 100

3.3.4 Kuramoto-Sivashinsky (KS) Model 101

3.3.5 Differential Sputter Erosion Models 102

3.3.6 Stress Field Induced Self-Organization 104

3.3.7 Impurity Seeding Models 104

3.3.8 Micro-region Model 105

Chapter 4 Properties of InP and Monte-Carlo Simulations of InP Surfaces under Ar^+ ion Irradiation 106

4.1 Properties of Indium Phosphide and Related Materials 107

4.1.1 Properties of Indium Phosphide 107

4.1.2 Properties and Applications of Indium and Indium Oxides 108

4.1.3 Properties and Applications of Si_3N_4 and CaF_2 110

4.2 Monte-Carlo Simulations of Ar^+ ion beam Irradiation of InP Surfaces 111

4.2.1 Dynamic Plot of Collision Cascades 111

4.2.2 Ion/Recoil Distribution 112

4.2.3 Energy Loss to Ionization 114

4.2.4 Creation of Damage in the Target 115

4.2.5 Sputtering Yield 116

Chapter 5 Ion Beam Directed Self-Assembly of Nanowire Arrays on InP (100) Surfaces 120

Table of Contents

5.1 Experimental Method 120

5.1.1 The Ion Beam Apparatus 120

5.1.2 Procedures of the Experiment 124

5.1.3 Deduction of Ion Dose 124

5.1.4 Methods of Morphology Characterization by AFM 126

5.2 Nanowire Fabrication by Ar^+ ion beam Bombardment on InP (100) Surfaces 140

5.2.1 Mophology Changes of Ar^+ Ion Beam Irradiated InP (100) Surfaces with different Irradiation Energies 142

5.2.2 Morphology Changes with Different Irradiating Ion Current Densities 143

5.2.3 Morphology Changes with Different Irradiating Ion Doses 146

5.2.4 Morphology Changes with Different Ion Beam Incident Angles 149

5.2.5 Dependence of Half-apex-angles of Cones upon Ion Current Densities Ion Doses, and Ion Incident Angles 151

5.3 Discussion of the Results 154

5.3.1 Discussion of Ripple and Nanowire Formation on Ar^+ Ion Irradiated InP (100) Surfaces 154

5.3.2 Ripple and Nanowire Formation from Mergence of Cones 156

5.3.3 Relationship between the Cone Mergence Model and Other Ripple Models 161

Chapter 6 Compositional Changes and Electronic Structures of Ar^+ Ion Beam Induced Nanowires on InP (100) Surfaces 163

6.1 X-Ray Photoelectron Spectroscopy Characterization of Compositional Changes in Ar^+ ion Beam Induced Nanowires on InP (100) Surfaces 163

6.1.1 Theory of Compositional Changes in Ion Beam Bombarded Surfaces of Compound Solids 164

6.1.2 Compositional Changes on Ar^+ ion beam Bombarded InP (100) Surfaces 165

6.2 Electronic Structures of Ar^+ ion Irradiated InP (100) Surfaces 185

Chapter 7 Morphology and Monte-Carlo Simulations of Ar^+ Ion Beam Irradiated Si_3N_4 Surfaces 192

Table of Contents

7.1 Introduction 192

7.2 Method of Experiment 193

7.3 Results and Discussion 193

7.4 Monte-Carlo Simulations of Ar^+ ion Bombardment on Si_3N_4 (100) Surfaces 198

7.4.1 Dynamic Plot of Collision Cascades 199

7.4.2 Ion-Range Distribution 200

7.4.3 Ion/Recoil Distribution 200

7.4.4 Energy Loss to Ionization and Phonons 202

7.4.5 Creation of Damage in the Target 203

7.4.6 Sputtering Yield 204

7.5 Tentative Conclusion and Future Work 207

Chapter 8 Summary 208

References 212

Fabrication and Characterization of Nanowire Arrays on InP (100) Surfaces

Introduction

Since the invention of the Scanning Tunnelling Microscope by Binning and Rohrer [1] at IBM in 1982, nanotechnology has become an active area of research in physics, materials science, and increasingly in chemistry and biology. Fabrication and characterization of nanostructures such as nanoparticles, nanotubes and nanowires has been one of the most intensely investigated subjects in recent years. Systems that have features or characteristic lengths between 1 and 100 nanometres exhibit unusual and interesting characteristics, e.g. quantized excitation, Coulomb blockade [2, 3], single electron tunnelling (SET) [2] and metal-insulator transitions. These phenomena occur because the structures are small enough for quantum mechanical effects to dominate. The ability to fabricate on the nanometre scale guarantees a continuation in the miniaturization of functional devices, especially in the microelectronics industry, when the current techniques of IC (integrated circuits) production based on photolithography approaches fundamental limits. Devices made using nanowire heterojunctions may be critical for nano- and molecular-electronics [4, 5]. Nanowires with regular periodicity may form building blocks of the future nanoelectonics industry. It is therefore important to explore the fabrication techniques and understand the properties of such structures.

Fabrication of nanowires by ion beam bombardment on solid surfaces is one of the most intensely investigated techniques in recent years. The technique has been explored in detail on ionic crystal CaF_2 (111) surfaces in earlier studies [6-8]. The initiated objective of this thesis was to explore the predicted generality of the interface stress-related mechanism elucidated there by seeking to create nanowire arrays on the covalently bound InP (100) surface.

The first chapter is an extensive review of recent advances in nanowire fabrication techniques both "top-down" and "bottom-up", with an emphasis of fabrication of

nanostructures by energetic particles. The second chapter is a general introduction to nanowire characterization methods grouped by characterization of morphology, electronic transport properties, mechanical properties, photonic properties and chemical composition.

Chapter 3 introduces basic concepts of the physics of ion beam interaction with solid surfaces and enumerates models of ion beam induced topography. Theoretical simulation of Ar^+ ion beam interaction with InP surfaces is introduced in chapter 4, after a review of properties of InP and related materials.

Chapter 5 presents new experimental results of Ar^+ ion beam directed self-assembly of ripples and nanowire arrays on InP (100) surfaces obtained in this study. Formation of nanowires on InP (100) surfaces under prolonged Ar^+ ion bombardment is explained by a model of mergence of tailed cones composed of excess indium due to preferential sputtering of phosphorus under certain experimental conditions. Stress field induced self-assembly of In ions as a result of preferential sputtering of P is proposed as the driver for the agglomeration and mergence of these cones.

Chapter 6 gives further evidence to support this model by combined analysis of the chemical composition by XPS (X-ray Photoelectron Spectroscopy) and tunnelling conductance measurement by STS (Scanning Tunnelling Spectroscopy).

Chapter 7 presents some attempts of nanowire fabrication by Ar^+ ion irradiation on LPCVD Si_3N_4 (100) surfaces, with some results of theoretical simulation by TRIM. The experiments suggest that the lack of mobility of Si on Si_3N_4 surfaces is not ideal for the fabrication of regular structures.

Chapter 1
Review of Current Techniques for Nanowire Fabrication

The microelectronic industry has lately marched into the fabrication of devices with feature size down to 65 nm [9]. Various techniques have been proposed for the sustaining miniaturization of IC (integrated circuits) line-width to smaller scale. It is well known in the field of nanoscience and technology that nanostructures can be fabricated by two fundamentally different approaches—designated bottom-up and top-down approaches [6]. The 'top-down' approach can be defined as generation of nanostructures on solid surfaces by material removal while the 'bottom-up' approach builds low-dimensional structures atom by atom. The following review enumerates some recent advances in the fabrication of nanowires with 'top-down' and 'bottom-up' techniques. Since ion beam nanofabrication is the focus of the experiments reported in this thesis, a detailed review of ion beam nanofabrication, especially on III-V semiconductor surfaces, is presented in this chapter.

1.1 The Top-down Approach

In the 'top-down' approach, bulk materials or thin films are used as the starting material and one of the following methods is used to create nanostructures.

1.1.1 Nanolithography

Conventional photolithography has been widely used in microelectronics industry for decades. It creates two-dimensional patterns in a resist film. The basic principle is to use photons to induce chemical reactions in photosensitive materials. A mask or aperture is used to localize the photochemistry spatially and a reduced image of the mask is

replicated onto a layer of photo-resist under the projection of light. Using this technique, the microelectronics industry succeeded in scaling down the feature size of IC to 0.135 μm. Further size reduction with this method calls for a shorter wavelength of radiation to be used for exposure, such as extreme UV or X-ray. In this wavelength region, however, there are several technical problems such as the great difficulty in constructing the required optics because of the lack of transparent materials suitable for lenses at these short wavelengths, protecting the mask from damage and distortion on exposure to high fluxes of energetic radiation, and the formidable cost of the entire system.

An extension of the resolution limit of conventional photolithography was realized by evanescent near-field optical lithography (ENFOL) as demonstrated by Alkaisi *et al* [10-12]. The principle of the technique is illustrated in Fig1.1.

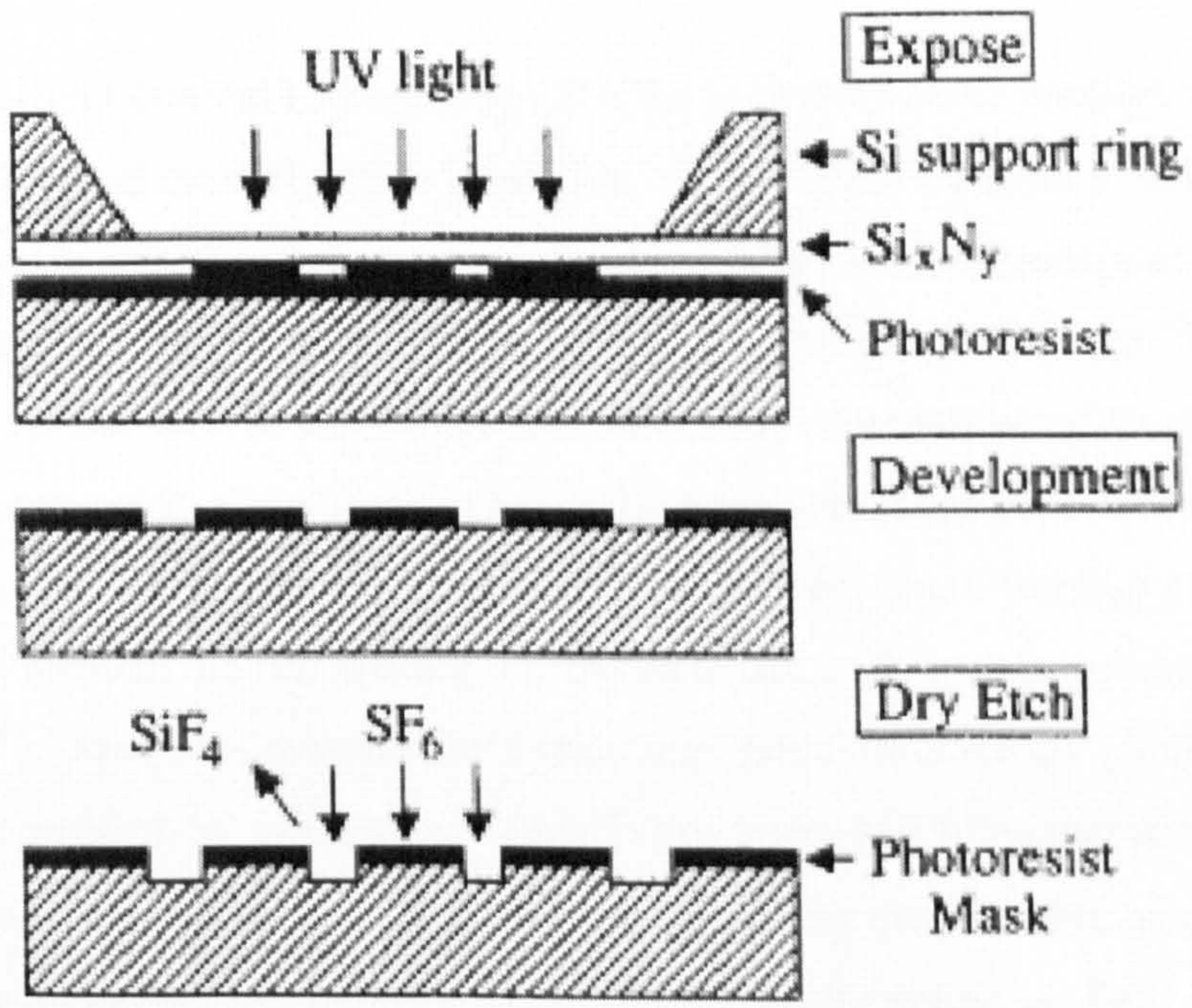

Fig 1.1 Schematic diagram illustrating the ENFOL process [10]. Photolithography is performed through a conformable mask held in intimate contact with a resist layer that is much thinner than the illuminating wavelength.

A conformable membrane mask is brought in close contact with a substrate coated with ultra-thin photo-resist in such a way that the mask-substrate gap (including the photo-

resist thickness) is much shorter than the wavelength of the exposing light source. These conditions introduce high spatial frequency evanescent components and propagating diffracted components in the optical field in the thin resist. The presence of these high-frequency components makes resolution beyond the diffraction limit of projection lithography possible. Subsequent processing includes exposure with broad band UV light, development, baking, pattern transfer with reactive ion etching (RIE) and lift-off. With this method, nanostructures of line width of 50 nm and periods of 140 nm were created on silicon. Simulations indicated the enticing prospect of resolution down to 10 nm using exposure from low-cost blue/UV sources. The ENFOL technique offers great promise for high-throughput, low-cost nanometre-scale patterning of large areas. The limitation of this technique is that the intensity in the evanescent field decays by a factor of 10 over a distance of $\lambda/4$, where λ is the wavelength of the light in the medium into which it propagates as it passes through the mask.

Scanning Near-field Optical Lithography (SNOL) is an alternative method of boosting the resolution beyond the diffraction limitation. In this serial method, a fibre-optic probe as a light source is brought to extreme proximity to a photo-resist to expose the resist, and patterns are generated by scanning the probe over the surface of the resist [13]. The height of the probe over the surface can be determined by any of a number of feedback loops, the most common being shear-force. Due to the propagation cut-off of the wave-guide mode in fibres with nanometre-sized apertures, only a very small fraction of the light can be transmitted through the tip, making it difficult to use such probes in lithographic applications [14]. Aperture-less near-field scanning optical microscopy (ANSOM) overcame this problem by using sharp metallic tips instead of fibre apertures to achieve nanometre-scale resolution. Fig 1.2 is a diagram showing the principle of aperture-less SNOL. The extremely sharp metallic tip presents a locally enhanced field with a high charge density at the tip end which induces a 'lightning rod effect' to pattern the surface at tens of nanometres resolution.

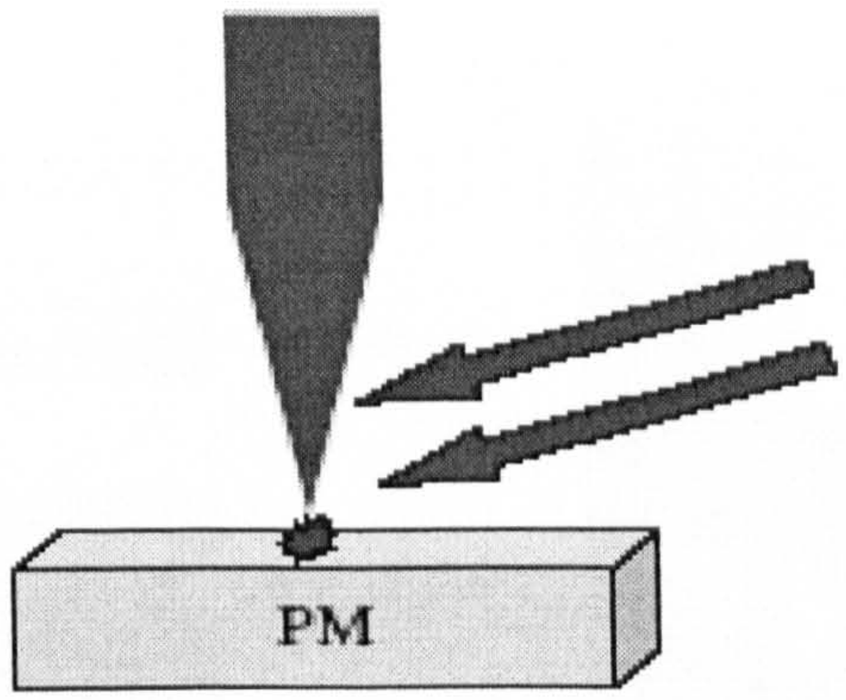

Fig 1.2. Experimental diagram [13] of SNOL

The apparent advantage of SNOL and ANSOM is that features less than 10 nanometers can be fabricated with ease. Unfortunately, pattern generation must occur in a serial fashion, which prevents it from industrial application.

Nano-imprinting lithography (NIL) [15, 16 17, 18] is in contrast to SNOL a parallel method offering lower cost, higher throughput, sub-10 nm nanolithography. It has the unique features of allowing large area nano-patterning by a step-and-repeat scheme, and generation of more complex structures from simpler ones by multiple imprinting. It generates resist relief patterns in a thermoplastic layer by physically compressing the resist that has been thermally softened, rather than by modifying the resist's chemical structure with radiation. In typical nano-imprint lithography [17], a mould with nanostructures on its surface is pressed into a thin resist that has been heated above its glass transition temperature (T_g) to endow the resist with fluidity. This fluidity enables the resist to conform to the mould pattern. After the resist is cooled below its T_g, the mould is removed. An anisotropic etching process, such as reactive ion etching (RIE), is used to remove the residual resist in the compressed region. Fig 1.3 illustrates the general method of Nano-imprint lithography.

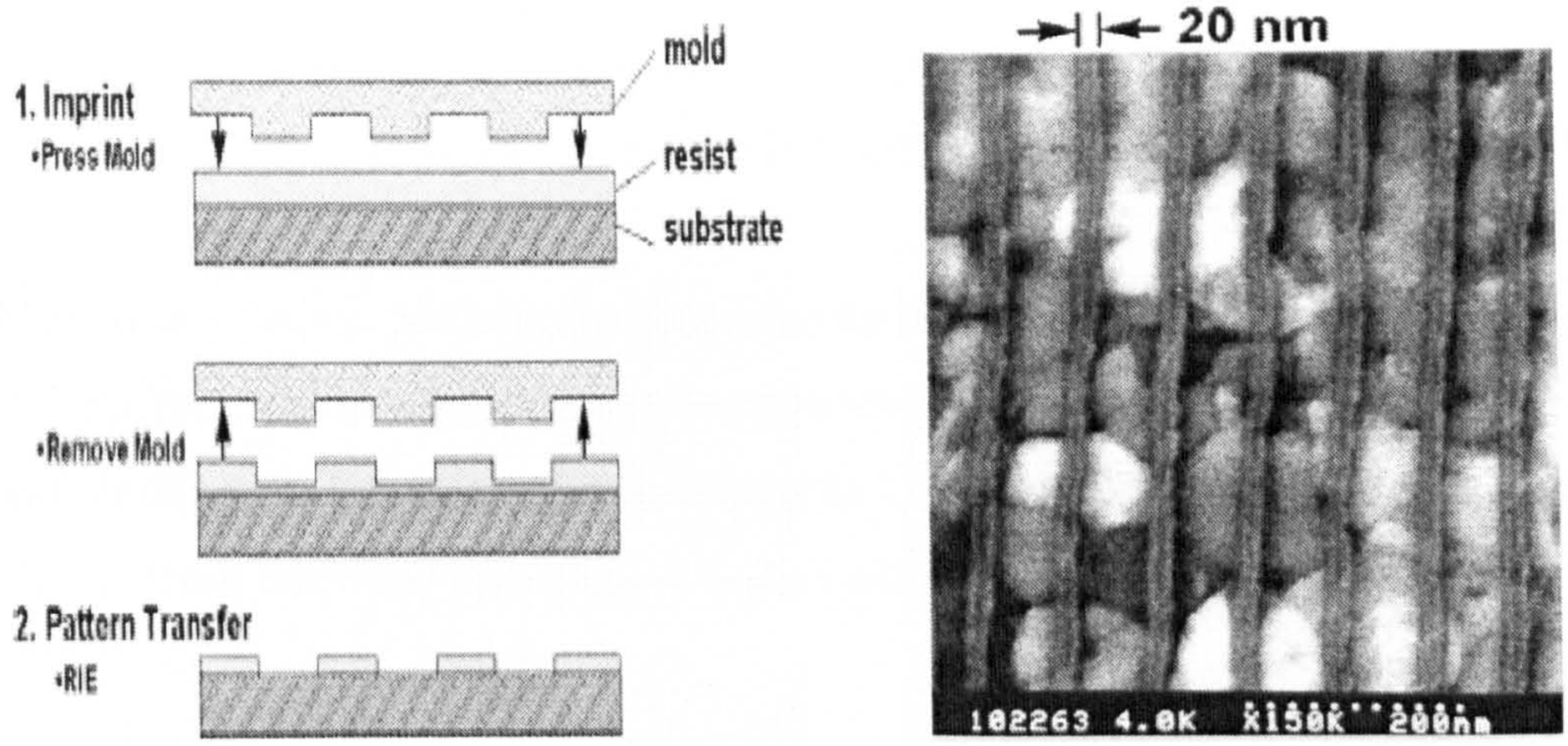

(a) (b)

Fig 1.3 (a) Schematic of nanoimprint lithography process [16]: (1) Imprinting using a mould to create a thickness contrast in a resist, and (2) Pattern transfer using anisotropic etching to remove residue resist in the compressed areas; (b) SEM micrograph[16] of nickel nanowire arrays with 20 nm linewidth and 80 nm period on a gold substrate fabricated by NIL and lift-off. Grains of the gold substrate are visible beneath the PMMA.

Obviously, mould generation is a prerequisite to the NIL process. Mass production of the moulds by Electron Beam Lithography remains a problem, and the lifetime of a mould is still a subject to explore.

Recently, Intel has proposed its 65 nm process technology based on strained silicon which raises drive current of CMOS (complementary metal-oxide semiconductor) transistors [9]. A very thin layer of single-crystal silicon with built-in stress was used in the CMOS device. At the molecular level, this silicon resembles a lattice enabling electrons to flow with less resistance.

1.1.2 SPM Nanostructuring

A scanning probe microscope-SPM (i.e. Scanning Tunnelling Microscope--STM, Atomic Force Microscope--AFM, Scanning Force Microscope--SFM, Scanning Near-field Optical Microscope--SNOM) can be used not only to image, but also to modify surfaces

on atomic scales. Scanning probes create nanostructures by means of material transportation [6, 19](AFM), ploughing of probes across surfaces [20-23] (Scanning Force Microscope) or material removal by intense field emission [21-29] (STM, AFM or SNOM).

In STM nanostructuring, patterns are generated by material removal due to the intense electric field between tip ends and sample surfaces which induces reduction and thermal annealing of the material underneath the tips (Fig 1.4). With this technique, patterns of width 25 nm were inscribed on a silicon oxide surface by Hiroshi Iwasaki [24].

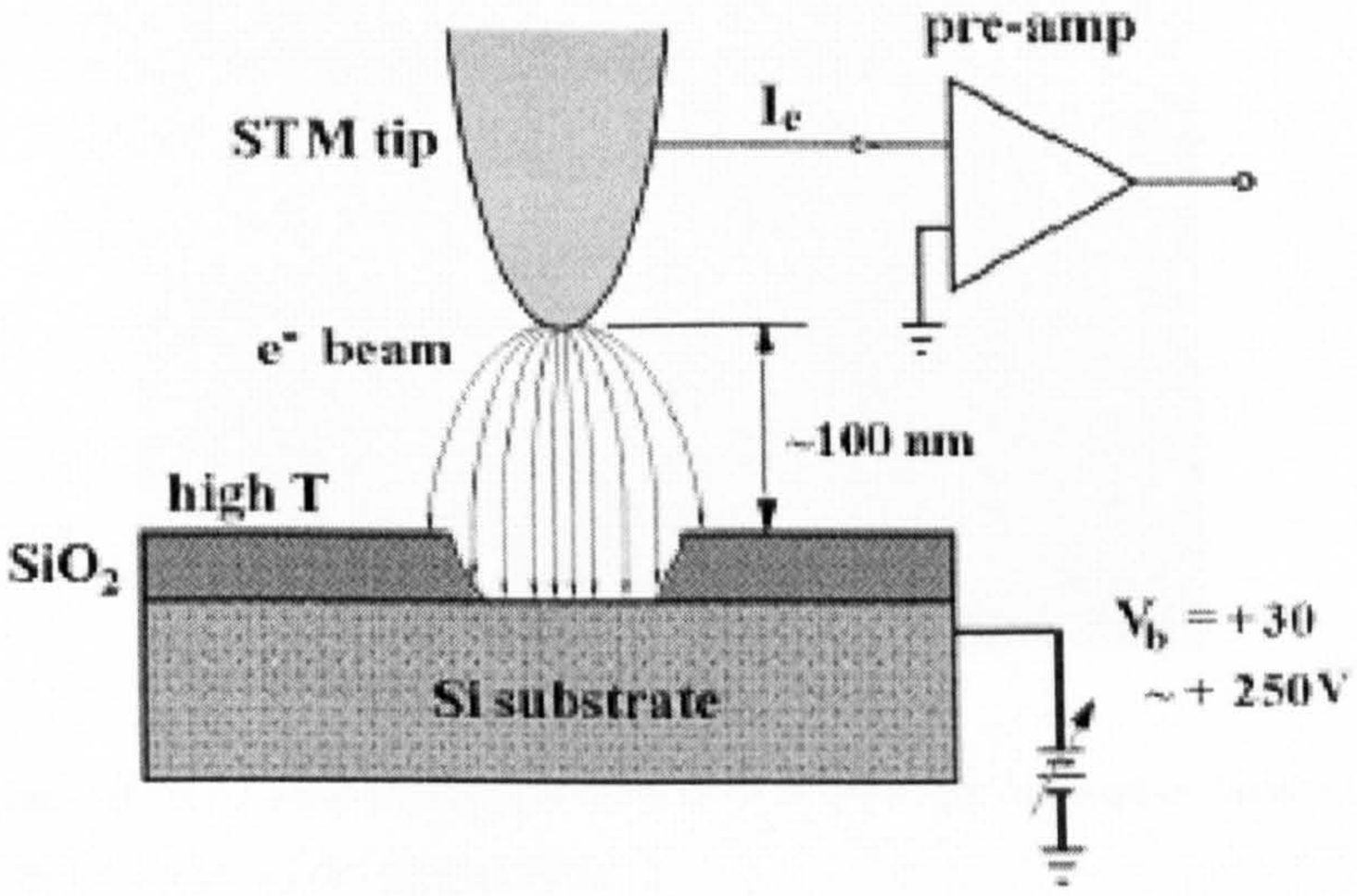

Fig 1.4 Schematic diagram of the STM nanostructuring[24]

A similar method was used to fabricate a feature size below 30 nm with AFM running in non-contact mode [30].

AFM has been used to fabricate a variety of nanostructures on 4-20 MLs (mono-layer) Ag thin films on top of cleaved (111) and ion-beam polished 4° miscut, vicinal CaF_2 (111) substrates[19]. The structures arise from AFM tip-induced material transportation. At low contact force, ambient AFM investigations of the structure of the deposited Ag layer revealed an island growth mode with an island density of $\sim 10^{12}$ cm^{-2}. Use of higher AFM tip contact forces material to be transported across the surface during scanning.

Nanowires with 5-7 nm width and 20-50 nm separation were formed under intermediate contact force conditions (Fig 1.5). A nanowire fabrication model was proposed in which the AFM tip deposits material at step edges due to the sudden increase in friction imposed by the presence of such substrate related topographic features.

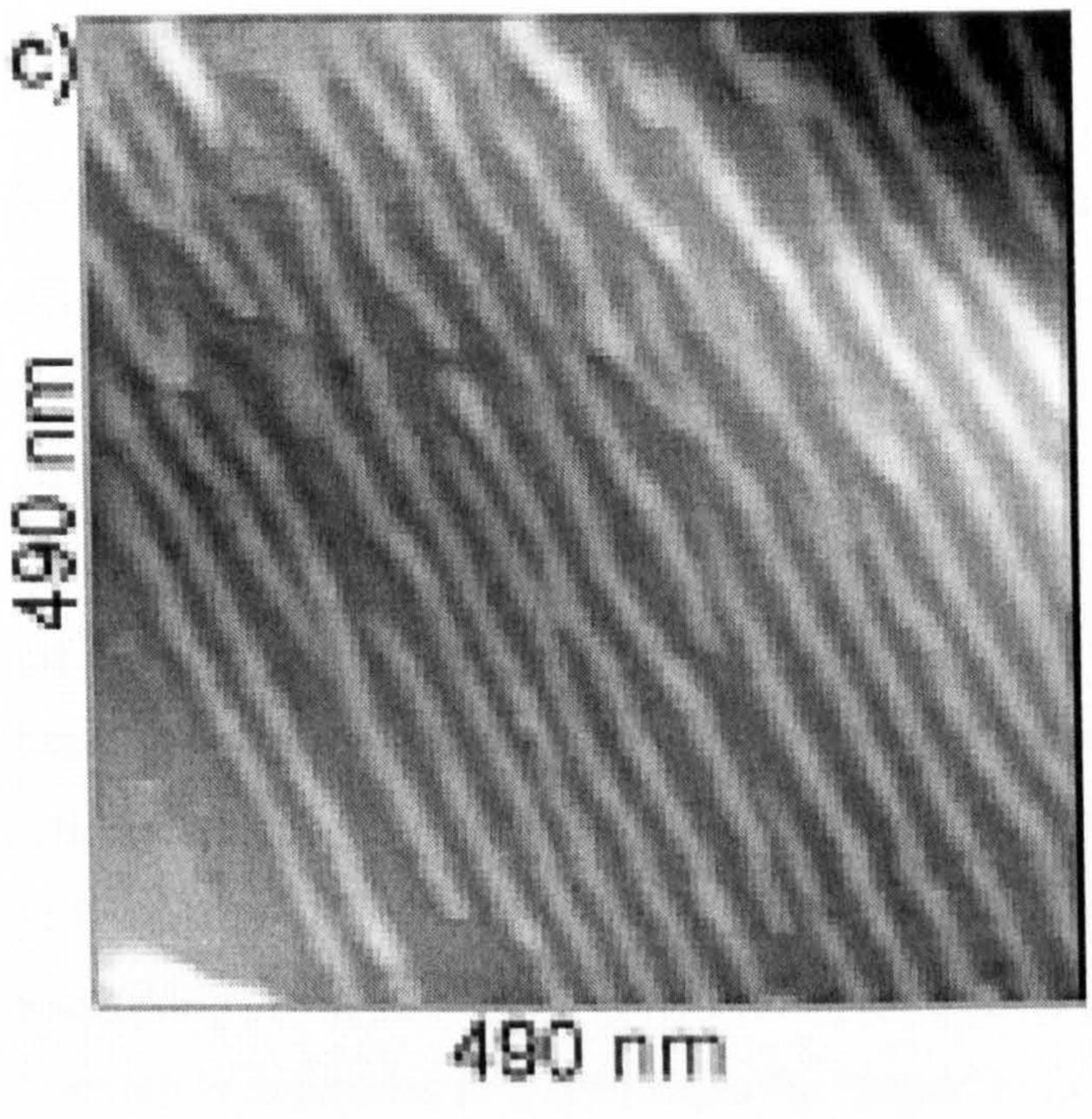

Fig 1.5 AFM micrograph of Ag nanowire arrays fabricated by AFM tip induced material transportation of Ag on CaF_2 at intermediate contact force [19]

Nanowires can also be formed by material transportation from AFM tips to sample surfaces by running an AFM in contact mode. For example, continuous gold nanowires with a width in the atomic range and a length of a few micrometers were written on a clean Si (111) surface in ultrahigh vacuum using a gold coated piezo-resistive cantilever in AFM contact mode [31]. The mechanism is believed to be related to the flow of electrons from the tip to the substrate because of the difference in Fermi level between Au (tip) and Si (substrate). The wire of dimension 7μm x 4 nm x 1 nm was shown to be metallic by *in situ* electron transport measurement.

In addition to AFM tip induced material transportation, running AFM in tapping mode with a strongly enhanced tapping force enables a furrow to be dynamically ploughed into

a substrate. This dynamic ploughing technique[22] was used to draw a line pattern 20 nm wide into a resist layer of a few nanometre thickness on top of a substrate material, followed by pattern transfer with wet chemical etching. The crucial point of this method is that the photo-resist must be both sufficiently thick to guarantee the masking capability against the etchant, and thin enough to let the tip penetrate the entire layer during the mask writing process. The limitation is the low speed (< 5 μm/s) in writing a mask.

A variation of this technique is to apply an external voltage pulse to the Z piezo scanner [32] so that the same effect occurs in STM nanostructuring. Using this method, reliable groove patterns with fully controlled width (between 4.28 nm and 9.20 nm) and depth [33] were fabricated on GaAs.

The above mentioned SPM nanostructuring techniques have been confined to research up to now due to the common drawback of an unbearably low writing speed. In order to solve this problem, Dip-Pen Nanolithography (DPN)[34-43] combined with multiple tips was invented to raise the writing speed by two orders of magnitude. The direct-write DPN process uses a scanning probe as a "pen" which is coated with molecules or materials (the "ink") which is deposited to a substrate (the "paper") via chemisorption or electrostatic interaction through a well-defined diffusion process (Fig 1.6).

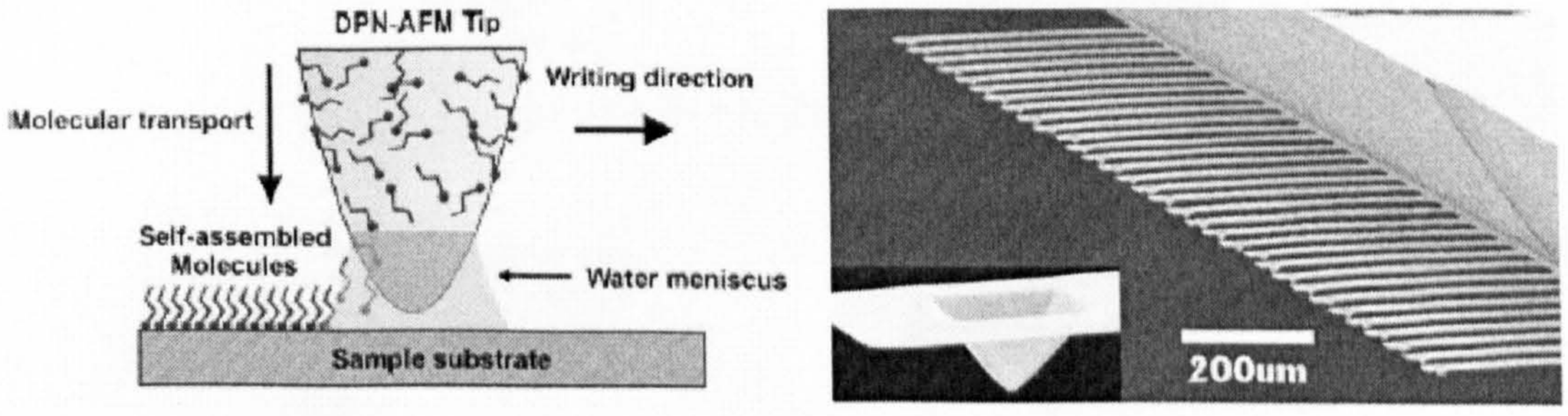

Fig 1.6 A schematic diagram of the DPN process [35]: (a) Schematic of DPN principle; (b) SEM micrograph of arrays of AFM probes.

It is possible to achieve ultra-high resolution features with line-width as small as 10-15 nm with 5 nm spatial resolution. The adoption of arrays of parallel AFM probes makes this process viable for manufacturing (Fig 1.6 b) with reasonable speed and cost.

1.1.3 Soft Lithography

Another method of top-down nanofabrication is the Soft Lithography technique[44-46] such as REplica Moulding (REM), Micro-Contact Printing (μCP)[44, 47], Micro-Moulding In Capillaries (MIMIC), Micro-Transfer Moulding (μTM), Solvent-Assisted MIcro-Moulding (SAMIM), and Near-field Phase-Shifting Photolithography (NPSP). These techniques use a patterned elastomer (usually PDMS) as the mould, stamp, or mask to generate or transfer the pattern.

Patterning of the elastomer is realized by pouring prepolymer (PDMS) onto a patterned rigid master (Fig 1.7 a) and removing it after curing. Fig 1.7 (b)-(c) gives three examples of Soft Lithography.

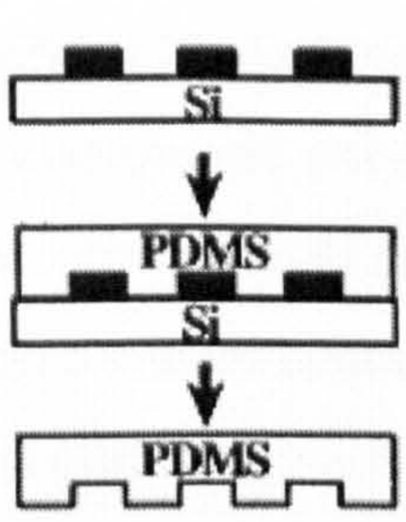

(a) Preparation of PDMS Mould

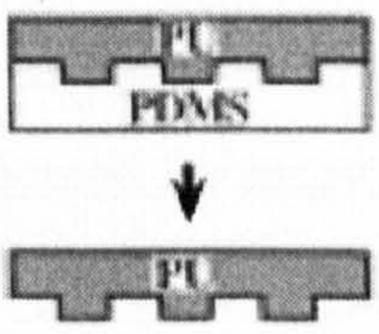

(b) REM

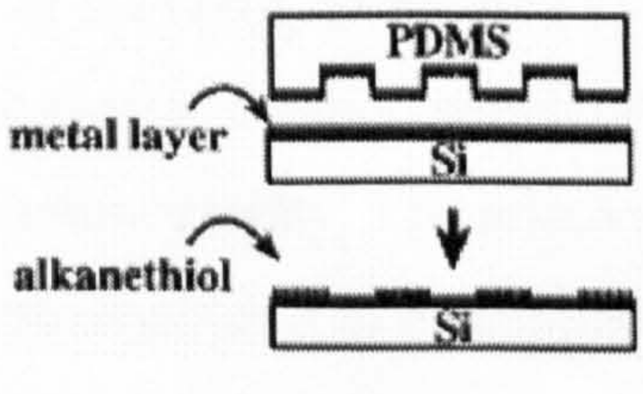

(c) μCP

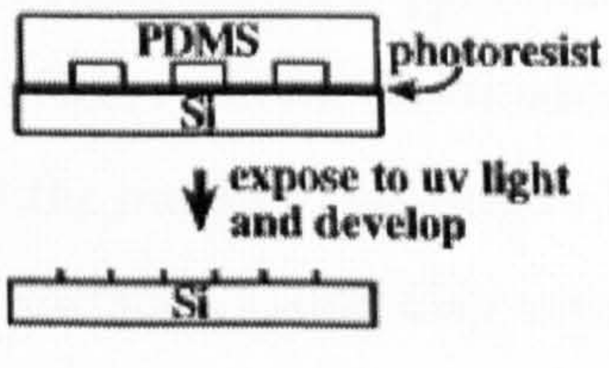

(d) NPSP

Fig 1.7 Schematic procedures of soft lithographic methods [46]

In Replica Moulding, an elastomer (e.g., PDMS) is cast against a rigid master and the elastomeric replica is subsequently used as a mould against which new replicas are produced in organic polymers. The new PDMS elastomeric mould can be easily separated from both the master and the replica due to its low surface energy. Replica moulding with elastomeric PDMS offers an economic option in nano-fabrication in that multiple copies of identical nanostructures from a single master can be produced rapidly. Using this method, nanostructures of lateral dimension of 35 nm were replicated with an accuracy of 5 nm in vertical dimension [48].

In Micro-Contact Printing (Fig 1.7 c), the elastomeric PDMS mould inked with a solution is used as a stamp to transfer the ink molecules to those regions of the substrate that contact the stamp. After rapid conformal contact between the stamp and the surface of the substrate, arrays of nanowires can be formed on the substrate by self-assembly of the ink mono-layers (SAMs). These patterned SAMs can also be used either as resists in selective wet etching or as templates in selective deposition [47].

Near-field Phase-Shifting Photolithography (NPSP) (Fig 1.7 d) uses masks constructed from "soft" organic elastomeric polymers which spontaneously and non-destructively come into conformal, atomic-level contact with layers of photoresist over areas that can exceed several hundred square centimetres without the need for external force. These phase-shifting masks effectively eliminate the gap between projecting regions of the mask and the resist, and atomic-level contact allows for exposure of the resist directly in the near field of the mask. Dust on the resist or the mask, non-uniformities in the thickness of the resist, or bowing of the mask or the substrate that supports the resist only locally deteriorate contact, which otherwise greatly affects correct positioning in contact-mode photolithography. The relative insensitivity of the masks to bowing or bending of the substrate enables it to be applied even to curved surfaces. Using elastomeric binary phase-shifting masks with conventional photo-resists and polychromatic, incoherent ultraviolet light, lines as narrow as 50 nm were generated on both flat surfaces and surfaces of cylindrical lenses by Younan Xia and co-workers [46].

Soft lithography is a promising technique for micro-fabrication of relatively simple, single-layer structures for use in cell culture, as sensors, as micro-analytical systems, in MEMS (MicroElectronic Mechanical System), and in applied optics. Although it offers great advantages over photolithography and other conventional micro-fabrication techniques for applications in which patterning of non-planar substrates, unusual materials, or large area patterning are the major concern, the success of reproducible and reliable nanofabrication depends on corresponding patterning of an elastomer, which makes the technique complicated.

1.1.4 Nanofabrication by Energetic Particles

Energetic particles such as electrons, atoms and ions can be used to induce nanostructures on solid surfaces. Typical examples are electron-beam lithography (EBL)[49, 50], ion beam nanofabrication [6-8, 51-70], and atomic-beam holography[71], etc.

Electron beams are used in the fabrication of nanostructures because of their extremely short wavelength and susceptibility to deflection and modulation with speed and precision by electrostatic or magnetic fields [60]. For example, low energy electron beams were used to fabricate islands on CaF_2 (111) surfaces [6, 72]. A shape transition of islands from a compact shape to an elongated shape was observed for the islands larger than 20 nm in diameter [6, 72]. The formation of elongated islands was explained as low energy electron-stimulated desorption of fluorine from a cleaved CaF_2 (111) surface.

Electron beam lithography (EBL) is a widely used technique to generate arbitrary micro/nano-structures on solid surfaces. A typical EBL technique consists of scanning a beam of electrons across a surface covered with a resist film sensitive to those electrons, thus depositing energy in the desired pattern in the resist film. The process of forming the beam of electrons and scanning it across a surface is very similar to what happens inside the everyday television or CRT display; but EBL typically has three orders of magnitude better resolution. The main application of EBL is in mask-making because of its flexibility in providing rapid turnaround of a finished part described only by a computer CAD (Computer-Aided Design) file. EBL is also used to directly write integrated

circuits [73] and produce small volume speciality products, such as GaAs integrated circuits and optical waveguides. The main attributes of the technology are: 1) it is capable of very high resolution, with beam spot sizes almost to the atomic level; 2) it is a flexible technique that can work with a variety of materials and almost infinite number of patterns; 3) it is slow, being one or more orders of magnitude slower than optical lithography; and 4) it is expensive and complicated - electron beam lithography tools can cost many millions of dollars and require frequent servicing to function properly.

Researchers from NEC [71, 74-76] reported an atom manipulation technique called atomic-beam holography (Fig 1.8). It enables direct pattern generation on a substrate by passing laser-cooled atoms through a computer-generated hologram. It is expected to be a technique with atomic resolution and high throughput. Figure 1.8 shows a schematic diagram of an experimental apparatus for the technique. The experiment was performed in a high-vacuum environment. Ne atoms coming from a deflector were slowed in a Zeeman slower by a counter-propagating laser beam. At the end of the Zeeman slower was a magneto-optical trap with a four-laser beam configuration. The Ne atoms were cooled and trapped around the point of zero magnetic field of the trap with the help of the four resonant laser beams which were directed toward the centre. The cooled atoms were released by applying another laser called the transfer laser, whose wavelength is different from that of the four resonant lasers, the atoms were pulled by the gravitational force, and fell nearly vertically. When the atoms reached a particular point, they had the same kinetic energies and hence the same De Broglie wavelength. Nanometre-scale wavelength (7.1 nm in this case) was obtained by adjusting the falling distance. Those atoms were then diffracted by the hologram and formed a reconstructed pattern which was detected below the hologram by using a micro-channel detector equipped with a fluorescent plate. The limitation of this technique is that trapping of Ne atoms needs ultra-low cooling (50 μK).

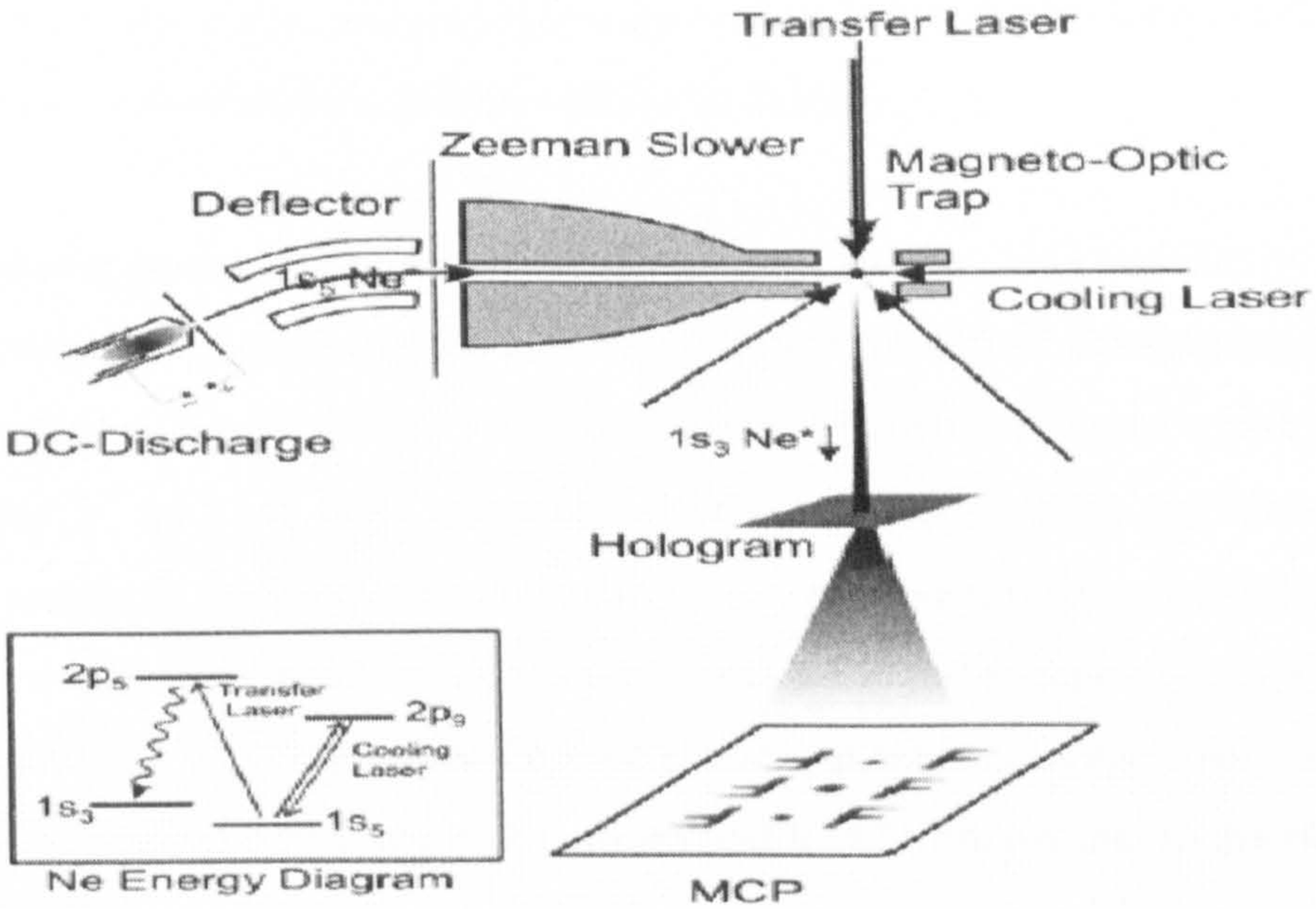

Fig 1.8 Schematic diagram of an experimental apparatus for atomic-beam holography [74]

Ion beams have been widely used in fabricating micro/nano structures. There are several names for this technique and its variants: ion beam bombardment, ion beam sputtering, ion beam irradiation, ion beam lithography, ion beam etching, and ion beam milling. For convenience we call this technique ion beam nano-fabrication. Typically an ion gun running in a UHV chamber generates ions in a confined plasma discharge and accelerates them in the form of a beam toward the sample. Nanostructures are generated under prolonged bombardment by these energetic ions due in many cases to the loss of surface atoms sputtered by the impinging ions.

Since ion beam nanofabrication is the focus of the experiments reported in this thesis, a detailed review of ion beam nanofabrication, especially on III-V semiconductor surfaces, is presented in this section.

Ion beam sputtering of solid surfaces produces various topographies e.g. dots [77-82], cones, islands [83], ripples [55, 59, 61, 62, 64, 66-68, 77, 81, 84-87], and nanowires [6-8, 78, 88]. Ion beam irradiation on semiconductor surfaces has been an active subject of research because of its efficiency in creating quantum dots in large quantities and arrays of nanowires in parallel over a

macroscopic area. These dots and nanowires are expected to be the building blocks for trace gas sensors, nanoelectronic and nanophotonic devices.

Previous studies reported fabrication of nanostructures on CaF_2 (111) surfaces by low-energy Ar^+ ion beam irradiation under grazing incidence condition. Grazing incidence ion-beam irradiation was used to create phase-separated domains and nanometer-scale calcium islands [6, 83] of 2 ML high, with a characteristic separation of 11 nm. The island and domain structures were explained by nanoscale stress domains related to local self-ordering of a single calcium ad-layer on phase-separated F^- and F-centre terminated mesoscopic domains [6, 83]. Preferential fluorine erosion on some cleavage steps was shown to form very long calcium nanowires of uniform width of 15 nm parallel to the step edge, explained by energy minimization of strained commensurate islands [6, 8]. Ion-beam irradiation under grazing incidence conditions was also successfully used to fabricate extended nanowire arrays (Fig 1.9) with exceptional long-range order on CaF_2 surfaces [6, 7]. Self-organization of stress fields associated with lattice-mismatched calcium layers on CaF_2 formed by ion-beam induced depletion of surface fluorine atoms was proposed as a model for the formation of these periodic nanoscale structures.

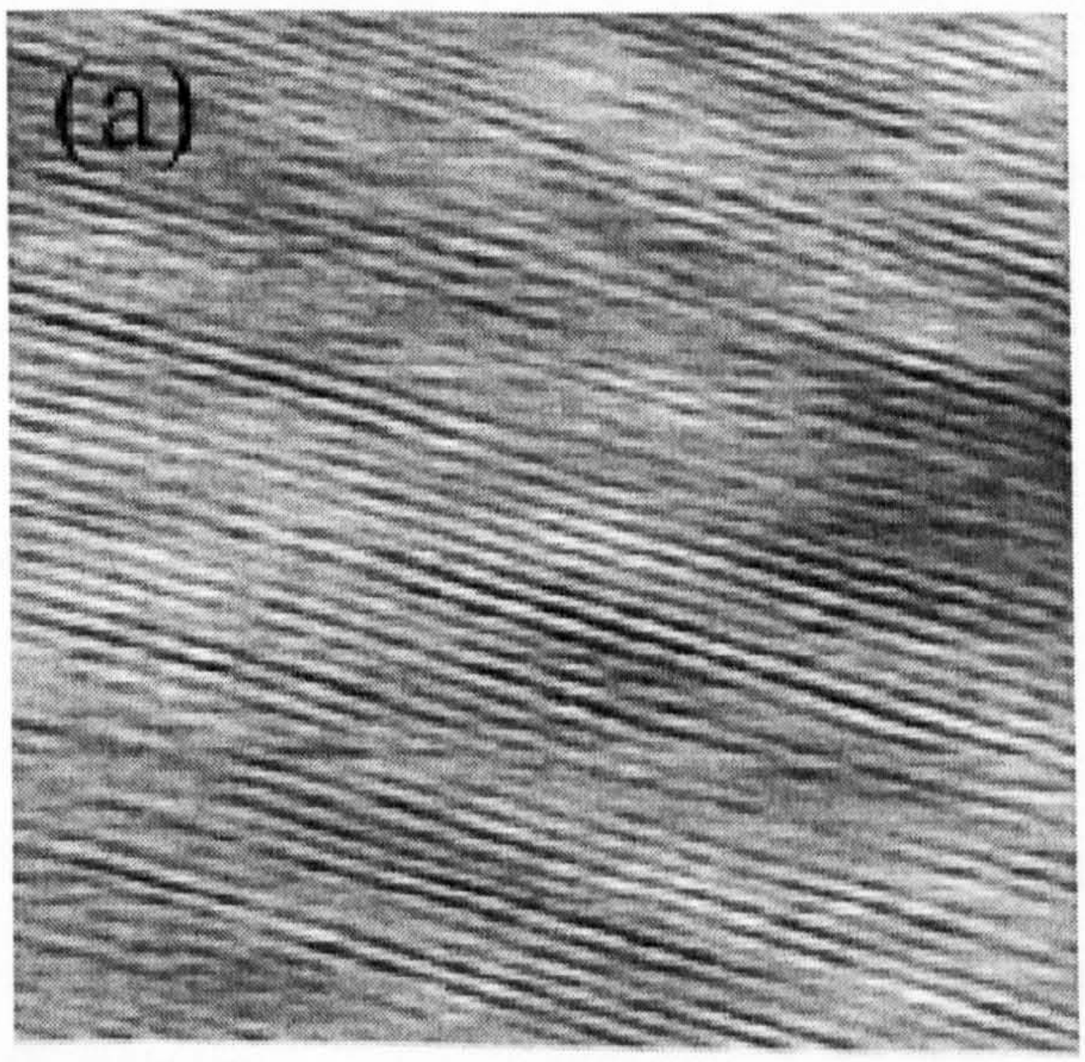

Fig 1.9 AFM topograph of a wire array [7] formed at a glancing incidence angle of 80°, area 390 x 390 nm^2. Sample irradiated at a fixed azimuthal orientation with a 4.5 keV Ar^+ ion beam and an ion fluence of 2.6 x 10^{15} ions/mm^2 at a grazing angle of 80°.

Because of its pervasive use in the semiconductor industry, silicon is the material which attracts most of the research among all the semiconductors. For example, regular isotropic distributed dots of size 20--50 nm and amplitude 2 nm have been reported [77](Fig 1.10) on p-type Si (100) surfaces irradiated by 0.5—1.8 keV Ar^+ ions under 75° incident angle at room temperature, with sample rotation during irradiation. The mean size of the dots was calculated from the full-width at half-maximum (FWHM) of the first order power spectral density (PSD) peak. The ordering of the dot patterns were found to increase with time of irradiation.

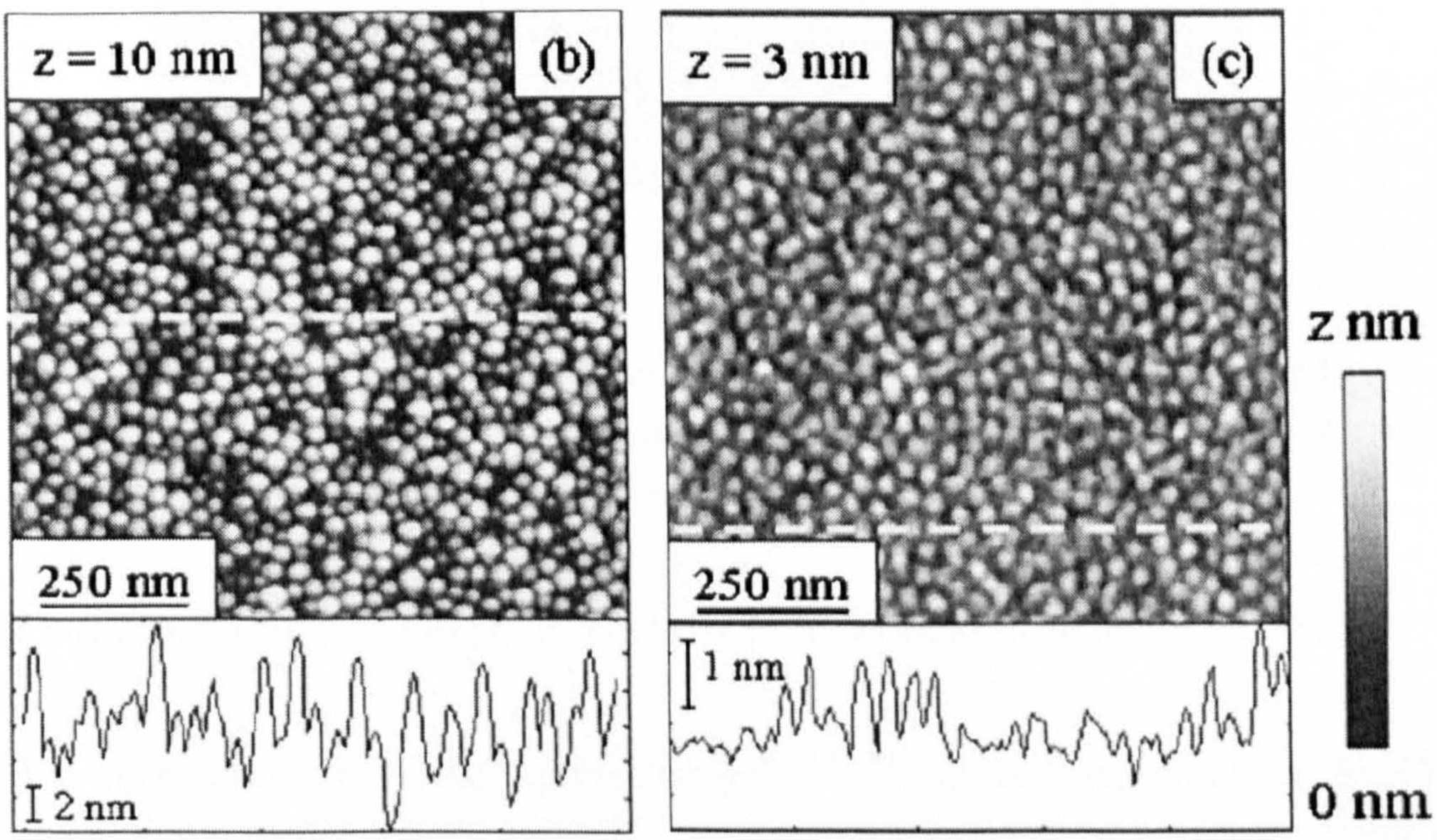

Fig 1.10 AFM images [77] of Ar^+ ion-beam eroded Si surfaces (j_{ion} = 300 μA cm^{-2}, T=285 K) at 75° ion-incident angles and ion energies: (b) E_{ion}=500 eV/20 min, (c) E_{ion}=1800 eV/60 min respectively. Image sizes 1μm x 1 μm.

J D Erlenacher reported ripples[55] (Fig 1.11) of wavelength 580 nm and amplitude 20 nm on Si (111) surfaces after 0.5 keV Ar^+ ion beam irradiation under 70° at elevated temperature (600 °C). The samples were kept fixed without rotation with ion beam projected along [1, -1, 0] direction.

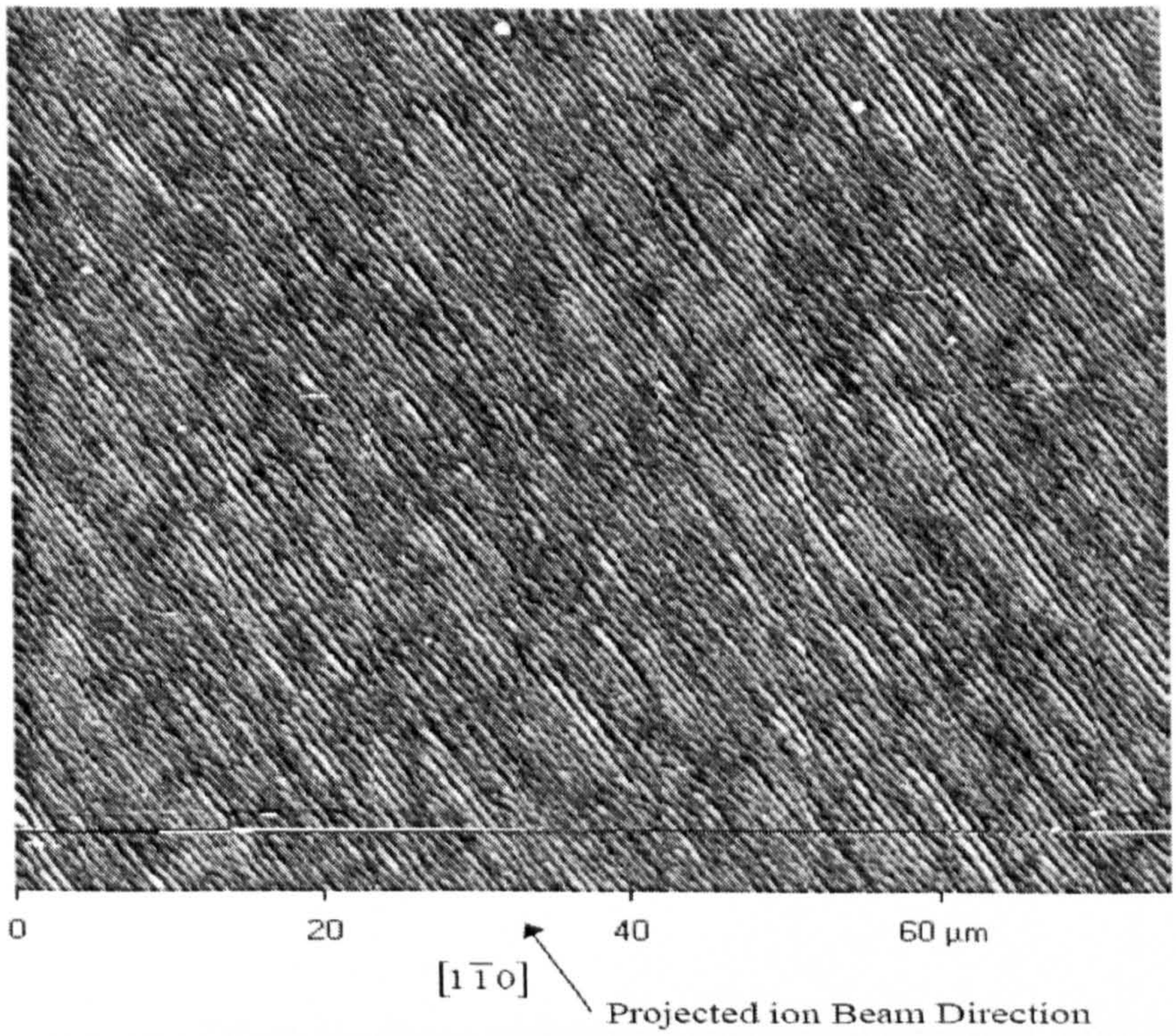

Fig 1.11 AFM micrograph of ripples on Ar^+ ion irradiates Si (111) surfaces [55]. Ripple wavelength = 580 nm; ripple amplitude = 20 nm. Irradiation parameters: energy = 500 eV, ion incident angle = 70°, J_{ion} = 10 mA/cm^{-2}, substrate temperature = 650° C, time = 4.5 hrs.

The same experiment failed to produce ripples with ion incident angle below 60°.

Similar ripple patterns were also reported on Ar^+ [59, 68, 84] and Ga^+ [67] ion irradiated Si (001) surfaces with sub-keV bombarding energy at temperatures ranging from 400 °C to 700 °C. The ripples were found parallel to the ion beam direction under grazing incidence conditions.

Recently, Yongqi Fu [89] reported straight ripples on room temperature sputtered Si (111) surfaces by 25 keV focused Ga^+ ion beams. Ripples of wavelength 600--2100 nm and depth 40—300 nm were fabricated under different combinations of experimental parameters. The ripple wavelength and depth were found to increase with the ion energy and dose, while the ripple wavelength increased and the depth decreased with ion incident angle. In another study[90], ripples of wavelength 2.5 μm and depth 130 nm were

obtained on 50 keV Ga^+ ion sputtered n-Si (100) surfaces at room temperature under 30° ion incident angle at a dose of 6.5 nC/cm^2.

In addition to silicon, Eric Chason [66] reported ripple formation on 1 keV Xe^+ ion irradiated Ge (001) surfaces. The ripples were found perpendicular to the surface component of the ion beam direction with ion beam projected 55° from the surface normal and substrate temperature 250 °C. The development of ripples was explained as curvature-dependent sputter yield.

For III-V compound semiconductors, dots, cones, ripples and nanowires have been produced on ion beam irradiated GaAs [91, 92], InSb [78, 82, 88], GaSb[82, 93], and InP [52, 69, 92] surfaces, etc.

Ion beam irradiation of GaAs induces undulating surfaces with small amplitude [92, 94-96]. Ripples were found perpendicular to the surface component of the ion beam direction on GaAs surfaces sputtered by 2.5—8 keV oxygen and cesium ions with ion incident angle between 37° and 42° to a dose rate between 2.5×10^{15} and 3×10^{16} $cm^{-2}s^{-1}$. No ripples were found at near normal or grazing incident ($\theta > 60°$) angles. For oxygen ion bombardment at room temperature [94, 96], the wavelength of the ripples remained approximately constant irrespective of the ion dose.

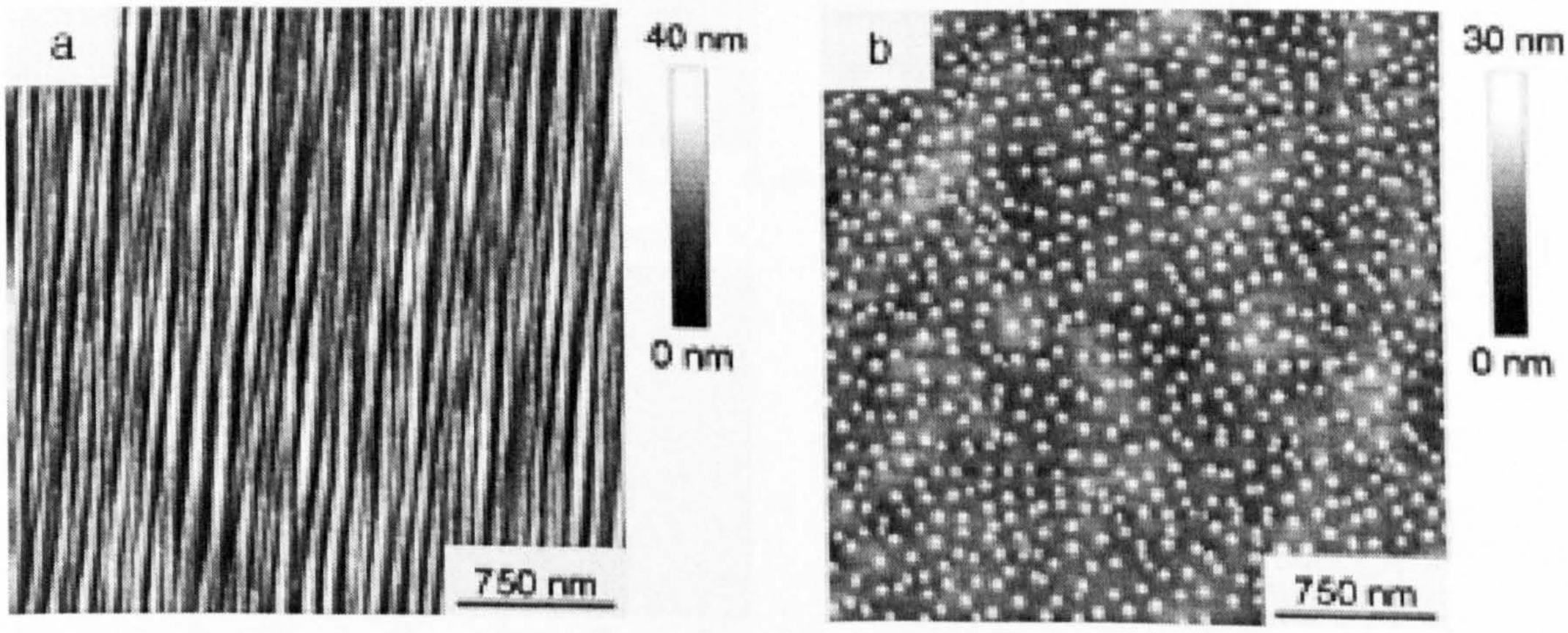

Fig 1.12 AFM images of InSb surfaces (3 μm x 3 μm) bombarded with Ar^+ ions at room temperature (Ref [97]) (E_{ion} = 500 eV, θ_{ion} = 80°, j_{ion} = 400 μAcm^{-2}, sputter time of 10 min): (a) no sample rotation and (b) sample rotation.

Dots and ripple structures were observed (Fig 1.12) on low energy (0.5 keV) Ar^+ ion sputtered InSb (100) surfaces at room temperature under grazing incident angle [97]. For the samples sputtered with sample rotation, isotropic distributed dots evolved with a mean separation of 110 nm and a lateral size between 40 and 60 nm. For the samples sputtered at fixed azimuth, ripples of wavelength 80 nm and amplitude 13 nm were formed along the surface component of the direction of the incident ion beam.

In another study, F. Krok and co-workers[88,Krok, 2003 #419] observed parallel wires of high density (Fig 1.13) on InSb (001) surfaces bombarded with 4 keV Ar^+ ion beam under 50° incident angle at a dose of 1×10^{14} to 6×10^{16} ions/cm^{-2} at room temperature, with ion beam projected along [1,-1,0] direction, perpendicular to the direction of surface reconstruction raw—[1,1,0], while bombardment with an ion beam parallel to the surfaces reconstruction rows produced sparsely distributed wires with random direction. The formation of parallel wires was explained as anisotropic diffusion of ad-particles activated by the primary ions and/or primary knock-on atoms carrying a fraction of the initial beam momentum.

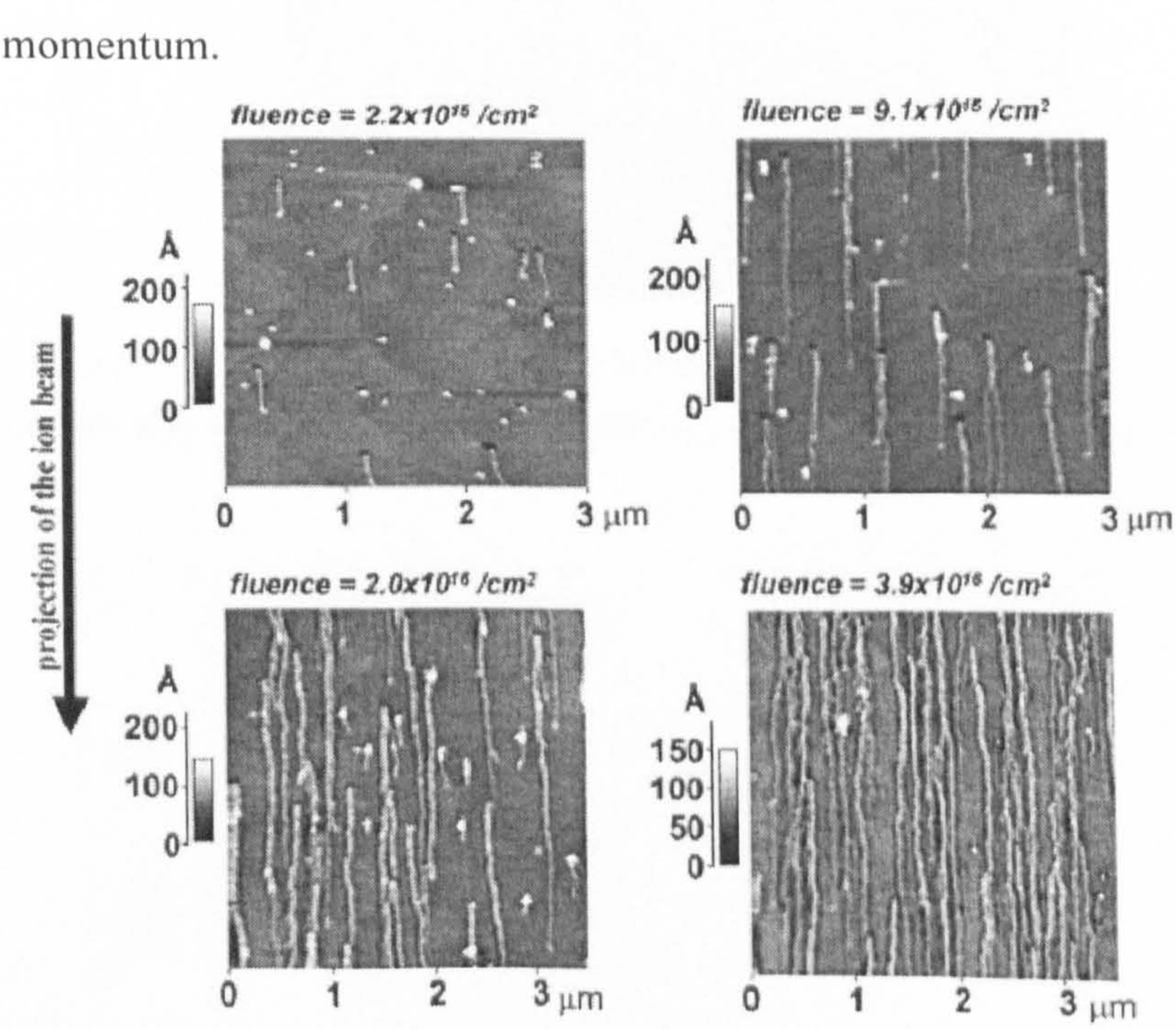

Fig 1.13 AFM images of ion bombarded InSb (0 0 1) surfaces with various fluences [88]. Ion-beam energy: 4keV; ion flux: 2.15×10^{15} ions/cm^2 s, ion beam incident angle: 50° (off normal)

Similar results were also documented on Ar^+ ion sputtered GaSb surfaces [81, 98]

Ion beam irradiation of InP induces dots [80, 97, 99], cones [80, 100, 101] and ripples [102-104]. For example, hexagonally close-packed dot arrays have been produced [81, 99] (Fig 1.14) by 0.5 keV Ar^+ ion irradiation of InP (100) surfaces under 30 incident angle with ion flux of 400 μAcm^{-2} and simultaneous sample rotation. The mean separation between the individual dots as well as the height of the dots were found to increase with temperature, and the dots produced at elevated temperature showed a truncated conical shape with side-wall angle greater that 80°.

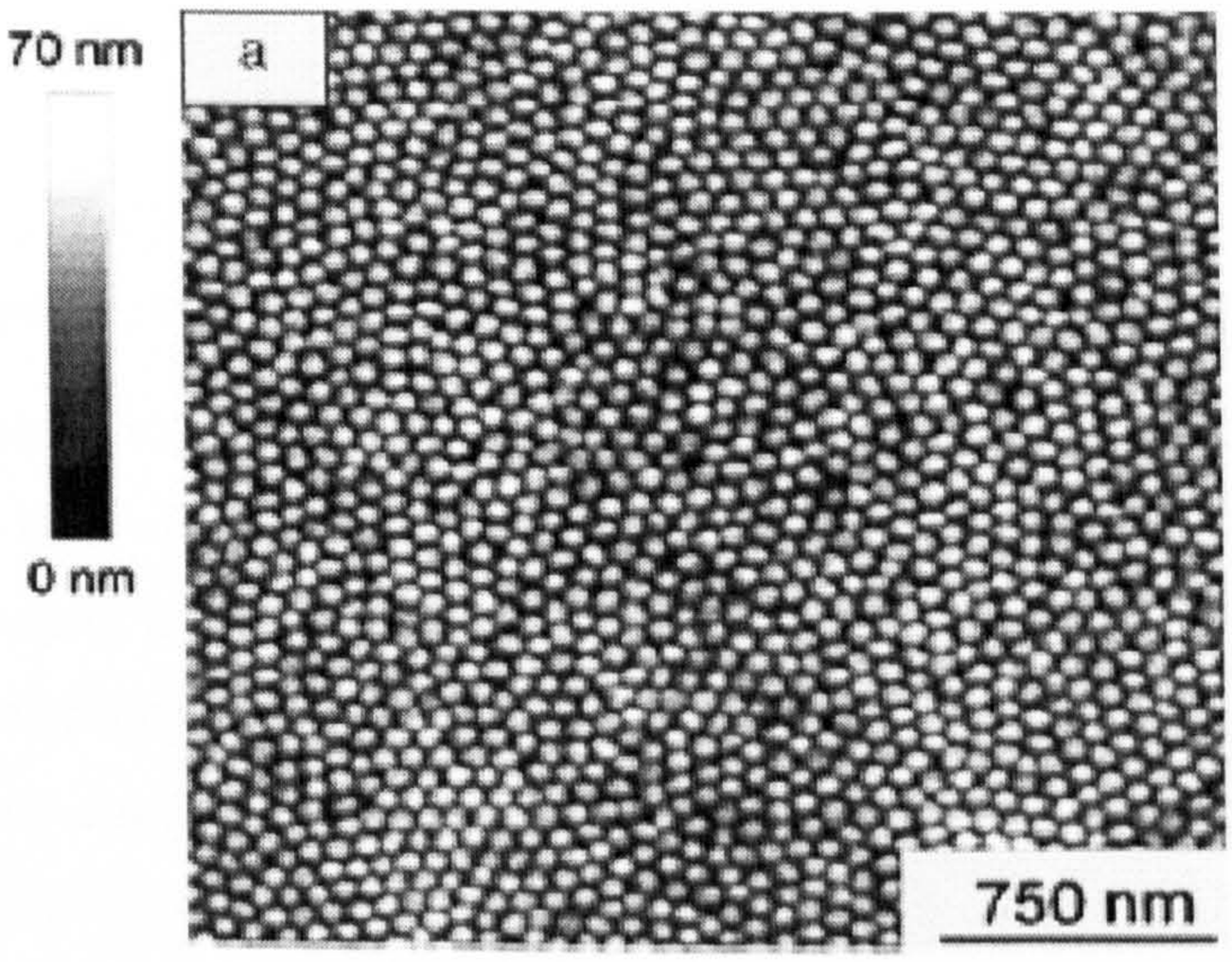

Fig 1.14 AFM image (3 μm x 3 μm) of self-organized InP dot pattern [81] produced by Ar^+ ion sputtering with E_{ion} = 500 eV, α_{ion} = 30°, J_{ion} = 400 μAcm^{-2}, sputter time of 90 min.

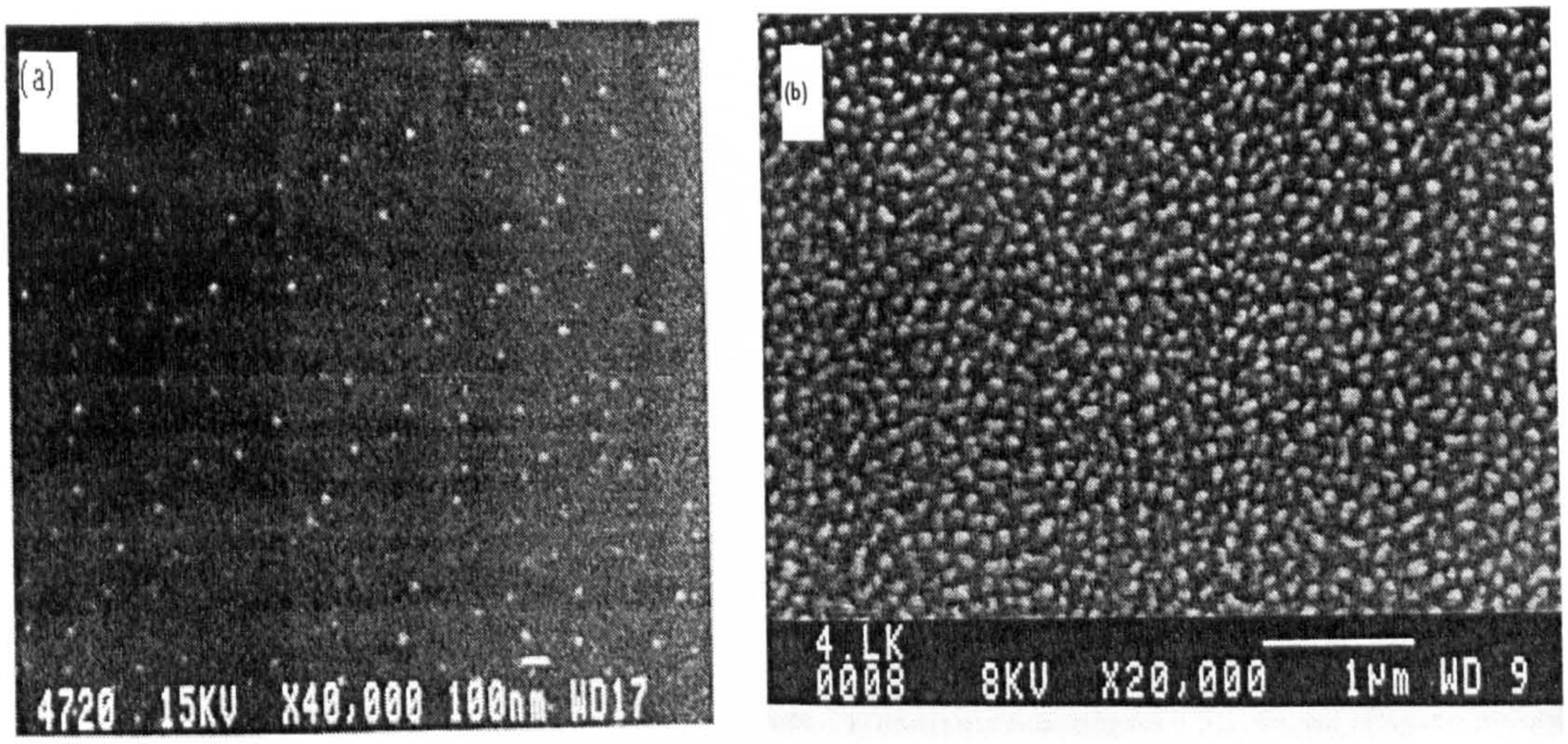

Fig 1.15 SEM micrographs depicting cone formation on InP wafers bombarded by Ar^+ ions [102]: (a) 10 keV to a dose of 3×10^{15} ions/cm^2; (b) 8 keV to a dose of 1.5×10^{16} ions/cm^2

The formation of cones [102] (Fig 1.15) on Ar^+ ion sputtered InP has been widely documented [79, 80, 102, 103, 105-112]. The cones were observed [102] to appear (Fig 1.15 a) at a dose of approximately 3×10^{15} cm^{-2} as small protuberances (~10 nm) that grow (Fig 1.15 b, dose densities ~10^{15} --10^{16} cm^{-2}) to sizes of 10 to 100 nm, with a slight increase in the surface roughness upon ion energy at energies below 1 keV. At a constant ion dose and energy, the size and density of these cones depend on the angle of incidence of the impinging ions, with a maximum obtained at an ion incidence angle of 41° to surface normal [102], and a minimum at grazing incidence [111, 112].

The increase in dot sizes and density upon increasing ion dose was also reported by Yoshihiko Yuba and co-workers [79], in which cones with mushroom-like tops (Fig 1.16) were found on InP samples irradiated at 2 keV Ar^+ ions at room temperature. The mushroom tops were ascribed to the deposition of the sputtered material.

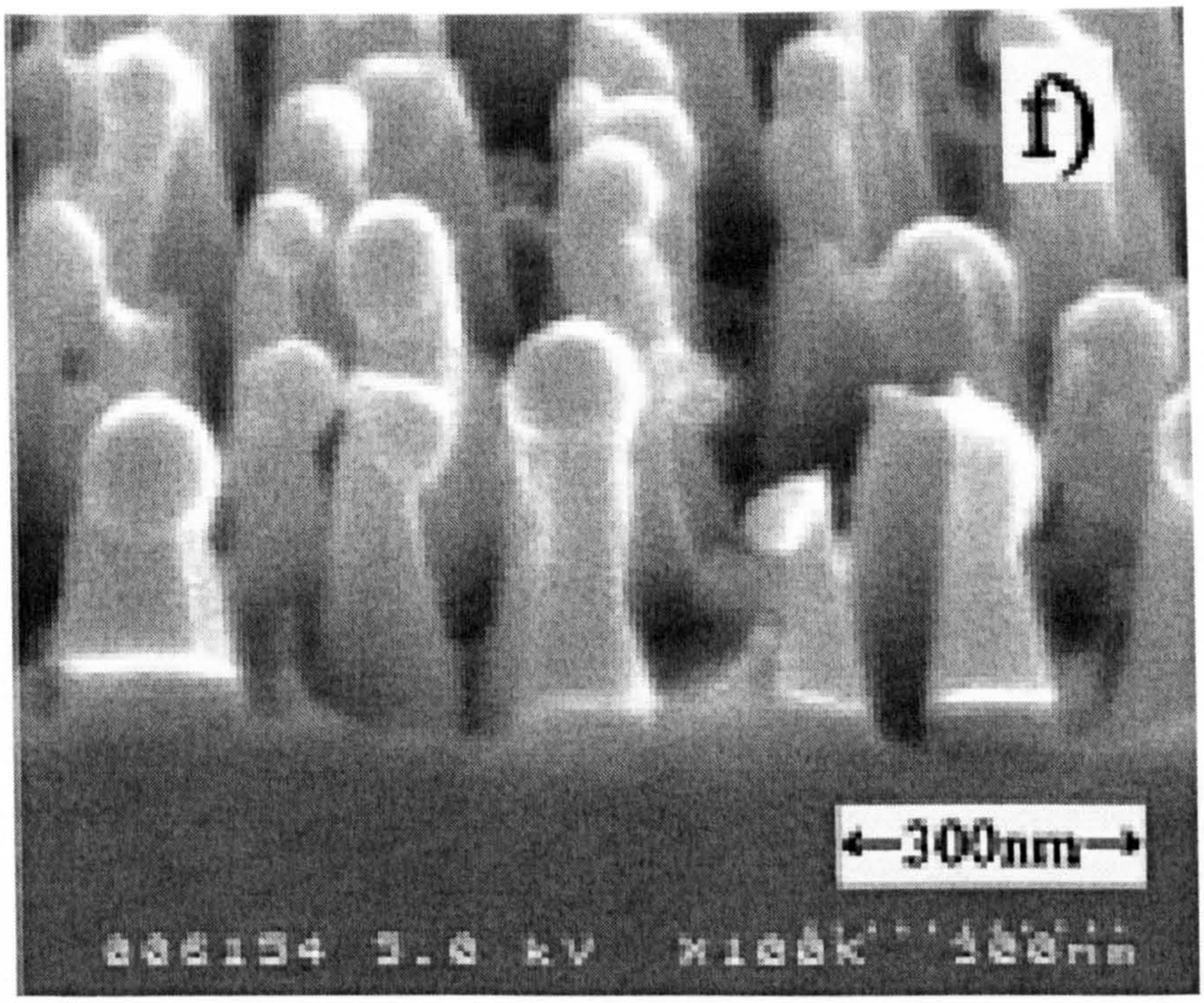

Fig 1.16 SEM micrograph [79] showing cones with mushroom-like tops on samples sputtered at 2 keV Ar^+ ions to a dose of 1.3 x 10^{18} cm^{-2} at room temperature

A study of O^{2+} ion irradiated InP (100) surfaces reported an increase in cone density and decrease in cone size with ion energy ranging 2 to 6 keV and ion incidence angles from 0 to 60° [113]. For ion energy above 6 keV and incidence angle larger than 60°, an opposite trend was observed. This was explained as mergence of small cones to form large cones at higher ion energy and grazing incident angles.

Different from the isolated cones (Fig 1.15), some research [102-104, 114] observed cones with tails (Fig 1.17) or spikes. These tailed cones were believed to originate from seeding (re-deposition) from the sample holder by impurity atoms [102, 114]. The tailed cones were also found in the experiment in this study and the mechanism for the formation of these cones will be discussed in detail in Chapter 5.

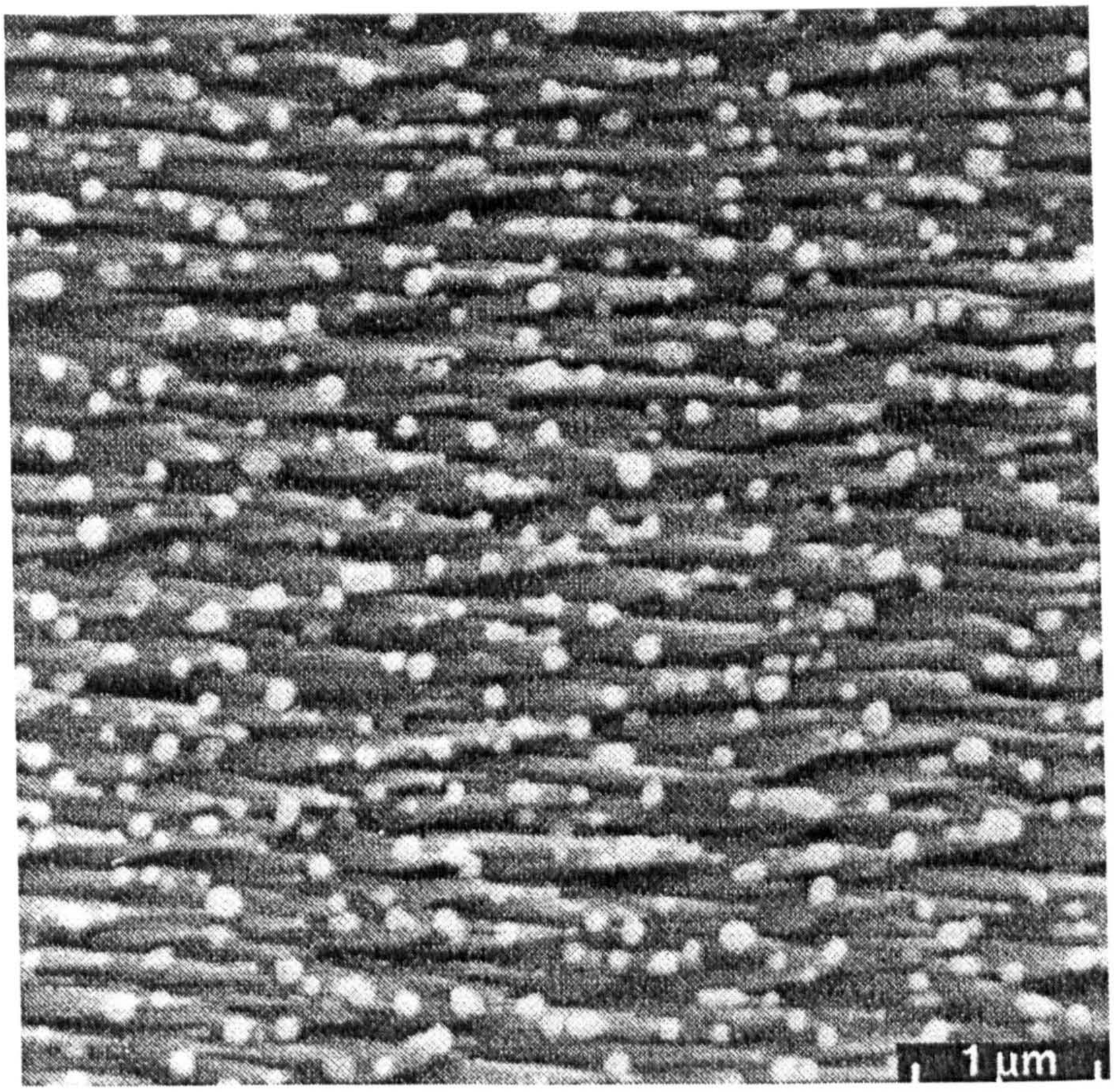

Fig 1.17 SEM image showing seeding cones formed on Ar^+ ion sputtered InP surface [102]

In contrast to the theory of impurity seeded cone formation, cooling InP samples to -183°C results in a suppression of cone formation [92, 107]. This indicates that an erosion process is not the only mechanism in cone formation on InP surfaces, but that the movement of atoms or InP molecules is a prerequisite for cone formation.

The development of ripple topography on InP surfaces sputtered at room temperature has been reported [102-104]. Malherbe and Van de Berg [102] demonstrated that the ripples gradually developed from cones with increasing dose density (Fig 1.18), and the orientation of the ripples was found to be perpendicular to the surface component of the ion beam with ion projected 71° from the surface normal[102]. Gries [103, 104] found that 45° incidence induced ripples along the direction of the ion beam.

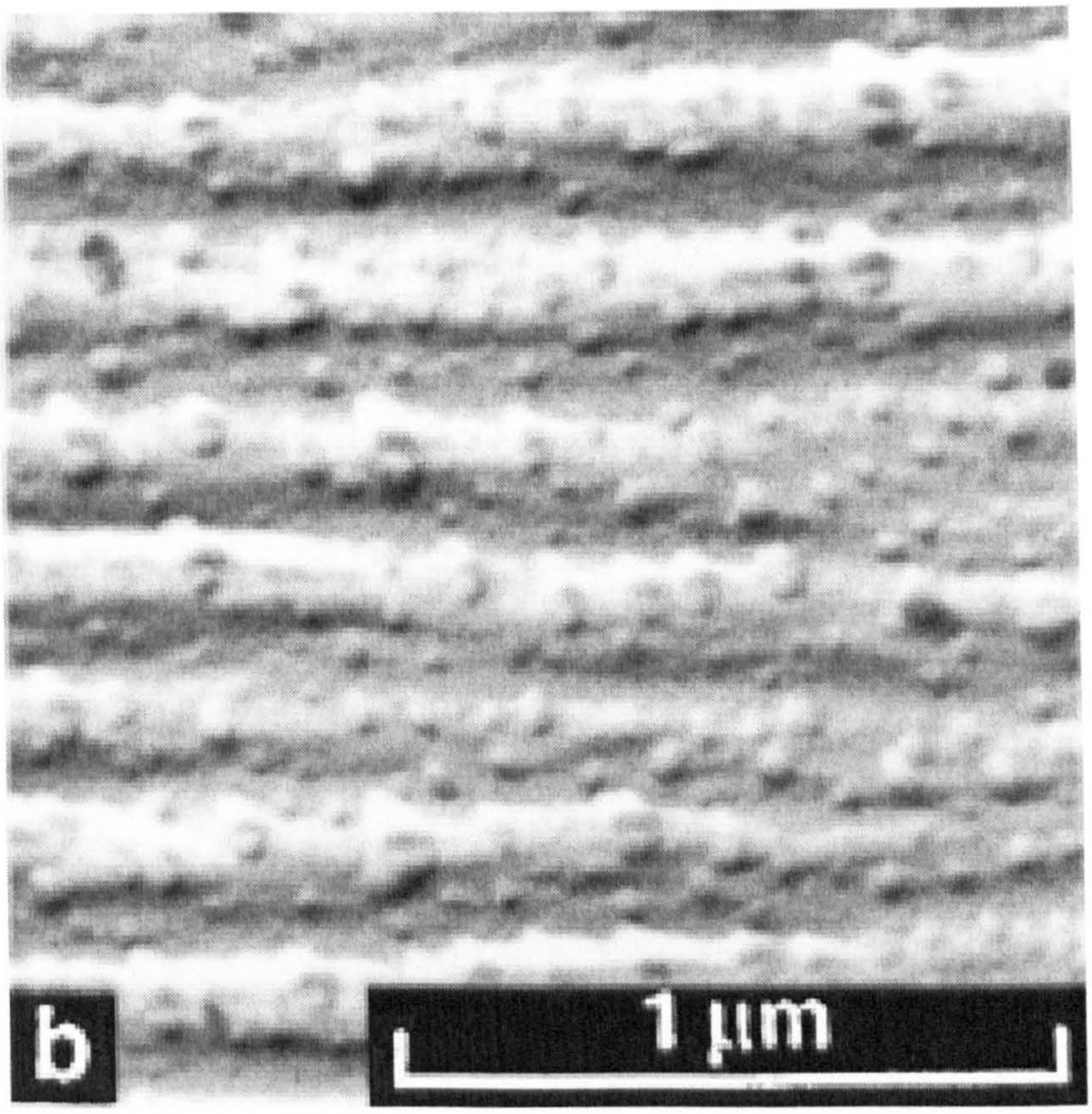

Fig 1.18 TEM micrographs of Cr-C replicas depicting the ripple development on InP following Ar^+ bombardment of InP at an angle of 71° to the sample normal [102].

Room temperature sputtering of InP by O^{2+} ions at an incidence angle of 47° [95]and by Cs^+ as well as by O^{2+} [92]ions at angle of incidence of 25° (for Cs^+) and 42° (for O^{2+}) also resulted in ripple formation. But no specification of ripple orientation was described.

As fabrication of nanowire arrays on InP (100) surfaces by Ar^+ ion beam constitutes the main subject of this research, it is necessary to have a general review of the results related to low-energy Ar^+ ion bombardment on InP surfaces. Although not an exhausted review, most of the published results for low-energy Ar^+ ion bombardment of InP surfaces are tabulated in table 1.1.

Table 1.1 Summary of published results of low–energy Ar^+ ion beam bombardment on InP surfaces (Results before 1990 were extracted from Ref [115])

Index plane	Ananlyzing techniques	Ion Energy (keV)	Ion Incident Angle (°)	Surface composition after bombardment	Surface topography after bombardment	Ref.
(100)	XPS*, AES*, LEED*	0.48	--	InP	--	116
(100)	SIMS*	0.5	45	In enriched	Textured	117
(100)	AES	--	--	--	Preferential sputtering effects observed	118
(110)	AES	0.5	--	$InP_{0.64}$	--	119
(-1,-1,-1)	AES	0.75	--	In enriched	--	120
(110)	AES	0.5	--	$InP_{0.82}$	In islands	121
(100)	XPS	4	--	In enriched	--	122
(100)	RBS*	1,2,3	45	In enriched	--	123
(110)	ELS* AES	2	--	In	ELS: 2—3 ML In AES: Microclusters of In	124
(110)	AES, RHEED*	0.5 1 1.5 3 0.5	0 0 0 0 45	$InP_{0.72}$ $InP_{0.82}$ $InP_{0.92}$ InP $InP_{0.52}$	SEM contrast (r~0.5 μm) observed after prolonged 3 keV bombardment ; no evidence of In microdropletes	110
(110)	AES	0.5-5	--	$InP_{0.54}$ $InP_{0.43}$	Textured No topography with sampled cooled to -183°	125
(110)	AES	0.5	--	$InP_{0.57}$	--	126
--	AES	0.25-1.5	--	In enriched	Cones	111, 114
(111)-n	ELS XPS	8	35.7 41 50 61	$InP_{0.48}$ $InP_{0.47}$ $InP_{0.47}$ $InP_{0.49}$	In islands	112

			68 77 81 85 89	$InP_{0.51}$ $InP_{0.52}$ $InP_{0.56}$ $In_{0.60}$ $In_{0.71}$		
(100)	AES, EPES*, ELS	<0.5	--	$InP_{0.33}$/P/InP	4 MLs of In crystallites with a coverage of 0.25	[127-130]
(100)	AES	<0.5	--	In-rich ML on P ML	--	[131]
(100), (110)	XPS	1-3	45	$InP_{0.5}$	--	[132, 133]
(100)	AES, ELS	0.5	0	$InP_{0.75}$	Textured	[134]
(100), (111)	XPS, ELS	--	--	In enriched	In islands	[135]
--	SEM*	0.2, 0.5, 0.8	0-75	--	In droplets at 0.8 keV; No In droplets at 0.2, 0.5 keV	[136]
--	AES	4		InP	Filament-type patterns of diameter 50—100 nm	[103]
(100)	AES, ELS	0.3	--	In enriched	In islands	[137]
(110)	ARAES* $\theta_e = 12°$ ARAES $\theta_e = 72°$, XPS, ELS	0.5, 1 2 4 5 4 4	55	$InP_{0.65}$ $InP_{0.61}$ $InP_{0.60}$ $InP_{0.5}$ $InP_{0.589}$ $InP_{0.5}$ $InP_{0.7}$	In clusters of the order of nanometers	[138, 139]
(100) (110)	AES	0.5-5	18 40 42 70	$InP_{0.68 \pm 0.07}$ $InP_{0.67 \pm 0.07}$ $InP_{0.78 \pm 0.07}$ $InP_{0.94 \pm 0.09}$	Textured	[115]
(100)	TEM*, AES, EELS*		7-10	InP	Cones and filament-type patterns	[140]
(110)	AES, SAM,	3	60	$InP_{0.72}$	Cones with slight	[92]

	XPS, ELS				enrichment in In	
(100) (110)	AES	0.5-5	0 11 30 41 52 60 71	$InP_{0.57 \pm 0.01}$ $InP_{0.57 \pm 0.01}$ $InP_{0.55 \pm 0.01}$ $InP_{0.59 \pm 0.02}$ $InP_{0.61 \pm 0.01}$ $InP_{0.65 \pm 0.01}$ $InP_{0.68 \pm 0.01}$	Cones	[141]
(100)	AFM	0.5-5	41	--	Seeding cones	[102]
(110)	AES	0.25 0.5 0.75 1.0 20	80 80 80 80 80	$InP_{0.77}$ $InP_{0.84}$ $InP_{0.80}$ $InP_{0.79}$ $InP_{0.55}$		[142]
(100)	AES, TEM	1-3	60	In	Filament-type patterns	[143]
(100)-n	AFM*, TEM	0.5 5	41 71	--	Cones & Ripples	[144]
(100)	AFM	0.5-5	41	--	Cones	[80]
(100)	SEM, TEM, EDX	3	60	InP	Sparsely isolated cones at 100°C; Ripples & micro-protrusions at RT; Fibrous-protrusions at -100°C	[100]
(100)	XPS, LEISS	3	--	$InP_{0.6}$	--	[145]
(100)	AFM	0.5	10+rotation 30+rotation 40+rotation 70+rotation 80+rotation	--	Hexagonally ordered close-packed array of cones or mounds with dimensions less than 100 nm	[97]
(100)	AFM	0.5	30+rotation	--	Hexagonally ordered close-packed array of dots of diameter 71 ± 8 nm	[81]

(100)	AFM	0.5	30+rotation	--	Hexagonally close-packed dot arrays with a mean dot diameter of ~70 nm.	[146]

*XPS—X-ray Photoelectron Spectroscopy;
*AES—Auger Electron Spectroscopy;
*LEED—Low Energy Electron Diffraction;
*SIMS—Secondary Ion Mass Spectroscopy;
*RBS—Rutherfold Backscattering Spectroscopy;
*ELS & EELS—Electron Energy Loss Spectroscopy;
*RHEED—Reflection High Energy Electron Diffraction;
*EPES—Elastic Peak Electron Spectroscopy;
*SEM—Scanning Electron Microscopy;
*ARAES—Angle Resolved Auger Electron Spectroscopy;
*TEM—Scanning Transmission Electron Microscopy;
*AFM—Atomic Force Microscopy.

It can be seen that bombardment with sample rotation generates cones or dots, while bombardment at fixed azimuth produces cones, filament-like structures and ripples. Almost all the results reported indium enriched surfaces after Ar^+ ion bombardment. The reason why an indium enriched surface is observed after Ar^+ ion bombardment on InP surfaces will be discussed in chapter 6. For surface topography development, although bombardment dose is not listed in table 1.1, one can find from the references given (e.g., Ref [102]) that ripples gradually develop from cones with increased ion dose, and ripple wavelength increases slightly with ion dose (e.g., ref [144]). Discussion of topography development and nanowire fabrication by Ar^+ ion beams on InP(100) surfaces from the current study will be presented in chapter 5.

1.2 The Bottom-up Approach

The bottom-up approach is a promising method for producing nanowires in large quantities. Nanowires are grown by vapour phase synthesis, templated synthesis or Electrodeposition, and molecular beam epitaxy (MBE), etc. Fabrication of regular, identical nanowires in large quantities is the most important subject that numerous researchers have explored with this technique.

1.2.1 Vapour Phase Growth of Nanowires

Vapour phase synthesis is the most extensively explored bottom-up approach to the formation of nanowires because of the simplicity and accessibility of the technique. In a typical process, the vapour species is first generated by evaporation, chemical reduction, or other kinds of gases reactions, these species are subsequently transported and condensed onto the surface of a solid substrate placed in a zone at a temperature lower than that of the source material. With proper control over the supersaturation factor, nanowires could easily be obtained in moderately large quantities.

Material evaporation can be realized by a heated furnace or quartz tube[147-149], laser[150-154], arc-discharge[155, 156], and sometimes enhanced by a plasma[157]. Among all the evaporation methods, laser assisted catalytic growth (LCG) aided with the analysis on the equilibrium phase diagrams is described as a general method for the synthesis of a broad range of compound semiconductor nanowires such as binary and ternary III-V (CaAs, GaP, GaAsP, InAs, InP, InAsP), II-VI (ZnS, ZnSe, CdS, CdSe), and IV-IV (SiGe) [150-153] wires.

The vapour based method features the vapour-liquid-solid (VLS) growth mechanism with the presence of intermediates that serve as catalysts between the vapour feed and the solid growth at elevated temperatures. A typical VLS process starts with the dissolution of gaseous reactants into nanosized liquid droplets of a catalyst metal, followed by nucleation and growth of single-crystalline rods and then wires. The one dimensional growth is mainly induced and directed by the liquid droplets, the sizes of which remain essentially unchanged during the entire process of wire growth.

Synthesis of nanowires of different materials by the vapour based methods has been intensely documented in recent years. Nanowires of Si[147, 148, 158-162], Ge[163, 164], Boron [165], SiO_2 [166, 167], SiC [168-171], silicon nitride [172], ZnO[173-175], MoO_2 [176, 177], CuO [178], indium oxide [154], GaN[179-182], indium nitride [183], Ga_2O_3 [184], B_4C[157], etc., have been reported.

1.2.2 Nanowire Formation using Templates

Some ordered systems such as anodic aluminium oxide (AAO) [185-192], surfaces with ordered structures [193], carbon nanotubes, etc., can be adopted as templates in the synthesis

of nanowires. Both AAO and hexagonal liquid crystals were used as templates to prepare parallel CdS nanowires[191]. Recently, Mei Lu and co-workers reported catalyst free CVD synthesis of Si nanowires templated by an alumina membrane [160, 194]. The membrane was isolated from the anodic oxidized aluminium substrate, cleaned, dried and heated in a quartz tube reactor at 900°C in the ambient of SiH_4 and H_2. Arrays of well-aligned silicon nanowires were found with HRTEM (high-resolution transmission electron microscope). The wires were confirmed to be defect free single silicon crystal with uniform diameter. The formation of the silicon nanowires without a catalyst was explained with the VLS mechanism. It was supposed that the internal pore surface within alumina behaves as a catalyst and the overcooling from the carrier gas (Ar) generates a temperature gradient which provides a driving force for nanowire growth.

By pressure injecting Bi liquid melt into the nanochannels of an anodic aluminium template, arrays of Bi nanowires with ultra-fine wire diameter and extremely high wire packing densities can be fabricated[195]. Using an array of polyanilline on an aluminium membrane support as a "second-order template", Co nanowires encapsulated with polyanilline were prepared [196]. By electroplating lead into nanopores of track-etched polymer membranes, arrays of superconducting Pb nanowires were generated by S. Dubois and co-workers [197].

The Si (001)-*2 x n* surface has been exploited as a template for spontaneous assembly of uniform indium nanowires [193]. After deposition of indium on the *2 x n* surface, indium atoms formed sparse dimer chains at a coverage of < 0.5 ML and developed into *2 x 2* re-construction at an indium coverage of 0.5 ML. With increased indium coverage, the indium dimer chains occupied most of the Si (001)-*2 x 1* surface and eventually developed into regular Si (001)-*2 x 2*-In domains separated by vacancy lines. These nanowires of 0.8 nm wide can withstand temperatures up to 150°C. The strategy also worked with Ga. An earlier report showed that adsorption of Bi on Si (001) surfaces induces 1 nm wide 'nanowires' that 'self-organize' over a length of several hundreds of nanometers without any defects [198, 199].

Mesosporus silicate templated synthesis of free standing Pd nanowires was prepared using chemical vapour infiltration (CVI) by Kyung-Bok Lee [200]. The synthesis involved loading an organo-metallic precursor into a template matrix via chemical vapour infiltration, followed by a mild thermal decomposition to generate Pd metal nanowires inside the template. After isolation of the freestanding Pd nanowires by removal of the silicate templates, nanowires of 3.7 nm, 4.6 nm and 8.8 nm in diameter and 50 to a few hundred nanometers in length were obtained from templates of different pore sizes.

Carbon nanotubes can be used as a template for the synthesis of carbide nanowires. The Zhengwei Pan research group demonstrated the synthesis of oriented SiC nanowires by reacting aligned carbon nanotubes with SiO at 1400 °C [201]. The SiC nanowires within the arrays have similar diameters (10-40 nm), spacing (~100 nm), and length (up to 2 mm) to those of the aligned carbon nanotubes. A field emission current of 10 $\mu A/cm^2$ was observed at applied fields of 0.7-1.5 V/μm, and current densities of 10 mA/cm^2 were realized at applied fields as low as 2.5-3.5 V/μm. The result represents the lowest field ever reported for any field-emitting materials at technologically useful current densities, indicating that the oriented SiC nanowires may have promising applications for vacuum microelectronic devices. Other oriented carbide (such as TiC, NbC, Fe_3C, or BC_x) or nitride (such as GaN or Si_3N_4) nanowires are expected to be able to be synthesized with this method.

Single crystal zinc oxide nanowires can be prepared by filling carbon nanotubes with zinc oxide via wet chemical techniques [202]. Crystalline zinc oxide was introduced into carbon nanotubes by immersing empty and dried opened tubes in zinc nitrate solution followed by filtration and calcinations. After burning off the carbon nanotubes at 750°C in air for 2 hours, hexagonal ZnO crystalline nanowires, with diameters in the range of 20-40 nm and lengths of up to 1 μm, were formed.

Nanowires of Au, Ag, Pt, and Pd can be produced in the capillaries of single-walled carbon nanotubes by a simple chemical method [203]. Suspended single-walled carbon nanotubes were used as substrates for deposition of various metals by evaporation [204].

Continuous nanowires of virtually any metal were obtained by using titanium, a metal which has strong interaction with carbon, as a buffer layer of nanotubes. The metal nanowires can be ≤ 10 nm in diameter with a continuous length up to tens of micrometers, which are difficult to fabricate by lithographic methods.

Jan Richter used DNA as a template to produce conductive nanowires[205]. Palladium nanowires exhibiting ohmic transport behaviour at room temperature were produced by chemical deposition of a thin continuous Pd film onto single DNA molecules. DNA-directed assemblies of Au nanowires can be prepared on complementary surfaces [206].

One of the major problems associated with the templated growth process is the difficulty in achieving a precise control over the composition and crystallinity of the final product. Nanowires synthesized using these methods were often polycrystalline in structure, and only a few schemes have led to the formation of single-crystalline products. For a templating process that involves chemical reactions on the surfaces of nanowires, if the product has a larger molar volume than the initial template, the reaction may automatically stop after a certain period of time when the stress accumulated around the template has reached the paramount value [207].

1.2.3 Nanowire Fabrication by Electrodeposition

Electrodeposition of metals at the cathode of an electrolysis cell provides a means of metal nanowire formation with high yield [208]. Using this method, Carbon-encapsulated Sn-Pb nanowires were generated by electrolysis of graphite in molten LiCl containing these metals. S. Bhattacharyya *et al* prepared silver nanowires within the pores of silica gels [209]. The gels were treated in the temperature range 523 to 823 K in order to change the pore diameter within the gel. The pores were then filled up with $AgNO_3$ after soaking the gel in silver nitrate solution. Subsequently, silver paste was applied on two opposite faces of the treated sample and silver nanowires of diameter ~40 nm and length ~0.3 mm were extracted between the two electrodes after applying a dc voltage of 8 V across the specimen for 30 minutes. A staircase current-voltage characteristic was observed in the direction of electrodeposition after the nanowires were disrupted by the application of a

dc voltage pulse. Silver [210] or copper [211] nanowires can also be formed in a polymeric film using this method. Electrodeposition of nanowires of various materials via alumina templates has been intensely documented recently[212-227].

1.2.4 Nanowire Growth by Molecular Beam Epitaxy (MBE)

Molecular beam epitaxy (MBE) was developed in the early 1970s as a means of growing high-purity epitaxial layers of compound semiconductors. Since that time it has evolved into a popular technique for growing III-V compound semiconductors as well as several other materials. MBE can produce high-quality layers with very abrupt interfaces and good control of thickness, doping, and composition. Because of the high degree of control possible with MBE, it is a valuable tool in the development of sophisticated electronic and optoelectronic devices. In MBE (Fig 1.19), the constituent elements of a material in the form of 'molecular beams' are deposited onto a heated crystalline substrate to form thin epitaxial layers. The 'molecular beams' are typically from thermally evaporated elemental sources, but other sources include metal-organic group III precursors (MOMBE), gaseous group V hydride or organic precursors (gas-source MBE), or some combination (chemical beam epitaxy or CBE). To obtain high-purity layers, it is critical that the material sources are extremely pure and that the entire process is done in an ultra-high vacuum environment. Another important feature is that growth rates are typically of the order of a few Å/s and the beams can be shuttered in a fraction of a second, allowing for nearly atomically abrupt transitions from one material to another. It is because of this feature that MBE is an important tool for nanostructure fabrication [228-230].

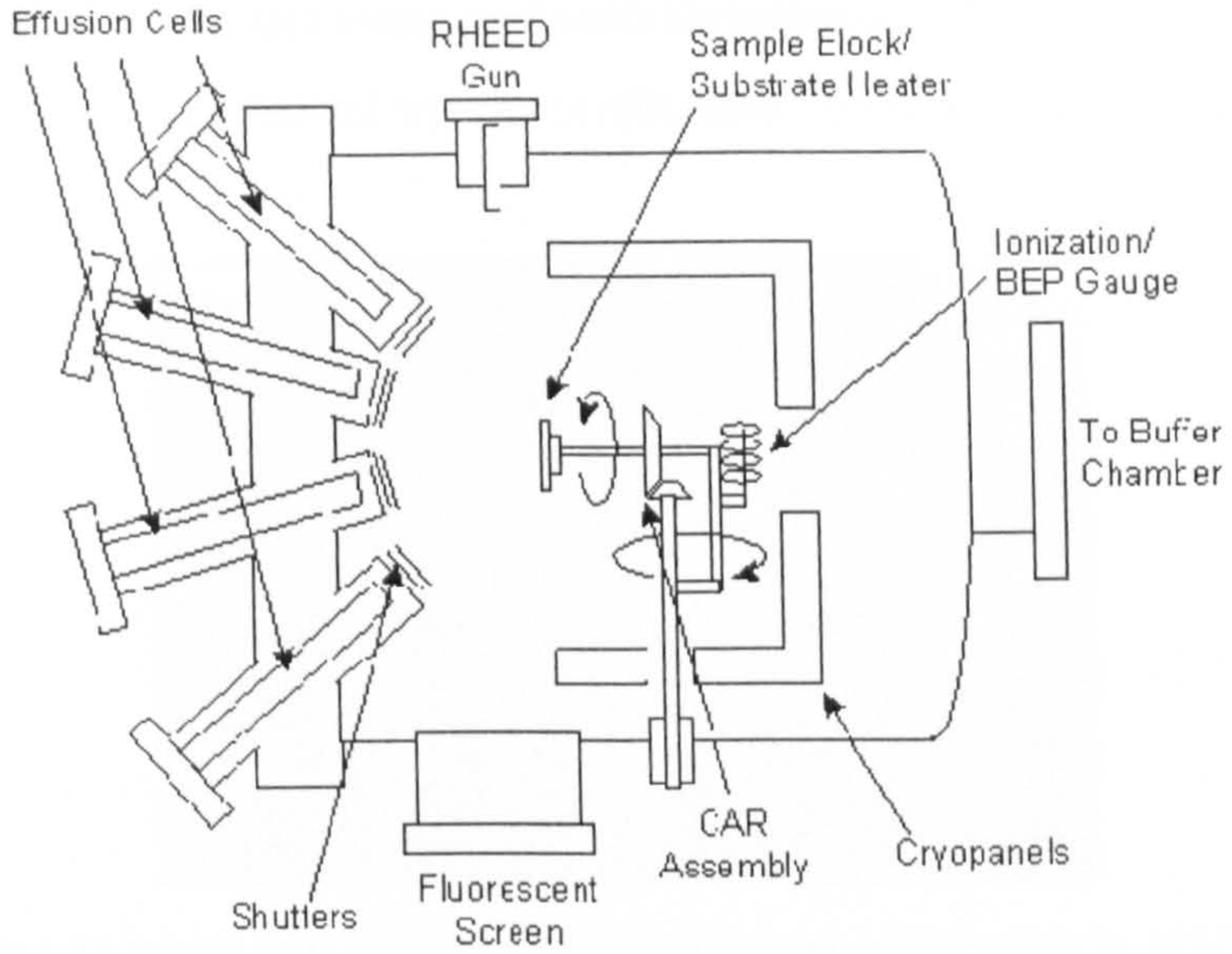

Fig 1.19 Diagram of a typical MBE system growth chamber [231]

For example, multi-layered InAs nanowire arrays were fabricated *in situ* on InP substrates by Hanxuan Li and co-workers using the MBE technique (Fig 1.20) [232]. Cross-sectional TEM images of stacked nanowire arrays showed that nanowires of one layer were positioned in the interstices of the previous layer (Fig 1.20 a) exhibiting strong anti-correlation in the growth direction. By varying the thickness of InAs, the uniformity of nanowires could be improved.

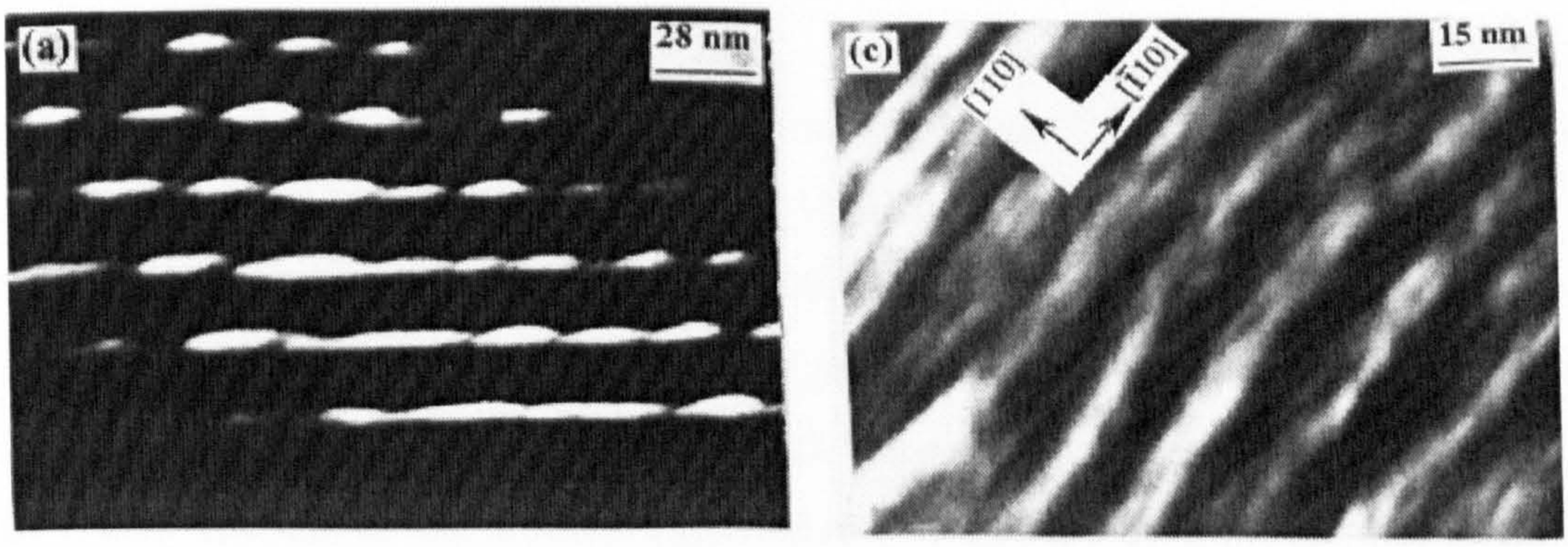

Fig 1.20 Cross-sectional TEM image of stacked nanowire arrays [232] with: (a) six-period InAs ~6.5 ML/$In_{0.52}Al_{0.48}As$ ~20 nm and (c) Plane-view TEM image of the sample in (a).

Fig 1.21 gives another example of MBE grown nanowire arrays. InAs nanowires of size 2 nm (H) x 24 nm (W) x 1 μm (L) and periodicity 24 nanometres were grown on InP (001) surfaces. Strong light emission centred at 1.55 μm was detected from these

nanowires at room temperature using a photoluminescence (PL) spectrometer. The growth mechanism was explained via the misfit strain between the layer and the substrate.

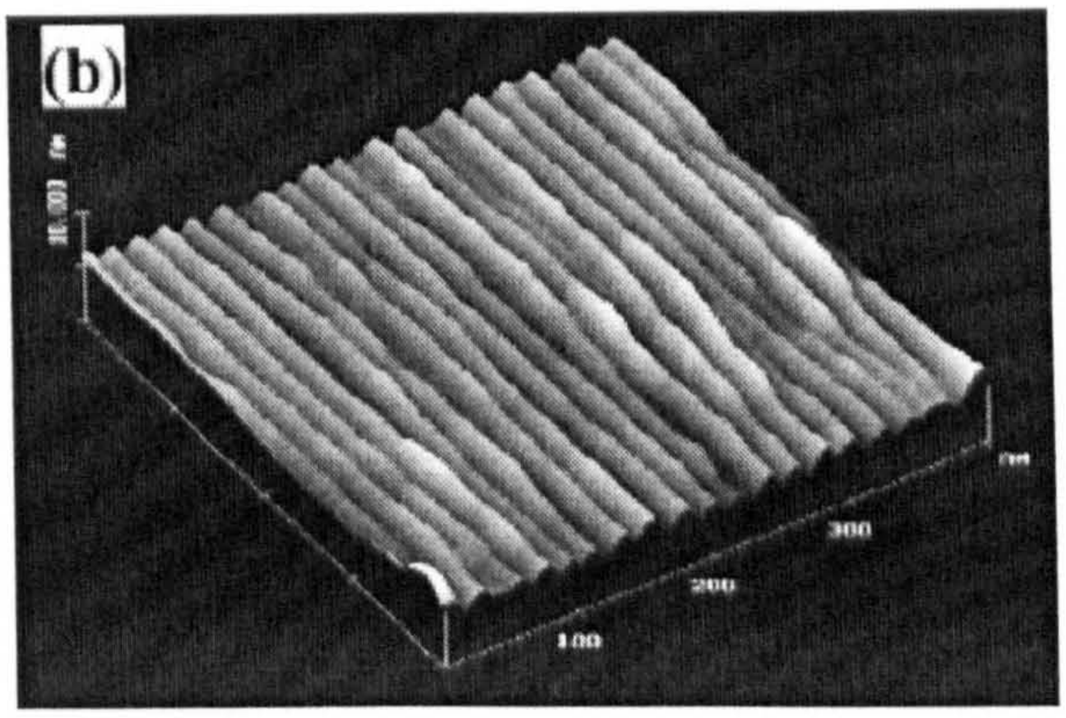

Fig 1.21 Arrays of InAs nanowires of InAs grown on InP (001) by MBE [233]

1.3 Combination of Top-Down and Bottom-up Approach

Nanofabrication using a stencil mask is a typical example of the combined top-down and bottom up approach. A stencil mask can be patterned with the proposed structures by photolithography (top-down), and evaporated material can be collimated using the mask (bottom-up). Using this technique Mandar M. Deshmukh *et al* [234] prepared Er wires 15-20 nm wide on silicon substrates.

Another technique combines AFM and epitaxial growth [235](Fig 1.22). Contact mode AFM was used to anodically oxidize the CVD deposited ultra-thin Si_3N_4 surface on Si(001), followed by H-termination with HF solution and plasma oxidation. The thin layer of SiO_2 on Si was then desorbed at high temperature. After second H-termination by H_2 plasma, lines of Si of 150 nm in width were epitaxially grown on a Si (001) surface by CVD. The lateral resolution is expected to be improved by using sharper tips. This technique is unlikely to be adopted by industry due to its limitation in resolution confined by anodic oxidation, and the low productivity related to serial AFM.

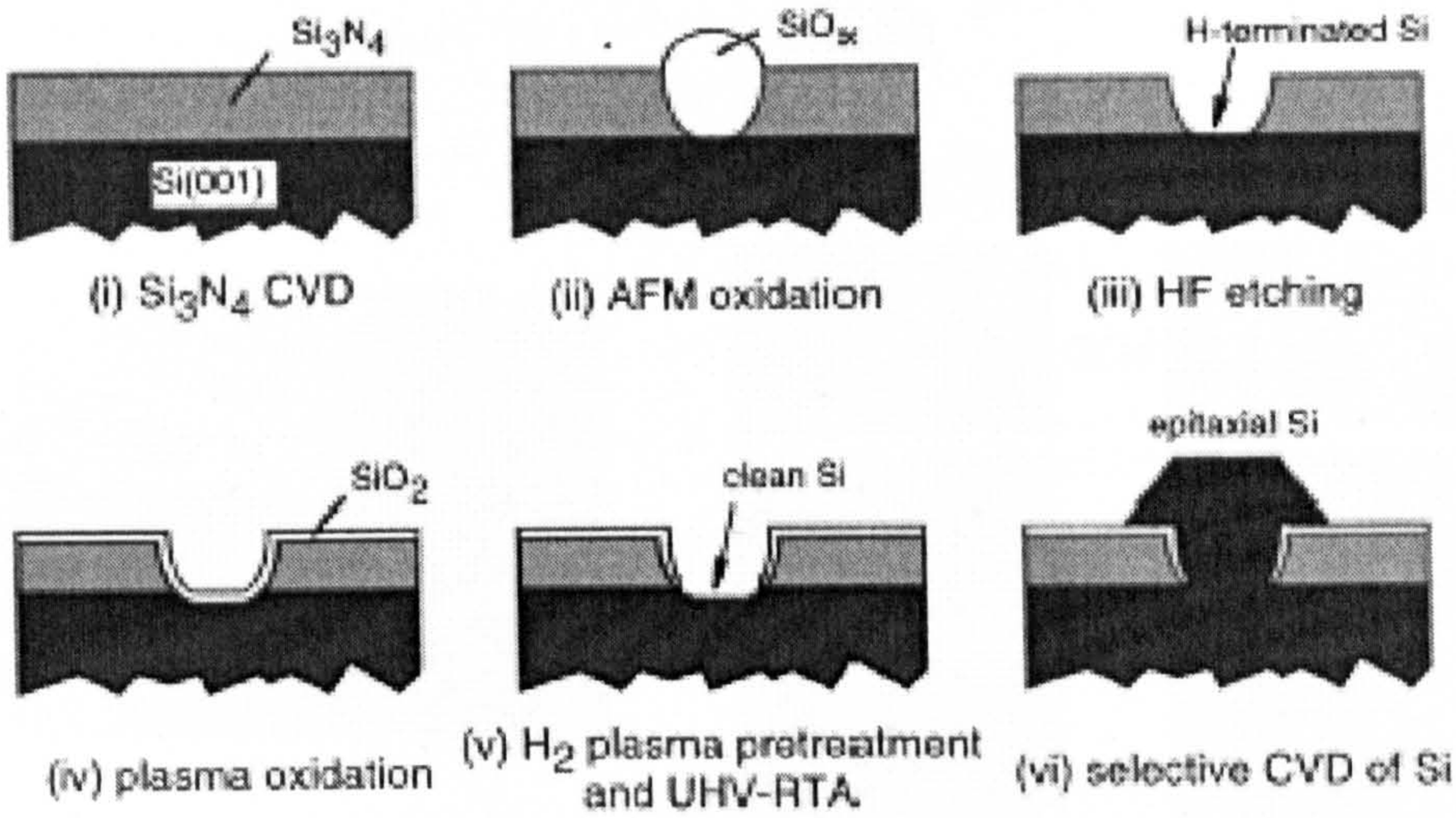

Fig 1.22 Procedures for preparation of a SiO_2 /Si_3N_4 bilayer mask and selective epitaxial growth of Si (Ref [235])

Takeyoshi Sugaya *et al* reported MBE fabrication of InGaAs quantum wires (QWRs) on V grooves photographically prepared on an InP substrate [236](Fig 1.23). The substrate had flat (311)*A* regions, and the V grooves, with an angle of 90°, consisting of (100) and (011) sidewalls, were formed along the [0, 1, -1] direction on a InP (311)*A* substrate using conventional photolithography followed by chemical etching in $HCl:H_3PO_4:H_2O_2$ (50:10:1 by volume) for 2 seconds. $In_{0.53}Ga_{0.47}As$ quantum wire layers sandwiched in between two $In_{0.52}Al_{0.48}As$ barrier layers were grown on the V grooves. Scanning electron microscopy (SEM) observations, cathode-luminescence (CL), and photoluminescence (PL) measurements of these structures were performed. The CL and PL measurements confirmed the luminescence peak arising from the QWRs. The trench-type quantum wires had a cross-section of 10 nm x 20 nm. Due to the low throughput of MBE, this method can be used only for research.

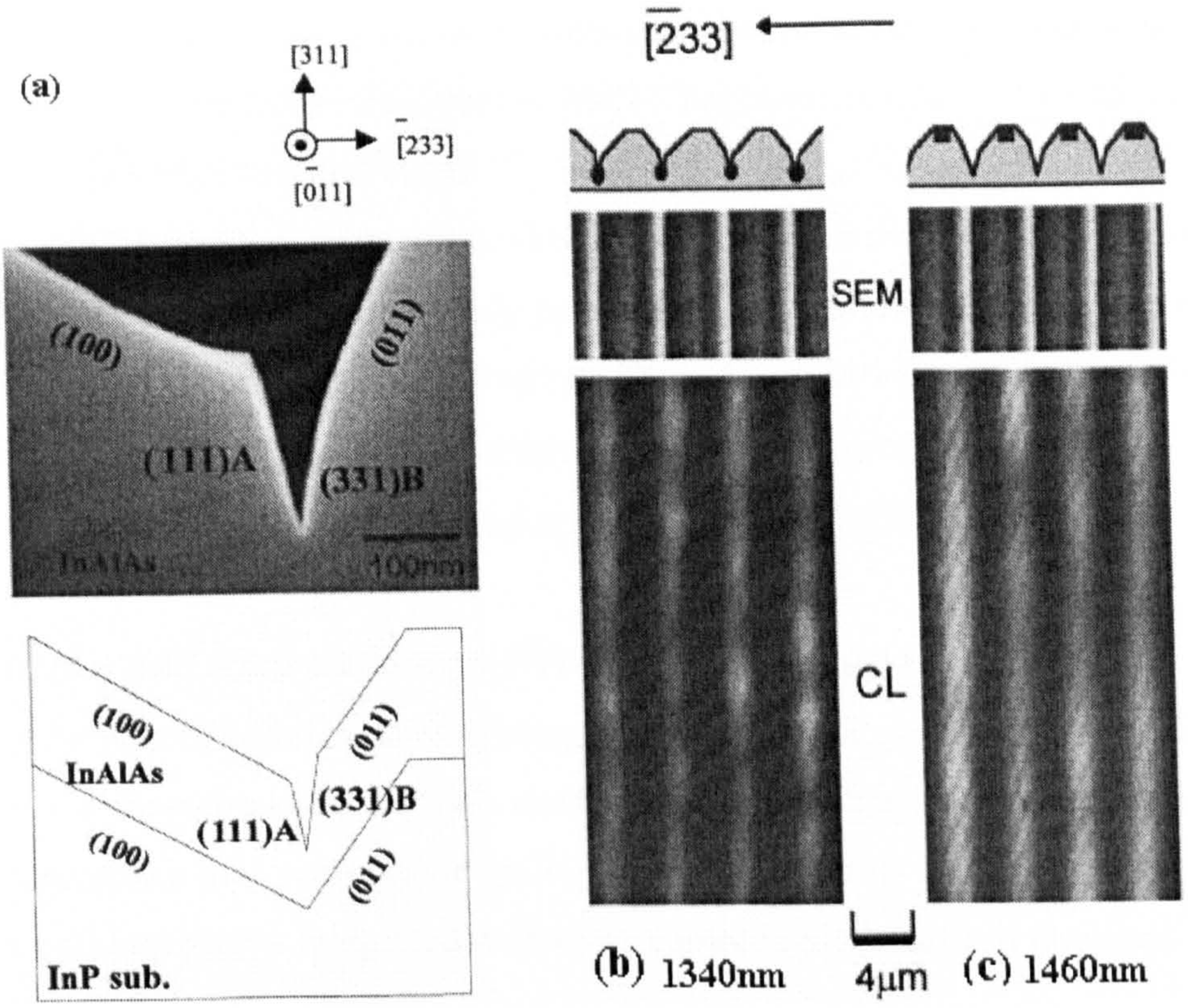

Fig 1.23 InGaAs quantum wires on V grooves on InP substrate [236]: (a) Cross-sectional view of the InAlAs trench structure perpendicular to [0,1,-1], as observed by SEM and a schematic of it. The trench structure of the InAlAs barrier layer consisted of (111)*A* and (331)*B* facets are grown on an InP (311)*A* V-grooved substrate under an As_2 source; (b)-(c): SEM and CL images of InGaAs QWRs and (311)*A* ridge QWLs (quantum wells). The emissions at (b) 1340 nm and (c) 1460 nm originate from InGaAs QWRs and (311)*A* ridge QWLs, respectively.

1.4 Potential Applications of Nanowires

Semiconductor nanowires are essential components for future nanoelectronics since they can exhibit a range of device function and at the same time serve as interconnections for larger scale miniaturization. They have already been used to create a striking array of delicate and ultra-miniature devices such as transistors, photodetectors and biosensors. Such devices promise to play a central role in the electronics and photonics industries of the future.

Nanowire versions of classic electronic devices have been subjected to intense research in recent years. Nanowire field-effect transistors (FETs) have been fabricated on a wide range of materials including Si [237], InP [238], GaN [239, 240], In_2O_3 [241], and ZnO [242]. In a series of studies over the past few years, the Lieber group pioneered the area of nanowire electronics with the fabrication of locally gated FETs [243], crossed-nanowire *p-n* junctions and LEDs [239], bipolar transistors and inverters [244], and various logic-gate structures and memory elements [245]. In general, the performance characteristics of nanowire electronic devices often challenge the best bulk and epitaxial single-crystal semiconductors.

As an example, field effect transistors (FETs) can be fabricated from nanowires[246, 247] by depositing the nanomaterial on an insulating substrate surface, making source and drain contacts to the nanowire ends, and then configuring either a bottom or top gate electrode. This basic approach may serve as the basis for hybrid electronic systems consisting of nanoscale building blocks integrated with more complex planar silicon circuitry.

Compositionally modulated (heterostructure) nanowires featuring internal *p-n* junctions have initiated the development of single-nanowire LEDs (light-emitting diodes), and other devices. Recent examples include VLS-grown Si and GaN nanowire rectifiers [248] and InP nanowire LEDs as well as rectifying multilayer metal rods fabricated by electrodeposition [249]. Modulated nanowires may offer several advantages over their monolithic counterparts in electronic applications, including decreased device sizes, simplified fabrication requirements, and enhanced control over the nature of the active interface. Complementary inverter-like structures have been assembled with lightly doped p and n type silicon nanowires by Yi Cui and Charles M Lieber [244].

Huang *et al.* [238] created crossed junctions comprising p-type Si nanowires and n-type GaN that can function effectively as diodes and field-effect transistors. Using these simple building blocks, they demonstrated the ability to fabricate the OR, AND, and NOR logic gates necessary for computation.

PN junctions can be created on silicon surfaces by electron beam lithography using InP nanowires[238]. Metal-semiconductor heterojunctions have been successfully fabricated between silicon nanowires and carbon nanotubes by a controlled catalytic growth technique [5]. Semiconductor nanowires can be cut, linked and welded in nanotubes at relatively modest temperatures [250]. This provides a new approach to integrate one-dimensional nanostructrues into functional devices and circuitry.

Striped nanowires (nanowires with quasi-square cross-section and low height-to-width ratio) might be assembled into complex circuits and faster computer chips. They might also serve as nanoscale light-emitting sources that could be integrated into light-speed opto-communication systems. Striped nanowires could even serve as powerful sensors of chemical and biological agents. Contact with extremely low concentrations of a chemical or biological agent is enough to cause a change in the electronic state of a striped nanowire, which can be used to identify the agent.

Semiconductor superlattices can be used as mirrors in microscopic lasers, or as waveguides to capture and confine light. If electrons are trapped in a thin layer of a semiconductor sandwiched between barriers of a different semiconductor, quantum wells are created that emit light. The colour of the light can be tuned by varying the well thickness. Leiber's group[251] at Harvard University has created superlattices containing compositionally modulated nanowires of alternating sections of gallium arsenide and gallium phosphide suggesting potential applications ranging from nano-barcodes to polarized nanoscale LEDs. Similar results have been reported by the Peidong Yong group [252].

Well faceted nanowires of micrometer scale length may be used for the observation of unique optical confinement and microcavity effects. Single-nanowire electrically driven lasers have been fabricated by the Leiber's group [253]. The nanowire nanolasers consist of single wires of cadmium sulphide emitting blue-green laser light at wavelengths of 495--500 nm. The nanowires act as a waveguide for the stimulated emission. The interface between the n-type nanowire and the p-type silicon forms a p–n junction, across which charge can be injected into the nanowires. There, recombination of charge carriers causes

emission of blue–green light. The nanowire lasers might be used to perform laser surgery with unprecedented precision. They may penetrate through cell walls without causing much damage. The nanowire lasers may also be used to build optical probes for chemical and biological sensors. Making use of the optical near-field offered by the nanowire lasers, laser lithography with very high resolution is expected to beat the current wavelength resolution limit. Other applications of nanolasers lie in super-high resolution laser printers, laser-powered biochips, optical computing (where information travels at the speed of light), and data storage (where short-wavelength UV lasers could pack four times the information on a CD as can the red lasers used today).

Electronic conductivity in semiconductor nanowires can be substantially enhanced by exposing these structures to photons of energy greater than their bandgaps. Peidong Yang and coworkers demonstrated [254] that photoconductivity in ZnO nanowires could be exploited to create fast and reversible UV optical switches with ON-OFF switching ratios of four to six orders of magnitude under low-intensity 365 nm light. Because the magnitude and decay time of the photo-response is highly dependent on the presence of ambient O_2, they suggested that the photocurrent in *n*-type oxide nanowires is a product of electron-hole pair formation and electron doping caused by the photo-induced desorption of oxidizing surface species, including oxygen.

The sensitive dependence of nanowire conductivity upon adsorbate molecules can be utilized to fabricate nanowire gas sensor [255]. Nanowire chemical sensors most often operate via chemical gating induced by the surface adsorption of analyte molecules, although other sensing mechanisms exist [256, 257]. Nanowire-based gas sensors have been fabricated by metal nanowires [258], ZnO belts [259] and nanowires [260, 261], In_2O_3 wires [262], polycrystalline SnO_2 wires [263], Ga_2O_3 nanowires, TiO_2 tubes arrays[264], and polymeric nanowires [265].

A nanowire thin-film transistor has been created by Duan *et al* [266] who grew p-type silicon nanowires by catalytic chemical vapour deposition. By dispersion of the wires into solution and assembly of the wires using flow-directed alignment onto the substrate

surface at room temperature, they created an oriented monolayer of nanowires with an average interwire spacing of 500-1000 nm, over areas as large as a four-inch wafer. Source and drain electrodes were defined using standard lithography followed by metallization. They have assembled nanowires into densely packed oriented thin films that can undergo conventional electronic fabrication processes. Since they only used conventional electronic fabrication processes, their technology may lead to the first practical and scalable nanomaterial-enabled electronics.

Zhaoning Yu *et a*l created GaAs metal-semiconductor-metal photodetectors (MSM-PD) using nanoimprint lithography (NIL)[267]. Compared with MSM-PD fabricated using electron-beam lithography and photolithography, the MSM-PDs fabricated using NIL do not show observable degradation in the device characteristics if the imprinting pressures are kept at 600 psi or below. NIL has a potential to become a tool for the mass production of nanoscale GaAs devices.

AFM can be used to fabricate tunnelling barriers and insulating gates in a two-dimensional electron gas (2DEG). An in-plane-gate transistor and a single-electron transistor working at low temperatures were fabricated on the surface layers of GaAs/AlGaAs heterostructures using AFM nanomachining by H. W. Schumacher and fellow workers [268]. Variation of the room-temperature resistance of the scratched lines tunes their low-temperature characteristics from tunnelling up to insulating behaviour.

AAO-templated ferromagnetic nanowires are proving useful in the emerging field of biomagnetics, in which magnetic nanostructures provide a means to sense biomolecules, sort cells, and perform other biological manipulations. For instance, noting that the large remnant magnetization inherent to nanowires permits their use in low-field environments, the Reich group has demonstrated the chemical functionalization of Au/Ni wires for biosensing [269] and developed an approach to magnetically trap [270] single wires in solution.

Complex nanowire electronics cannot be produced economically with the current mixture of bottom-up and top-down construction. To yield a viable technology, breakthroughs must be made in the true self-assembly of nanowire mixtures into useful architectures. Controlling the placement and connectivity of groups of nanostructures is probably the greatest challenge in one-dimensional nanoscience.

This thesis describes attempts at nanowire fabrication by ion beam bombardment on semiconductor surfaces. The ultimate objective of this research is to fabricate densely populated arrays of nanowires of regular cross-section on semiconductor surfaces by ion beam bombardment so that possible active behaviour such as lasing action could be explored. Ultimately, thus-fabricated nanowires may function as nanoelectronic building blocks for the future generations of electronic devices.

Chapter 2

Characterization of Nanowires

Characterization of nanowires involves analysis of their morphology, chemical composition, electron transport properties, mechanical properties, and photonic properties. In order to perform these measurements, various tools such as Scanning/Transmission Electron Microscopy [271, 272], Scanning Tunnelling Microscopy[273-275], Atomic Force Microscopy[274, 275], Auger Electron Microscopy, X-ray Photoelectron Microscopy, etc, have been used to reveal an increasingly comprehensive understanding. As numerous literature sources have already provided a sound description of these techniques, this chapter will be confined to a brief introduction to these methods and their application to nanowire characterization.

2.1 Universal Tools for Nanowire Characterization

This section presents a brief introduction to the principle and instrumentation of some primary techniques for nanowire morphology characterization.

2.1.1 Scanning and Transmission Electron Microscopy

The application of scanning electron microscopy (SEM) and scanning transmission microscopy (TEM) in nanostructures is generally for morphology analysis.

SEM is generally considered a micro-analytical technique which is able to image or analyse materials that can not be generally observed with the resolution offered by visible-light-based techniques. The maximum resolution [276] of an optical microscope is $K\lambda/A$, where K is a constant between 0.6 and 0.8, λ is the wavelength of light source, and A is the numerical aperture of an object. Due to the particle-wave duality of an electron, the wave length λ of an electron accelerated from a state of station by a voltage V can be calculated as $\lambda = h/(2meV)^{1/2}$, where h is the Plank constant, m is the mass of electron, e is the elemental charge. A voltage of 100 keV yields an

electron wave of wavelength 0.037 Å. This is the typical wavelength of an electron used in an electron microscope. This wavelength is 100 thousand times shorter than that of natural light. The theoretical resolution [276] of an electron microscope is calculated to be 2 Å. In practice, a typical [277] high resolution SEM (HRSEM) can obtain a resolution of 1 nm.

The SEM (Fig 2.1[278]) uses electrons instead of light to form an image. A beam of electrons is produced at the top of the microscope by heating of a metallic filament. It then passes through electromagnetic lenses which focus and direct the beam down towards the sample. Once it hits the sample, other electrons (backscattered or secondary) are ejected from the sample. Detectors collect the secondary or backscattered electrons, and convert them to a signal that is sent to a viewing screen similar to the one in an ordinary television, producing an image. In this way a bright image will be the result of high secondary electron emission, while the primary influence on high emission is the surface structure of the specimen. The end result is therefore brightness associated with surface characteristics and an image which looks very much like a normally illuminated subject.

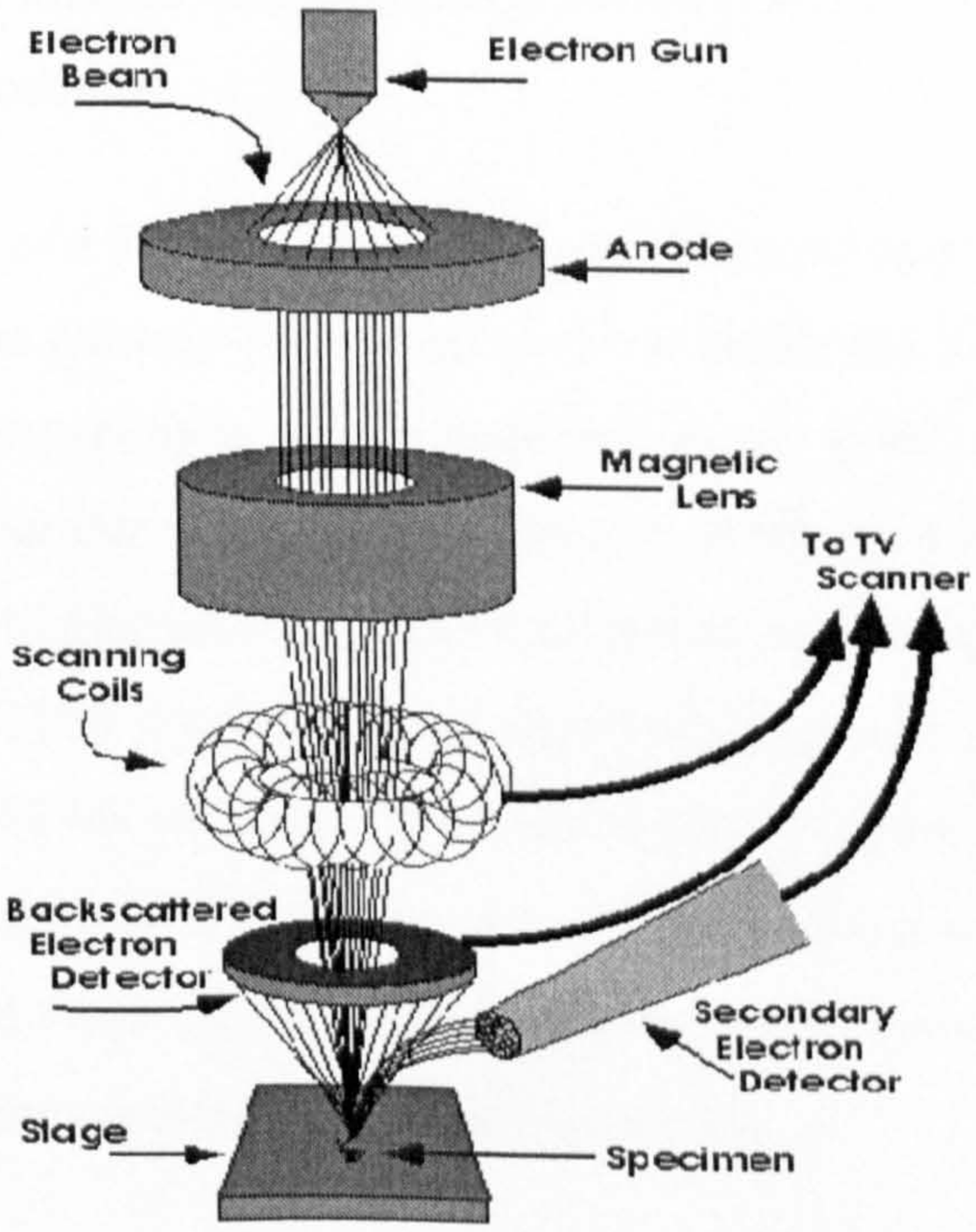

Fig 2.1 Schematic diagram [278] of SEM

Since the SEM uses electrons to produce an image, most conventional SEM's require that the samples be electrically conductive. Non-conductive samples will generally charge under the influence of the electron beam and render secondary electron images of poor quality. In order to view these samples, the samples must be covered with a thin layer of a conductive material.

In an SEM, the apparent illumination is a function of particle emission upon energetic electron bombardment rather than visible light that we are familiar with. Since materials are bombarded with high energy electrons which have been accelerated with tens of thousands of volts, damage to samples can occur. Hence, SEM topography analysis is not an ideal option for samples with ultra-fine nanostructures which are sensitive to bombardment induced damage. Besides, the enormous technical expenditure is disadvantageous.

The set-up of a transmission electron microscope (TEM) is similar to that of a SEM. The key difference is that instead of focusing and scanning on the samples, the electron beam illuminates the area to be imaged, passes through the area, and an image is acquired by collection of scattered electrons.

The acceleration voltage of a TEM is usually between 50 and 150 kV, or higher. The higher it is, the shorter the electron wavelength and the higher the resolution. But the resolution of electron microscopy is usually restricted by the quality of the lens-systems and especially by the technique with which the sample preparation has been achieved. Because the wavelength of electrons is much smaller than that of light, the optimal resolution attainable for TEM images is many orders of magnitude better than that from a light microscope. Thus, TEMs can reveal the finest details of internal structure - in some cases as small as individual atoms (0.2 nm -- 0.3 nm). Magnifications of 350,000 times can be routinely obtained for many materials, whilst in special circumstances, atoms can be imaged at magnifications greater than 15 million times.

A crucial factor affecting TEM analysis is that materials must be specially prepared to thicknesses which allow electrons to transmit through the sample, much like light is transmitted through materials in conventional light microscopy. For this reason, TEM is usually used to observe thin slices of specimens.

Analytical techniques associated with the TEM and SEM includes elemental analysis by the measurement of x-rays emitted by the sample under electron bombardment. In addition, the angle of electrons diffracted out of the beam by interaction with the sample can be recorded to determine the spatial arrangement of atoms in the sample.

SEM and TEM suffer from several drawbacks, such as relatively poor resolution and contrast in the case of SEM, and complicated and time-consuming sample preparation in the case of TEM.

2.1.2 Scanning Tunnelling Microscopy

Scanning tunnelling microscopy (STM) has been a powerful tool for the determination of the structural and electronic properties of surfaces. This section introduces a basic understanding of surface morphology and electronic structure characterization by STM.

2.1.2.1 Principle of Morphology Analysis by STM

The basic principle of scanning tunnelling microscopy (STM) (Fig 2.2)[279] is based on measuring the tunnelling current between a metallic tip, which is sharpened to a single atom point, and a conducting material. A probe tip typically made out of tungsten is attached to a piezodrive, which is a system of very sensitive piezo crystals which will expand or contract in reaction to an applied voltage. By using the piezo to position the tip within a few Ångstroms of the sample, the electron wavefunctions in the tip and the sample overlap, leading to a tunnelling current when a bias voltage is applied between the tip and the sample. The tunnelling current is amplified and fed into a computer while processing a negative feedback loop to keep the current constant. A constant current yields roughly a constant tip height, so the shape of the surface can be reproduced by the path of the tip, which can be inferred directly from the voltage supplied to the piezoelectric drivers. The computer, by collecting the z distance data, can image a three

dimensional plot on-screen. This plot will be related to the electron density of the sample surface. Attempts can then be made to relate this to the positioning of atoms on a conductive surface.

Another commonly used mode in STM imaging is the constant height mode. In this mode, the tip height remains constant above the average surface, and small features are reflected in fluctuations of the current, rather than in the tip height [280]. However, this mode of imaging is only practical in special cases where the surface is extremely flat, and is not fundamentally different from the usual "constant current" mode.

The idea behind STM is that there is a certain driving force for an electron to move from one surface to another of lower potential. Classically, this is not possible unless a direct connection such as a wire is connected between the two surfaces. On an atomic sized scale, however, when the distance between two surfaces is small enough (e.g., a few radii), there is a finite probability that an electron will tunnel from one surface to the other of lower potential.

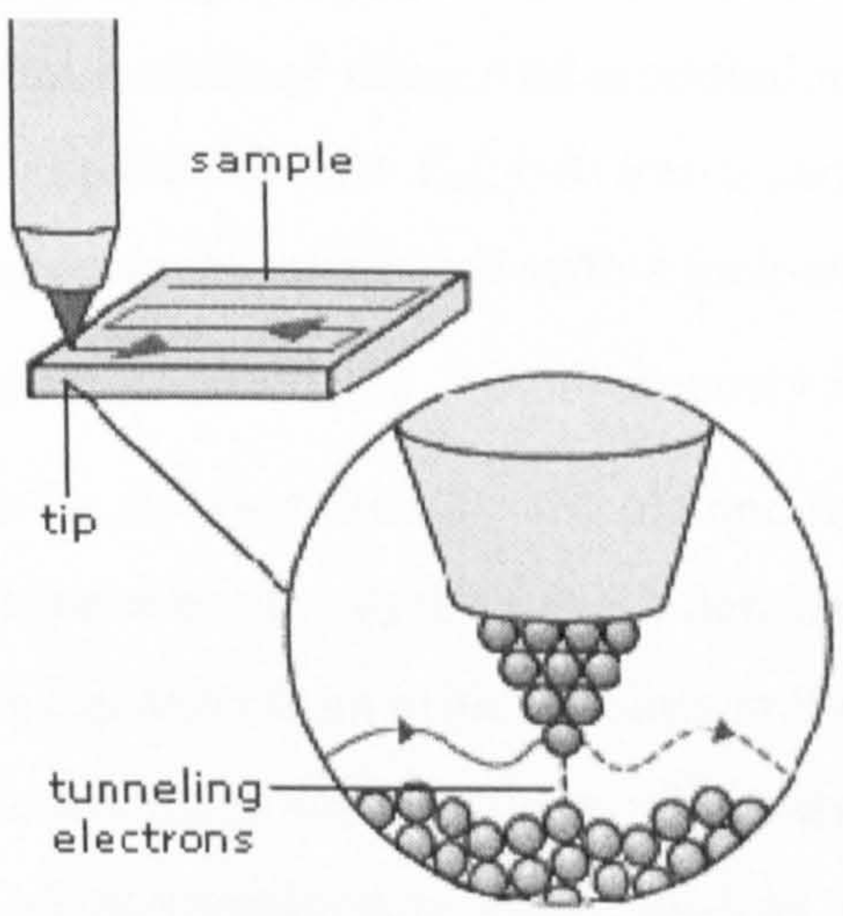

Fig 2.2 Schematic diagram [279] of the principle of a STM

Because the distance measurements are so miniscule, vibrations from the environment must be minimized. Vibration in the low frequency regime (< 20 Hz, originating from vibrations from building and resonance of certain system components) can be damped by suspension of the microscope on long tension wires or levitation of the system on an air

table. Vibration in the medium frequency regime (20 to 200 Hz, originating from mechanical vibrations from motors, resonances of the table and chamber that are acoustically excited, and unattenuated acoustic noise) can be isolated by mounting the scanner assembly on a stack of materials of different elastic moduli or suspending the scanner on tension springs with eddy current damping. High frequency vibrations (>200 Hz, originating from resonances of the piezo elements) can be eliminated from the signal with electrical filters without affecting the part of the signal that represents the structural information [274].

2.1.2.2 Scanning Tunnelling Spectroscopy by STM

The fact that the tunnelling current in STM flows through a region as small as ~ 5 Å in diameter[281]enables STM for spectroscopic analysis on an atom-by-atom basis. Hence, a method called Scanning Tunnelling Spectroscopy (STS) is widely used to analyse tunnelling conductance and band structure of surface features in nanometre or atomic scales. In STS, the tunnelling *I/V* (or *dI/dV*) curves are acquired simultaneously with the topographic STM image of the sample surface. In a typical current image tunnelling spectroscopy (CITS) [281]a high frequency sinusoidal modulation voltage $V_{mod}\,\omega_{mod}$ is superimposed on top of the constant dc bias V_{dc}, between a sample and a tip. The ac component of the tunnelling current is measured with a lock-in amplifier, with the in-phase component directly giving $dI/dV\big|_{V=V_{dc}}$ simultaneously with the sample topography. At low bias voltages (when V_{dc} is lower than the sample and tip work functions), structures in *dI/dV*-- V_{dc} are associated with the surface density of states. Structures in the surface density of states can arise from critical points in the surface-projected bulk band structure, or may arise from true surface states, which are generally associated with surface reconstructions. The interpretation of these low-bias *dI/dV* measurements is generally based on the WKB (Wentzel-Kramers-Brillonuin) approximation for the tunnelling current [281]

$$I = \int_0^{eV} \rho_s(e,E)\rho_t(r,E-eV)T(E,eV,r)dE \tag{2.1}$$

$$\frac{dI}{dV} = \rho_s(r,eV)\rho_t(r,0)T(eV,eV,r) + \int_0^{eV} \rho\ (r,E)\rho_t(r,E-eV)\frac{dT(E,eV,r)}{dV}dE \tag{2.2}$$

where $\rho_s(r,E)$ and $\rho_t(r,E)$ are the density of states of the sample and the tip at location r and energy E, measured with respect to their individual Fermi levels, and $T(E,eV,r)$ is the tunnelling transmission probability.

The first term in eqn (2.2) is the product of the density of states of the sample, the density of states of the tip, and the tunnelling transmission probability. The second term contains the voltage dependence of the tunnelling transmission factor, which contributes a smooth background on which the spectroscopic information is superimposed.

Structures in dI/dV as a function of V can be assigned to changes in the density of states via the first term of eqn (2.2). Consequently, these measurements can provide a measure of the density of states as a function of energy at any particular location on the surface.

One of the most frequently used methods in STS analysis is dubbed current imaging tunnelling spectroscopy (CITS) in which I/V curves (each at a fixed sample-tip separation) are rapidly acquired at each position that the tip scans. Technically a sample-and-hold circuit halts the feedback loop for a few hundred microseconds to maintain the position of the tip while the voltage is ramped for the I-V measurement. After a short delay to damp capacitance transients, feedback resumes at the stabilization voltage V_{stab}. By collecting the I-V curves rapidly compared to the scan speed of the tip, both the topography of the sample and spatially resolved tunnelling I-V characteristics are acquired at each location in a two dimensional raster scan over the surface, providing spatial correspondence between each point in the topographic scan and the I-V spectroscopic scan.

In practice it is difficult to extract quantitative information about the density of states of the sample because the density of states of the tip and the voltage-dependent tunnelling transmission probability $T(E, eV)$ are almost always unknown. Feenstra *et al*[282] proposed a normalization procedure to eliminate the distance dependent tunnelling probability as

$$\frac{dI/dV}{I/V} = \frac{d(\log I)}{d(\log V)} = \frac{\rho_s(eV)\rho_t(0) + A(V)}{B(V)} \qquad (2.3)$$

which equals unity at $V= 0$. $A(V)$ is a background term containing the influence of electric field in the gap on the decay length κ, and B(V) normalizes the tunnelling transmission probability over the density of states. Hence, structure in $(dI/dV)/I/V$ reflects $\rho_s(eV)$ if $A(V)$ and $B(V)$ are assumed to vary slowly with voltage. Although $(dI/dV)/I/V$ does not directly yield the density of states of the sample, features in the $(dI/dV)/I/V$—V curves can be used to assess if the measured sample is metallic or semiconducting.

2.1.3 Atomic Force Microscopy

The atomic force microscope (AFM) is an essential tool for imaging surface topography on a scale from Ångstroms to 100 microns. As a large portion of experimental results presented in this research was collected by an AFM, this section provides a detailed introduction of the principle and applications of surface characterization by AFM.

2.1.3.1 Principle of Morphology Characterization by AFM

The basic objective of the operation of the AFM is to measure the forces (at atomic level) between a sharp probing tip (which is attached to a cantilever spring) and a sample surface. Images are taken by scanning the sample relative to the probing tip and measuring the deflection of the cantilever as a function of lateral position. A schematic of an atomic force microscope is shown in Fig 2.3.

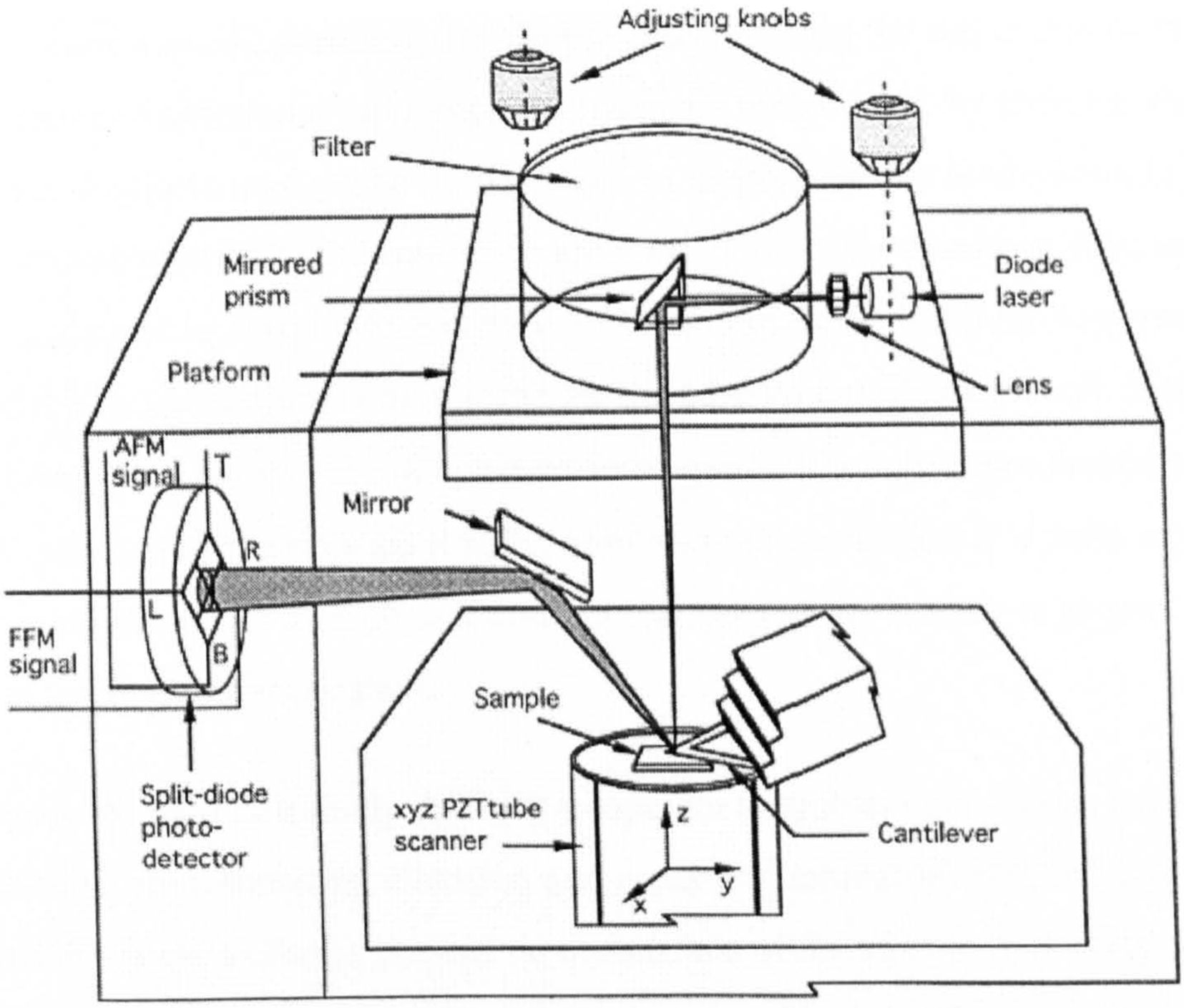

Fig 2.3 Schematic [283] of a commercial AFM

The sample is mounted on a piezoelectric scanner allowing extremely precise movement in the x, y, and z directions. The sample is then rastered in the x and y directions under a sharp tip. This tip is mounted at the free end of a cantilever (as shown) upon which a laser beam is focused. The beam is reflected from the back of the cantilever to a set of four photosensitive diodes. These detect the deflection of the laser beam arising from the cantilever moving as the sample is rastered. The tip is held several nanometres above the surface using a feedback mechanism that measures surface-tip interactions on the scale of nano-Newtons. The tip is brought into continuous (contact mode) or intermittent (tapping mode) contact with the sample and raster-scanned over the surface. In principle, the deflection of the cantilever is associated with the force exerted on the tip. In contact (or dc) mode scanning, keeping the deflection (and hence, the force) constant by varying the vertical position of the tip produces a constant force image analogous to constant current STM. When the tip is sufficiently close to the surface that Van der Waals interactions dominate, it keeps track of the surface topography, and the image represents the topographic structure of the surface. In another word, the height of the sample is

measured by continuously scanning the sample and recording the deflection of the cantilever. Three-dimensional topographical maps are constructed by plotting the local height against the horizontal probe tip position. In tapping (or ac) mode scanning, the vibrational characteristics of the cantilever are used. Generally speaking, the cantilever is driven to oscillate at its resonant frequency (ω_0), the amplitude (both the magnitude and the sign) of the force gradient is monitored for the case where the cantilever is initially oscillated away from resonance. A constant force gradient image is produced by varying the vertical position of the tip such that the amplitude of oscillation at a particular frequency is constant. As a result, a topographical map of the surface is generated by keeping the force gradient constant.

Tapping mode AFM is extremely difficult to operate in ambient conditions because it is very sensitive to environmental vibration and water contamination. A thin layer of water contamination which is always present on the surface of the sample inevitably forms a small capillary bridge between the tip and the sample and causes the tip to jump-to-contact. For these reasons, the results presented in this research (Chapter 4) are collected with AFM running in contact mode.

2.1.3.2 Tip-surface Interactions in AFM

The interaction between an AFM tip and a sample can be divided into two—short-range interaction and long-range interaction. The former occurs when the tip is in contact with the sample with Van der Waals forces predominating, while the latter happens when the tip is lifted above the surface with electric or magnetic forces dominating [284]. With the tip approaching the sample to a distance of a few nanometers, Van der Waals forces are sufficiently strong to move the cantilever. Van der Waals interactions consist of three components: polarization (permanent dipole moments), induction (the contribution of induced dipoles), and dispersion (instantaneous fluctuation of electrons occurring at the frequency of light causing optical dispersion). Typical long-range interactions are electrostatic attraction or repulsion, current induced or static-magnetic interactions, and capillary forces due to the surface energy of water condensed between the tip and the sample.

The tip-surface interaction can be interpreted graphically by a force-distance curve. Fig 2.4 is an example of a contact mode AFM force-distant curve [283] obtained in air on a Si surface with a Si_3N_4 cantilever.

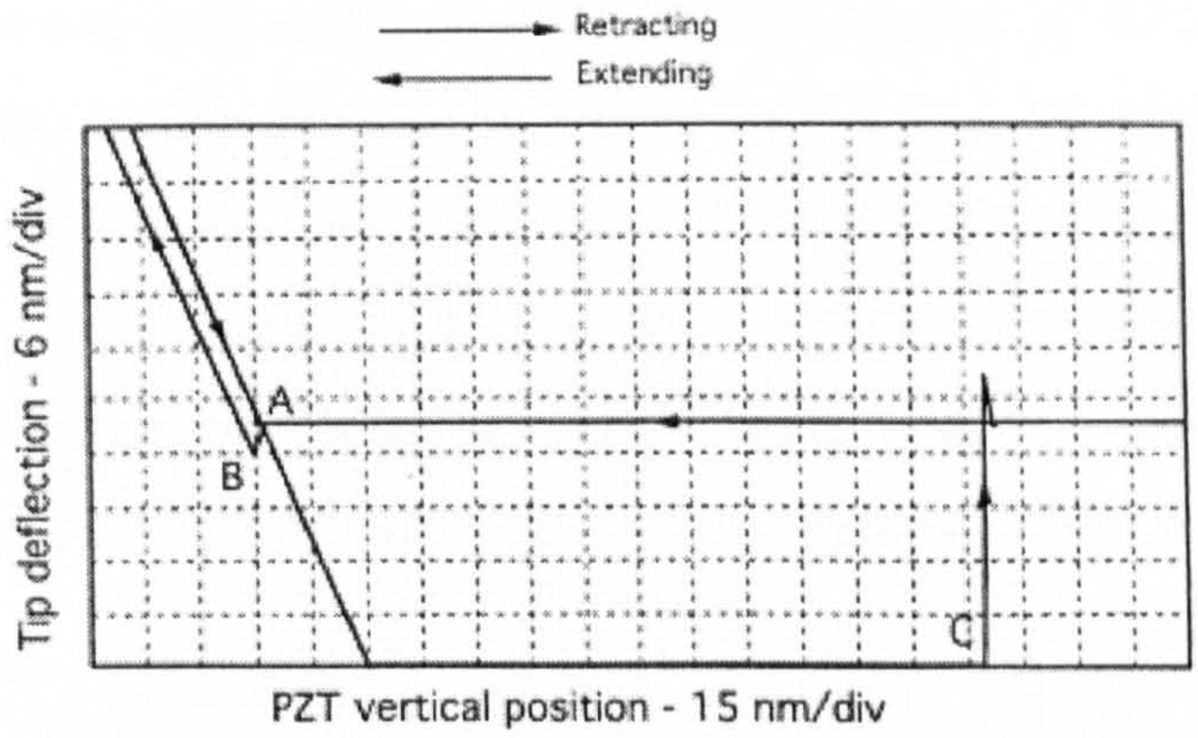

Fig 2.4. Typical force-distance curve [283] for a contact between Si_3N_4 tip and single-crystal silicon surface in measurements made in the ambient environment. Contact between the tip and silicon occurs at point B; tip breaks free of adhesive forces at point C as the sample moves away from the tip.

The horizontal axis represents the distance the piezo (and hence the sample) travels and the vertical axis gives the deflection of the tip. As the piezo extends, it approaches the tip, which is at this point in free air and hence shows no deflection. This is indicated by the flat portion of the curve. As the tip approaches the sample within a few nanometers (point A), an attractive force exists between the atoms at the end of the tip and the atoms on the sample surface. The tip is pulled towards the sample and contact occurs at point B on the graph. From this point on, the tip is in contact with the surface and as the piezo further extends, the tip gets further deflected. This is represented by the sloped portion of the curve. As the piezo retracts, the tip goes beyond the zero deflection (flat line) because of attractive forces (Van-der-Waals forces and long range meniscus forces), into the adhesive regime. At point C, the tip snaps free of the adhesive forces, and is again in free air. The horizontal distance between points B and C along the retrace line gives the distance moved by the tip in the adhesive regime.

The adhesive force (F) is calculated by multiplying the distance (ΔZ) with the stiffness (k, or spring-constant) of the cantilever:

$$F = k\,(\Delta Z) \tag{2.4}$$

In topography measurement, this force must be minimized before acquisition of any image to prevent the delicate nanostructures from deformation by AFM tips. A force curve [285] (Fig 2.5) can be referenced to minimize contact force by adjusting the deflection set-point of the cantilever to the zero deflection point and beyond [285]. The set-point for minimum contact force is usually adjusted slightly negative so that it lies between the flat part of the force curve, and the tip of the retraction scan where the cantilever pulls off the sample surface V_{CSmin} [285](Fig 2.5). The practical procedure will be described in detail in Chapter 5.

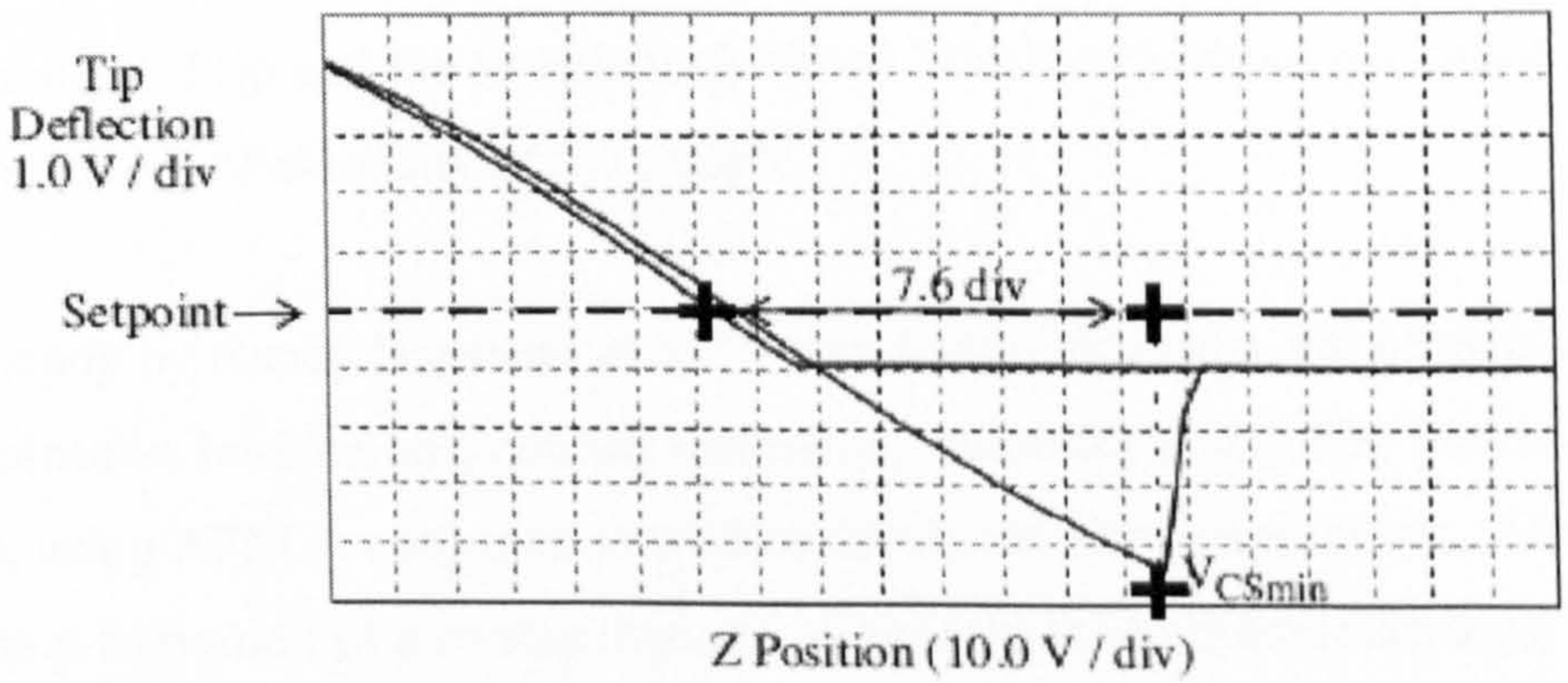

Fig 2.5 Schematic diagram showing calculation of contact force [285].

Contact mode AFM is mostly used to obtain topographic details on hard surfaces including metals, semiconductors and insulators.

In addition to topography measurement of nanostructures, AFM is an important tool in the characterization of mechanical properties of nanostructures, which is discussed in detail in the next section.

2.1.3.3 Characterization of Mechanical Properties of Nanowires by AFM

The main challenge for charactering the mechanical behaviour of a single nanostructure is its ultra-small size that prohibits the application of conventional techniques. Early research in nanomechanical property characterization by Nancy Burnham [286] reported an ambient AFM configured as a nanoindenter of force and depth resolution of 1 nN and 0.02 nm respectively, to study the elasto-plastic properties of materials including elastic modulus and hardness, the surface forces associated with the tip–surface interaction, and the adhesive forces associated with small contacts. The experiment was performed on surfaces of graphite (elastic), gold (plastic) and a piece of rubber band (elastomer). Nanoindentation curves were acquired by plotting tip load as a function of penetration depth. The elasto-plastic properties were determined from the loading and unloading curves. The modulus of elasticity was determined from the loading part of an indentation curve, or from the elastic contribution to an unloading curve, for an elastic material. Hardness was calculated from the maximum load divided by the projected area of contact between the AFM tip and the sample (calculated from the radius of curvature of the tip) after the recovery of elasticity of the sample.

Another study by Nancy Burnham *et al* [287] reported mechanisms and properties of inter-metalic adhesive interactions, contact formation, nanoindentation, and mechanical response, using AFM in conjunction with molecular dynamic simulation. The results showed that formation of a contact between a hard tip (nickel) approaching a soft metallic substrate (gold) is associated with an atomic scale instability. This instability leads to a jump-to-contact phenomenon which involves an inelastic response of atoms in the proximal interfacial region of the gold substrate. Indentation of the surface by advancing the tip beyond the point of contact led to the onset of plastic yielding, adhesion induced atomic flow, and generation of slip on the surface of the gold substrate. Separating the tip from the substrate resulted in adhesion induced wetting of the tip by gold atoms, adherence of a gold monolayer to the nickel tip, formation of an atomically thin connective neck, and eventual fracture. In addition, retracting the tip from the sample after indentation gave rise to extension of the substrate and formation of a connective crystalline neck which elongates, while reducing cross-sectional area, by structural transformations involving elastic and yielding stages. The research motivated a critical

assessment of the range of validity of continuum theories and reformulation of contact mechanics formalism to incorporate an atomistic description of the processes of adhesion, deformation, wetting, and fracture.

The Burnham group also demonstrated the application of the AFM based technique in the measurement of local mechanical spectroscopy with nanometer scale lateral resolution [288], using the principle of variable temperature scanning local-acceleration microscopy (T-SLAM). Running AFM in contact mode, a sample was vibrated at a frequency just above the resonance of the tip-sample system so that the inertia of the tip prevented it from completely following the imposed displacement, inducing non-negligible forces and elastic deformation of the sample. Contact stiffness was obtained from the measurement of the residual displacement of the tip, and mapping the contact stiffness by recording the amplitude and phase of the tip's motion at different temperatures, gave rise to local mechanical spectroscopy. The lateral resolution of T-SLAM was limited not only by the contact radius between the tip and the sample, but also by thermal drift.

Recently, based on nanowire bending under lateral load on an AFM tip, Wu *et al* [289] measured the full spectrum of mechanical properties ranging from Young's modulus through yield strength and plastic deformation to failure. It was found that Young's modulus of Au nanowires is independent of diameter, and the smallest diameter wire has the largest yield strength of up to 100 times that of bulk materials. In contrast to bulk nanocrystalline metals, plastic deformation in Au nanowires was characterized by strain-hardening. Such results demonstrated that dislocation mechanisms (dislocation glide and pile-up) exist down to diameters of 40 nm.

Molecular dynamics simulation (MDS) was used by Kang and Hwang [290] to study elongation and shearing deformations of Cu nanowires with stretch velocity. The results showed that as the strain-rate increases, the first yield and the magnitude of the force relaxation decrease, the period of yielding becomes shortened, and the strength of rupture decreases. MDS was also applied to investigate the effects of high strain-rate on the phase transition of metallic nanowires [291;292]. Ikeda *et al* [291] found that at high strain-rates,

the crystalline phases of the single-crystal Ni and NiCu random alloy nanowires transform continuously to the amorphous phase, exhibiting a dramatic change in atomic short-range order and a near vanishing of the tetragonal shear elastic constant perpendicular to the tensile direction. Branicio and Rino [292] found that Ni nanowires subjected to a uniaxial high strain-rate ($\geq$ 7% ps^{-1}) change continuously from the crystalline to the amorphous phase. They also observed a significant influence of the surface effects on the Young's modulus and force constant when nanowires with different cross sections were considered. Due to the importance of contact mechanics in the process of designing nanodevices and optimizing nanostructured materials, MDS has been recently used by Luan and Robbins [293] to test the limits of contact mechanics under ideal conditions. Their results indicated that the atomic-scale surface roughness which is caused by discrete distribution of atoms leads to dramatic deviations from continuum theory.

The frictional force between an AFM tip and a sample with nanowire structures can be detected by the AFM. Most of the recent AFMs offer this feature called friction force microscopy (FFM) or lateral force microscopy (LFM), which can measure both normal and lateral forces simultaneously. This is realized by sensing the bending in normal direction and torsional motion of the cantilever with a quadruple Photodiode [294]. Running AFM in the so-called friction mode, the sample is scanned back and forth in a direction perpendicular to the long axis of the cantilever beam. A friction force between the sample and the tip will produce a twisting of the cantilever. As a result, the laser beam will be reflected out of the plane defined by the incident beam and the beam reflected vertically from an untwisted cantilever. This produces an intensity difference of the laser beam received in the left and right quadrants of the photo-detector (Fig 2.3). The intensity difference between the left and right detectors is directly related to the degree of twisting and hence to the magnitude of the friction force. In this way, a friction force image can be acquired simultaneously with the topography for the same area scanned. As an example, R. W. Carpick *et al* [295]studied the variation of frictional force with externally applied load for a Pt-coated AFM tip in contact with the surface of mica cleaved in ultrahigh vacuum. Their results demonstrated that the concept of a friction coefficient is

not valid in the elastic single-asperity regime for nanometer-sized contacts between mica and Pt measured in UHV. Rather, the frictional force is proportional to the contact area between the tip and the sample. Ernst Meyer and co-workers [296] at the University of Basel observed transition between stick-slip and continuous sliding using a lateral force microscope. Silicon-tipped cantilevers were monitored as they slid along atomically uniform crystals of sodium chloride. By varying the normal load on the cantilever tip, the system could be made to enter (and return from) a state of ultra-low dissipation with no mechanical instabilities or stick-slip behaviour. These data were modelled successfully using a Tomlinson model, in which friction is the result of mechanical instabilities that give rise to phonons. The results support the idea that vibrational mechanisms can cause energy dissipation in a variety of geometries.

A specially built force microscope capable of measuring forces as low as 15 pN (15×10^{-12} N) was devised by Dienwiebel and co-workers [297] to find evidence for "superlubricity" in graphite. A graphite flake was captured on the end of a tungsten tip and the friction measured as it was slid along a crystalline graphite substrate (the contact area of the flake was estimated to be a mere 96 atoms). The flake was then brought in and out of perfect commensurability with the graphite surface by rotating it into positions where the atoms were no longer aligned. High levels of friction were found in the commensurate positions and extremely low levels of friction were observed when the surfaces were incommensurate. It was tacitly assumed that extremely low friction coefficients and/or extremely high interfacial slip levels at the atomic level are in some way linked to macroscopic lubriciousness. Problems remain that the coefficients of friction measured in nanotribological experiments and in macroscopic "tribotests" differ by orders of magnitude.

Bhushan [283] reported characterization of nanoscale wear, nanomachining and nanoindentation hardness with an extremely hard tip. A three-sided pyramidal single-crystal natural diamond tip was used at relatively high loads of 1 mN--150 mN. The tip has an apex angle of 80° and a radius of about 100 nm and was mounted on a stainless

steel cantilever beam with normal stiffness of about 25 N/m. For scratching and wear studies, the sample was scanned in a direction perpendicular to the long axis of the cantilever beam at a rate of 0.5 Hz, so that friction can be measured during scratching and wear. The tip was mounted on the beam such that one of its edges is perpendicular to the long axis of the beam so that wear along the beam axis is higher than that perpendicular to the beam axis during scanning. For boundary lubrication studies, an area of 2 μm x 2 μm was scanned at various normal loads ranging from1 to100 mN for a selected number of cycles. The same method was also used to do boundary lubrication measurements. While in this case, a Si_3N_4 tip scanned over an area of 1 μm x 1 μm with a normal load of 300 nN and a scanning speed of not more that 2 μm/s to observe any wear scar. Bhushan demonstrated a method for the measurement of Young's modulus of elasticity of nanowires using AFM nanoindentation [283], in which the scan size was set to zero and a normal load applied to make the indents using a diamond tip. During this procedure, the tip was continuously pressed against the sample surface for about two seconds at various indentation loads. Nano-hardness was calculated by dividing the indentation load by the projected residual area of the indents. Young's modulus was calculated from the slope of the indentation curve during unloading.

Zhang L. Wang reported measurement of Young's modulus of individual nanowires with *in situ* transmission electron microscopy (TEM) [298-300]. The measurement was performed on a specific nanotube whose microstructure was determined by transmission electron imaging and diffraction. By applying to the nanowire an oscillating voltage whose frequency could be tuned, mechanical resonance was induced in the nanowire. When the applied voltage frequency equals the natural resonance frequency of the nanowire, resonance was observed directly under the TEM. The Young's modulus of the nanowire was derived from the observed resonance frequency. In addition, the TEM also observed electric-field emission induced structural damage at the tip of a carbon nanotube with increased voltage. This technique provides a quantitative understanding of structure-property relationship for nanowire-like materials.

For topographic characterization of fragile nanostructures, the frictional force between an AFM tip and a sample must be minimized if the AFM is to be run in contact mode.

2.1.3.4 Electrostatic Imaging by AFM

Running an AFM in non-contact mode, with application of a bias to the tip with respect to a conductive surface, the tip can be made sensitive to electrostatic forces. For a conductive surface with a constant potential, the force between the tip and the surface is given by (see Sergei V. Kalinin and Dawn A. Bonnell[301], on which this section is based)

$$F(z) = \frac{1}{2}(\Delta V)^2 \frac{\partial C(z)}{\partial z} \qquad (2.5)$$

where $F(z)$ is the force, $\Delta V = V_{tip} - V_{surf}$ is potential difference between the tip and the surface, z is the vertical tip-surface separation, and $C(z)$ is the tip-surface capacitance.

An example of this technique is scanning surface potential microscopy (SSPM), or Kelvin probe microscopy (KPM) [301], in which the surface potential is measured by adjusting the potential offset on the tip and keeping the first harmonic response of the capacitance force zero. SSPM is used for the characterization of current carrying devices, especially analysis of integrated circuits, with high spatial resolution.

The tip-surface capacitance is a function of tip-surface separation, tip shape, and topography of sample. Based on the principle of electrostatic interaction (eqn. 2.5), an AFM tip can also be used to locally probe the tip-surface capacitance. An AFM running in this mode is called a scanning capacitance microscope. This method is used to map a two-dimensional dopant profile of semiconductoe devices.

Another example of a biased tip is the measurement of resistivity of a sample by detection of DC or AC current through the tip-surface junction, designated scanning spreading resistance microscopy (SSRM). Measurement of the current at constant bias voltage provides local resistivity mapping that can be related to the chemical composition.

2.2 Characterization of Electronic Transport Properties of Nanowires

Nanowires with diameters reduced to tens of nanometres offer ballistic systems in which the electrons are confined to one degree of freedom and hence fundamental new features like quantized electrical conductance occurs. A ballistic system [302] enables the motion of electrons in ultra-small regions in semiconductor structures at very high electric field with velocities much higher than their equilibrium thermal velocity. Electrons in such a system are not subjected to scattering. The intriguing ballistic transport spawned a great deal of research interest in various materials. Investigation of electronic transport properties has been extensively performed on nanowires of metal[212, 303-314], semiconductors[241, 246, 315-318], and other conductive materials[319, 320]. Some theoretical studies have also been reported [321-324].

2.2.1 Conventional Two-Terminal Method for the Measurement of I-V Curves of Nanowires

Experimentally[241, 317, 318, 325], prior to an electrical transport measurement, a single nanowire is isolated and placed onto an insulating or semiconducting substrate. Electrodes with ohmic contacts to the nanowire are deposited after pattern definition by E-beam lithography. A DC or AC voltage is then scanned across the two electrodes and I-V curves are recorded by a computer. Fig 2.6 gives a typical result [317] of I-V measurement for a single ZnO nanowire.

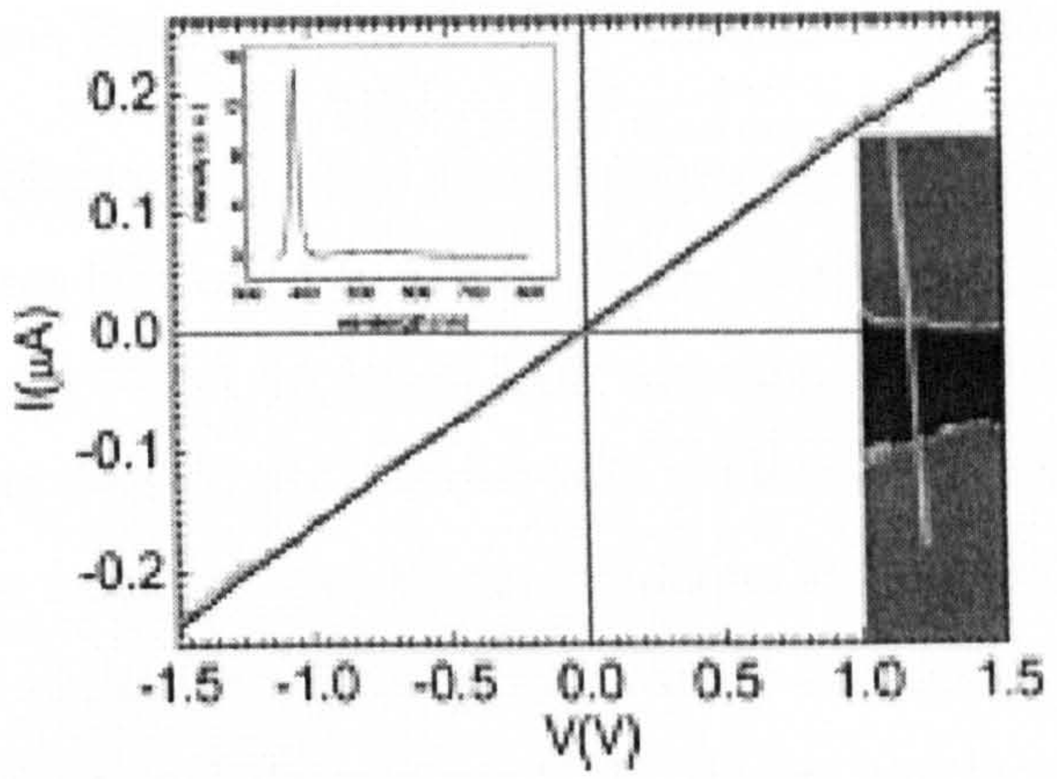

Fig 2.6 The typical characteristics of *I -V* curves of ZnO nanowire[317]. Top left inset: PL spectrum of ZnO nanowires measured at room temperature. Right inset: Scanning electron microscope image of a ZnO nanowire with gold electrodes

2.2.1.1 Basic Problems of the Two-Terminal Method

Electrical contact is a crucial issue in studying the electronic transport properties of semiconducting nanowires. In order to avoid the formation of Schottky barrier, for a p-type semiconducting nanowire, the work function of the metal used for evaporation of electrodes must be greater than that of the nanowire [325]. An Ohmic contact can be fabricated by E-beam lithography [317, 326] or focused ion beam (FIB) deposition[327, 328]. If the measured resistance is proportional to the length of the nanowire segment, an Ohmic contact can be demonstrated.

Isolation of a single nanowire from a cluster or a group of nanowires is a basic problem for the characterization of electronic transport properties of individual nanowires. Nanowires can be isolated either chemically or physically. As an example of physical isolation, nanotube nanotweezers created by Philip Kim and Charles M. Lieber[329] were utilized for nanoscale manipulation and measurement. The carbon nanotube arms serves as conducting wires to the nanoworld. Individual GaAs nanowires were grasped by nanotweezers from the entangled sample, and then the current-voltage characteristic was studied. Extraction of single nanowires can also be realized by ultrasonic dispersion [327, 328].

2.2.1.2 Review of Some Results from the Two-Terminal Method

The E Giovine research group reported a measurement of I-V characteristics in the quasi-ballistic regime of wires fabricated on (100) Si/SiGe heterostructures exhibiting a high mobility 2D electron gas [330]. A depletion layer was found exhibiting a critical width W_c ~200 nm. Wires wider than W_c are metallic with a linear dependence of conductance on the wire width. Wires narrower than W_c are insulating and exhibit a threshold voltage for conduction V_t, which varies considerably from wire to wire and is attributed to a barrier present at the two dimensional electron gas (2DEG)/wire interface.

Sung-Wook Chung *et al* [237] reported fabrication of two-terminal silicon nanowire (SiNW) devices contacted with Ti/Au electrodes. The 15-35 nm diameter nanowires grown using SiH_4 chemical vapour deposition via Au or Zn particle-nucleated vapour-solid growth at 440°C exhibited a diode-like current-voltage character.

The Charles M. Lieber group examined the electrical transport properties of single crystal n-type and p-type silicon nanowires doped by boron and phosphorus during laser catalytic growth [246]. Two-terminal, gate-dependent measurements made on individual boron-doped and phosphorus-doped silicon nanowires showed that these materials behave as p-type and n-type, respectively. Estimates of the carrier mobility made from gate-dependent transport were consistent with diffusive transport and indicated reduced mobility in smaller diameter wires. Temperature-dependant measurements made on heavily doped SiNWs showing no evidence for single electron charging at temperatures down to 4.2 K suggested that the SiNWs possess a high degree of structural and doping uniformity.

Young-Jo Ko *et al* [316] scrutinized the effects of various impurities on coherent electronic transmission in Si nanowires several nanometers wide. Atomic-scale imperfections such as vacancies, substitutional defects, and incomplete surface passivation were found to induce a significant deterioration in the electron conduction. In the case of multiple vacancies, it was found that a zero conductance region around the wire sub-band edge and conductance peaks at higher energies easily develop in these extremely narrow wires.

Several shallow dopants and surface disorder distributed along the wire generally induce suppressed and oscillating conductance as a function of electron energy, with the suppression and amplitude of the conductance oscillation being larger in narrow wires. The calculations imply significant limitation to quantum operation of extremely narrow Si quantum wire devices and emphasize the importance of high quality fabrication techniques.

Electron field emission characteristics of the SiNWs of 18-22 nm diameters synthesized by laser-ablation were studied based on current-voltage measurements and the Fowler-Nordheim equation [315]. Decreasing the diameter and the H_2 plasma treatment of SiNWs improved their field emission characteristics.

Zhibao Zhang and co-workers presented a detailed study of electrical transport properties of single-crystal bismuth nanowires embedded in a dielectric matrix [303, 304]. Measurements of the resistance of Bi nanowire arrays with different diameters (60-110 nm) were carried out over a wide range of temperatures (2.0-300K) and magnetic fields (0-5.4 T). Wire boundary scattering was found to be the dominant scattering process for carriers in the undoped single-crystal Bi nanowires at low temperatures, while less important for heavily Te-doped samples, consistent with general theoretical considerations. The quantum confinement of carriers was believed to play an important role in determining the overall temperature dependence of the zero-field resistivity.

Combining conventional photolithography and micromachining techniques, Hideo Fujii *et al* fabricated an air-bridge-structured silicon nanowire of 15-100 nm in width and thickness and 300-600 nm in length on a silicon-on-insulator (SOI) substrate[331, 332]. Current-voltage curves showed ambient dependency of the conductance and negative-resistance-like conductivity and hysterisis.

2.2.2 The Four-Probe Method

Four-probe I-V characterization (Fig 2.7) [333] is a typical method for the measurement of the electronic transport properties of semiconductors. According to the four-probe

method, the two-dimensional resistance per square (surface resistivity) $\rho(\Omega./sq)$ is given by:

$$\rho = \frac{V_{BC}}{I_{AD}} F \tag{2.6}$$

where I_{AD} is the electric current flowing between probes A and D, V_{BC} is the voltage difference detected between probes B and C , and F is the correction factor.

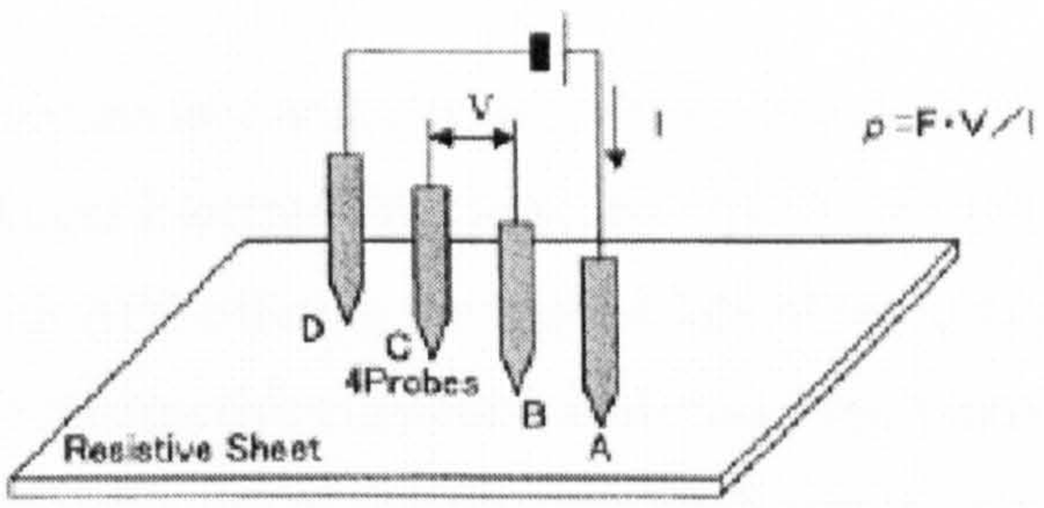

Fig 2.7 Schematic of principle of four-probe method

Application of the four-probe method to the measurement of resistivity of nanowires calls for accurate positioning of the four probes (e.g, STM tips) with the help of SEM, and Ohmic contact between the probes and nanowires.

2.3 Non-destructive Characterization of Chemical Composition (XPS, AES, etc) of Nanowires

Surface composition analysis techniques generally involve a beam of particles hitting a surface, and analysis of the particles emitted from the surface reveals the elemental information. The incident or probing beam consists of photons, electrons, ions or atoms, and the same is true for the particles emitted from the surface. The properties of the emitted particles that are analysed are primarily energy or mass.

Since surface analytical techniques reveal the surface composition of the sample, it is vital that the top layer should not be contaminated by residual species from the chamber's atmosphere. The rate of deposition of gas species on the sample surface at a pressure of

10^{-6} mbar is roughly a monolayer per second, as can be found from the kinetic theory of gases. In order to avoid interference of background particles with the analysis of the surface, the monolayer deposition time should be much longer than the analysis time. This can be achieved by lowering the pressure of the analysis chamber to the ultra-high vacuum range (10^{-9} to 10^{-11} mbar), where a monolayer deposition time extends from roughly 15 minutes to more than 24 hours. Almost all surface analytical techniques require a UHV environment in the analysis chamber.

The most commonly used surface analysis techniques include X-ray Photoelectron Spectroscopy (XPS), Auger Electron Spectroscopy (AES), and Ion Scattering Spectroscopy (ISS), with AES offering the highest lateral resolution[334] of 0.1 μm. Although currently non-destructive elemental analysis of individual nanowires has not been reported due to the difficulty of locating and analysing a single nanowire simultaneously and with great precision, meticulous application of these techniques to nanostructures is possible and can render composition information about nanowires on a macroscopic scale.

2.3.1. X-Ray Photoelectron Spectroscopy

X-ray photoelectron spectroscopy (XPS, also called electron spectroscopy for chemical analysis, ESCA) is a surface sensitive analytic tool to study the surface composition and electronic state of a sample. It uses x-rays to knock electrons out of inner-shell orbitals (Fig 2.8). The kinetic energy ($E_{kinetic}$) of these photoelectrons is measured by the energy of the x-ray radiation (hv) and the electron binding energy ($E_{binding}$) as given by:

$$E_{kinetic} = hv - E_{binding} \tag{2.7}$$

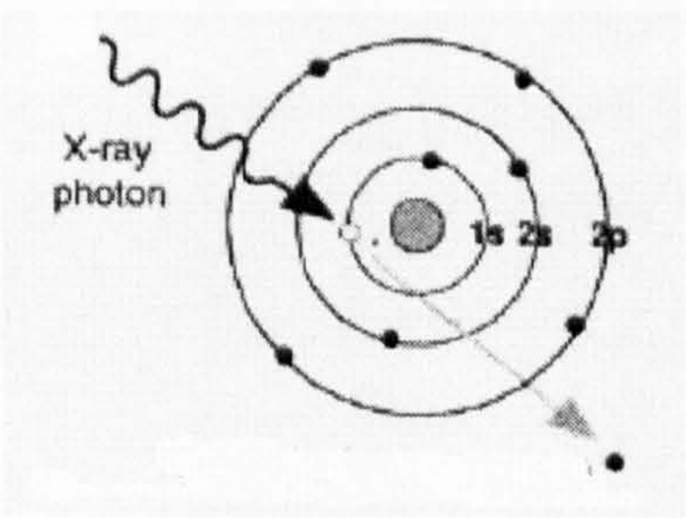

Fig 2.8 Schematic of principle of XPS: photo-ejection of an O1s electron

The energy of the photon is usually enough to eject not only valence electrons but also the core electrons of an atom. Because the energy of core electrons is very specific for the element that the atom belongs to, the spectrum (intensity of emitted electron as a function of energy) gives information on the elemental composition of the shallow surface region. Because of the fundamental interest in the electron binding energy, a spectrometer is usually set up to record the spectrum on this energy scale directly.

2.3.1.1 Introduction to XPS Instrumentation

X-rays are generated by bombardment of a metallic target with high-energy electrons. A small portion of the bombarding electrons induces vacancies in inner shells of the target atoms and electrons of less tightly bound higher levels fall to fill the vacancies with simultaneous emission of X-ray photons. A Kα X-ray is generated when an electron falls from the L shell to the K shell [335]. Materials used for XPS sources are commonly magnesium and aluminium, because of the combined consideration of high energy and small line width of the soft X-rays of Mg *Kα* (E = 1253.6 eV, ΔE = 0.7 eV) and Al *Kα* (E = 1486.6 eV, ΔE = 0.85 eV)[336]. The energy spread of a monochromatic Al *Kα* source is much narrower than that of a Mg *Kα* source or a non-monochromatic Al *Kα* source [337].

Fig 2.9 is a block diagram [335] of a basic XPS instrument, consisting of an x-ray source, specimen, lens, energy analyser, and a detector mounted in a ultra-high vacuum (UHV) chamber. The x-ray source illuminates the specimen with monochromatic soft X-rays. Photoelectrons ejected from the irradiated specimen are collected by a lens system which focuses them into an energy analyser. Electrons selected by the analyser are then collected and recorded by an electron detector. The spectrometer is run by the power supplies and the control and logic circuitry. The user interface usually includes a computer, a keyboard and a visual monitor. The output is either an electron energy spectrum or a map (or image) of the distribution of chemical element from a small part of the sample surface. A typical XPS instrument is shown in Fig 6.1 (Chapter 6).

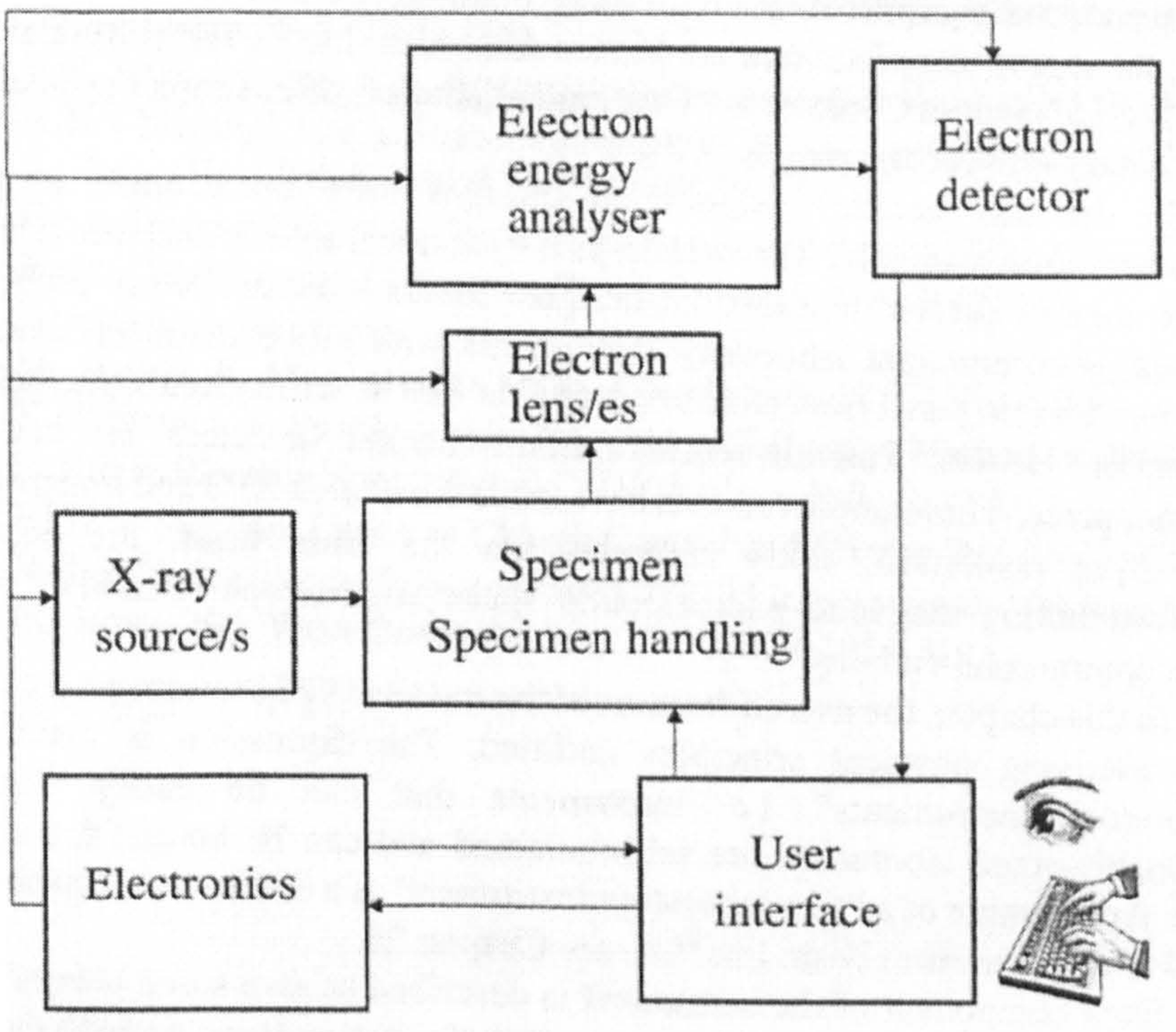

Fig 2.9 Block diagram of the essential components of an XPS instrument [335]

The surface sensitivity of XPS is a few nanometers, because the photoelectrons that are analysed originate from the outmost 1—10 nanometers on the sample, roughly the mean free path of XPS photoelectrons in solids.

2.3.1.2 Numerical Calculation of X-ray Photoelectron Spectrum

Quantification by XPS calls for knowledge of photoionisation cross section, inelastic electron mean free paths, influence of elastic electron scattering, surface excitations, surface roughness, and the energy dependence of the spectrometer transmission function [338]. Let $F(E_0, \Omega)d^2\Omega dE_0$ be the flux of electrons excited from an energy interval dE_0 at E_0 into the solid angle element $d\Omega$, then the number of electrons emitted per second, per unit energy and solid angle Ω is given by[338]:

$$J(E,\Omega) = \int dE_0 F(E_0,\Omega) \int f(z) G(E_0, \frac{z}{\cos(\theta)}, E) dz \qquad (2.8)$$

where $G(E_0,R;E)dE$ is the probability that an electron with initial energy E_0 has energy in the interval (E, $E + dE$) after having travelled the path length R, and $f(z)$ is the number of atoms per unit volume at depth z, and θ is the angle of emission with respect to the surface normal.

Calculation of $G(E_0,R;E)dE$ involves $K(E,T)$, the differential inelastic electron scattering cross section, with $K(E,T)dRdT$ being the probability that an electron of energy E will lose energy dE in the interval (T, $T + dT$) after having travelled a path length dR in the solid. For most of the energy spectra, the total energy loss is small compared with the primary electron energy, $K(E,T)$ is independent of E, $K(E,T) \approx K(T)$, Landau in Ref [338] showed that:

$$G(E_0,R;E) = \frac{1}{2\pi}\int_{-\infty}^{\infty} e^{ix(E_0-E)}e^{-R\Sigma(x)}dx \qquad (2.9)$$

with

$$\Sigma(x) = \frac{1}{\lambda_i} - \int_0^{\infty} K(T)e^{-ixT}dT \qquad (2.10)$$

where x is an integration variable without physical significance.

The Landau expression (2.9) can be calculated numerically by Taylor expansion or convolution [338].

The inelastic scattering cross section $K(T)$ in eqn.(2.10) may be calculated either from the dielectric function of the solid or experimentally by analysis of reflected electron energy loss spectroscopy (REELS). In the development of methods to exploit peak shape for extraction of quantitative information, Tougarrd [338] introduced a concept of universal cross-section, a general method based on the observation that the product $\lambda_i(E)K(E,T)$ depends strongly on T, moderately on the specific solid, and weekly on E. For solids with a narrow plasmon structure, a three-parameter universal cross section is given by:

$$\lambda_i(E)K(E,T) = \frac{BT}{(C-T^2)^2 + DT^2} \tag{2.11}$$

where the three parameters B, C and D have been determined for different classes of materials. For silicon dioxide, $B = 299$ eV^2, $C = 542$ eV^2, $D = 275$ eV^2.

In addition to $G(E_0,R;E)$, calculation of the spectrum $J(E,\Omega)$ from eqn.(2.8) requires that the in-depth concentration distribution of atoms $f(z)$ and the initial excitation energy $F(E, \Omega)$ are known. As a highly surface sensitive analysis technique, quantification by XPS relies greatly on surface morphology [338], which is depicted in eqn.(2.8) by $f(z)$. In XPS analysis of surface nanostructures, inappropriate assumption of $f(z)$ may introduce the biggest error in quantitative analysis. $F(E, \Omega)$ can be calculated numerically[338], provided that $f(z)$ is given for a specific profile. Practically, spectrum inversion—removal of background from the collected spectrum—is used to determine the undistorted spectrum (the relative peak area), if the analysed peaks do not overlap.

The true background to a spectrum depends on both the composition of the sample and the depth distribution of the elements present [339]. For a practical XPS analysis, some relatively simple backgrounds, namely, Linear, Shirley, and Tougaard, are commonly adopted.

A linear background [338] is a straight line drawn from a point close to the peak on the low kinetic energy side of the peak, E_{min}, to a point on the high kinetic energy side, E_{max}.

The Shirley background [340] is a simple background whose intensity is proportional to the total intensity of the peak area above the background. It is an iterative procedure [338]

$$F^n(E) = J(E) - k_n \int_E^{E_{max}} F^{n-1}(E')dE' \tag{2.12}$$

where $J(E) = F^0(E)$ is the measured spectrum, $F^n(E)$ is the final spectrum, and k_n is found from $F_n(E_{min}) = 0$.

The linear background is widely used for polymers, while the Shirley background is mostly used for metals [339].

The Tougaard background [338] is an accurate algorithm which relies on a quantitative description of the physical process leading to the background. For materials with a sharp plasmon structure and homogeneously or exponentially distributed in-depth profiles, using the three-parameter cross-section, equation (2.11), the algorithm for background correction is:

$$F(E) = J(E) - B_1 \int_{E}^{E_{max}} J(E') \frac{E'-E}{[C-(E'-E)]^2 + D(E'-E)^2} dE' \qquad (2.13)$$

where $C = 1643$ eV^2, B_1 is a constant adjusted to give zero intensity in a region around 30-50 eV below the peak structure. The Tougaard background has the advantage that it defines a peak over a narrow energy range, making it superior in background shape control to the Shirley algorithm.

2.3.1.3 Practical Analysis of X-ray Photoelectron Spectra

In an X-ray photoelectron spectrum, the photoelectron emission is energy analysed to produce a spectrum of electron intensity as a function of energy (binding energy). The intensity of a peak in an XPS spectrum is measured by integrating the recorded counts per seconds minus a computed background over an energy interval delimiting the peak. In order to quantify a sample, the integrated intensity must be adjusted for both relative sensitivity of the various photoelectric lines and energy dependent instrumental and measurement artefacts before computing the elemental composition for a surface.

A spectrum with binding energy ranging from 0 to 1250 eV is referred to as a survey-scan or wide-scan (Fig 6.2). In a survey-scan spectrum, discrete peaks whose energies obeying equation (2.7) reflect the corresponding shell structure (core levels) of the atomic electrons. These arise from elastic photoemission in which a photoelectron is ejected from an atom in the solid and escapes from the surface with no energy loss. In Fig 6.2, with binding energy increased from 0, band levels appear from closely-spaced valance

bands (4d, etc.) to tightly bound core levels (3d, 3p, etc.). The peaks are seen to sit on a step-like background which rises with increasing binding energy.

The background originates primarily from two sources [340]—intrinsic characteristic loss and inelastic scattering. The intrinsic loss is introduced by intrinsic excitation which occurs at the same time as the transfer of energy to the core level electron. In the energy transfer process, some of the energy of the out-going electron is used to excite an electron in an outer shell into an excited state. Therefore, the kinetic energy of the electron emitted from the core level will have an energy less than the energy calculated by eqn (2.7). As a result, both the electrons of the inner shell and the outer shell contribute to the background in the final spectrum and produce features called ionisation loss peaks (or shake-up satellites). The background due to inelastic scattering is the result of loss of energy through one or more extrinsic inelastic processes which appear as a background extending from the peak energy down to zero kinetic energy.

Core levels are routinely labelled [341] by the nomenclature nl_j, where n is the principal quantum number, l (= 0, 1, 2, 3, 4, …, designated s, p, d, f, …) is the orbital angular momentum quantum number and j is the total angular momentum quantum number,

$j = (l + s)$ where s $(= \pm ½)$ is the spin angular momentum quantum number. The s levels are singlets but all other levels ($l > 0$) are doublets with the two possible states different in energy as a result of the unpaired electron left in an orbital following photoionisation having its spin and orbital angular momentum vectors either parallel or anti-parallel.

Analysis of an XPS spectrum usually involves identification of elements at the surface by the peaks of photoelectrons related to the levels in the emitting atoms by their characteristic binding energy. Peak width of the measured photoelectron depends on the natural width of the level ionised, the energy spread in the X-ray beam, and the energy resolution of the analyser. In most cases, the binding energies of the core levels give unambiguous identification of the elements in the sample analysed. However, the same atom in different chemical environments can give rise to different values of binding energies—the so called "chemical shifts". In other words, chemical shifts originate from

the variations in electrostatic screening experienced by core electrons as the valence and conduction electrons are drawn towards or away from the specific atom. In addition to the variation of chemical environment, differences in oxidation state, molecular environment and co-ordination number all provide different chemical shifts. Consequently, chemical shift of a photoelectron peak is usually used to interpret surface chemistry. However, in the case of insignificant chemical shift, Auger peaks (the next sub-section) in the spectrum can be used to resolve more detailed information about surface chemistry.

Chemical shifts of core levels are routinely analysed by curve fitting in which the component binding energies can be resolved accurately and the intensities of the overlapped core level components can be quantified. Curve fitting [342] involves the determination of changes in binding energy and the application of chemometrics to find small shifts. The physics behind curve-fitting is the optimum partition of the contributions from individual transitions to the recorded envelop using predefined line-shapes for modelling the underling transitions. Curve fitting can be carried out by synthesis of a spectrum by digital or analogue methods to sum a series of functions representing individual peaks to produce a final function that closely represents the experimental spectrum [343]. The fitting can be a direct addition of guessed component peaks (curve synthesis) or a least squares refinement (curve fitting) of the component peaks based on initial curve synthesis.

Two factors of prime importance to successful curve fitting methods are the choice of an appropriate fitting function and a proper consideration of the background.

The most commonly used functions for curve fitting are Gaussian or Lorentzian, or a convolution of Gaussian and Lorentzian—the Voigt Function. Practically, the Voigt convolution integral is approximated [339] by equations (2.14) and (2.15) below

$$GLP(x;F,E,m) = \exp[-4\ln 2(1-m)\frac{(x-E)^2}{F^2}]/[1+4m\frac{(x-E)^2}{F^2}] \qquad (2.14)$$

$$GLS(x,F,E,m) = (1-m)\exp[-4\ln 2\frac{(x-E)^2}{F^2}] + m/[1+4\frac{(x-E)^2}{F^2}] \qquad (2.15)$$

The above two equations act as mappings between a pure Gaussian (with $m = 0$) and a pure Lorentzian (with $m = 1$), where m is the mixing parameter, x is the abscissa, F is a parameter representing single full width at half maximum (FWHM). The difference between eqn. (2.14) and (2.15) is that eqn. (2.14) is a product (GLP) of a Gaussian with a Lorentzian where m acts as a non-linear blending between the two basic functions, while eqn. (2.15) is a linear summation (GLS) of the two functions through the mixing parameter. Choosing eqn. (2.14) can effectively reduce Lorentzian tails.

For background correction, Linear, Shirley and Tougaard Backgrounds are routinely used, as has been described in the previous sub-section.

Quantitative elemental analysis can be carried out provided a single survey scan is acquired under proper condition. The surface compositions (in atomic percentage, At%) are determined by subtracting a background from each major elemental peak in the spectrum, measuring the peak areas and applying a sensitivity factor. A homogeneous analysed depth is assumed. In a survey scan spectrum, the intensity of a peak is directly proportional to the density of the atom from which it derives. For a homogeneous solid (at least homogeneous within the sample depth analysed), the relative atomic concentration C_A of an element A is [344]

$$C_A = \frac{\frac{I_A}{S_A}}{\sum_{i=1}^{n}\frac{I_i}{S_i}} \qquad (2.16)$$

where C_A is usually expressed as atomic percentage (%) of all the elements detected. I_i is the measured intensity (peak area) of the i^{th} element; n is the total number of elements detected; S_i is the relative sensitivity factor (dependent on the photoionisation cross section) of the i^{th} element. For elements with low cross-section core levels, the detection limit of XPS is typically within 0.1 atoms percent [344].

The analysis of XPS can itself induce change in surface composition and topography due to the effect of the incident X-rays. Consequently, the exposure time of a sample to the x-ray used for analysis should be as short as possible to minimize possible sample damage.

2.3.2. Auger Electron Spectroscopy

The Auger process is initiated by creation of a core hole - this is typically carried out by exposing the sample to a beam of high energy electrons (typically having a primary energy in the range 2 - 10 keV). Such electrons have sufficient energy to ionise all levels of the lighter elements, and higher core levels of the heavier elements.

Auger electron spectroscopy probes the chemistry of a surface by measuring the energy of electrons emitted from that surface when it is irradiated with electrons of energy in the range 2--10 keV. Some of the electrons emitted from the surface have energies characteristic of the element from which they were emitted, and in some cases, the bonding state of those atoms. The physical process by which these electrons are made is called the Auger Effect (Fig 2.10).

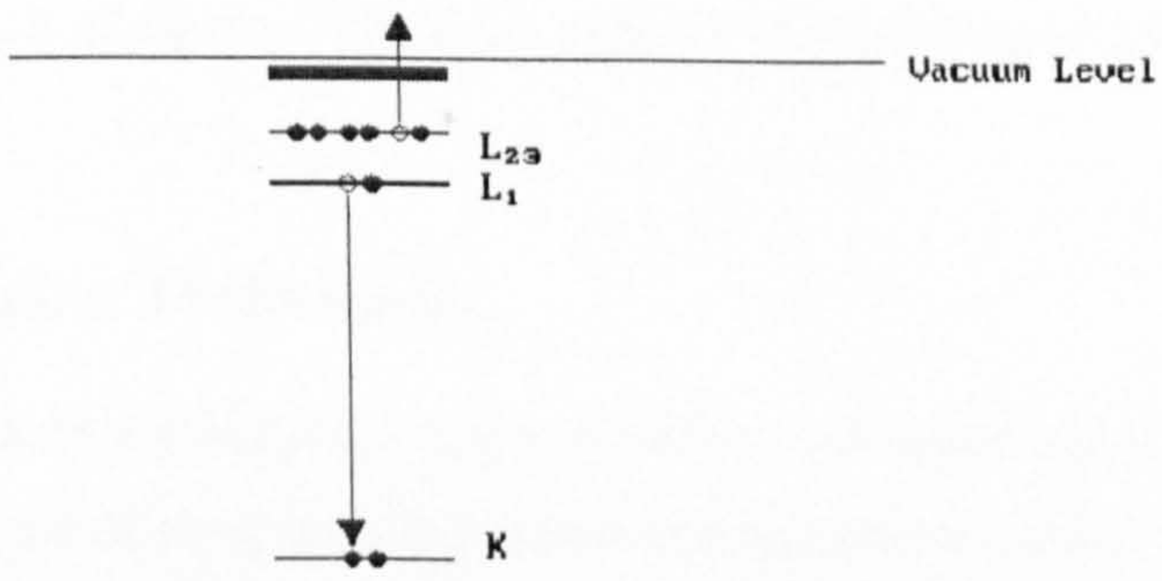

Fig 2.10 Schematic of the process of Auger Emission

In this example, irradiation of the sample with a primary electron beam ionises an atom by exiting an electron in the K shell. The ionised atom that remains after the removal of the core hole electron is in a highly excited state and will rapidly relax back to a lower energy state by Auger emission: one electron falls from a higher level to fill the initial core hole in the K-shell and the energy liberated in this process is simultaneously

transferred to a second electron; a fraction of this energy is required to overcome the binding energy of this second electron, the remainder is retained by this emitted *Auger electron* as kinetic energy. In the Auger process illustrated, the final state is a doubly-ionized atom with core holes in the L_1 and L_{23} shells. The characteristic energy of this ejected electron is

$$K_E = E_K - (E_{L1} + E_{L23}) \tag{2.17}$$

where K_E is the kinetic energy of the emitted electron (Auger electron), E_K, E_{L1} and E_{L23} are the binding energies of electrons in the K, L_1 and L_{23} shells. Because these orbital energies are determined by the element of the atom, the composition of a surface can be measured.

Auger electron spectroscopy is useful as a surface analytical technique because the energies of the electrons emitted are typically in the range of 50 eV to 3 keV, and at this energy they cannot escape from more than a few nanometres deep in the surface. The technique is commonly used in conjunction with another technique like SEM.

AES is a technique often described as more sensitive than XPS [345]. Some AES systems have spatial resolution of 10 nm [346] that are capable of analysing chemical composition of a single nanowire.

2.3.3. Ion Scattering Techniques

Ion scattering is a relatively simple, non-destructive, real-space technique, which can be applied for the analysis of sample composition and sample structure. By projecting accelerated ions onto a sample and analysing the angle and energy distributions of the scattered ions, information of the chemical composition and structure of the sample can be acquired.

Traditionally, ion scattering analysis is divided into three energy regimes: high-energy ion scattering (HEIS, energy range 0.2-2 MeV), medium-energy ion scattering (MEIS, energy range 50-200 keV), and low-energy ion scattering (LEIS, or ion scattering spectroscopy-ISS, energy range 1-10 keV). The major difference between the former two

energy regimes and LEIS is that quantitative analysis of the composition is easier in the high energy than in the low energy regime [347]. For surface structure analysis, HEIS and MEIS determine the position of surface atoms relative to the bulk-atom positions, while LEIS measurements reveal relative positions between surface atoms.

The principle of ion scattering techniques is illustrated in Fig 2.11.

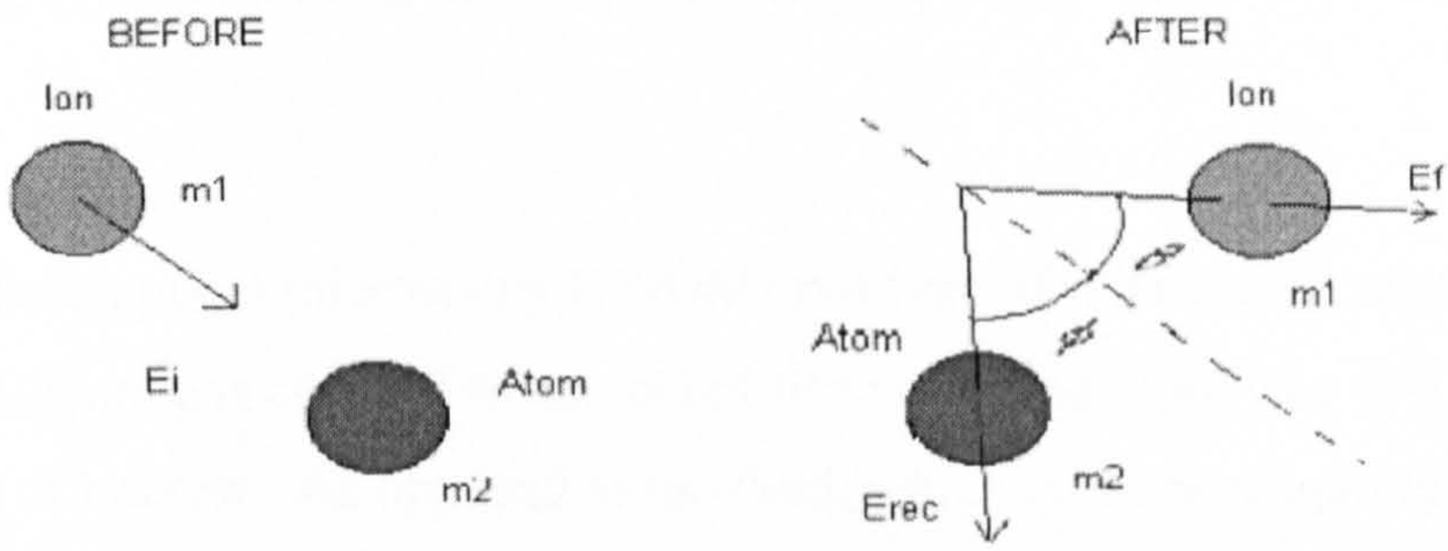

Fig 2.11 Schematic [348] of principle of LEIS

The energy of the scattered ions is approximated by [348]

$$F_f = \left(\frac{\cos\theta \pm \sqrt{\left(\frac{m_2}{m_1}\right)^2 - \sin^2\theta}}{1 + \frac{m_2}{m_1}} \right)^2 \cdot E_i \tag{2.18}$$

$$E_{rec} = \frac{4\frac{m_2}{m_1}\cos^2\Phi}{\left(1 + \frac{m_2}{m_1}\right)^2} \cdot E_i \tag{2.19}$$

where m_1 and m_2 are the atomic mass of the ions and the specimen, θ and Φ are the angles of the scattered and recoiled ions measured with respect to the surface plane, E_i is the initial energy of the projectile ions, E_f and E_{rec} are the energies of the scattered and recoiled ions. It can be seen that the scattered ion energy is directly related to the mass of the scattering atom.

2.4 Characterization of Photonic Properties of Nanowires

Investigation in light-emitting nanostructures has been an active area of research due to the unique physical properties and potential applications of the structures, including optoelectronic devices and microanalysis [238, 349, 350]. Lasing action from single nanowires can be excited either by pulsed laser or electric pulses. Characterization of the lasing action from single wires and its dependence on the morphology of the wire can be facilitated by high-resolution near-field optical imaging and spatially resolved spectroscopy.

Scanning near-field optical microscopy (SNOM) is a type of microscopy where a sub-wavelength light-source is coupled to an optical fibre held and scanned a few nanometers above a surface of interest. As opposed to far-field, which is the propagating wave electromagnetic radiation that is readily detectable with human eyes, the optical near-field is a non-propagating electric field that exists at a sub-wavelength distance around a light-scattering or fluorescent particle [351]. The operational principle (Fig 2.12 a) [352] behind near-field optical imaging involves illuminating a specimen through a sub-wavelength sized aperture whilst keeping the specimen within the near-field regime of the source. The aperture-specimen separation is kept to less than half the diameter of the aperture so that the source does not have the opportunity to diffract before it interacts with the sample. The resolution of the system is determined by the aperture diameter as opposed to the wavelength of light used.

An image is built up by raster-scanning the aperture across the sample and recording the optical response of the specimen through a conventional far-field microscope objective. By illuminating a sample with the "near-field" of a small light source, optical images can be constructed with resolution well beyond the usual "diffraction limit", and typically about 50 nm.

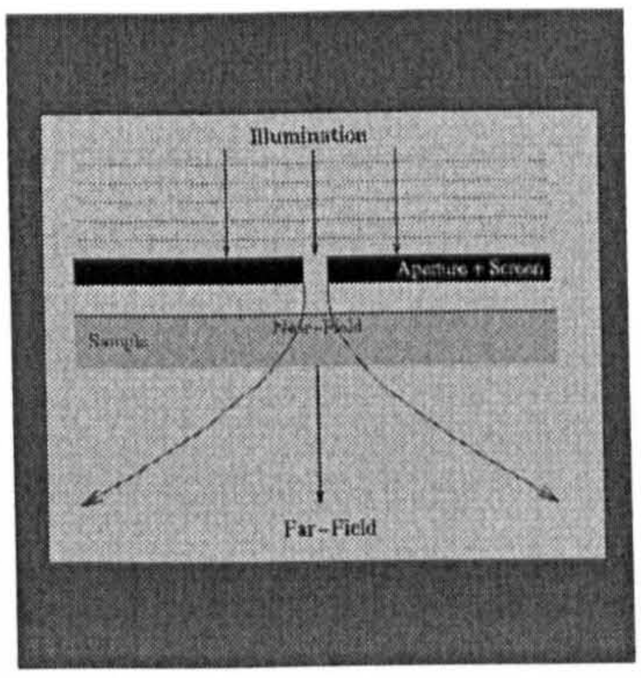

(a)

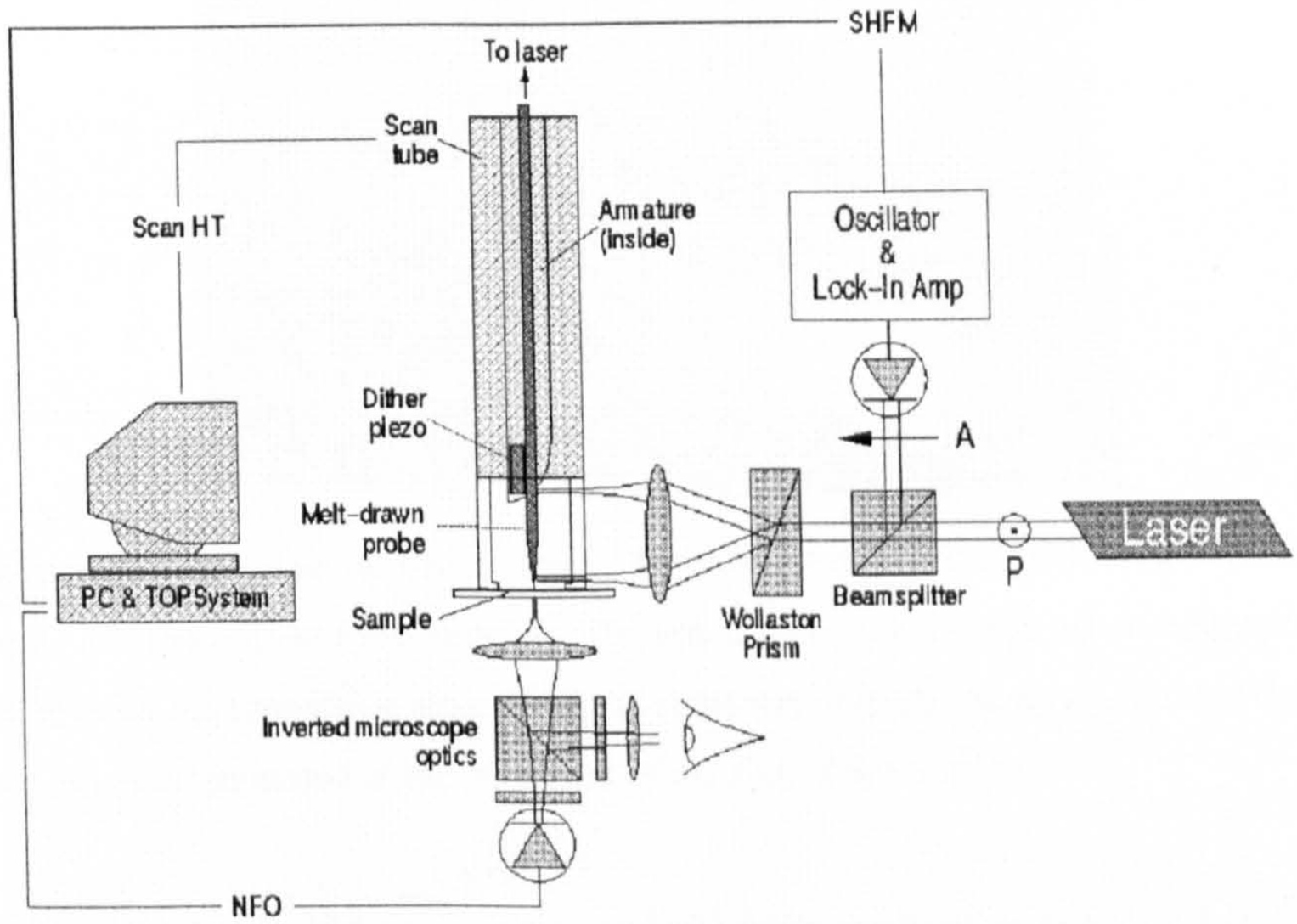

(b)

Fig 2.12 Schematic of SNOM [352]: (a) Principle; (b). Instrumentation

An STM tip can induce light emission in a narrow gap between the tip and the sample surface. The light detected at far-field distance offers information about the photon creation process in the tunnelling gap and the subsequent light propagation process from the tunnelling gap to a far-field distance. STM induced light emission from nanostructures on hydrogen-terminated Si (100) surface was mapped spatially and analysed spectroscopically in the visible spectral range by M. Sakurai[353]. The experiment was performed in an UHV chamber. After formation of nanostructures on a hydrogen terminated surface, patterns of silicon dangling bonds were fabricated by the extraction of H or D atoms using the STM tip. Isolated Ag nanoclusters were deposited on isolated Si

dangling bond sites. STM-induced light emission experiments were performed at room temperature. The photons emitted from the tip-sample regions were collected by an optical fibre bunch mounted in the UHV chamber (Fig 2.13) [354].

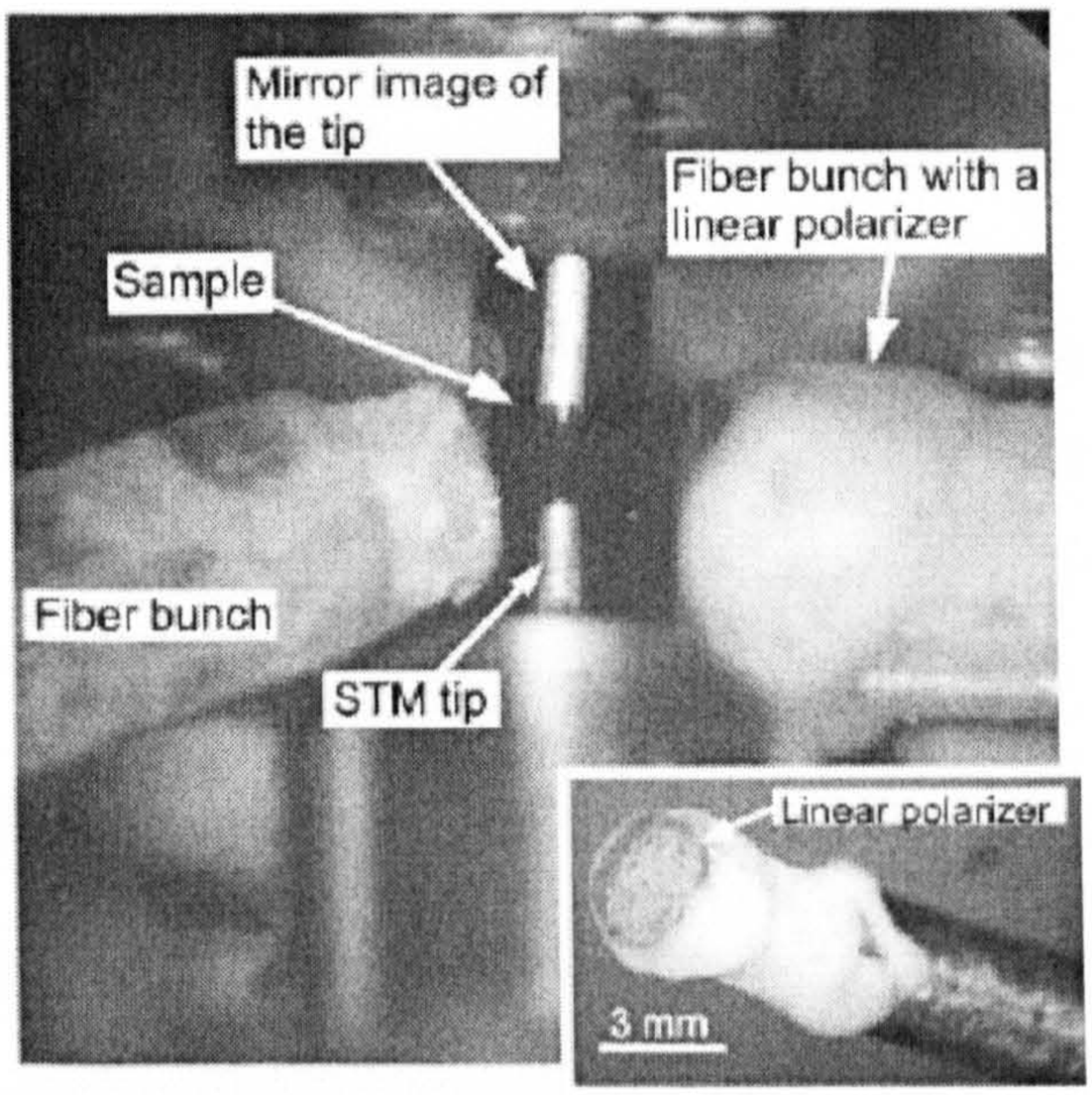

Fig 2.13 Photograph [354] of the photon-emission STM focusing on the part including the STM tip, the sample, and the optical fibre bunches. The left fibre bunch collects all components of the light emitted from the tunnelling region and the right one collects linearly polarized light. Inset: A linear polarizer mounted at the end facet of the right fibre bunch.

A photon map was obtained by a water cooled photomultiplier tube and the optical spectra were acquired through a charge coupled device (CCD) detector and a spectrograph. The method based on STM-induced light emission has been widely applied to the study of luminescence of semiconductors with high spatial resolution.

The above mentioned are confined to characterization of morphological, mechanical, electron transport and photonic properties of nanowires. Characterization of nanowires can also deals with magnetic, reactivity, and other properties, which are not considered in this thesis.

Chapter 3

Theory of Ion Beam Induced Topography on Solid Surfaces

In this project, ion beam bombardment is used to generate nanowires on InP (100) surfaces. It is essential to understand the physics of ion beam interaction with solid surfaces, and the mechanism of nanowire formation with this technique. In this chapter the sputtering mechanisms relevant to the erosion processes arising from ion beam bombardment of solid surface are discussed, followed by a brief review of ion beam induced topography models.

3.1 A Brief Introduction to the Physics of Ion Beam Interaction with Solid Surfaces

Ion beam technology usually introduces the surface of a solid (target) in vacuum to a directed flow of ions. These ions are often extracted from a gas discharge plasma as a spatially restricted beam and accelerated by electric fields to the required energy. The discharge plasma is generated inside a special device -- the ion source. For the purposes of surface modification the kinetic energy regime from about 100 eV to 5000 eV is often used, and for other goals such as ion implantation, energies up to a few hundreds of keV are routinely used. In a typical ion beam equipment, the ion source is spatially separated from the target so that the ion beam parameters are fully independent of the parameters of the target environment.

Ion bombardment of a solid surface generally causes erosion, which is known as sputtering. Sputtering occurs on all kinds of material surfaces under all kinds of heavy particle bombardment. Even electrons and photons can give rise to considerable erosion effects in certain classes of materials. It is common knowledge that only about 5% of ion energy contributes to sputtering (Fig 3.1b), most of the ion energy is dissipated in heating. Other processes include ion reflection (Fig 3.1b), electronic stopping (Fig 3.1a), nuclear reactions, ion induced radiation, and creation of plasmons [355]. The energy distribution in

these mechanism changes with ion energy and mass. In the high energy regime, inelastic process is the primary energy loss mechanism (mostly electronic loss), with displacement collisions dominating at lower energy and loss into heat once the ion has slowed below a critical energy. Heavy ions give rise to very dense dispalcement cascade and create more displacement collisions than light ions. A typical ion sputtering mechanism is described as follows.

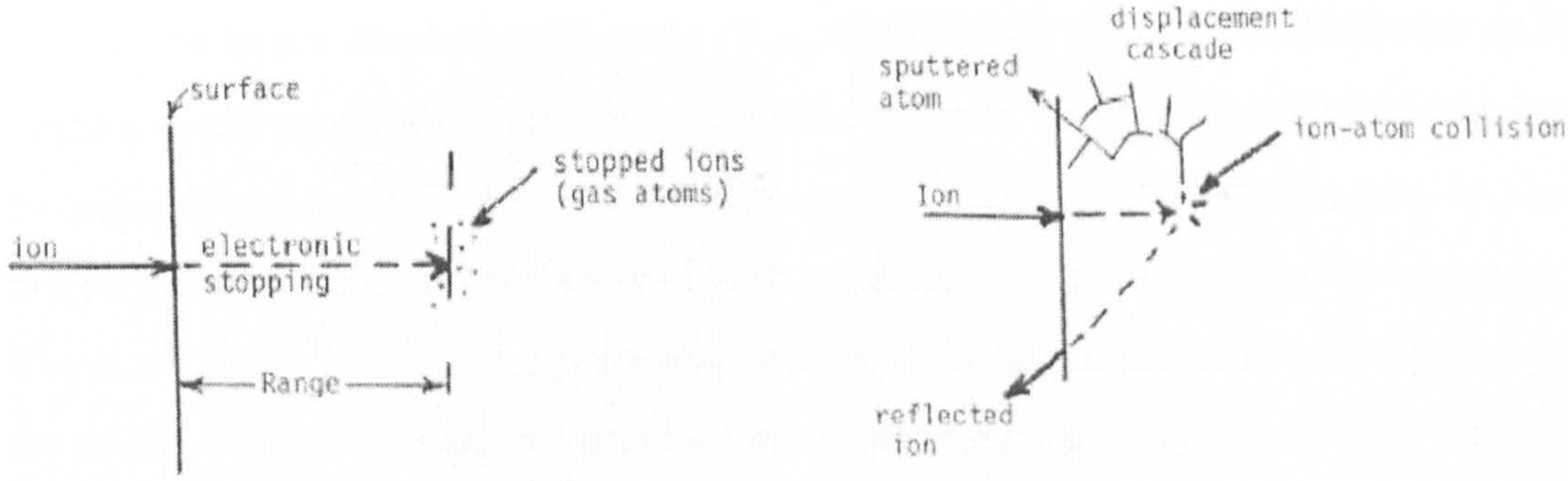

(a) Electronic stopping (b) Sputtering and ion reflection

Fig 3.1 Schematic of ion-surface interaction [356]

Ions with energy 0.1--5 keV and masses of 20--250 *amu* have the velocities of about a few tens of thousand meters per second. When the bombarding ions (e.g., argon, xenon, oxygen, nitrogen or their mixes) are chosen such that their mass is comparable to that of the target's atoms, they efficiently transfer their momentum to the target's atoms. The excess momentum leads to movement of the bombarded target atoms which will transfer in collisions the energy and momentum from the bombarding ions to the atoms adjacent to the bombarded atoms within the target. And these atoms, in turn, transfer the energy and momentum to their adjacent atoms and so on. This process gives rise to a collision cascade. It is obvious that in a collision cascade the successive momentum is shared over time with more and more atoms, so that each successive atom gets less energy and momentum than the preceding one. The inter-atomic bonds tend to pull the displaced atoms back to their equilibrium positions. Some atoms are given enough energy to overcome these binding forces and are either displaced from their equilibrium positions or ejected out of the target, especially those on the surface. Atoms on the surface have

coupling forces weaker than that between bulk atoms and under the same conditions they are more likely to break their bonds with the adjacent atoms. For those atoms which do not have enough energy, the inter-atomic forces will pull them back to their previous positions after a series of damped oscillations.

As a brief extension of the discussion, when the kinetic energy of the incoming particles exceeds the lattice displacement energy E_{disp} of the target atoms—the minimum energy to knock a target atom far enough into the lattice so that it will not immediately hop back to its original site, about 15-40 eV for most metals [357]—atoms of the lattice may be pushed to new positions, causing surface and bulk migrations of atoms and surface damage. Displaced atoms lose an energy corresponding to the lattice (or bulk) binding energy—the energy of a lattice site, or vacancy formation energy, usually 1-2 eV [357]. When a surface atom is given energy greater than the surface binding energy E_{surf} (less than 10 eV [357]) — it will be ejected into the gas phase in a process called physical sputtering. Since ion bombardment can create a surface that is far from its thermodynamic equilibrium i.e. metastable surface phases, the incident particles can also induce a chemical reaction which produces an unstable compound at the surface: dubbed chemical sputtering.

Sputtering gives rise to surface erosion. The erosion rate is determined by the *sputtering yield Y* which is defined as the average number of emitted atoms per incident particle. It depends on the type and state of the bombarded surface, the characteristics of the incident particle, and the experimental geometry. The ion-bombardment erosion caused by noble-gas ions on clean metal and semiconductor surfaces invokes physical sputtering.

Physical sputtering effects are not expected to differ between ions and neutral atoms. Because at low energies (10 eV--10 keV), in general, the potential energy of the incoming particle contributes to electron transitions, while the kinetic energy primarily goes into lattice-atom vibrations or displacements [358]. For this reason, the term "ion" when mentioned in the context of surface sputtering is actually used as a synonym for "primary projectile" and does not bear any meaning as to the charge state of the particle.

When the kinetic energy of the projectile particles reaches the 100–1000 eV range, kinetic emission of gamma (secondary) electrons starts and adds to the potential (Auger) emissions. At yet higher energies (well into the keV range), the scattering cross-sections become so small that the collision cascades within the bulk of the target material goes far below the surface. Sputtering, a surface atomic scale process, thus becomes first very insensitive to particle energy, and then actually decreases with increasing energy. Finally, at MeV energies, the processes involved enter the realm of radiation damage [358].

A great amount of research in sputtering over the last six decades has been motivated by interest in a great variety of subjects [357, 359]. In fusion energy research, sputtering addresses the concerns of reactor wall erosion and plasma contamination; in micro-electronics, sputter deposition or etching are ideal fabrication or surface modification processes; in surface analysis, depth profiling, composition and structure analysis, sputtering is used as a common tool. As the technology of miniaturization marches into nanoscale, ion beam sputtering on solid surfaces is becoming an established technique in fabricating various nanostructures in a single step.

A quantitative treatment of physical sputtering requires an understanding of the energy transfer mechanisms in atomic collision and penetration phenomena. Depending on the regimes considered and the various degrees of approximation invoked, a detailed understanding of sputtering also requires physical inputs that include genuine surface and bulk properties, projectile kinetic (and possibly potential) energy and incident angle, atomic masses of the collision partners and, perhaps most importantly, an accurate model of ion-atom and atom-atom interaction potentials.

Physical sputtering can be discussed with a classical two-particle elastic scattering model as shown in Fig 3.2.

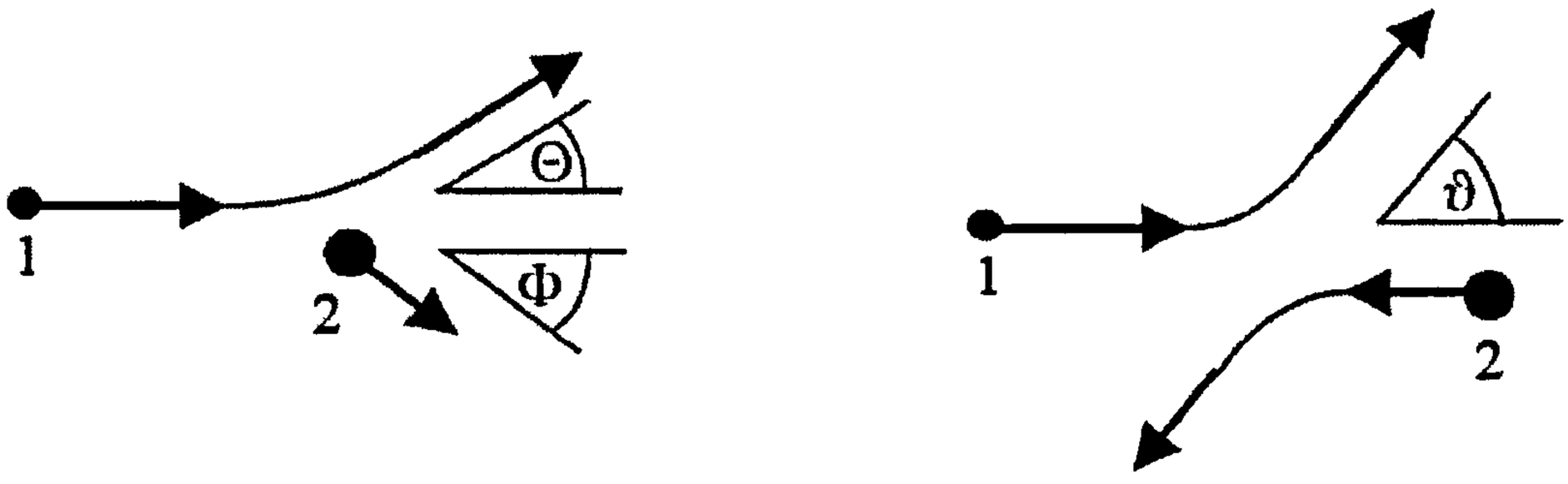

(a) (b)

Fig 3.2 Classical two-particle scattering; (a) in laboratory coordinates, and (b) in barycentric coordinates. "1"—projectile, "2"—target atom (at rest in laboratory coordinates).

The energy T transferred by the incoming particle with energy E to the target particle is a result of elastic-collision theory (see for example Ref. [360]) dictated by the conservation laws of energy and momentum

$$T = \gamma E \sin^2 \frac{\vartheta}{2} = \frac{4M_1M_2}{(M_1+M_2)^2} E \sin^2 \frac{\vartheta}{2} \qquad (3.1.1)$$

Where ϑ is the scattering angle in the center-of-mass frame of reference for the two particles (Fig 3.2 b), γ is the energy-transfer coefficient, and M_1 and M_2 are the atomic masses of the projectile and the target particle respectively. In order to get the cross-section for the energy transferred, the probability for each final scattering angle is needed.

To obtain the details of the scattering trajectory, a static, central-force potential field $V(r)$ can be introduced so that ϑ is given by the integration of the single equation of motion along the collision path [360]

$$\vartheta = \pi - \int_{-\infty}^{+\infty} \frac{b\,dr}{r^2\left[1 - \frac{V_{(r)}}{E_C} - \left(\frac{b}{r}\right)^2\right]^{\frac{1}{2}}} \qquad (3.1.2)$$

This is the general orbit equation for two-body central-force scattering, where E_c is the kinetic energy of the center of mass, b is the collision impact parameter, and r is the distance between the two particles. It is valid as long as kinetic energy and momentum

are conserved for the system, and as long as the central potential force is static and spherically symmetric. With eqns. (3.1.1) and (3.1.2), one can then proceed in principle to calculate the collision cascade numerically.

Sputtering by elastic collisions can have three regimes: the single knock-on, the linear cascade and the spike regime [361]. In single knock-on events, primary recoil atoms receive an energy sufficient to get sputtered but not to generate recoil cascades; in linear cascades, recoil atoms generated by ion-atom collisions are given enough energy to generate secondary knock-on atoms among the lattice atoms; and finally, in the spike regime, the density of recoil atoms in a limited region is such that most atoms are considered to be in motion.

The spike regime, or even the linear collision cascade regime, becomes less important at energies near threshold. From results of elastic-collision theory (Fig 3.2), unless both particles are in motion, where

$$\vartheta_{\max} = \begin{cases} \pi & for\ M_1 < M_2 \\ \arcsin\dfrac{M_2}{M_1} & for\ M_1 > M_2 \end{cases} \qquad (3.1.3)$$

the scattering angle for an incoming heavy ion is necessarily smaller than $\pi/2$, and atoms sputtered as a result of (few) low-energy collisions are more likely to be sputtered at grazing incidences [362-364]. It's worth noting here that for low energy and heavy ions, the predominant sputtering mechanisms will be those that do not require backscattering of the ion from the interior of the target.

3.2 Quantification of Ion Bombardment – Monte Carlo Simulation of Ion Interaction with Solid Surfaces Using TRIM 2000

The effects of ion bombardment on solid surfaces can be quantified by a comprehensive scientific program called TRIM (the TRansport of Ions in Matter) included in the scientific software package SRIM (the Stopping and Range of Ions in Matter). SRIM is

based on the work by Ziegler and Biersack on stopping theory [360], and is freely distributed by James F Ziegler[365].

In SRIM, all ion-atom collisions receive a quantum mechanical treatment, and the stopping and range of ions can be calculated in the energy range 10 eV–2 GeV. The calculations of the ion-atom screened Coulomb collisions use statistical algorithms to allow for jumps between calculated collisions before the collision results are averaged over the trajectory gap, and interactions between overlapping electron shells (electronic stopping) are included. TRIM accepts complex, multilayered and multi-component (including biological) targets with up to eight layers, each of different materials. Solid or gas targets can be treated, although differently, and the ion angle of incidence with respect to the surface normal can be specified. Using a ZBL potential, TRIM calculate both the final 3D distribution of the ions and the kinetic phenomena associated with the ion's energy loss: target damage, sputtering, ionization, and phonon production. All target atom cascades in the target are followed in detail. The program can be interrupted and resumed at any time. Plots of the calculation can be saved and displayed. The initial version of TRIM was written in 1980, and the physics underlying TRIM is described in Ref. [360].

For the particular purpose of calculating surface sputtering with TRIM, three material input parameters are of importance: the surface binding, lattice displacement, and lattice binding (the minimum energy required to remove an atom from a lattice site) energies, E_{surf}, E_{disp}, E_{Latt}, with the former two parameters defined in section 3.1. These parameters are automatically selected from the table integrated in the TRIM program, provided that the molecular equation of the target material is given. Other parameters in running TRIM are the species and energy of the bombarding ions, the angle of incidence of the ions with respect to the surface normal, and the depth of the target. The sputtering yield can in particular be very sensitive to the surface binding energy.

With TRIM running, various plots can be displayed dynamically. These include a dynamic plot of collision cascades called depth vs. y-axis plot; an ion-range distribution

plot; an ion/recoil distribution plot showing both of the distributions of ions and recoiled atoms with depth; an ionization plot showing energy loss of ions to the target electrons; a target damage plot showing the distribution of target displacements and vacancies along the depth; and so on. Sputtering yields can be displayed dynamically in one of the data boxes of the interface.

A detailed description of Monte-Carlo simulation by TRIM for Ar ion irradiation of InP will be given in chapter 4.

3.3 Models of Ion Beam Induced Morphology on Solid Surfaces

Ion beam interaction with solid surfaces can generate various structures such as dots, cones, islands, ripples, and nanowires, as reviewed in chapter 1. In order to understand the formation mechanisms of these structures, various models have been proposed. This section reviews some of the most frequently used morphology models, with an emphasis on the Bradley-Harper (BH) ripple model.

3.3.1 Some Basic Concepts in Surface Physics

Before the discussion of various models of ion beam induced morphology, it is necessary to give a clear explanation for some of the basic concepts that will be used in these models.

3.3.1.1 Surface Relaxation

Surface relaxation is a subtle rearrangement of surface layers involving adjustments in the layer spacings perpendicular to the surface without changing either the periodicity parallel to the surface or the symmetry of the surface[366](Fig 3.3). Atoms near a surface are located in an asymmetric environment. On a surface, the bulk positions of atoms no longer match the lowest energy state. This drives the surface atoms into new locations that correspond to the state of minimum free energy. In the simplest cases, minute displacements from singular positions are required to achieve the equilibrium structure.

The most common displacement is relaxation, in which the structure of each plane of atoms parallel to the surface remains singular, but the spacings between the outermost few planes reduce compared to the bulk values.

A relaxed surface (Fig 3.3 b) shows that the first layer of atoms is often drawn in slightly towards the second layer (i.e. $d_{1\text{-}2} < d_{bulk}$). The driving force for a surface relaxation originates from the imbalance between the symmetrical forces of the bulk and the forces of the un-relaxed surface.

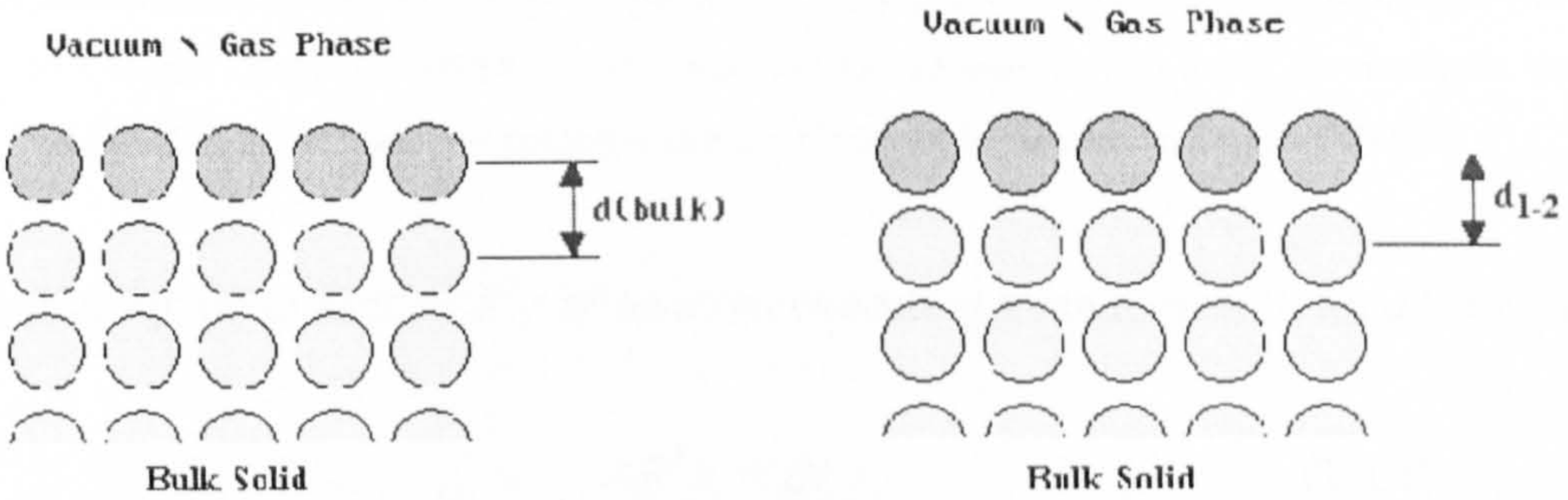

(a) Un-relaxed Surface

(b) Relaxed Surface ($d_{1\text{-}2}<d_{bulk}$)

Fig 3.3 Schematic of surface relaxation [366]

3.3.1.2 Surface Diffusion

Diffusion, in general, refers to the motion of species in solids in the direction of a concentration gradient. At any finite temperature, the atoms at the surface of a perfect crystal are vibrating at some frequency, and each atom strikes the potential energy barrier separating it from its nearest neighbours. Self-diffusion of an atom across a perfect surface starts [367] when the thermal energy fluctuations give the atom sufficient energy for it to leave its initial site in the surface and become an ad-atom in a neighbouring position of potential energy minimum. The frequency for an atom to escape from a site depends upon the height W (Fig 3.4) of the potential energy barrier it has to surmount.

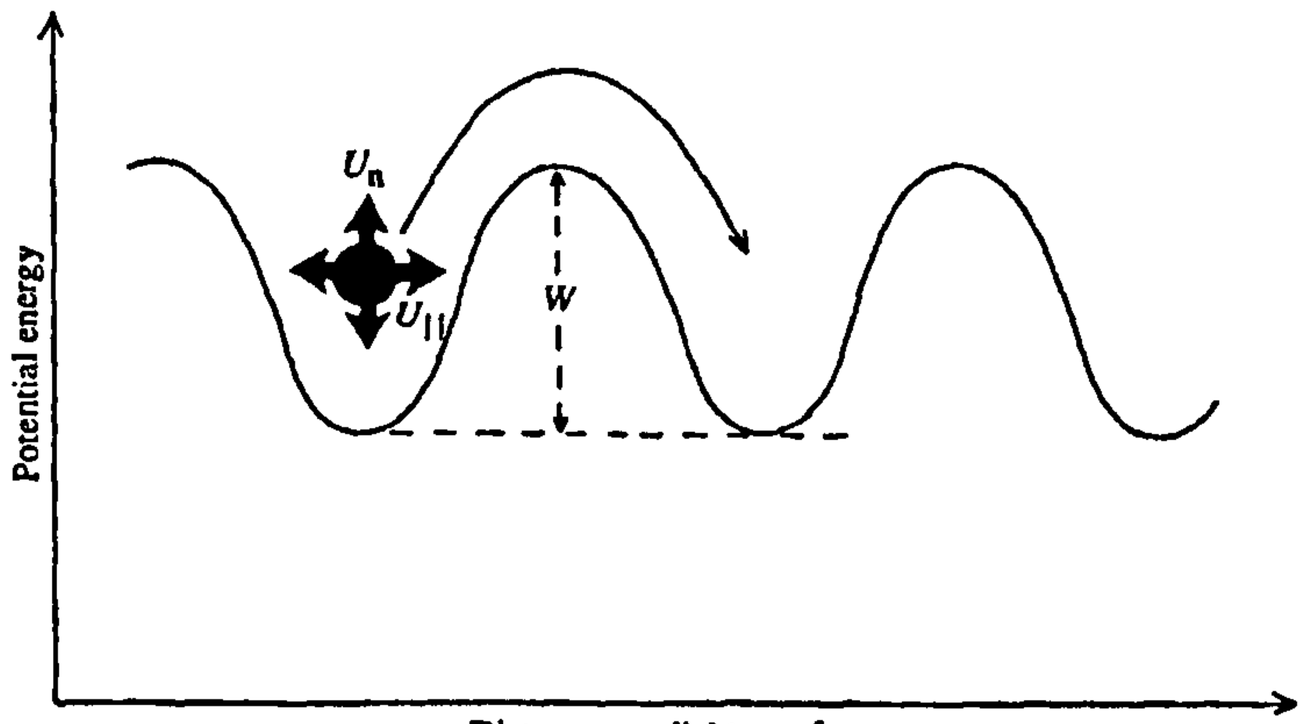

Fig 3.4 Schematic of surface diffusion [367]. An atom vibrating with amplitude u_n and $u_{//}$ normal and parallel to a simple sinusoidal potential energy surface. The probability that it will surmount the barrier of height *W* and reach another potential energy minimum is proportional to exp*(-W/kT)*.

The mean square distance $<R^2>$ of an atom executing a random walk for a time *t* is given as:

$$<R^2> = Dt \qquad (3.3.1)$$

and

$$D = D_0 exp\ (-W/kT) \qquad (3.3.2)$$

where *D* is the diffusion coefficient expressed in square centimetres per second, and *W* is the height of potential energy barrier.

Surface diffusion, in this work, is restricted to the movement of the atoms on the surface subjected to ion bombardment.

3.3.1.3 Surface Reconstructions

A reconstructured surface refers to a clean surface taking on structures that differ substantially from the ones predicted from the underlying bulk structure [274]. The most well-known and complicated of a reconstructured surface is Si (111). Surface reconstructions induce changes in surface atomic density compared to that in the bulk.

3.3.2. Theory of Ripple Formation by Bradley and Harper (BH)

Fabrication of regular micro/nano-structures on solid surfaces by low-energy ion-beam sputtering has been an intense subject of research for several decades. As early as 1965, I. Finnie and Y. H. Kabil [368] created a regular ripple pattern on a solid surface by eroding the sample with a stream of particles at off-normal incidence. The wave vector of the ripple structure was parallel to the surface component of the incident stream. But the first theory of ripple topography induced by ion bombardment of a solid surface did not come out until 1988 when R. Bradley and J. Harper (B-H)[70] derived an expression for the erosion rate of a surface as a function of the ion flux and ion beam orientation relative to the overall surface normal using a calculation of sputter yield due to Sigmund's transport theory of sputtering that describes preferential sputtering in the linear cascade regime[361, 369, 370].

3.3.2.1 Brief Introduction to the BH Ripple Model

B-H demonstrated that the yield variation with the local surface curvature induces an instability, which leads to the formation of periodically modulated structures. This instability is caused by the competition between roughening (curvature dependent sputtering also termed as negative surface tension) and smoothing (surface diffusion also termed positive surface tension) process [70]. For a non-planer surface as shown in Fig 3.5, the variation in sputtering yield with the local surface curvature induces an instability which results in the different erosion rates for troughs and crests, the former being eroded faster than the latter because of shorter distance the energy has to travel from the impact point to the surface [56].

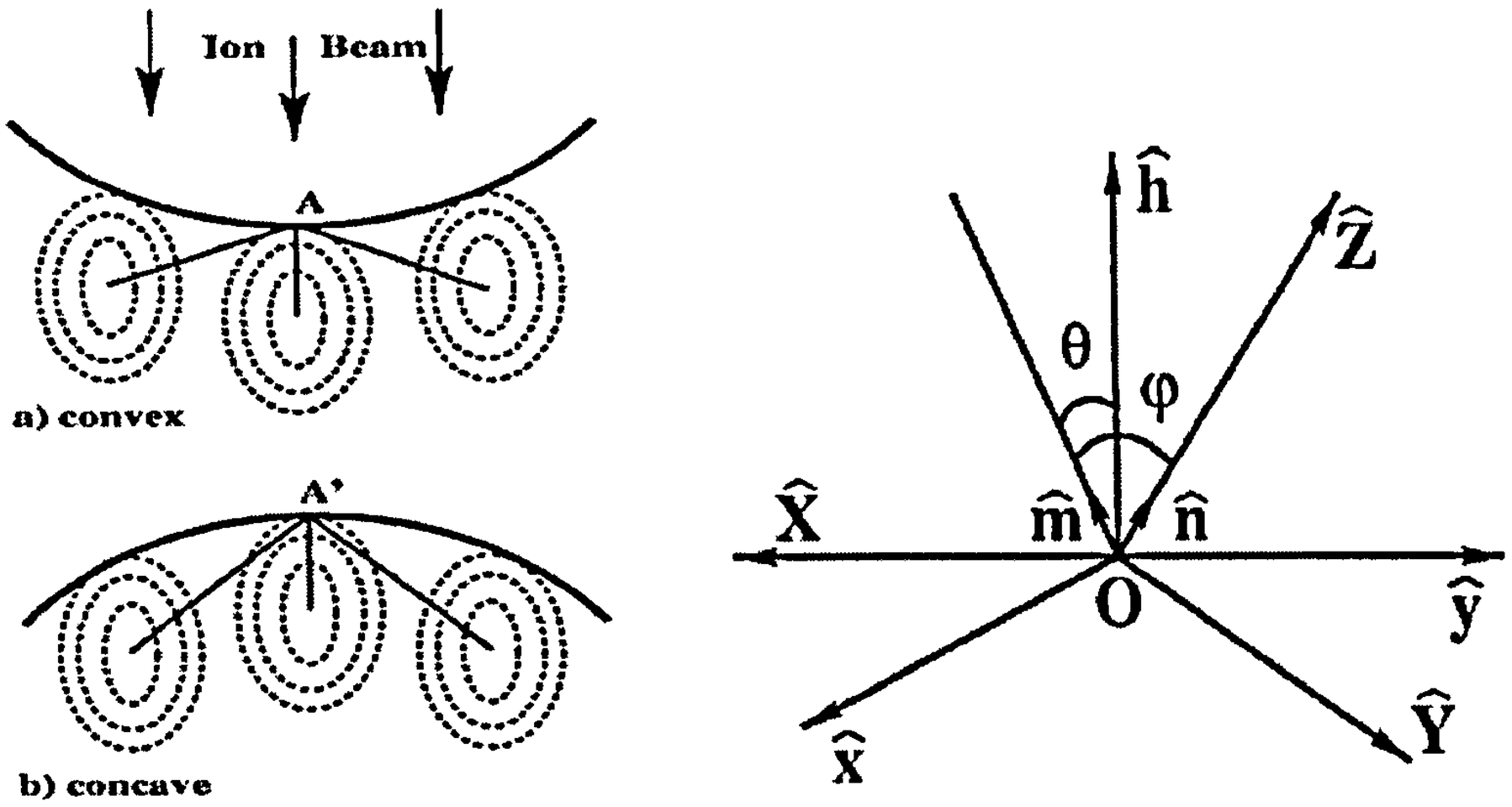

Fig 3.5 Schematic illustration of the physical origin of the instability during ion erosion of non-planar surfaces [56]. A surface element with convex geometry (a) is eroded faster than that with a concave geometry (b), due to the shorter distances (solid lines) the energy has to travel from the impact point to the surface (A or A' points), the dotted curves represent the equal energy contours of the neighboring sites receiving energy from the penetrating ion stopped at the center of the circles;

c) Illustration of the local reference frame $(\hat{X}.\hat{Y}.\hat{Z})$. The $\hat{Z}$ axis is parallel to the local normal to the surface $\hat{n}$. The ions arrive in the surface along $-\hat{m}$. The $\hat{X}$ axis is in the plane defined by $\hat{Z}$ and $\hat{m}$, while the $\hat{Y}$ axis is perpendicular to this plane. The laboratory coordinate frame $(\hat{x}.\hat{y}.\hat{h})$ has its $\hat{h}$ axis perpendicular to the flat substrate, $\hat{h}$ and $\hat{m}$ define the $(\hat{x}.\hat{h})$ plane and $\hat{y}$ is perpendicular to it. The incident angle measured in the local reference frame is φ, and θ in the laboratory frame.

Consequently, any surface perturbation increases exponentially in time. Viewing the surface profile as a smooth analytical function of coordinates, B-H assumed that the surface can be locally approximated by a quadratic form. For the erosion mechanism, described in Fig 3.5, the erosion rate depends on the local curvature. Combining the curvature dependent erosion velocity with the surface smoothing mechanism due to surface diffusion, B-H derived a linear equation for surface morphology evolution,

$$\frac{\partial h}{\partial t} = -\upsilon(\theta) + \nu_x(\theta)\frac{\partial^2 h}{\partial x^2} + \nu_y(\theta)\frac{\partial^2 h}{\partial y^2} - B\nabla^4 h \qquad (3.3.3)$$

where $h(x,y,t)$ is the height of the surface at any position (x,y), $\upsilon_{(\theta)}$ is the erosion rate, $\nu_x(\theta)$, $\nu_y(\theta)$ are the effective surface tensions generated by the erosion process, dependent on the angle of incidence of the ions, θ, B is the relaxation rate due to surface diffusion ($B = D_s\gamma\sigma / n^2 k_B T$), n is the number of atoms per unit volume in the solid, σ is the areal density of diffusing atoms, γ is the surface free energy per unit area, D_s is the surface self-diffusivity (or diffusion coefficient), and $k_B T$ is thermal energy. The physical instability, illustrated in Fig 3.5, leads to the negative signs of ν_x and ν_y coefficients in eqn (3.3.3).

ν_x and ν_y are not only dependent in a complex way on the incident angle and ion beam parameters describing the range, the amount of energy deposited, and the longitudinal and transverse width of the energy deposition, but also linearly proportional to the ion flux.

The first three terms on the right-hand side in eqn (3.3.3) reflect the contribution of ion induced roughening, while the last term depicts the effect of surface diffusion driven by surface energy minimization, which counterbalances the roughening process and smoothes the surface morphology.

The balance between the roughening and smoothing process makes eqn (3.3.3) linearly unstable, and the resulting surface morphology is dominated by the evolution of the fast growing Fourier component, k_C, whose amplitude exponentially dominates all the others. This mode is observed as the periodic ripple structure. Using linear stability analysis, B-H derived from eqn (3.3.3) the dominant ripple wavelength as

$$\lambda_C = \frac{2\pi}{k_C} = 2\pi\sqrt{\frac{2B}{|\nu|}} \qquad (3.3.4)$$

Where ν is the largest in absolute value of the two negative surface tension coefficients, ν_x and ν_y. The calculation also predicts that the direction of the ripple wave vector is a function of the angle of incidence: for small incident angle $\theta(0 \le \theta \le \theta_C)$ the ripple wave vector is parallel to the ion direction, while for large $\theta(\theta_C < \theta < \pi/2)$ it is perpendicular to it. Here θ_C is a critical angle above which the wave vector of a forming ripple will be perpendicular to the beam. That is, under grazing angle conditions a ripple will grow with its valleys and ridges parallel to the direction of the ion beam.

At high temperatures and low fluxes, the fastest growing wavelength λ_c is given by

$$\lambda_C = (JT)^{-1/2} e^{\frac{-\Delta E}{k_B T}} \tag{3.3.5}$$

Where J is the ion flux, and ΔE is the activation energy for surface self-diffusion.

Features with wavelength λ_C and initial amplitude $h_{0(\lambda_c)}$ will grow exponentially in amplitude according to

$$|h(\lambda_c, T)|^2 = h_{0(\lambda_C)}^2 \exp(R_{\lambda_C} t) \tag{3.3.6}$$

where the rate of growth at λ_C is

$$R_{\lambda_c} = -|\nu| k_C^2 - B k_C^4 \tag{3.3.7}$$

3.3.2.2 Experimental Evidence for BH Ripple Theory

Numerous experiments have observed the development of ripples on surfaces of silver[61, 62, 87], copper[64, 85, 86], graphite[63], carbon[371], silicon[55, 58, 59, 65, 67, 68, 84, 372-375], germanium[66, 67, 376], GaAs[69, 91], InP[69, 100], GaAs[69, 92], and so on. Most of these experiments were performed under quite similar conditions (ion energy 0.5-5 keV and ion flux 5-50 $\mu A/cm^2$). The periodicity can range from tens to thousands of nanometres. Techniques applied for the measurement of surface morphology include scanning electron microscopy (SEM)[92], scanning tunnelling microscopy (STM), atomic force microscopy (AFM)[55, 376], and light scattering spectroscopy (LiSSp)[84], etc..

The periodic ripple structure is very similar to nanowire arrays reported by Matthias Batzill[7]. Fig 3.6 is an example of ripple structure after Ne^+ ion bombardment on Ag (110) surface reported by S. Rusponi *et al* [87]. In Fig 3.6, images (a) and (b) were taken after normal incidence sputtering at T_S = 400 K and T_S = 320 K (diffusion regime) respectively. These two images clearly show the formation of nanostructures which reflect the substrate symmetry [a checkerboard of pits with a lateral extension of about 55 nm in the square symmetry case of Ag (001) and a rippled structure with a wavelength of 35 nm in the rectangular symmetry case of Ag (110)]. Images (c) and (d) were taken after grazing incidence sputtering at T_S = 200 K and T_S = 180 K (erosion regime) respectively. In this case, independently of the substrate symmetry and orientation, the surface was characterized by ripples aligned along the ion-beam direction with wavelengths of 12 and 20 nm respectively.

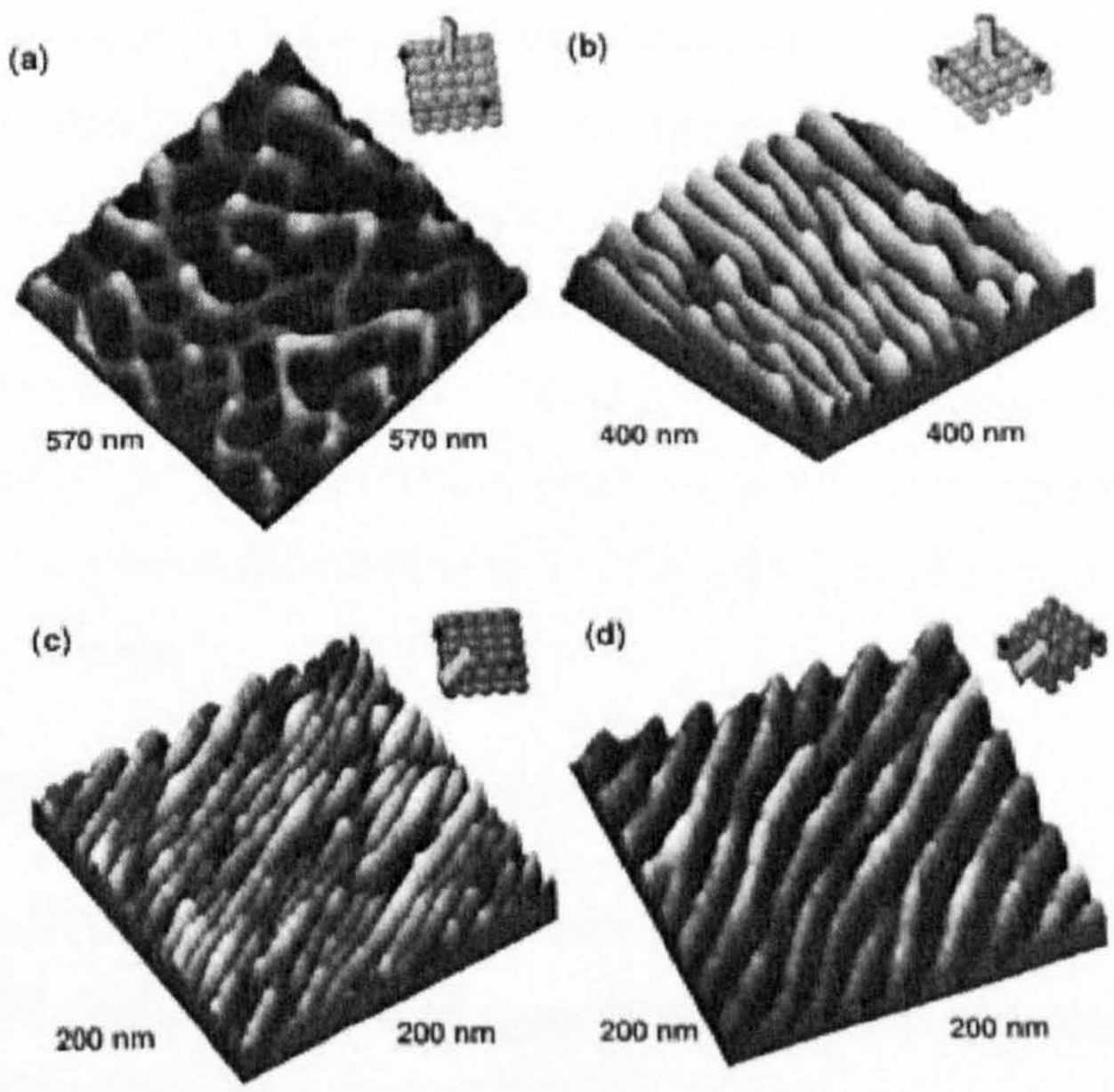

Fig 3.6 Three-dimensional view of the surface morphologies [87] resulting after 20 min Ne^+ bombardment of Ag (001) [(a) and (c)] and Ag (110) [(b) and (d)] at an ion flux Φ =5 $\mu A/cm^2$

The insets show a model representation of the crystalline substrate where the principal crystallographic directions and the ion-beam direction are indicated by black and grey arrows respectively. S. Rusponi et al [87] stated that for ion sputtering of monocrystalline materials at normal incidence, although erosion does not select any preferential direction, surface diffusion is biased by the lattice structure which forces adatoms and vacancies to move along the energetically favoured crystallographic directions and hinders them from descending atomic steps. Because of this effect, an adatom (vacancy) reaching a descending (ascending) step will be bounced back on the terrace producing a net uphill (downhill) current of defects. This causes a diffusion-induced surface instability leading to the growth of mound-like structures. On a surface with square symmetry, like Ag (001), surface diffusion proceeds with equal rates along the two equivalent [110] directions and square pyramids-like mounds and pits are developed. Conversely, for a substrate with a rectangular lattice, like Ag (110), the rate of defect diffusion is different along the two unequivalent [110] and [001] directions, so that elongated mounds (ripples) are produced which reflects this asymmetry. For sputtering at off-normal incidence, however, the ion beam direction introduces a breaking of symmetry and establishment of a preferential erosion direction. At room temperature, the diffusion processes dominate and the surface morphology is similar to the case of normal incidence sputtering. However, in the regime of low temperature, erosion effect is so effective that ripples are developed along the ion beam direction (Fig 3.6 c and d), independent of the surface crystallographic orientation.

3.3.2.3 Corrections to the BH Ripple Theory

Equations (3.3.4) to (3.3.6) show that the wavelength and amplitude of ripples depends on the material of the surfaces, the temperature of the substrates, the energy and the fluence (or dose) of ion beam, the species of the bombarding ions, the incident angle of the ion beam to the bombarding surfaces, and the time of bombardment. Among all these parameters, substrate temperature and ion flux are two sensitive factors. This can be seen by separating out just the flux dependence from equation (3.3.3) to get [84]:

$$\lambda_C \propto J^{-\frac{1}{2}}\left[\frac{D_S(T)\sigma(J,T)}{kT}\right]^{1/2} \qquad (3.3.8)$$

where J is the ion flux and $\sigma(J,T)$ is the steady state concentration of mobile species on the surface which depends on both the ion flux and the temperature. For example, under grazing incidence, Ne^+ ion bombardment on Ag (001) surfaces can create ripples with wavelength between 12 nm and 35 nm at temperatures ranging from 180 K to 200 K (Fig 3.6), while for silicon, Ar^+ bombardment on Si (111)[55] surfaces induced ripples with wavelength of 580 nm and amplitude of 20 nm at temperatures ranging from 723 K to 923 K. For III-V compound semiconductors, ripple formation can be found after17 keV Cs^+ ion bombardment on InP at room temperature, while the same beam had to produce ripples on GaAs at elevated temperatures (348 K to 363 K)[92]. For insulators, regular ripples with a period of 30 nm can be fabricated by low energy ($\leq$1000 eV) Xe ion beam sputtering on SiO_2 surfaces at an angle of 54.9° from the surface normal at room temperature[376]. Reports [55, 67, 68] show that silicon bombarded with low-energy Ar^+ ions under oblique incident angles can generate regular ripples at elevated temperatures (400° C-650° C), but no ripples have been documented to be generated at room temperature on silicon surfaces with argon ion bombardment, as confirmed by the present study (not presented in this thesis).

Different ion species can produce different morphology on samples of the same material. As a typical example, sputtering of GaAs with noble gas ions at elevated temperatures (225° C) produced SEM flat surface, while sputtering of GaAs with oxygen or cesium ions led to the formation of ripple structure[69]. Si bombarded with 8 KeV O_2^+ ions at 39° incident angle produced pronounced ripples whereas Ar^+ ion bombardment on Si failed to produce any topography [375].

In order to account for the ripple formation on metals in a restricted temperature range (270-320K)[61], S. Rusponi *et al*[86] claimed that in metals, surface diffusion (driven by surface energy minimization) prevails over erosion (induced by ion bombardment) in determining the final morphology. At low temperatures (Ts<250K), the dominant process—in-channel jump—inhibits the interlayer mass transport and no periodic

structures can be developed but holes and islands; when 250<Ts<320K, the effect of interlayer diffusion along one particular direction becomes so strong that the mechanisms of in-channel-jump and jump-descent act together to create deep holes and hills-and-valleys structures because the mass redistribution is always along that particular direction; interlayer mass transport along the direction perpendicular to that particular direction will be activated if Ts>320K and the surface becomes smooth. While in non-metals the morphology is mainly caused by erosion [377].

Cirlin *et al* [54] reported that the amplitude of ripples formed at 3.0 keV was greater than that produced with 7.0 keV, illustrating that the ripples grew faster at low energy. This can be regarded as a qualitative evidence for equation (3.3.8).

Although ripple wavelength and orientation reported by most of the above experimental studies are in good agreement with the prediction of the linear theory by B-H, some results cannot be explained. The B-H equation (3.3.3) is linear, predicting unbounded exponential growth of the ripple amplitude. It cannot account for the stabilization of the ripples and for kinetic roughening. Furthermore, the B-H model cannot account for low temperature ripple formation since the only smoothing mechanism it considers is of thermal origin. At low temperatures the ion energy and flux dependence of the ripple wavelength also disagree with the B-H prediction. Hence, theoretical interest in improving the B-H model has been extensively documented.

By inclusion of the contribution of relaxation due to ion bombardment induced viscous flow on SiO_2 surfaces in equation (3.3.7), T. M. Mayer[376] proposed a modified expression for the rate of development of periodic features

$$R_\lambda = R_{\lambda_c} - k_C F \qquad (3.3.9)$$

Where F is the relaxation rate due to viscous flow (equal to $\frac{\gamma}{\eta}$, η is the coefficient of viscosity). A large value of F will suppress the high frequency structures (induced by the term k_C^4 in equation 3.3.7) to such an extent that ripple formation will disappear.

Cuerno *et al*[377] introduced a stochastic model stating that the time evolution of the surface roughness crosses different scaling regimes and in a precise interval, determined by the balance between diffusion and erosion rates, the height of the interface is almost periodic, independent of the nature of the sample. S. Park [378] *et al* deduced an expression for the crossover time τ

$$\tau \approx \left(B/\sigma^2\right)\ln(\sigma/\upsilon) \qquad (3.3.10)$$

Here, σ refers to effective surface tension, υ refers to erosion rate, proportional to the ratio between flux and penetration depth. Ripples will be developed with their orientation following the prediction of the linear theory of B-H for $t<\tau$; while for $t>\tau$, the non-linear terms they added to equation (3.3.7) will either destroy the ripple morphology by kinetic roughening[379, 380] or induce a new morphology with the wave vector toward one particular direction[64], independent of the azimuth angle of the beam to the sample surface, due to anisotropic surface diffusion.

3.3.3 Kardar–Parisi–Zhang Model

The time evolution of a nonequilibrium interface can be described by the Kardar–Parisi–Zhang (KPZ) equation [381]

$$\frac{\partial h}{\partial t} = \nu\nabla^2 h + \frac{\lambda}{2}(\nabla h)^2 + \eta \qquad (3.3.11)$$

where ν is the effective surface tension. The first term on the right-hand side describes the relaxation of the interface due to the surface tension and the second is the lowest order nonlinear term incorporating lateral growth or erosion. The noise, $\eta(x,y,t)$, has a Gaussian distribution reflecting the random fluctuations in the growth process, and is a set of uncorrelated random numbers with zero mean.

If $\lambda = 0$, eqn (3.3.11) describes the equilibrium fluctuations of an interface which tries to minimize its area under the influence of the external noise.

For an anisotropic substrate under ion bombardment with the ions arriving under oblique incidence in the x–h plane (see Fig 3.5 c), the x and y directions along the substrate will

not be equivalent, and anisotropy is expected to appear in the erosion equation, leading to an anisotropic equation of the form

$$\frac{\partial h}{\partial t} = \nu_x \frac{\partial^2 h}{\partial x^2} + \nu_y \frac{\partial^2 h}{\partial y^2} + \frac{\lambda_x}{2}\left(\frac{\partial h}{\partial x}\right)^2 + \frac{\lambda_y}{2}\left(\frac{\partial h}{\partial y}\right)^2 + \eta(x,y,t) \qquad (3.3.12)$$

The anisotropy leads to surface tension and nonlinear terms that are different in the two directions, which are incorporated in the growth equation by considering different values for the coefficients ν and λ. Changing the sign of λ_x or λ_y can induce morphological phase transitions from power law scaling to logarithmic.

3.3.4 Kuramoto-Sivashinsky (KS) Model

The morphological evolution of a sputter-eroded surface can be approximated by the noisy nonlinear Kuramoto–Sivashinsky (KS) equation [382-384]

$$\frac{\partial h}{\partial t} = \nu_x \frac{\partial^2 h}{\partial x^2} + \nu_y \frac{\partial^2 h}{\partial y^2} - D_{xx} \frac{\partial^4 h}{\partial x^4} - D_{yy} \frac{\partial^4 h}{\partial y^4} - D_{xy} \frac{\partial^2}{\partial x^2}\frac{\partial^2 h}{\partial y^2} + \frac{\lambda_x}{2}\left(\frac{\partial h}{\partial x}\right)^2 + \frac{\lambda_y}{2}\left(\frac{\partial h}{\partial y}\right)^2 + \xi(x,y,t)$$

(3.3.13)

where ν_x and ν_y are the effective surface tensions generated by the erosion process; D_{xx}, D_{yy}, and D_{xy} are the ion induced effective diffusion constants; λ_x and λ_y describe the curvature-dependent erosion rates in each direction; and $\xi(x,y,t)$ is an uncorrelated white noise with zero mean, reflecting the randomness resulting from the stochastic nature of ion arrival to the surface. At low temperatures all the coefficients in eqn. (3.3.13) depend on experimental parameters such as the ion beam flux J, energy E, incident angle θ; while at high temperatures D is the relaxation rate due to surface diffusion, depending on surface temperature[70]. For the sputter erosion process $\nu < 0$ and $D > 0$, the signs of λ_x and λ_y are affected by the incident angle of the ion beam [383, 384].

For example, the KS model was used to investigate the dynamics of the formation of sputter-induced quantum dots (QDs) and holes on surfaces of metals and semiconductors [385]. B. Kang *et al* [385] claimed that in the early stage of the sputtering process, the surface

is dominated by small wavy perturbations arisen from the interplay between the ion induced instability and surface relaxation. Under normal incidence, the system is isotropic in the (x, y) plane, and these ripple precursors are randomly oriented, generating short wormlike structures on the surface. After some characteristic time τ, these structures get in contact with each other and grow into isolated but close packed islands reminiscent of quantum dots (for $\lambda > 0$), or holes (for $\lambda < 0$). As time increases, the non-linear terms in eqn. (3.3.13) turn on breaking the up-down symmetry of the surface, and the surface becomes rough, destroying the overall uniformity of the islands or holes.

3.3.5 Differential Sputter Erosion Models

In the Sigmund sputter-induced topography model [370], the sputter erosion rate of a material is proportional to the rate of energy deposition, and the spatial dependence of the energy deposition function leads to the development of surface features which can be further enhanced by the angular dependence of the sputter yield. An ion releasing its energy at point P (Fig 3.7) inside the bulk of the material contributes an amount of energy to the surface point O that may induce the atoms in O to break their bonds and leave the surface. Assuming an amorphous target, the average energy deposited at point O due to the ion arriving at point P follows a Gaussian distribution [369]:

$$E(r) = \frac{\epsilon}{(2\pi)^{3/2}} \exp\{-\frac{Z'^2}{2\sigma^2} - \frac{X'^2+Y'^2}{2\mu^2}\} \qquad (3.3.14)$$

where Z' is the distance from point P to point O measured along the ion trajectory, and X', Y' are measured in the plane perpendicular to it. ϵ denotes the total energy

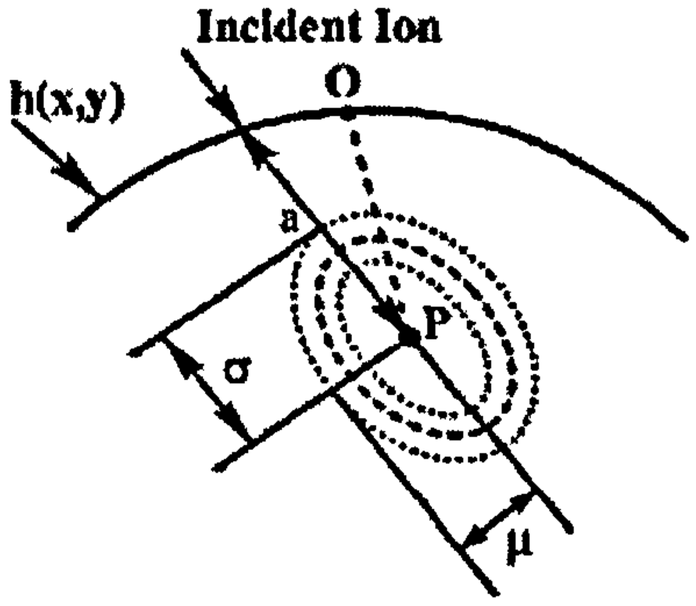

Fig 3.7 Schematic illustration of the energy distributed by an incident ion [56]: An incident ion penetrates the bulk of the material and stops at point P, where all its kinetic energy is released and spread out to the neighboring sites following a Gaussian form with widths σ and μ.

carried by the ion and σ and μ are the widths of the distribution in directions parallel and perpendicular to the ion beam respectively. The erosion velocity at an arbitrary point O is determined by the total power $\mathcal{E}_0$ contributed by all the ions deposited within the range of distribution (eqn 3.3.14). Ignoring shadowing effects and re-deposition of the eroded material, the normal erosion velocity at the point O is given by

$$V_0 = p\int_{\mathcal{R}} \phi(r)E(r)dr \qquad (3.3.15)$$

Where the integral is taken over the region $\mathcal{R}$ of all points at which the deposited energy contributes to the total power $\mathcal{E}_0$, $\phi(r)$ is a local correction to the uniform flux J due to variation of the local slopes, and the material constant p depends on the surface binding energy and scattering cross-section [369, 370] as

$$p = \frac{3}{4\pi^2}\frac{1}{NU_0C_0} \qquad (3.3.16)$$

where U_0 is the surface binding energy and C_0 is a constant proportional to the square of the effective radius of the inter-atomic interaction potential.

The model predicts that a microscopically flat surface is unstable under high-dose ion bombardment. The local sputtering yield is significantly reduced on top of a spike or a ridge, and increased on the bottom of a groove or a crater, unless atom migration acts as a dominant smoothing effect. Sputtering produces small irregularities like craters, the trace behind a sputtered cluster, a region of high sputtering yield because of lattice damage, or a small island of impurities. In the case of a narrow cone, the lateral dimension of the cone is considerably smaller than that of a collision cascade, most of the cascades will miss the top of the cone and hit somewhere underneath. As a result, the sputtering yield on top of the cone will be drastically reduced. For the length scale comparable to the penetration depth of the ions, the model can be used to predict the nucleation of surface topography.

Similarly, G. Carter [386] proposed models in which surface topography is developed by the erosion effect of ion bombardment. The model predicted some surface contours using the variation of the sputtering yield with ion incident angle and spatial variations of ion flux

densities. J. B Malherbe [69] claimed that the maximum sputter yield occurs in the ion incident angle of 60° to 80° range. He pointed out that the sputtering yield also varies with the crystal orientation, grain boundaries and bombardment induced dislocations.

The B-H, KPZ, KS, and the deferential sputter erosion models are representative of theoretical endeavor in the explanation of morphologies on surfaces under ion bombardment. They can only be solved numerically. Following are some of the ripple models derived from various experimental results.

3.3.6 Stress Field Induced Self-Organization

In the fabrication of large-area periodic Ca nanowire arrays by glancing incidence ion bombardment of CaF_2 (111) surfaces, M. Batzill *et al* explained their periodic nanoscale structures as self-organization of stress fields associated with lattice-mismatched calcium layers on CaF_2 formed by ion-beam induced depletion of surface fluorine atoms[7, 8]. Because of the 2% lattice mismatch between Ca and CaF_2 under Ar^+ ion bombardment, tensile stress was expected to appear in the substrate beneath the adatom islands (nanowires), and compressive stress between the wires. Such stress fields and the associated repulsive forces between fluorine depleted Ca islands led to ordering of such systems into periodic stress domains. The range of the stress fields is big enough to exceed the inter-atomic distances so that the orientation of domains is independent of particular crystallographic directions. Therefore, the orientation of the wires can be arbitrarily defined by the ion beam direction.

3.3.7 Impurity Seeding Models

Surface morphology developed from sputter cone formation has been explained as impurity seeding [387-389]. An impurity having a lower sputtering yield than its surroundings initiates a cone due to the faster erosion of its surroundings. This surface discontinuity grows to a conical protrusion as a result of the variation of sputtering yield with the angle of incidence of the ions. These seeded cones are characteristic of their circular cross-section and groove or trench at the base of the cone [387]. The groove is formed by locally enhanced sputtering of ions reflected from the cone walls [390]. Generally it is unlikely that

radiation induced topography development on semiconductor surfaces can be explained by this model because of the high purity and monocrystalline nature of the semiconductor materials and the cleanliness of the UHV environment. However, in the case of preferential sputtering of a muti-component semiconductor, the enriched ions could act as contaminants or impurities so that a difference in the sputtering yields is created between the enriched ions and their surroundings, resulting in growth of cones.

Rossnagel and Robinson [391] claimed that the seeded impurity atoms migrate on the surface by thermally activated surface diffusion and gather into localized clusters. These clusters then initiate the formation of conical structures that grow with prolonged sputtering. Wehner [389] proposed that seeded cones are the result of an interplay of whisker growth, surface movement of atoms, and the effect of sputtering.

3.3.8 Micro-region Model

A micro-region model was proposed by Gries *et al* [103, 104] to explain sputter cone formation on InP surfaces. The model assumes that ion bombardment generates an ensemble of micro-crystallites and non-crystallites aggregations of atoms on InP surfaces. The majority of the crystalline micro-regions are so small that most interstitials, produced in collision events between the bombarding ions and substrate atoms, can reach an interfacial boundary rather than recombine with a bombardment-induced vacancy. These atoms are then transported by interfacial and surface diffusion to some special growth points in the crystalline regions of the surface where crystal stubs continue to grow. In order to explain the competition between the growth process and the damage production at the growth sites, these special growth points were postulated to be either screw dislocations or a step source of subatomic height either on a surface crystallite of the target material or on a faulted island. Ion bombardment-induced compressive stresses favour diffusion toward the surface. This crystal growth proceeds until the damage and sputter rate by ion bombardment exceeds the growth rate.

Chapter 4

Properties of InP and Monte-Carlo Simulations of InP Surfaces under Ar ion Irradiation

Earlier studies[6-8] used CaF_2 to create nanowires. In this research, InP and Si_3N_4 are the materials chosen to fabricate nanowires. In the next two chapters, it will be found that Ar^+ ion bombardment of InP induces In enriched surfaces, and exposure of the bombarded surfaces in air causes oxidation of indium. It is therefore important to have a general idea of the properties of CaF_2, InP, Si_3N_4, In and indium oxides, so that the experimental results can be explained with care. A comparison of the properties of CaF_2, InP, and Si_3N_4 may suggest trends in the expected behaviour of these materials under ion bombardment.

The general properties of CaF_2, InP, and Si_3N_4 are tabulated in Table 4.1 as follows:

Table 4.1 Physical Properties of InP, Si_3N_4 and CaF_2

Property \ Material	InP	Si_3N_4	CaF_2
Structure	**Zinc Blende**	**Trigonal**	**Cubic-Fluorite**
Lattice Parameter a_0 at 300K	**0.586 nm**	**a = 0.775 nm c = 0.562 nm**	**0.546 nm**
Density at 300K	**4.81 $g.cm^{-3}$**	**3.44 $g.cm^{-3}$**	**3.18 $g.cm^{-3}$**
Linear Expansion Coeff. at 300 K	**4.56 x 10^{-6} K^{-1} ***	**. . . K^{-1}**	**18.85 K^{-1}**
Resistivity* at 300K for $n = 10^{15}$ cm^{-3}	**1.3 Ω.cm ***	**10^{14} Ω.cm**	**. . .**
Thermal Conductivity* at 300 K	**0.68 $W.cm^{-1}K^{-1}$ ***	**. . . $W.cm^{-1}K^{-1}$**	**0.97 $W.cm^{-1}K^{-1}$**
Melting Point**	**1335 K ****	**1215 K**	**1360 K**
Energy Gap Eg at 300 K	**1.344 eV**	**5 eV**	**0.17 eV**
Diffusion constant of Cations (cm^2/s)	**1 x 10^5**	**6 x10^{-2}**	**…**
Diffusion Barrier Height of Cations (eV)	**3.85**	**5.0**	**0.9**

Values of InP are extracted from Ref [392]; Values of items with the symbol "*" for InP are abstracted from Ref [393]; Values of items with the symbol "**" are abstracted from Ref [394]; Values of Si_3N_4 are extrcted from Ref [395] and [396]; Values of CaF_2 are abstracted from Ref [397]; Values of diffusion barrier height of cations are extracted from: InP [398], CaF_2 [399], and Si_3N_4 [400].

4.1 Properties of Indium Phosphide and Related Materials

Indium Phosphide (InP) is the material used by this research. Ar^+ ion bombardment of InP induces In enriched surfaces. Exposure of the bombarded surfaces in air causes oxidation of indium. It is important to have a general idea of the properties of In, InP, and indium oxides, so that the experimental results can be explained with care.

4.1.1 Properties of Indium Phosphide

Indium Phosphide (InP) is a direct band-gap semiconductor material whose energy gap allows the direct generation and detection of light at wavelengths suited for long distance optical fibre communications. It has been used to fabricate a variety of different lasers and photodetectors operating in the 1.3 to 1.55 μm spectral range. Other material properties of InP such as high electron mobility (~9 x SiGe and 2 x GaAs) and high breakdown voltage (~2 x SiGe) make it suitable for high-speed and high breakdown voltage electronic applications. Table 4.1 contains a list of some physical properties of InP.

InP has a cubic crystal structure similar to that of diamond. However, the lattice contains two different types of atoms, In and P. Each atom has four covalent bonds, but they are bonds with atoms of the other type. This structure is referred to as the zinc-blende lattice, named after zinc-blende (ZnS) as shown in Fig 4.1.

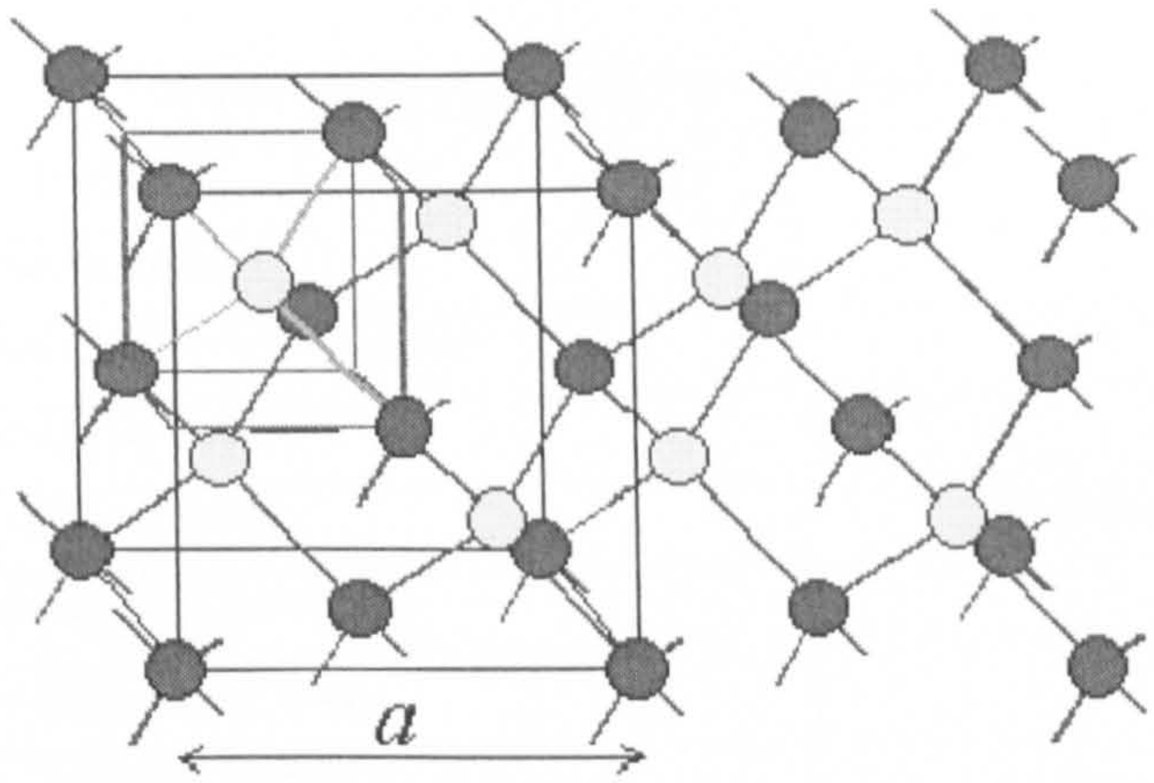

Fig 4.1 The Zinc Blende crystal structure of InP (Ref [401]).

The resistivities of InP samples are determined by their impurity content, which determines the carrier concentration. If InP crystals did not contain electrically active impurities or active defects, they would be semi-insulating, with a calculated room temperature resistivity of the order of magnitude of 10^9 Ω cm.

Exposure of a clean surface of III - V compounds to air or aqueous solutions will cause oxide formation by adsorption and chemical reaction. The existence of native surface oxides is important for material processing and has a bearing on device performance through the influence of surface electronic states controlling the energy band structure in the near surface region. InP has a great tendency to form the phosphate $InPO_4$, in addition to the oxides of the element [402].

4.1.2 Properties and Applications of Indium and Indium Oxide

Indium metal and alloys dissolve in hot mineral acid [403]. Physical properties of indium are tabulated in Table 4.2 below.

Table 4.2 Physical properties of indium [404]

Property	Value
Atomic number	49
Relative atomic mass ($^{12}C = 12.000$)	114.82
Melting point (C°)	1564
Crystal structure	Tetragonal: a=3.523 Å, c=4.9455 Å
Closest distance of atoms (Å)	3.253
Ionic radius of In^{3+} (Å)	0.62
Density at 20 °C (g cm^{-3})	7.31
Electrical resistivity at 20 °C (nΩ m)	83.7
Heat of sublimation (J mol^{-1}) *	237,391
Thermal conductivity at 0 °C (W m^{-1} K^{-1})	81.6
Thermal expansion, linear coefficient at 20 °C (x 10^6 K)	24.8

* From Ref [405]

Indium combines with Group V elements such as antimony or phosphorus to produce semiconductor compounds [404]. Indium serves as a seal for joints in vacuum systems. Because of the high transparency to visible light, Indium oxide (In_2O_3) is used as a conductive film for liquid crystal displays.

Indium can have three forms of oxides [406]: indium oxide (I)—In_2O, indium oxide (II)—InO, and indium oxide (III)--In_2O_3. In_2O_3 can be obtained by heating indium hydroxide or indium nitrate in air [407], or by sputtering and evaporation [408, 409]. It decomposes at 2000 °C. It is acid soluble but not alkalines soluble [406]. A more detailed discussion of In_2O_3 reactivity can be found in Chapter 6. The ambient temperature form of In_2O_3 has the type-C rare-earth sesquioxide structure [407] with vacancies in the oxide lattice such that the coordination of In atoms, although six-fold, is highly irregular. The electrical properties of pure In_2O_3 rely steadily on the oxidation state of the metal constituent. The creation of oxygen vacancies contributes significant conduction electrons responsible for low resistivity in un-doped oxygen deficient In_2O_3. A high vacancy concentration creates an impurity band that overlaps the lower part of the conduction band resulting in a degenerate semiconductor [410]. This makes In_2O_3 a very important material in

microelectronic applications. For example, in its non-stoichiometric form, In_2O_3 behaves as a highly conducting semiconductor with a direct band-gap of 3.6 eV and an indirect band-gap around 2.4 eV [411]. This makes it a candidate in some applications of high transparency in the visible and high reflectivity in the infrared light range. In its stoichiometric form, In_3O_2 is an n-type semiconductor. It is used as a resistive element in integrated circuits. Stoichiometric In_2O_3 is also commonly doped with tin oxide (SnO_2) to make indium tin oxide (ITO), which is used in transparent and conductive thin films for various types of displays, energy efficient windows and photovoltaics. Recent research shows that In_2O_3 nanowires have great potential to be used as nanoelectronic building blocks and ultra-sensitive chemical sensors [241, 262, 411].

4.1.3 Properties and Applications of Si_3N_4 and CaF_2

The general properties of Si_3N_4 and CaF_2 have been tabulated in table 4.1. This sub-section presents some brief comment on the properties and applications of these two types of materials.

The crystal structure of Si_3N_4 is a silicon-nitrogen tetrahedron in which a silicon atom lies in the center and four nitrogen atoms at each corner. Silicon nitride (Si_3N_4) is an insulating material. In microelectronic device fabrication, it can be deposited on top of a die to protect the die from mechanical damage and corrosion. It is reported that Si_3N_4 is highly resistant to diffusion of Si and N [400]. The dominant convalent bonds are the reason for a very low atomic mobility. Besides, Si_3N_4 is almost impenetrable to moisture and ionic contaminants such as sodium (Na) [395].

Calcium fluoride is an ionic insulator with a cubic single crystal structure. It has a low birefringence, and a good transmittance from vacuum UV to infra-red. It is primarily used as an optical material in lens for cameras, photolithography and IR spectroscopy. CaF_2 thin films can be used as gate insulators for thin-film transistors (TFTs), anti-reflection coatings, and optical waveguides [412].

It is commonly known that the strength of an ionic bond (e.g. CaF_2) is much weaker than that of a covalent bond (e.g. Si_3N_4). This would lead to a very low potential barrier (W in eqn (3.3.2) in an ionic bond, and a very high potential barrier in a covalent bond, as listed in the bottom row of table 4.1. Therefore, a great difference in the diffusion constant exists between an ionic and a covalent bond for the crystals under ion bombardment. This difference could lead to different mechanisms of morphology formation on the crystal surfaces under ion bombardment. One of the aims of this research is to find out the difference in surface morphology generation among CaF_2, InP and Si_3N_4.

4.2 Monte-Carlo Simulation of Ar^+ Ion beam Irradiation of InP (100) Surfaces

The theory of Monte-Carlo simulation of ion interaction with solid surfaces has been introduced in Section 3.2. This section provides some results of Monte-Carlo simulations of Ar^+ ion irradiation on InP (100) surfaces. In the calculations on InP presented in this section, the lattice displacement energy was 25 eV, which is suggested by the TRIM table (Ref. [357]). The lattice binding energy, lost by the atoms as they leave their lattice site and assumed to go into phonons, was left at the value of 3 eV indicated in the TRIM table. Reasonable changes in either the lattice displacement energy or the lattice binding energy does not lead to significant changes in the sputtering yield in this energy range. Finally, the surface binding energy of In and P was evaluated to be 2.46 eV and 0.62 eV respectively, from the heat of sublimation of the corresponding element (237,391 J/mol for In and 59,034 J/mol for white P)[405]. With 2 keV Ar^+ ion bombardment of InP at 72° incident angle, TRIM simulation generates a ratio of sputtering yield of P/In = 8.5/4.5 = 1.9, indicating preferential sputtering of phosphorus from InP.

4.2.1 Dynamic Plot of Collision Cascades

Dynamic plots of collision cascades on Ar^+ ion bombarded InP surfaces are shown in Fig 4.2. The red dots represent collisions between the ions (Ar^+) and target atoms (In and P), in which the target atoms are knocked from their lattice sites. The green dots are collisions between recoiling target atom, indium, phosphorus, and other target atoms.

The recoiling target atoms cause collision cascades which dominate the damage process. A dot is only plotted if the energy transfer is large enough to displace the atom from its lattice site.

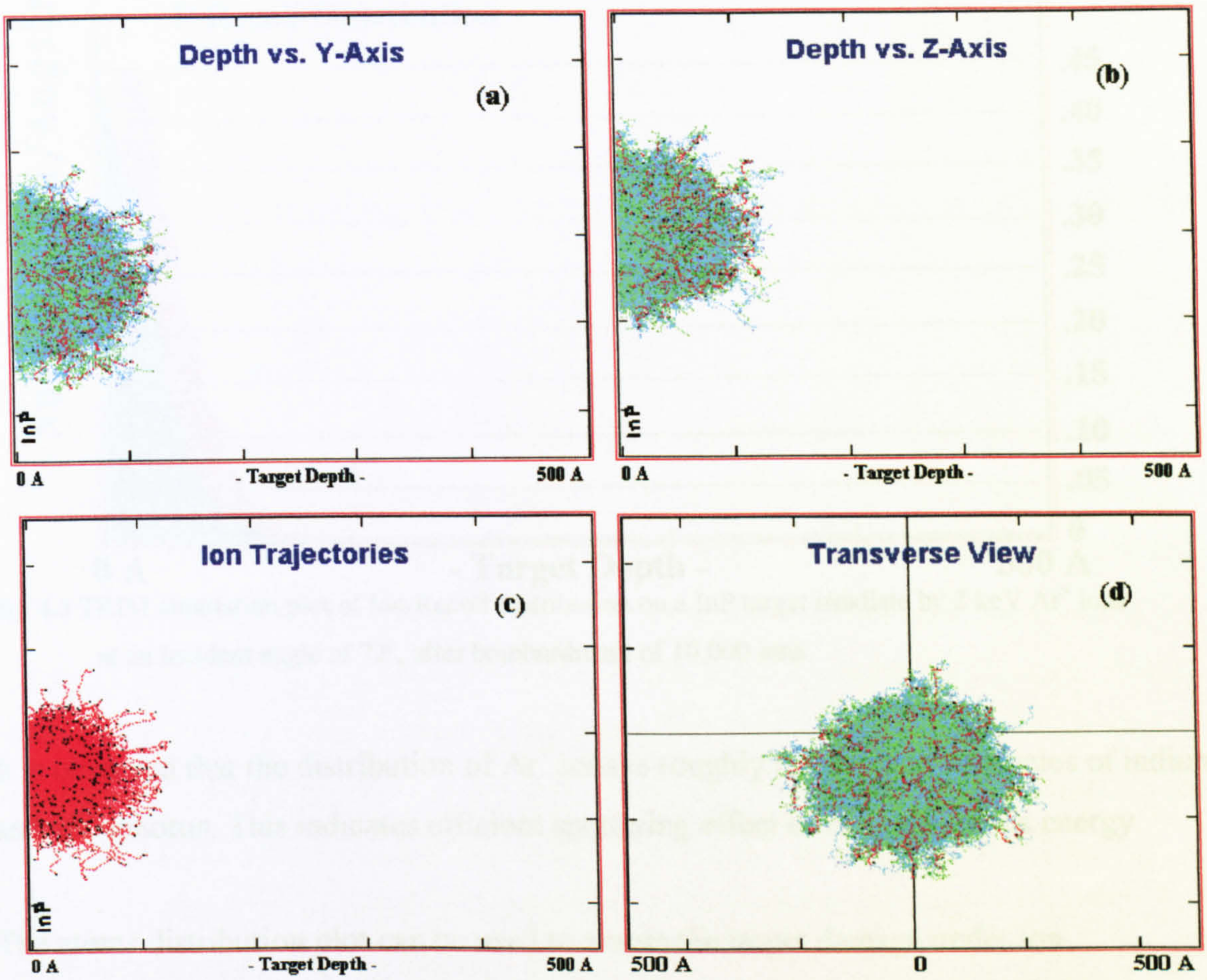

Fig 4.2 TRIM simulation plot of the collision cascade of Ar^+ ion bombardment on InP surface after bombardment of 30,000 ions: (a) XY longitudinal; (b) XZ longitudinal; (c) XY ions only; and (d) YZ lateral Ion energy = 2 keV, ion incident angle = 72°.

4.2.2 Ion/Recoil Distribution

Fig 4.3 is an Ion/Recoil distribution plot showing both the distributions of ions and recoiled atoms as a function of depth. The recoil distribution shows the distribution of all the indium and phosphorus atoms knocked out of their lattice sites, leaving vacancies.

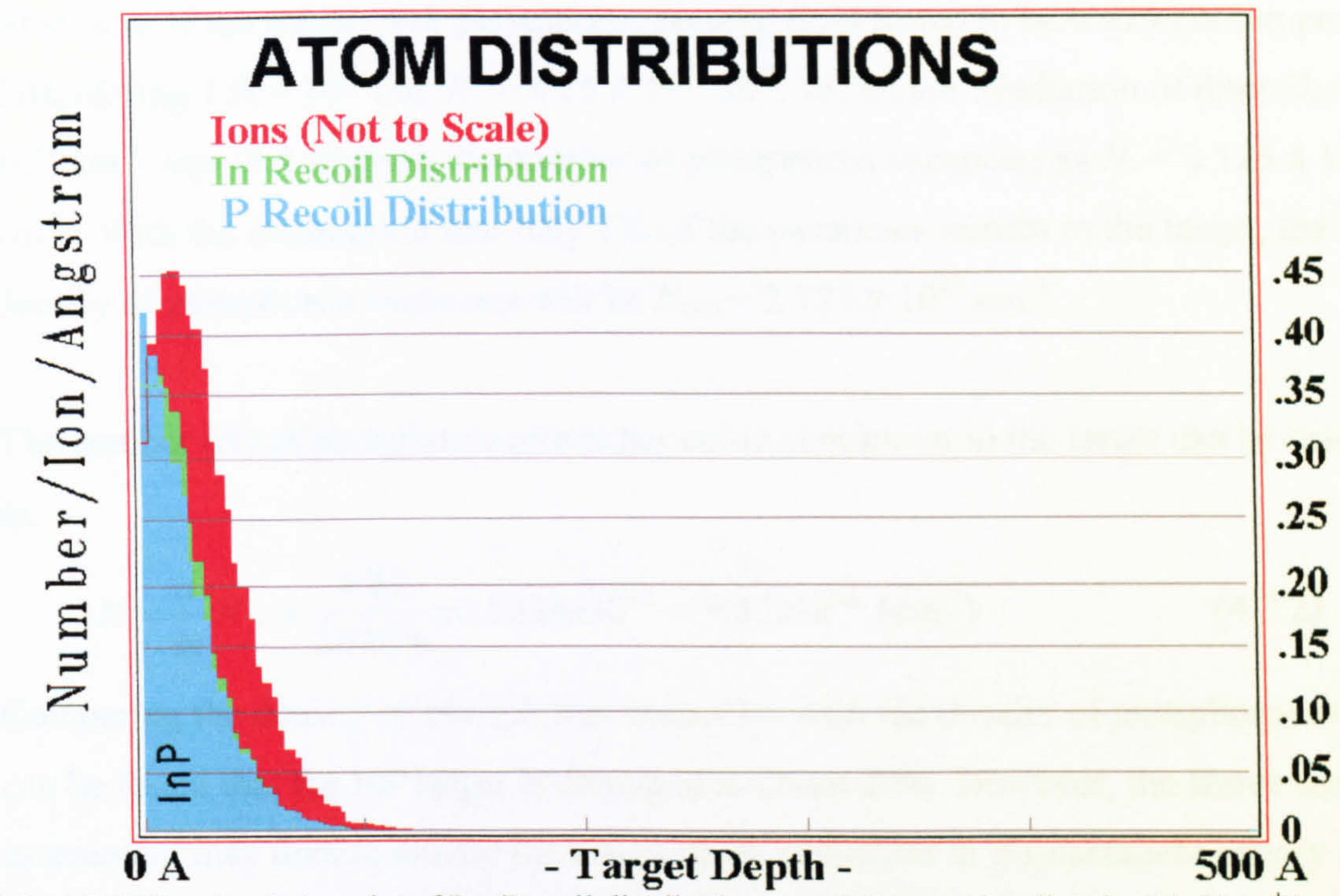

Fig 4.3 TRIM simulation plot of Ion/Recoil distribution on a InP target irradiate by 2 keV Ar^+ ions at an incident angle of 72°, after bombardment of 10,000 ions.

It is observed that the distribution of Ar^+ ions is roughly the same as vacancies of indium and phosphorus. This indicates efficient sputtering effect of Ar^+ ions at this energy.

The atoms distribution plot can be used to assess the target damage under ion bombardment, as long as the percentage vacancies retained in the target is known. Supposing 99 % of the damage self anneals, leaving only 1 % to contribute to the amorphous phase, the structure of the InP surface irradiated by 2 keV Ar^+ ions at 72° incident angles to a dose of 5×10^{16} cm^{-2} can be assessed as follows.

Let D_s be the dose of ion irradiation, d and m the density and molecular weight of that target material, N_v the volume density of the vacancies created by ion irradiation, R_v the rate of vacancy generation, and N_A the Avogardro number. The number of vacancies created by ion irradiation of dose D_s can be calculated as

$$N_v = R_v D_s \qquad (4.2.1)$$

R_v can be found from the peaks of recoil distribution curves in Fig 4.3. The unit of the vertical axis "Number/Ion/Ånstrome" refers to the number of recoils generated for each

Ånstrome of ion travel. For phosphorus recoils, R_v is found to be 0.425 per ion per Å. Considering 1 Å = 10^{-8} cm, $R_v = 4.25 \times 10^7$ cm^{-1}, for an ion irradiation of dose $D_s = 5 \times 10^{16}$ cm^{-2}, eqn (4.2.1) gives the number of phosphorus vacancies as $N_v = 2.125 \times 10^{24}$ cm^{-3}. With the assumption that only 1% of the vacancies remain in the target, the final density of phosphorus vacancies will be $N_{v(f)} = 2.125 \times 10^{22}$ cm^{-3}.

The number (N) of phosphorus atoms per cubic centimeter in the target can be calculated as:

$$N = \frac{d}{m} N_A = \frac{4.81}{30.974} x 6.0224 x 10^{23} = 9.35 x 10^{22} \ (cm^{-3}) \qquad (4.2.2)$$

Comparing the density of phosphorus vacancies with the density of phosphorus atoms, it can be found that the InP target is damaged to about 22%. However, the above damage assessment may underestimate the effect of the reduction in displacement energy of the target atoms under ion irradiation. With the accumulation of damages, the coupling of the target lattice becomes looser and looser so that atoms are easier to dislodge. These changes in the crystal integrity are not included [365] in TRIM. As a result, the density of phosphorus vacancies could be much bigger than the TRIM estimation. Considering this factor, the actual density of phosphorus vacancies could reach 50% of the density of phosphorus atoms in the target, and the target would probably be amorphous

4.2.3 Energy Loss to Ionization

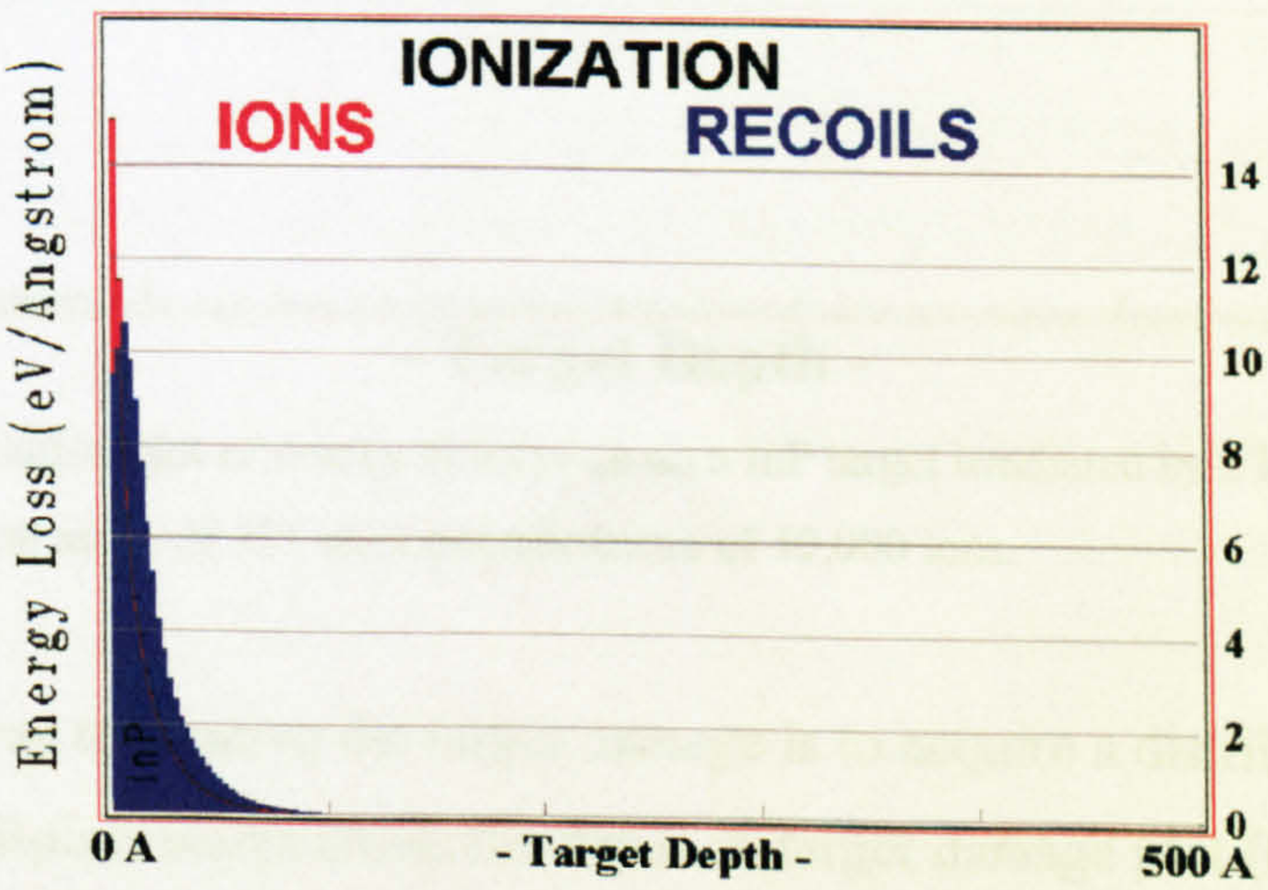

Fig 4.4 TRIM simulation plot of energy loss to ionization on a InP target irradiated by 2 keV Ar^+ ions at an incident angle of 72°, after bombardment of 10,000 ions.

Fig 4.4 is the ionization plot showing energy loss of Ar^+ ions to the InP target electrons. The electrons in the InP target absorb energy from the bombarding Ar^+ ions and the recoil atoms, with the subsequent release of energy as heat.

It can be observed from Fig 4.4 that for 2 keV Ar^+ ion irradiation of InP, most of the ion energy is lost to the electrons of recoil atoms, i.e., In or P. Only a small portion of the ion energy contributes to ionization of the target.

4.2.4 Creation of Damage in the Target

Target damage can be observed by plotting the energy absorption by the target atoms as a function of depth. Fig 4.5 shows that for 2 keV Ar^+ ion irradiation of InP, P atoms absorb more energy than In atoms.

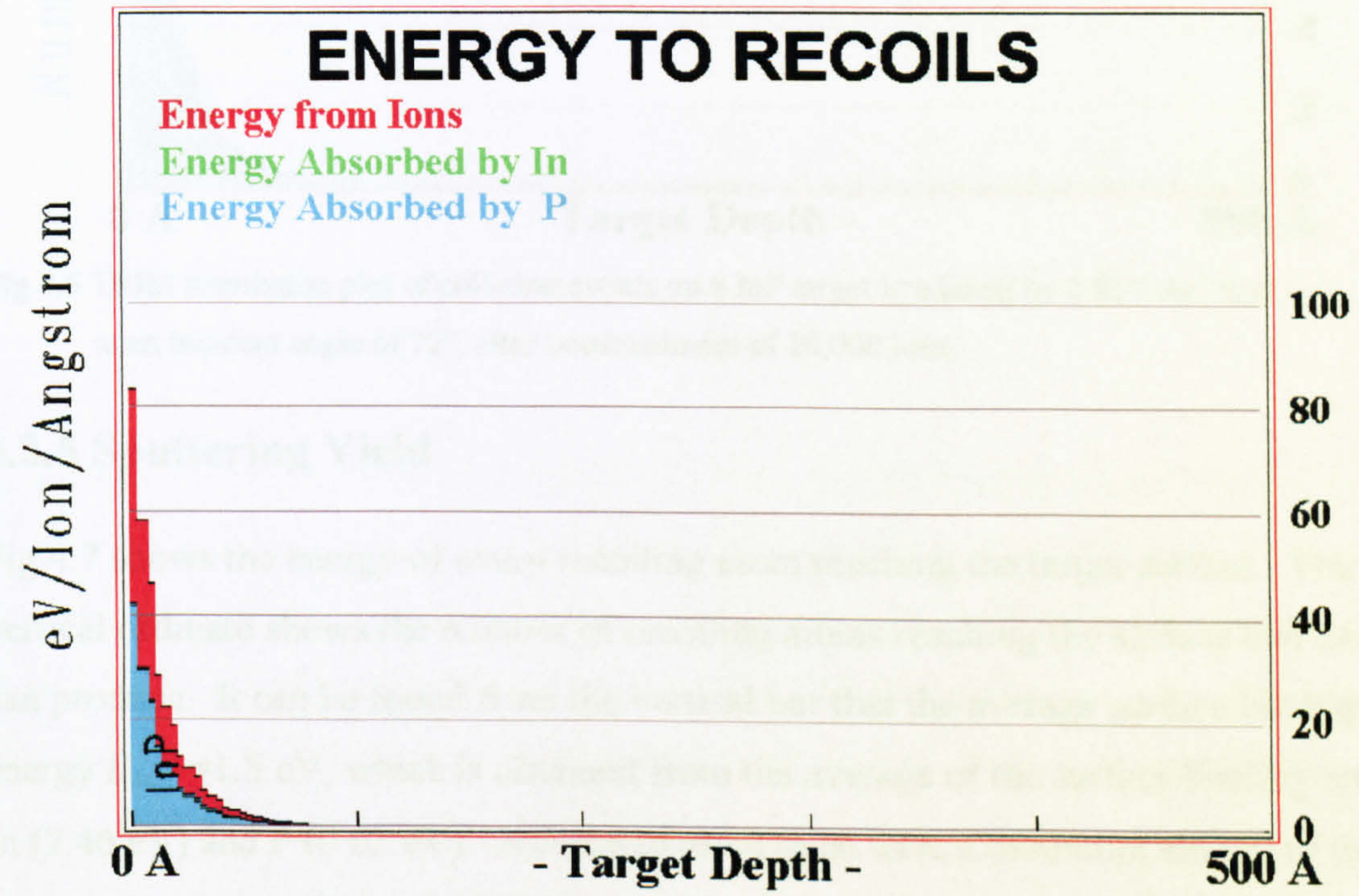

Fig 4.5 TRIM simulation plot of energy absorption on a InP target irradiated by 2 keV Ar^+ ions at an incident angle of 72°, after bombardment of 10,000 ions.

A more direct way to observe the target damage is to acquire a distribution of target vacancies and displacements along the depth. A target damage plot (Fig 4.6) can be invoked while TRIM is running. In Fig 4.6, the target displacement curve shows the total

target displacements, which is the number of atoms knocked off their target lattice sites. It can be found that the target vacancies curve is lower than the target displacements curve, indicating fewer vacancies than displacements.

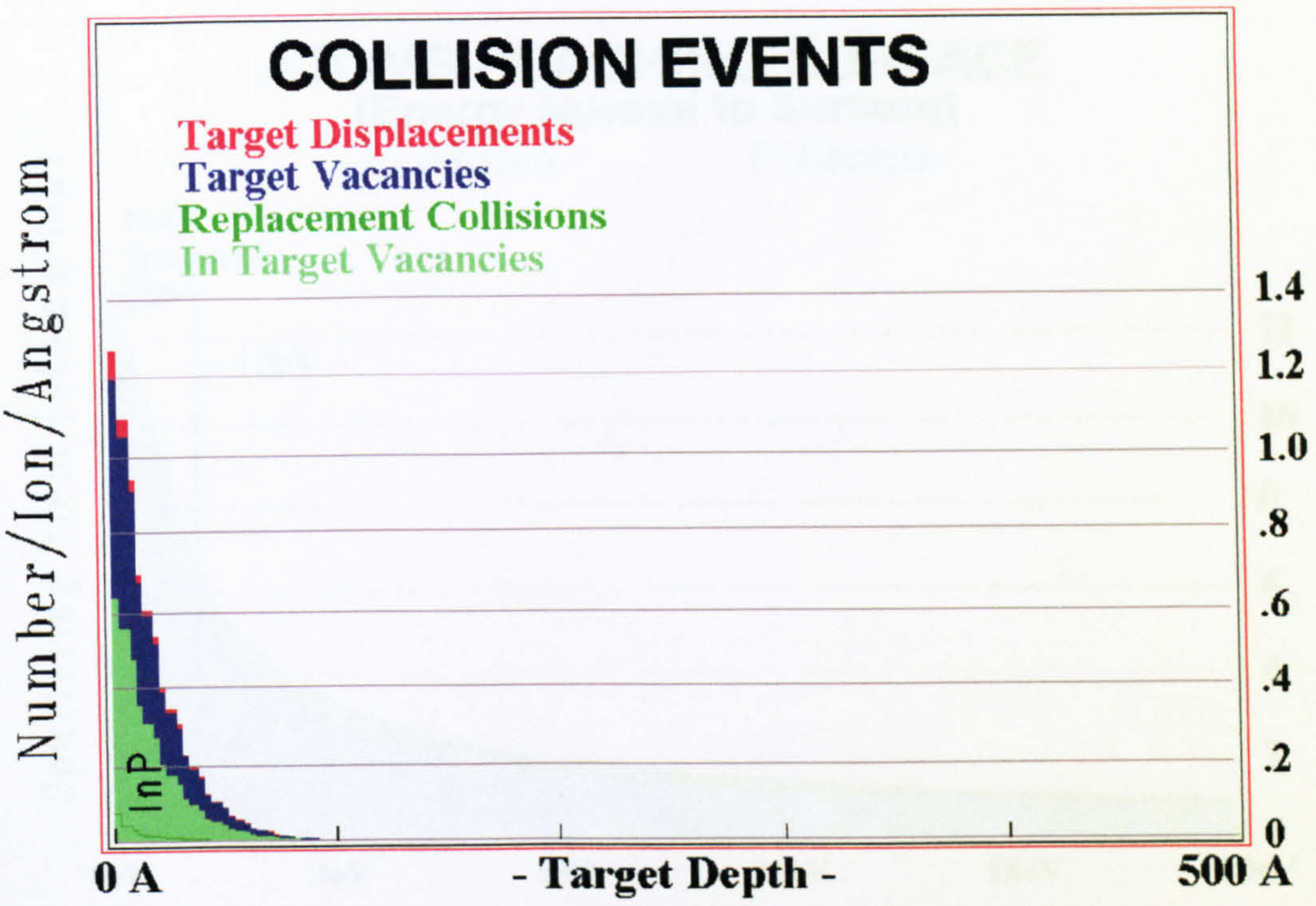

Fig 4.6 TRIM simulation plot of collision events on a InP target irradiated by 2 keV Ar^+ ions at an incident angle of 72°, after bombardment of 10,000 ions.

4.2.5 Sputtering Yield

Fig 4.7 shows the energy of every recoiling atom reaching the target surface. The vertical ordinate shows the number of recoiling atoms reaching the surface that each ion can produce. It can be found from the vertical bar that the average surface binding energy E_{surf} =1.5 eV, which is obtained from the average of the surface binding energy of In (2.46 eV) and P (0.62 eV). A recoiled atom must have a minimum energy of this value to be sputtered. At 1.5 eV, the number of atoms which reached the surface with more than this energy can be found from Fig 4.7 to be 7 and 5.5 for In and P respectively. This gives a sputtering yields of 7 atoms/ion and 5.5 atoms/ion for In and P respectively. It implies that In may be preferentially sputtered. In fact, the sputtering yields for In and P have to be calculated from their own surface binding energy individually. One can find from Fig 4.7 that the actual sputtering yield is approximately 4.5 atoms/ion for In and 8.5

atoms/ion for P, with their corresponding surface binding energies 2.46 eV and 0.62 eV. This agrees with the number shown in the "Sputtering Yield" table on the TRIM interface (not shown in Fig 4.7).

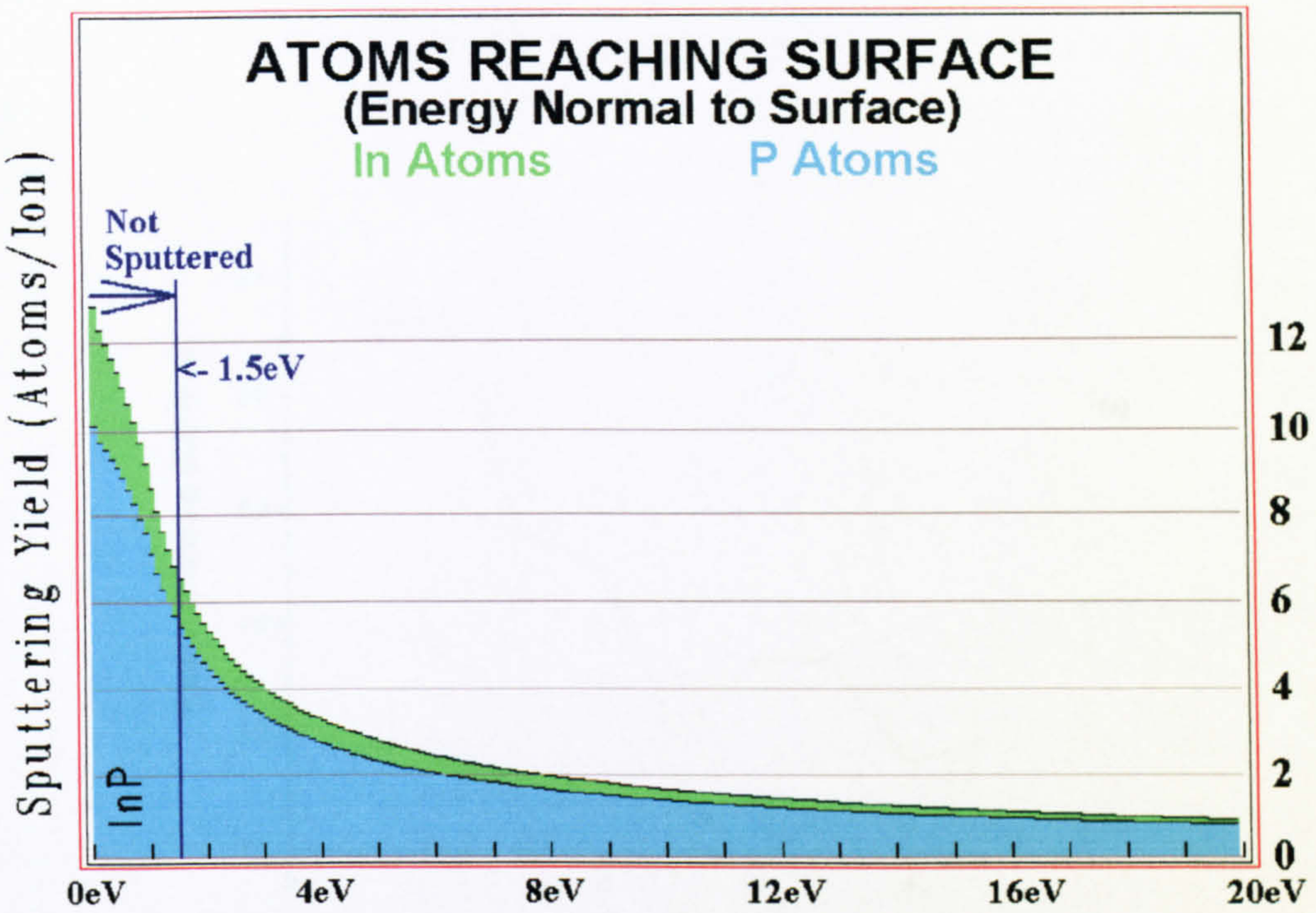

Fig 4.7 TRIM simulation plot of Sputtering (Integral) on a InP target irradiated by 2 keV Ar^+ ions at an incident angle of 72°, after bombardment of 10,000 ions.

The actual sputtering yield of In and P will be higher than the simulated results because of the reduction in surface binding energy. This is mainly due to the amorphisation of the surface under ion bombardment. However, the dependence of sputtering yield upon ion energy and ion incident angle can be assessed by TRIM. Following are some results of the dependence of the ratio of the sputtering yield of P to In in relation to bombarding energy and ion incident angle and ion energy.

Fig 4.8 (a) shows a decreasing sputtering yield ratio P/In upon ion energy, indicating reduced preferential sputtering of P at higher ion energy. This implies that the sputtering yield of In increases faster with ion energy than that of P. More pronounced preferential sputtering of P is expected to be observed at lower ion energies. In chapter 5, 2 keV will

be used to create nanowires. At this energy, a medium P/In yield ratio is predicted by Fig 4.8 (a).

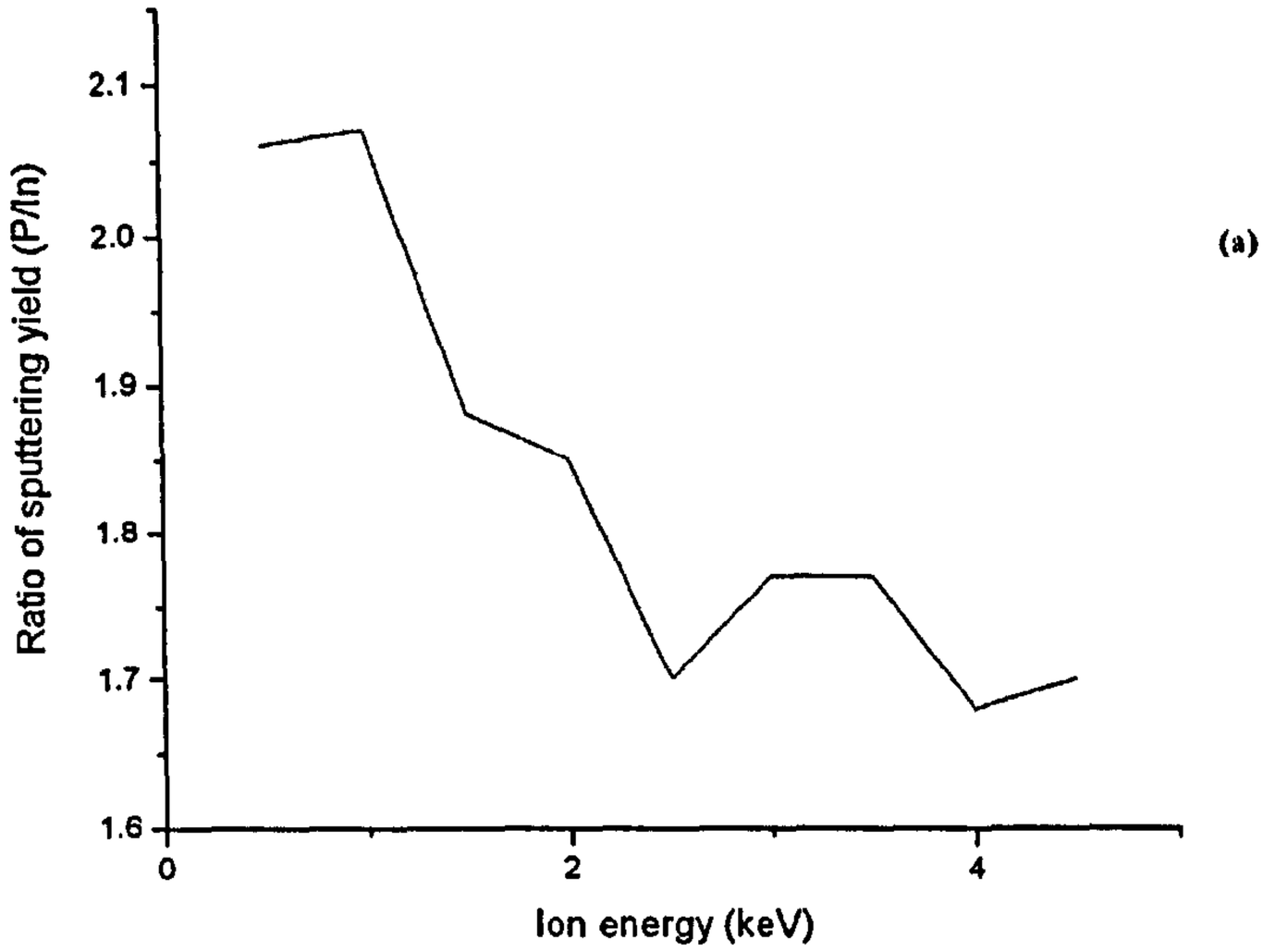

Fig 4.8 TRIM simulated results of sputtering yield ratio P/In dependence of (a) ion energy and (b) ion incident angle.

Fig 4.8 (b) shows that although the P/In ratio fluctuates it manifests strong preferential sputtering of phosphorus with a general tendency to decreasing P/In ratio upon increasing ion incident angle. This is in agreement with the early experimental results published by Hou et al [112]. The In/P ratio is expected to reach a maximum at ion incident angles of 30° and 60°, and a minimum at around 77°. At 72°, the P/In ratio is 1.83.

Chapter 5

Ion Beam Directed Self-Assembly of Nanowire Arrays on InP (100) Surfaces

In this chapter, a comprehensive delineation of the experimental method of fabrication of nanowire arrays on InP (100) surfaces by Ar^+ ion bombardment is described in detail. The experiment shows that nanowire arrays of regular shape and periodicity can be fabricated under certain experimental conditions. Based on the atomic force microscopy (AFM) analysis of various morphology of Ar^+ ion bombarded InP (100) surfaces, a cone-mergence model is proposed to account for the physical mechanism of nanowire formation by this technique.

5.1 Experimental Method

Ion bombardment of InP (100) surfaces was performed in an ultra-high vacuum (UHV) chamber. The chamber was equipped with an ion gun and a sample manipulator. Samples were transferred from the load-lock to the main chamber followed by Ar^+ ion beam sputtering. The sputtered samples were then brought out of the chamber for morphology characterisation with a Digital Instrument's Multi-Mode SPM operating in air. Electronic structures of the sputtered samples were examined by an Omicron VT_STM system in UHV conditions. Stoicheiometric analysis of the fabricated nanowires was carried out with x-ray photoelectron spectroscopy (XPS) (chapter 6).

5.1.1. The Ion Beam Apparatus

The experimental set-up is shown in Fig 5.1 (a) with a schematic diagram Fig 5.1 (b).

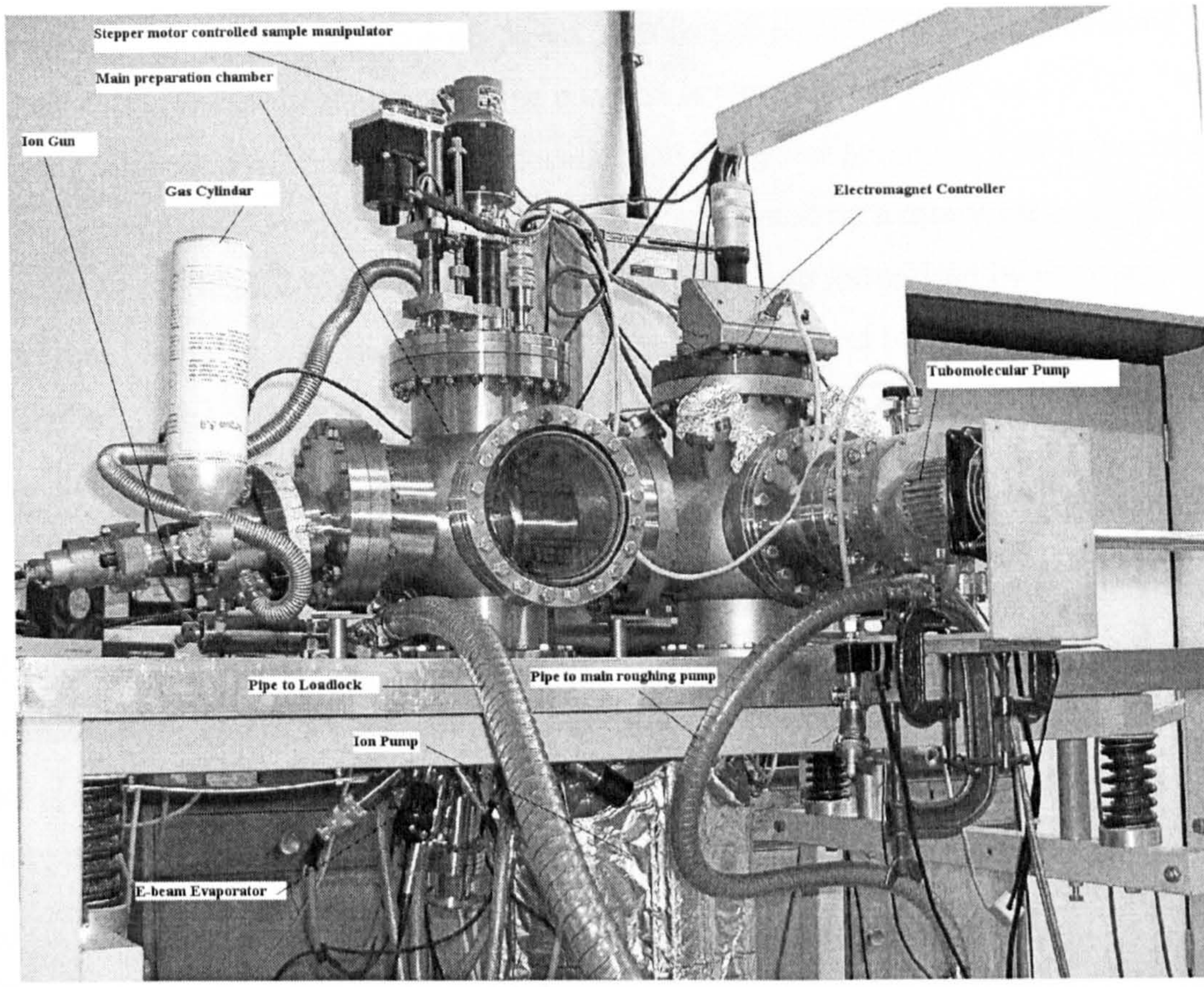

(a)

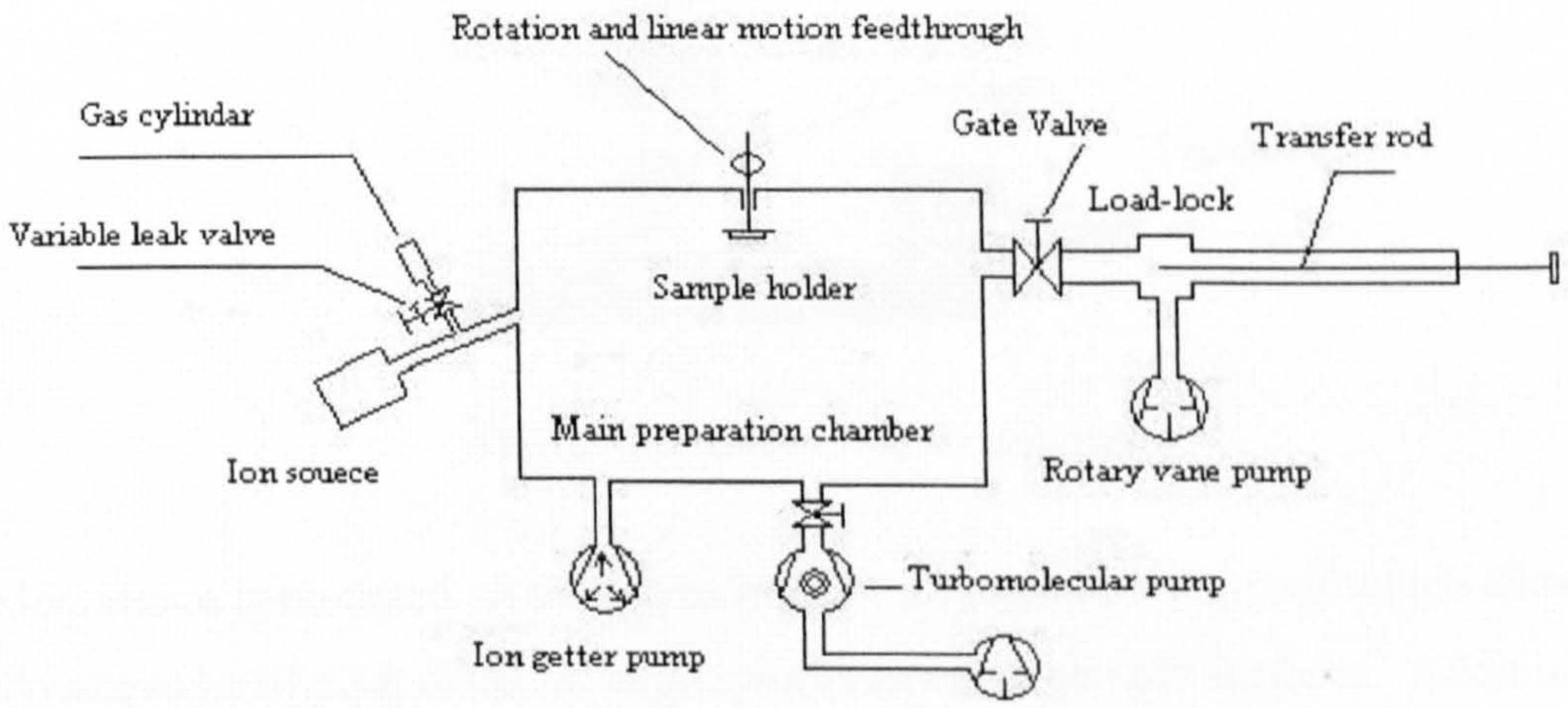

(b)

Fig 5.1 Sample preparation chamber: (a) Photograph of the ion beam machine; (b) Schematic diagram. For simplicity, a spare chamber and two e-beam evaporators on the bottom of the main chamber are omitted in Fig 5.1 (b).

The system was initially built for ion beam polishing of samples at grazing incident angles [51, 413]. The main chamber can be pumped to a pressure lower than 8×10^{-10} mbar with a combination of rotary, turbomolecular, and ion getter pumps. A gate valve isolates the main chamber from the load-lock which was evacuated by a rotary vane pump. Samples can be loaded to the base inside the load-lock and introduced by the transfer rod to the main chamber with the opening of the gate valve at load lock pressures lower than 0.05 mbar. The pressure in the main chamber can be recovered to lower than 5×10^{-8} mbar in less than half an hour after the introduction of a sample from the load-lock.

The sample manipulator is schematically drawn in Fig 5.2. With a magnet fixed on top of the sample holder, the sample can be picked up by a coil with a ferromagnetic core mounted at the end of a linear motion feed-through. The ferromagnetic core enables the sample to stay attached to the manipulator. The sample can be unloaded by using a current pulse sent though the coil producing a repulsive magnetic force.

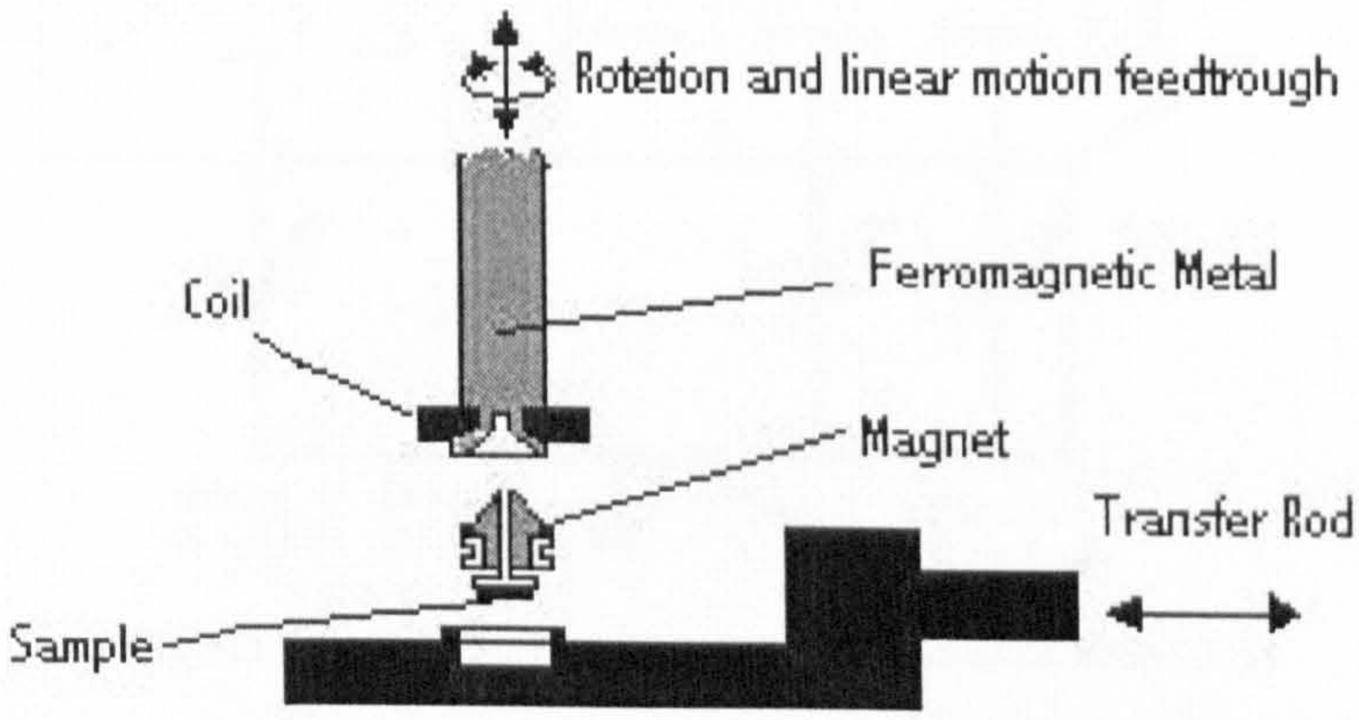

Fig 5.2 Schematic of sample manipulator

The ion source is mounted on the main chamber through a port aligner which allows the ion source to be tilted at different angles with respect to sample surfaces. Additionally, the scanning control unit of the ion source allows the ion beam to be deflected up to 90° from the axis of the source. Although the combination of these two adjustments gives a wide range of sputtering angle adjustment, the limit of the vertical travel range of the sample holder confines the sputtering angle to 60° to 86°. The height of the sample is

adjusted by the rotation and linear motion feed-through driven by a computer controlled stepper motor.

The ion source is an extractor type IQE 12/38 (Fig 5.3) [414]. The ion generation takes place in a collision chamber. Thermal electrons emitted from a circular iridium ribbon filament are accelerated by an anode grid with a100 V potential. Neutral particles present in the volume between the filament and the anode are ionized by these accelerated electrons which can cross the anode volume many times. Electrons ejected from the ionized atoms can then be accelerated to produce second ionization, and so on. This specially shaped anode increases the probability of collision and makes the use of an additional magnetic field unnecessary.

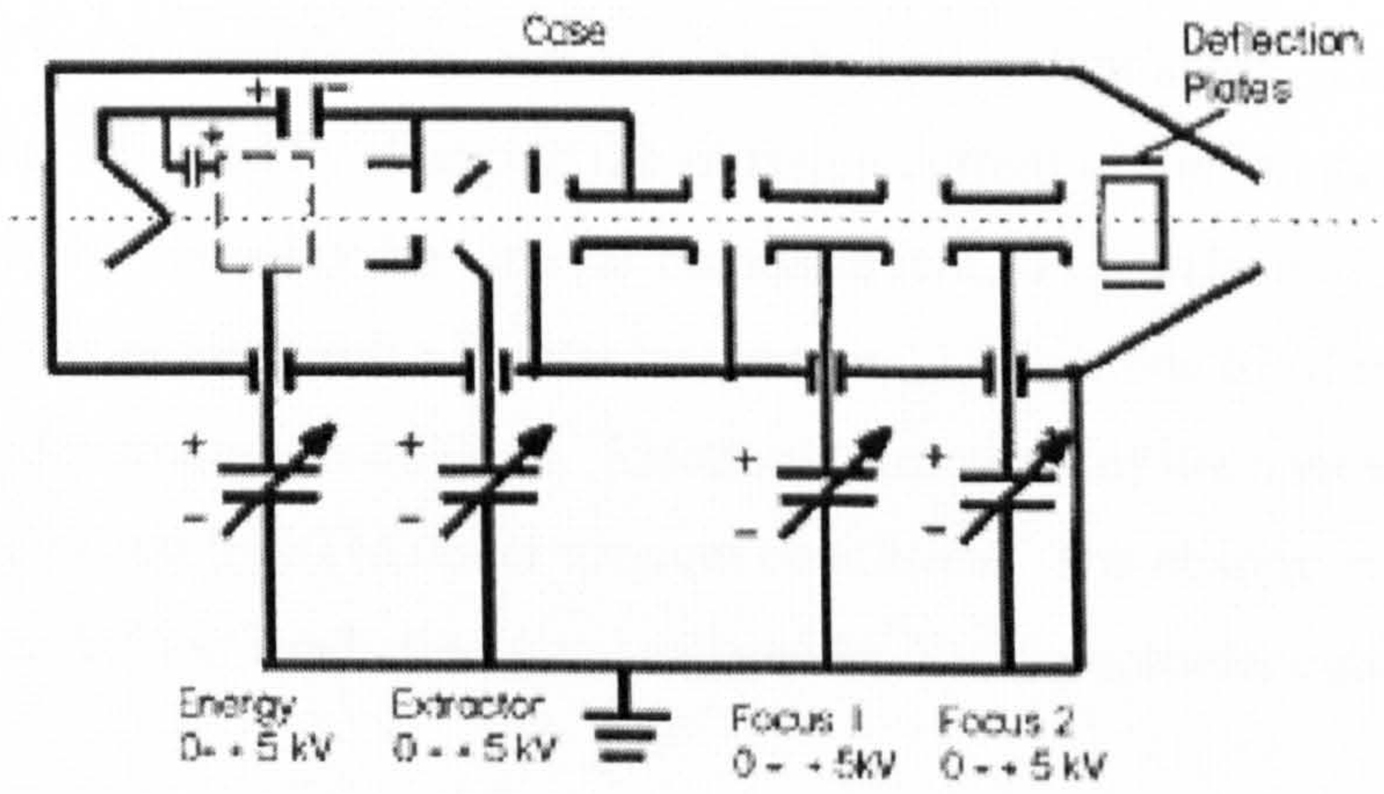

Fig 5.3 Schematic of the Fine Focus Ion Source IQE-12/38

The ions are then extracted from the source volume by a voltage of about 150 V and are accelerated to energies up to 5 keV. A single ion-optic lens placed directly behind the extractor electrode focuses the ions to a beam diameter of 0.1 mm. An aperture with an opening of 1 mm is placed in the image plane allowing about 85% of the extracted ions to pass.

Two tubular lenses placed behind the aperture focus the ion beam on a target 200 mm away from the source volume. Between the lenses and the target are two pairs of parallel

plates set at an angle of 90° to each other, which are used to position and raster the ion beam on the sample.

5.1.2 Procedures of the Experiment

Intrinsic InP (100) samples were cleaved in air, mounted on a sample holder, loaded to the load lock and transferred to the UHV chamber equipped with the 0.5-5 keV ion gun. The sample was then attached to the linear and rotational manipulator. The chamber was pumped to a base pressure of 6×10^{-9} mbar, and the operating pressure was increased to 1×10^{-6} mbar by leaking high purity Ar gas into the working chamber. An ion beam focused to a diameter of 0.2 mm was projected at the centre of the samples by adjusting the sample position, the angle of the ion gun and the deflection angle of the ion beam. InP samples were scanned by a 2 keV ion beam across a defined area at room temperature under a range of ion current density, ion dose and beam incident angle. The ion current on the sample was adjusted by changing the emission current of the ion gun. The ion dose was changed by choosing the time for bombardment. The surface morphologies of the samples were examined with a Digital Instruments' MultiMode SPM running in AFM contact mode under ambient conditions. Electronic structures of the nanowire arrays were then characterized by STM under vacuum conditions. The change in chemical composition after Ar^+ ion irradiation was analyzed by X-ray photoelectron spectroscopy (XPS).

5.1.3 Deduction of Ion Dose

In this work, samples were placed at a distance of 50 mm (d_2) from the source volume (Fig 5.4). Hence, ion beams focused to a diameter of 0.2 mm (h_1, from Ref [415]) on the default sample plane (d_1 = 20 mm to the source volume) yield a diameter of h_2 on the actual sample plane, according to the equation:

$$h_2 = \frac{d_2}{d_1} h_1 = \frac{50}{20} x0.2 = 0.5(mm)$$

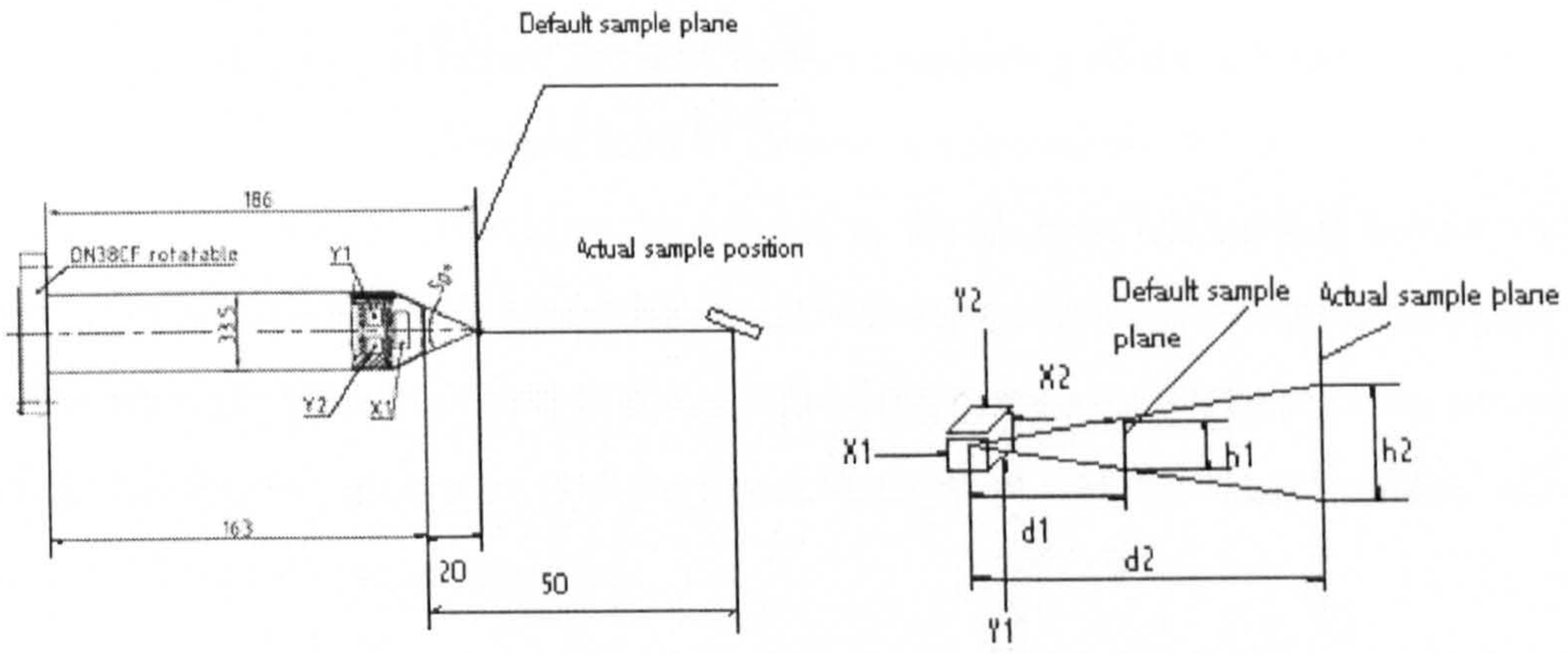

Fig 5.4 Geometry of sample position against ion source

Similarly, a defined scan width of x_1 (= 2 mm, horizontal direction) on the default sample plane yields a final scan width x_2 on the actual sample plane:

$$x_2 = \frac{d_2}{d_1} x_1 = \frac{50}{20} x2 = 5(mm)$$

Experimentally, ion beams were projected on the sample at grazing incident angles. Therefore, ion beams with a defined scan width of y_1 (= 4 mm, vertical direction) can scan over the entire length of the sample plate of diameter of 12 mm. This yields an effective scanned area of

$$A = x_2 y_2 = 5x12 = 60(mm^2) = 0.6cm^2$$

Assuming that ion beams are strictly confined to the area A and the contribution of secondary electrons can be neglected, the ion dose D, which is defined as the total number of bombarding ions per unit area on the sample surfaces, can be expressed as:

$$D = \frac{It}{A} = Jt \qquad (5.2.1)$$

Where I stands for the ion current measured on sample surfaces, J is the ion current density, and t is the total sputtering time. From eqn (5.2.1), a 20 minutes' Ar^+ ion bombardment with $J = 7\ \mu A/cm^2$ yields an ion dose of $5.2 \times 10^{16}\ cm^{-2}$.

Without charge neutralization, sustained ion bombardment on a sample can lead to the built-up of charges, and hence prevent further sputtering of the sample surface because of Coulomb repulsion. This could lead to incorrect calculation of the ion dose. The problem was solved by attaching the sample to the plate of the sample holder with a small piece of conductive carbon tape (the area of the tape was smaller than that of the sample so that possible contamination to the sample during ion bombardment was avoided). The sample holder was grounded and the low resistivity of the InP sample would allow positive charges to be neutralized.

5.1.4 Methods of Morphology Characterization by AFM

Acquisition of good AFM images that reflect actual structures on sample surfaces calls for meticulous consideration based on comprehensive understanding of the operation of an AFM. Great care should be paid in processing the results obtained with an AFM in order to avoid improper manipulation of data. Fig 5.5 (a) is a photograph of the Digital Instruments' Multi-Mode SPM. It can run in many modes, including STM, AFM contact and tapping modes, and LFM (Lateral Force Microscope). In this research, contact mode AFM was used with square beam ultra-sharp silicon cantilevers (CSC12, μMasch, Fig 5.5 b) with a curvature radius of $R < 10$ nm, a full tip cone angle $< 20°$, and a spring constant $k = 0.03$ N/m.

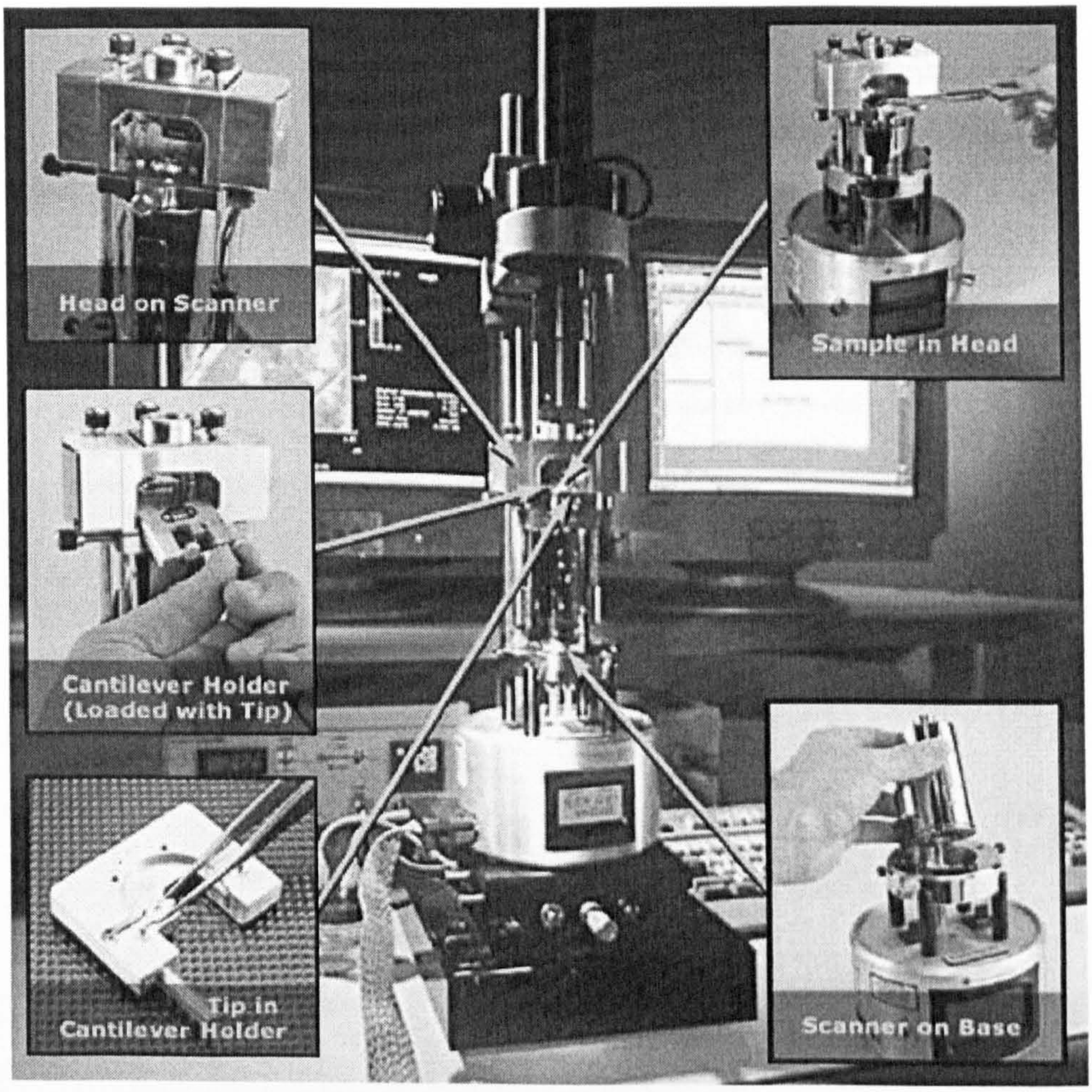

(a) Digital Instruments' Multi-Mode SPM [416]

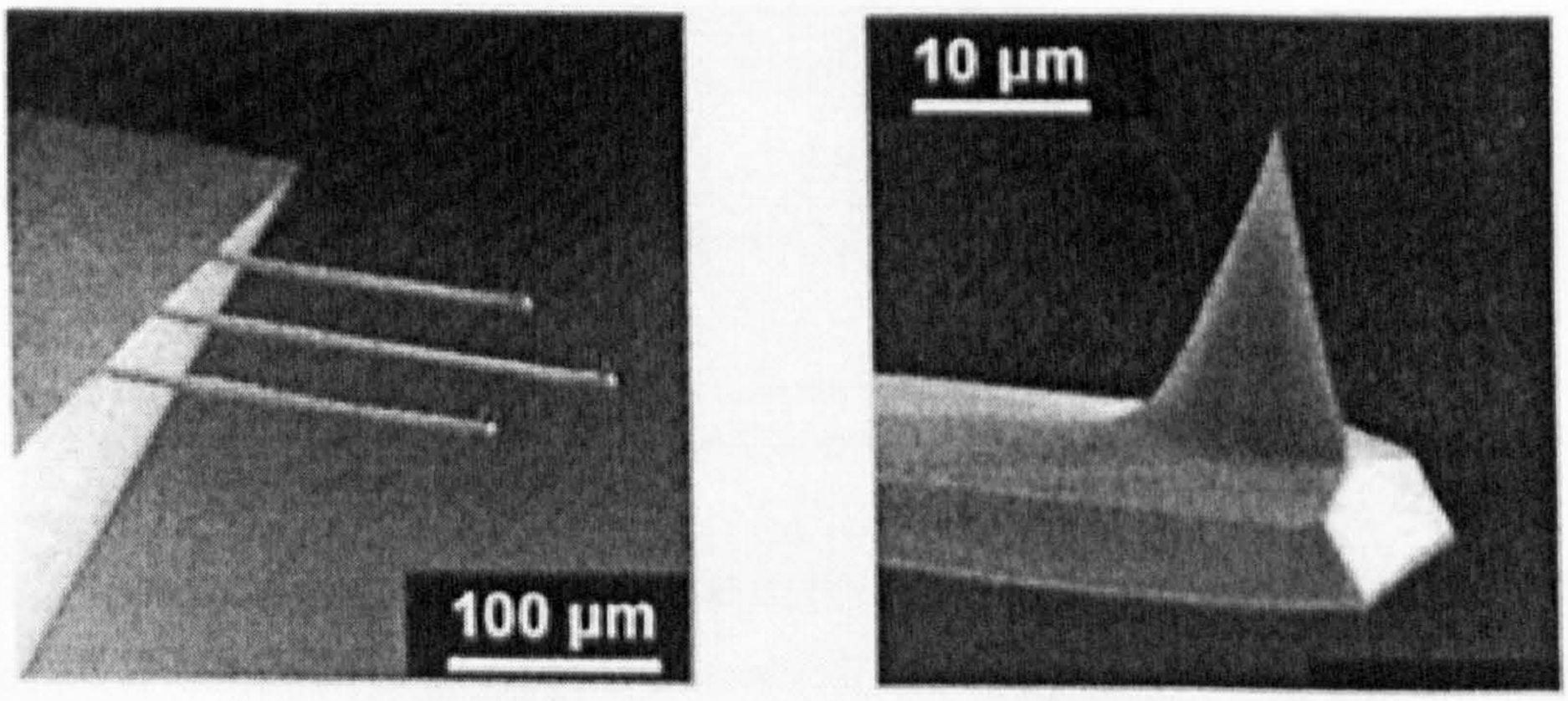

(b) SEM image of the ultra-sharp silicon cantilever CSC12/15

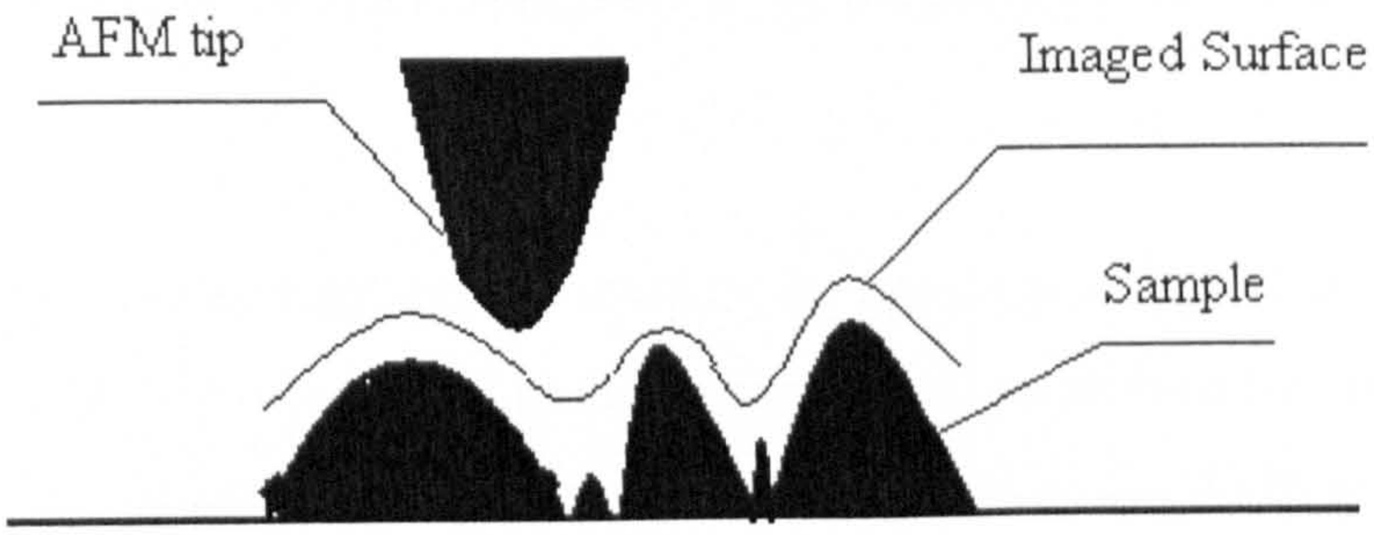

(c) Illustration of limited AFM resolution. Small structures can not be resolved by an AFM tip or their size appears to be larger due to the finite tip curvature.

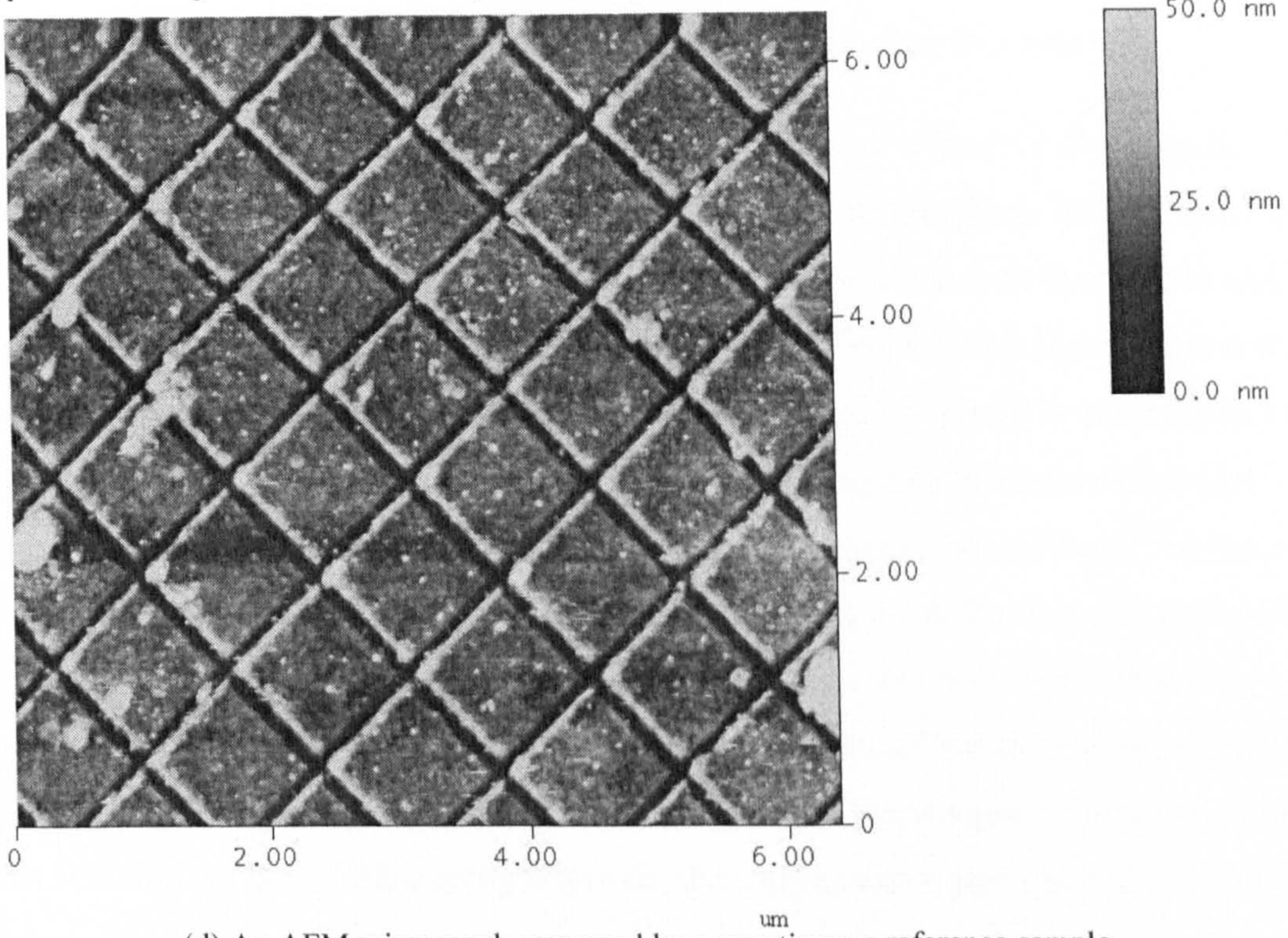

(d) An AFM micrograph measured by a new tip on a reference sample.

Fig 5.5 Photograph of Digital Instruments' Multi-Mode SPM (a); μMasch silicon cantilever (b); a schematic illustrating the limitation of AFM resolution (c); and an AFM micrograph measured by a new tip on a reference sample (d).

An AFM image is actually a convolution of the surface topography and the tip profile. The lateral resolution of an AFM is limited (Fig 5.5 c) by the radius of curvature and the apex angle of the tips used, as well as the topography of the imaged surface. As a result, small islands can not be resolved if they are hidden in-between larger islands, and small surface features tend to appear larger in AFM images due to the influence of the finite tip

size. All the data generated in this research are to be weighted by the curvature radius of 10 nm.

An AFM tip may be worn or damaged. A worn or damaged tip will produce false image of the sample surfaces. Tip monitoring in this research was performed by measuring the patterns on the reference sample offered by Digital Instruments. An AFM micrograph measured by a new tip on the reference sample is shown in Fig 5.5 (d).

5.1.4.1 Minimization of Forces and Optimization of Scanning Parameters

An AFM tip can interact with a sample surface by long-range attractive forces (e.g., electrostatic attraction or repulsion, current-induced or electromagnetic interactions, and capillary forces due to the surface energy of water condensed between the sample and the tip), short-range attractive forces (mainly Van der Waals Forces), and short-range inter-atomic repulsive forces. Minimization of the forces exerted on the tip is essential in order to keep the damage of the sample by the tip during scanning to a minimum after tip-sample interaction in contact mode. In the Digital Instruments' MultiMode^{TM} SPM, the set-point can be adjusted to increase or decrease the cantilever deflection and therefore, the contact force of the tip on the sample. Tip force minimization was performed by gradually reducing the set-point offset until the tip pulls free of the surface (this gives the pull-off value of Set-point offset), Then increasing the set-point again to let the tip regain contact with the surface, followed by lowering the set-point to a point just above the pull-off value. This gives the minimum tip forces required to measure the morphology of the sample surface.

Fig 5.6 is a typical contact mode AFM force plot of an ultra-sharp silicon cantilever on a sputtered InP (100) sample. The contact force can be calculated by eqn. (2.4). The cantilever spring constant was given as $k = 0.03\ N/m$. ΔZ (in eqn. 2.4) was found (from Fig 5.6) to be $0.37\ div \times 13.06\ nm/div \times 12.5\ nm/V = 60.4\ nm$ (where $12.5\ nm/V$ was the sensitivity of the piezo). The force on the tip is calculated from eqn. (2.4) to be $F = 0.03\ n/m \times 60.4nm = 1.8\ nN$.

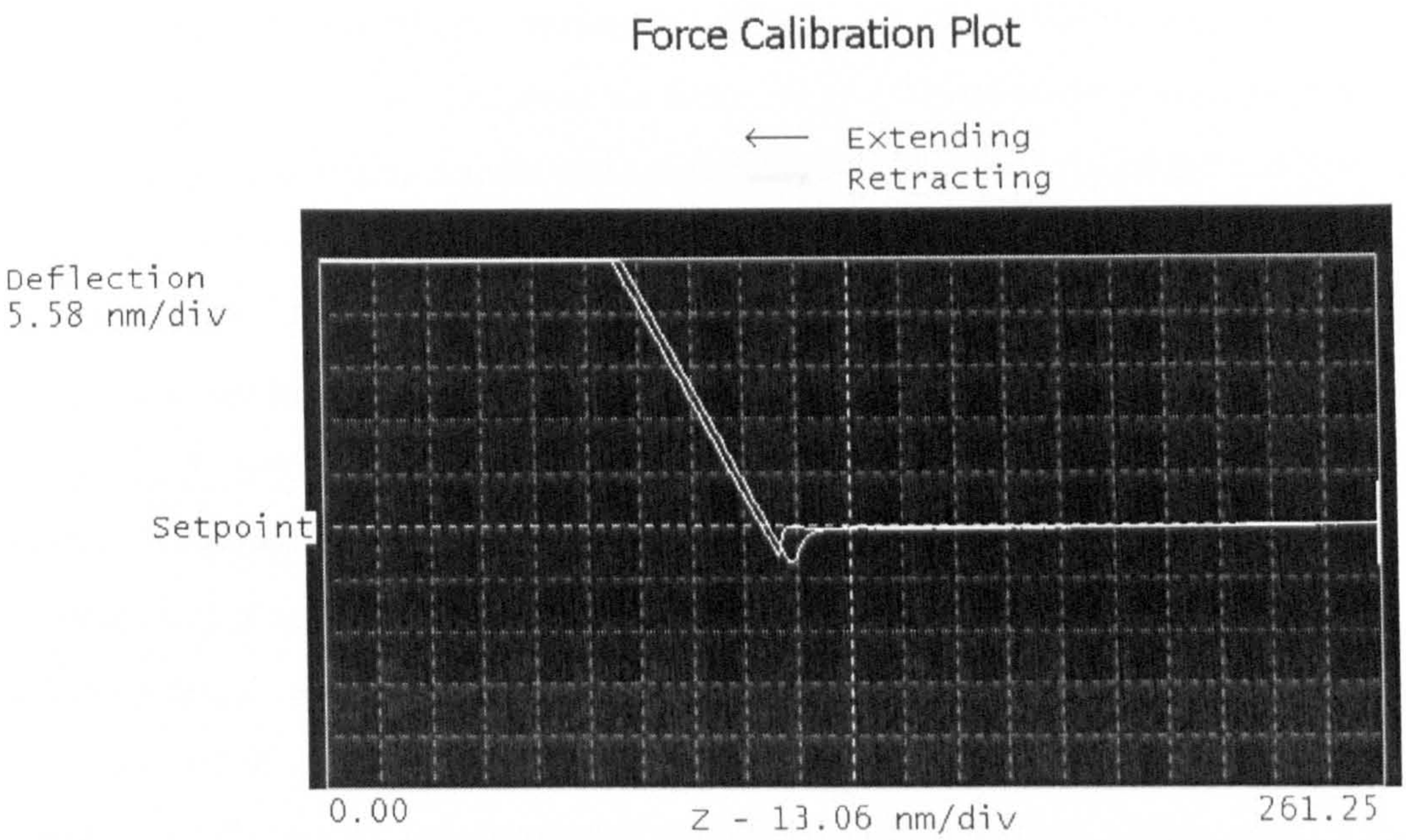

Fig 5.6 A typical force calibration plot of an ultra-sharp silicon cantilever on a sputtered InP (100) surface

In most instances, contact AFM is used for the collection of height morphology. To collect height data, the feedback gains must be sufficiently high so that the tip keeps track of the sample surface with minimal cantilever deflection. Before image acquisition, optimization of feedback gains was performed by gradually increasing the feedback gains until the piezo oscillates and then slightly reducing the gains until the oscillation disappears.

5.1.4.2 Analysis of AFM Images

Analysis of AFM images can be grouped into two stages: those that compensate for instrumental defects and those that quantify surface information.

5.1.4.2.1 Compensation of Instrumental Defects from AFM Data

An AFM image is acquired with surface information, instrumental defects and noise. In order to extract only surface information from image or spectroscopy data, acquisition artefacts due to instrument defects and noise must be removed. All of the commercial SPMs (AFMs) are equipped with image processing software to eliminate these artefacts. In most cases, "Flatten" is performed to an image acquired on predominantly flat samples with sporadic tall features to reduce instrument defects. The theory behind it is that every AFM image includes a plane containing the deviation due to the impossibility of bringing a tip into absolutely perpendicular contact with a sample plane. This background plane is calculated from a least squares fit and then simply subtracted from the data, leaving $z'=A*(x) + B*(y)$, where A and B are constants. Sometimes a curvature can be found in the background of an AFM image. This is usually caused by the nonlinearity of the scanner (Fig 5.7) or very low frequency vibration. Compensation of this kind of image distortion is done by using a polynomial of order n for the subtraction rather than a plane, so that $z'=A*(x^n)+B*(y^n)$, where an n of 4 or less is usually sufficient.

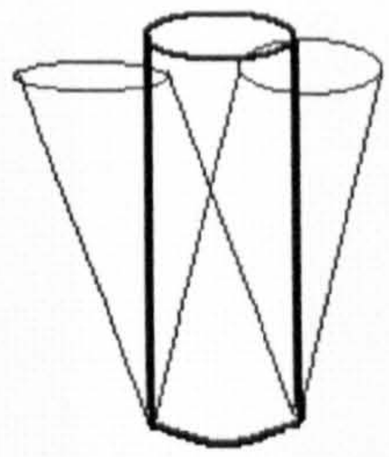

Fig 5.7 Schematic of the non-linearity of a piezo-tube

Fig 5.8 gives an example of an AFM image acquired with the Digital Instruments' MultiMode^{TM} SPM on an Ar^+ ion beam bombarded InP (100) surface before and after application of "Flatten".

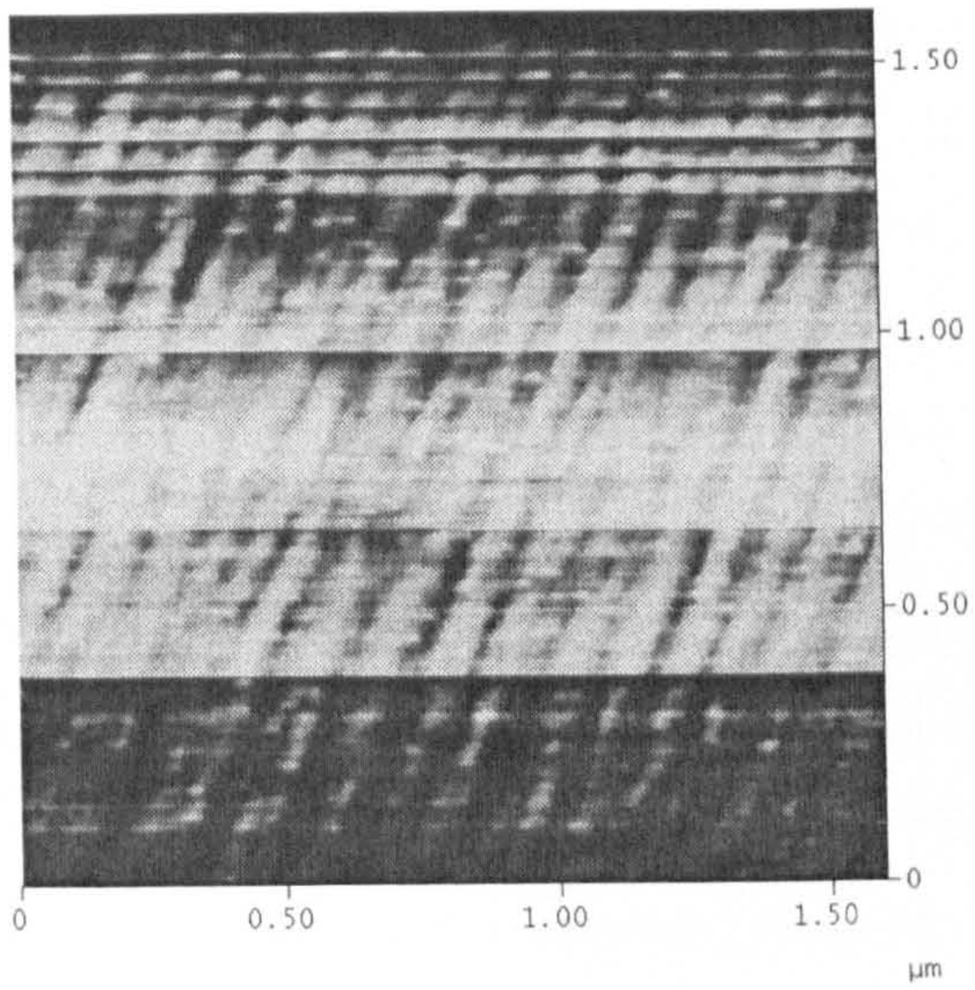

(a)

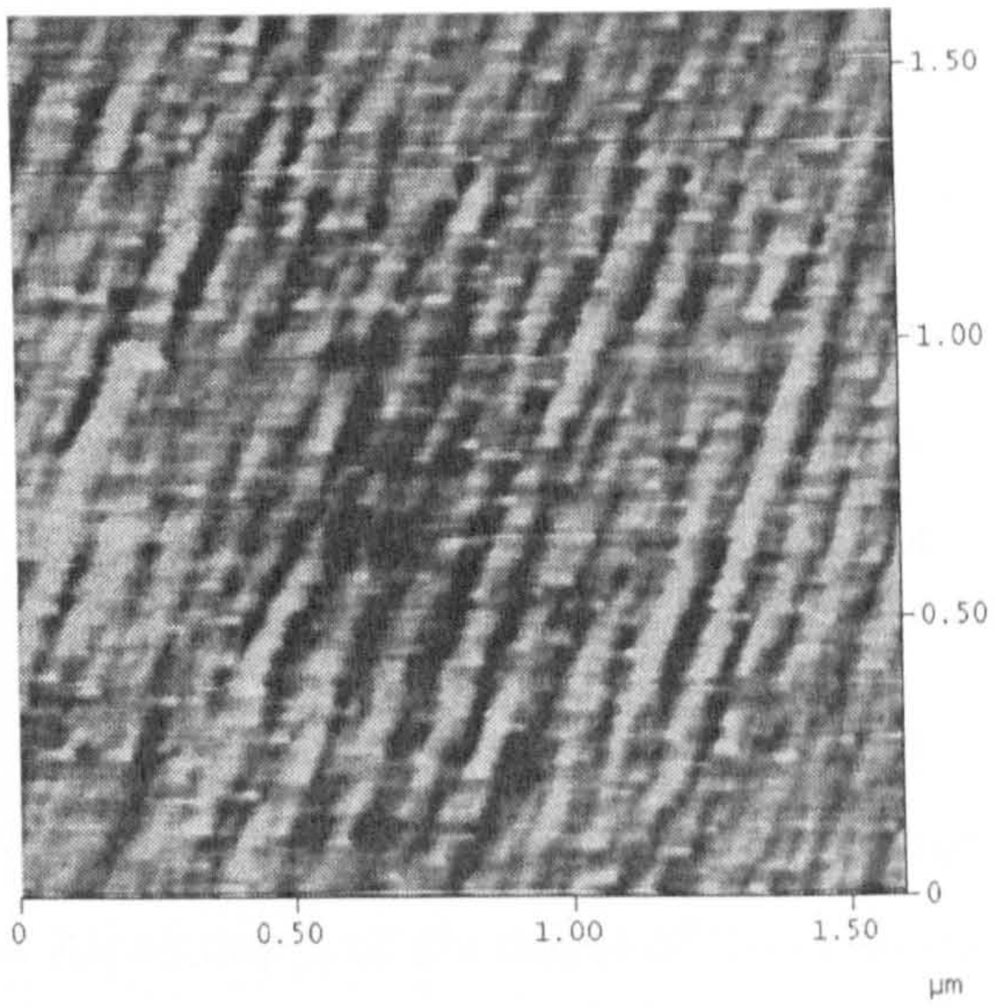

(b)

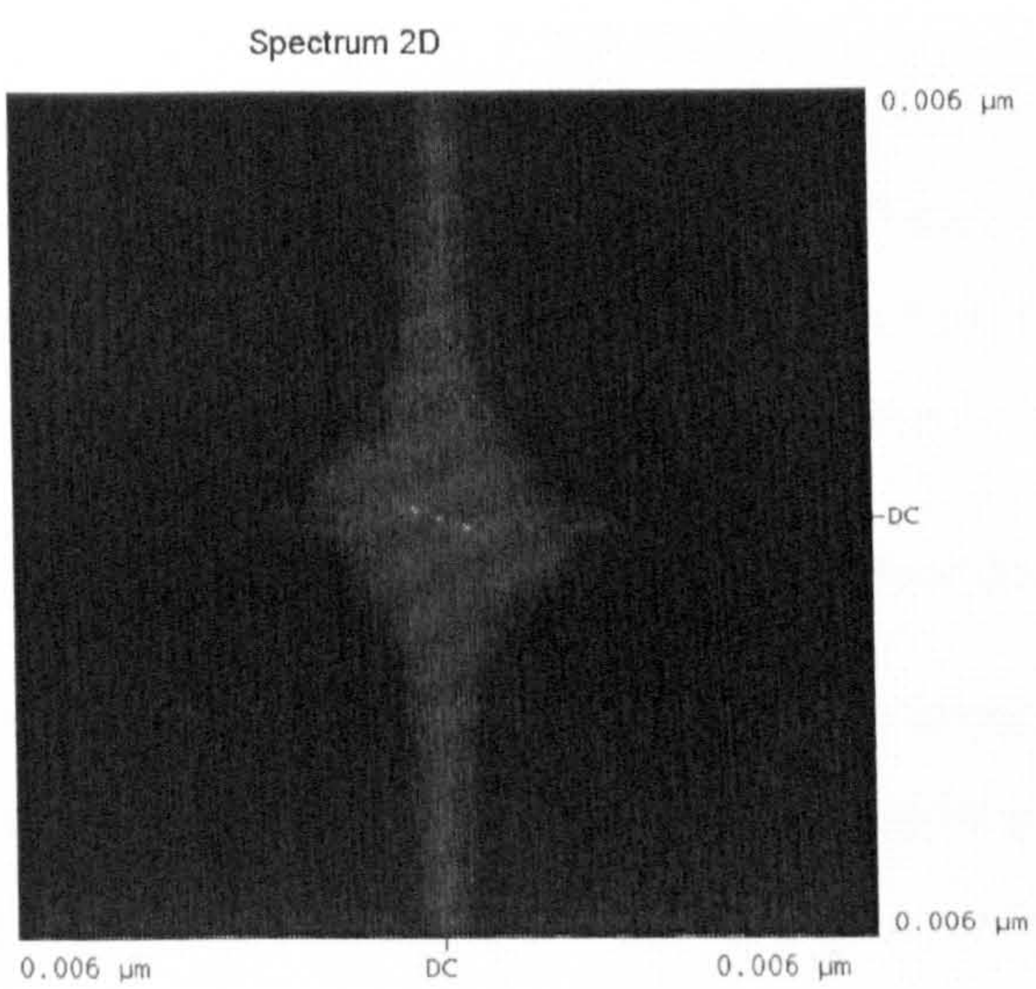

(c)

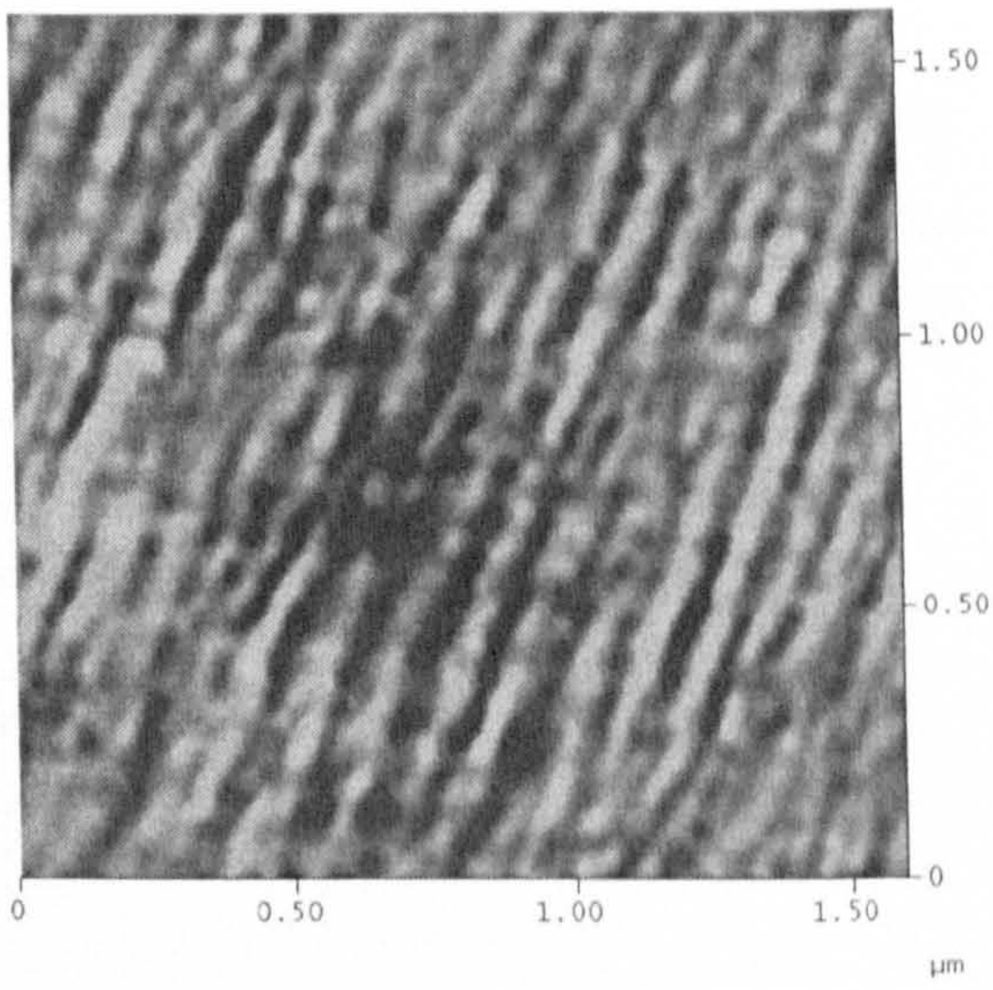

(d)

Fig 5.8 Comparison of an AFM image before and after off-line image processing command "Flatten": (a) Original AFM image obtained on an Ar^+ ion beam irradiated InP(100) surface; (b) The same image after image "Flatten" processing; (c) 2D Fourier transform spectrum of (b); (d) Inversion of (c) after selectively removing the noise components in (c).

Tip jumps and incompletely suppressed high frequency noise are other sources of instrumental artefacts which can be eliminated from AFM images with simple filters. High pass and low pass filters are used to multiply each pixel by a matrix that weights

nearby pixels and averages the values. As a result, the measured heights of features over a single pixel are reduced.

2-D Fourier transform can be used to eliminate intermediate frequency electrical noise from AFM data. By calculating a 2-D Fourier transform of the data and selecting the data to be retained or the noise to be removed, an inverse transformation reveals clear structures if there are any periodic structures in the otherwise non-2D Fourier transformed samples. However, there is a risk to image content being simultaneously removed, which unknowingly introduces artefacts into the processed data. Hence, great caution must be taken in applying these filters. An example of the effect of 2-D Fourier transform filtering is displayed in Fig 5.8 (d).

In order to keep artefacts of image processing to a minimum, all the AFM images in this thesis hereinafter are processed with "Flatten". Analysis and results are generated from these flattened data. Fourier Transform Spectra are used only to show the structures with periodic components. No further filtering or inversion of the spectra was performed.

5.1.4.2.2 Quantitative Analysis of Surface Structure from AFM Images

Qúantifying aspects of surface structure involved in this thesis are confined to feature height, feature width or diameter, feature length, and where appropriate, periodicity or wavelength.

5.1.4.2.2.1 Analysis of Feature Height

The Digital Instruments' Multi-Mode SPM offers many off-line commands for quantitative analysis of features on an image. The "*Average Grain Size*" command can be used to determine average height of selected features or the entire area of an AFM image. It analyzes larger numbers of grains and grain groups by making calculations based on two thresholds. One threshold contains the maximum number of grains, and the other is the maximum surface area (above a user-defined threshold plane). A histogram of grain size can be produced and used to identify specific grains. The mean size and diameter, total number of peaks, and the total number of grains are calculated and

displayed. Grains may be analyzed singly or in aggregates. "Grains," as used here, are defined in terms of conjoined pixels having a height above or below a given threshold height. Fig 5.9 is an example of analyzing feature height using the "Grain Size Average" command.

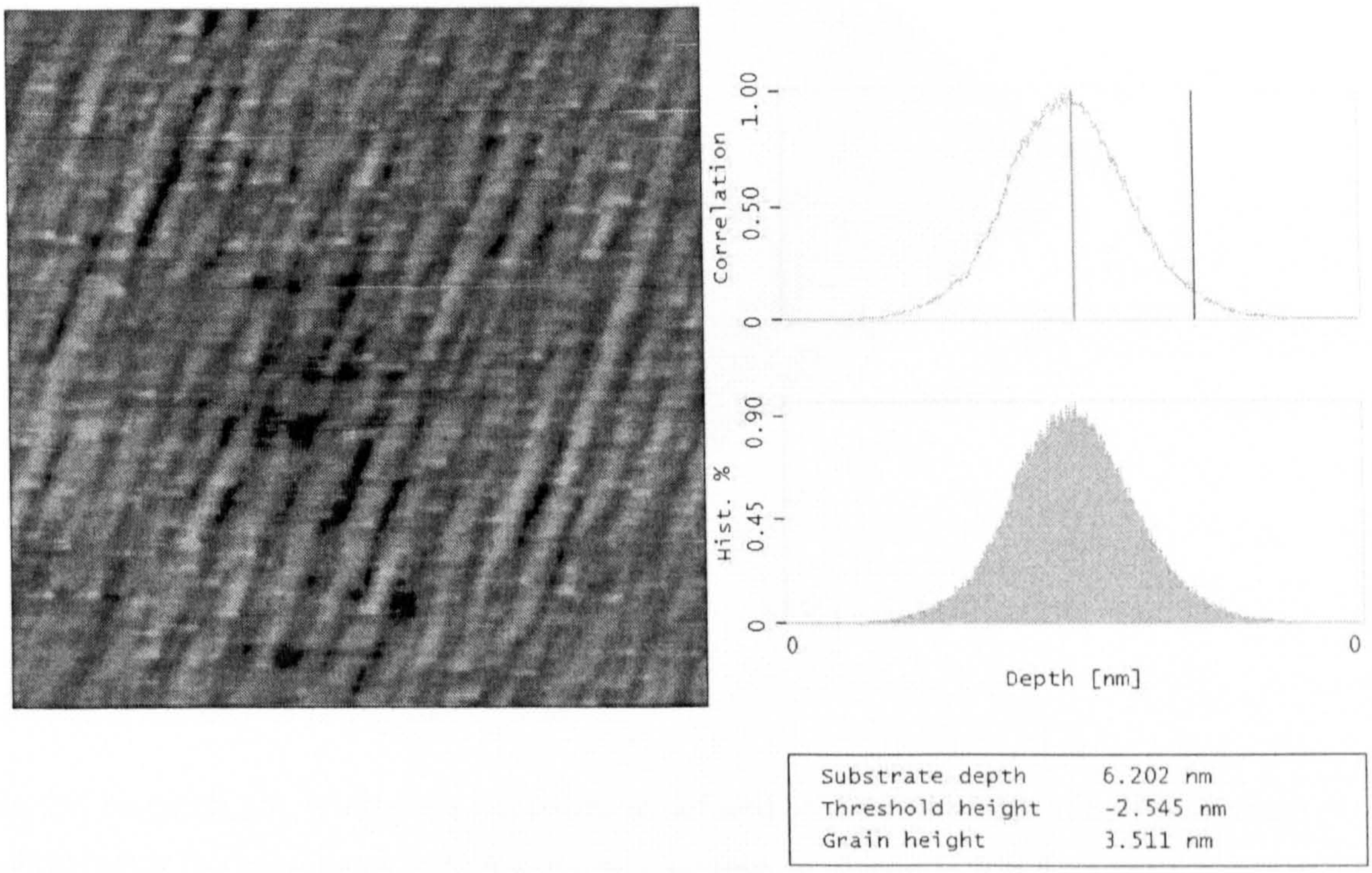

Fig 5.9 AFM image after applying "Grain Size Average" command to Fig 5.8 (b).

At the upper right corner of Fig 5.9 is the pixel height correlation diagram of the top-view image on the left. In normal mode, the green slider determines the maximum threshold height of the grains. As the red slider is moved to the right, sample areas below the threshold are removed from the image (black), leaving only the raised area of the grains behind. Statistics for the whole AFM image are displayed in the box at the bottom right of Fig 5.9, from which average feature height is read as "Grain height".

"Grain Size Average" is an ideal command in rendering height data from images overwhelmingly composed of grains, particles, islands or cones. However, there may be a debate about the justification of using "Grain Size Average" command to generate height data of wire-like structures as shown in Fig 5.10. As an example, Fig 5.10 shows arrays of wires with grains or cones superimposed on top of wires. Actually, a long wire

with superimposed cones as a whole is recognized as a long grain upon execution of the "Grain Size Average" command. This justifies the application of the command.

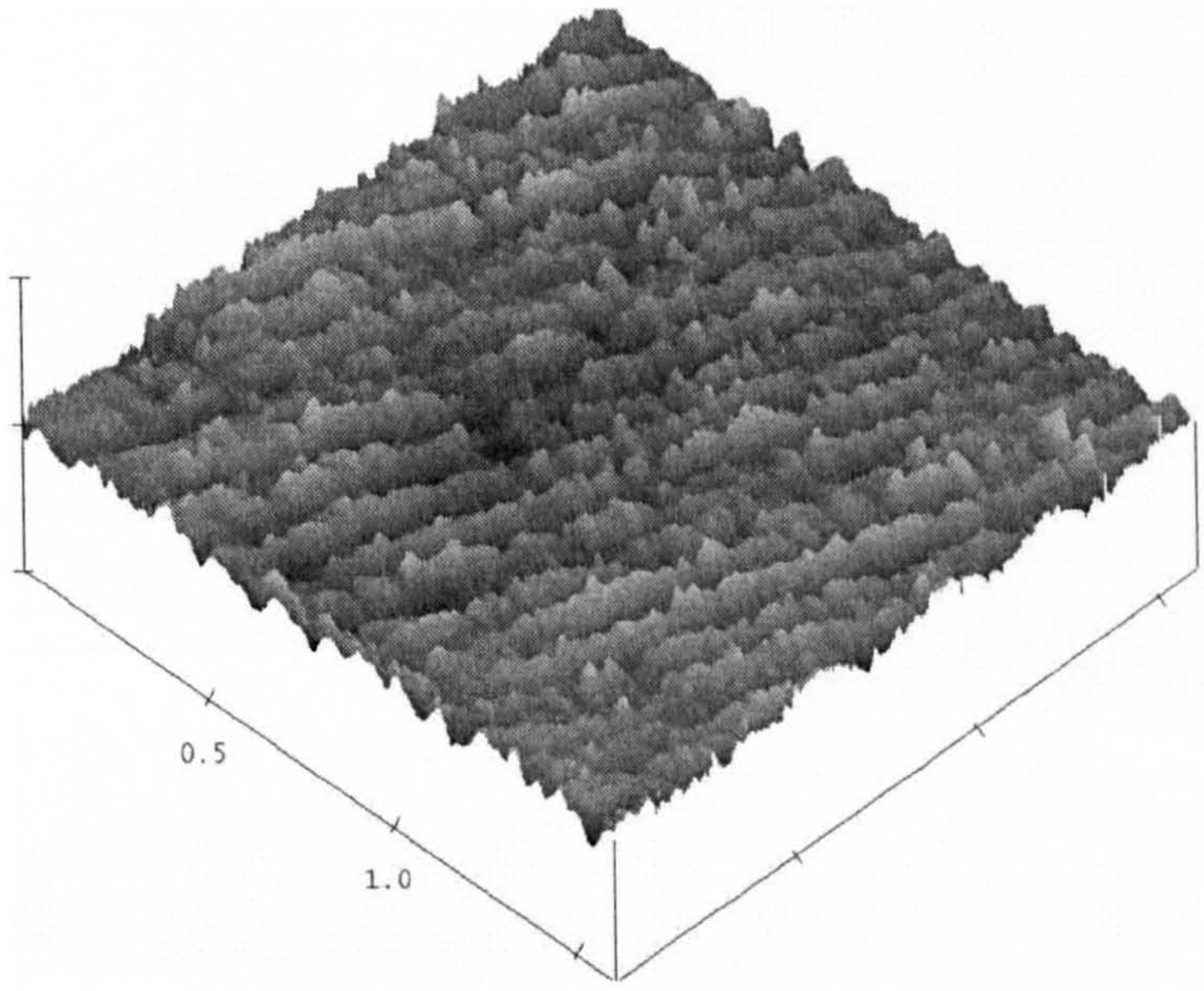

Fig 5.10 Three-dimensional view of AFM image in Fig 5.8 (b)

5.1.4.2.2.2 Analysis of Feature Width

In this research, the width of a nanowire is defined as the full width at half maximum (FWHM) if the wire has a bell-shape cross section as shown in Fig 5.11 (a). Measurement of wire-width was based on the cross-section analysis of AFM images illustrated in Fig 5.11 (b). Fig 5.11 (c) shows the line profile corresponding to the cross section selected in Fig 5.11 (b). The measured wire-width data are displayed in the data box of the interface in which the horizontal distance between the two locations selected by the two arrows in Fig 5.11 (a) and (b) gives the wire width of the measurement.

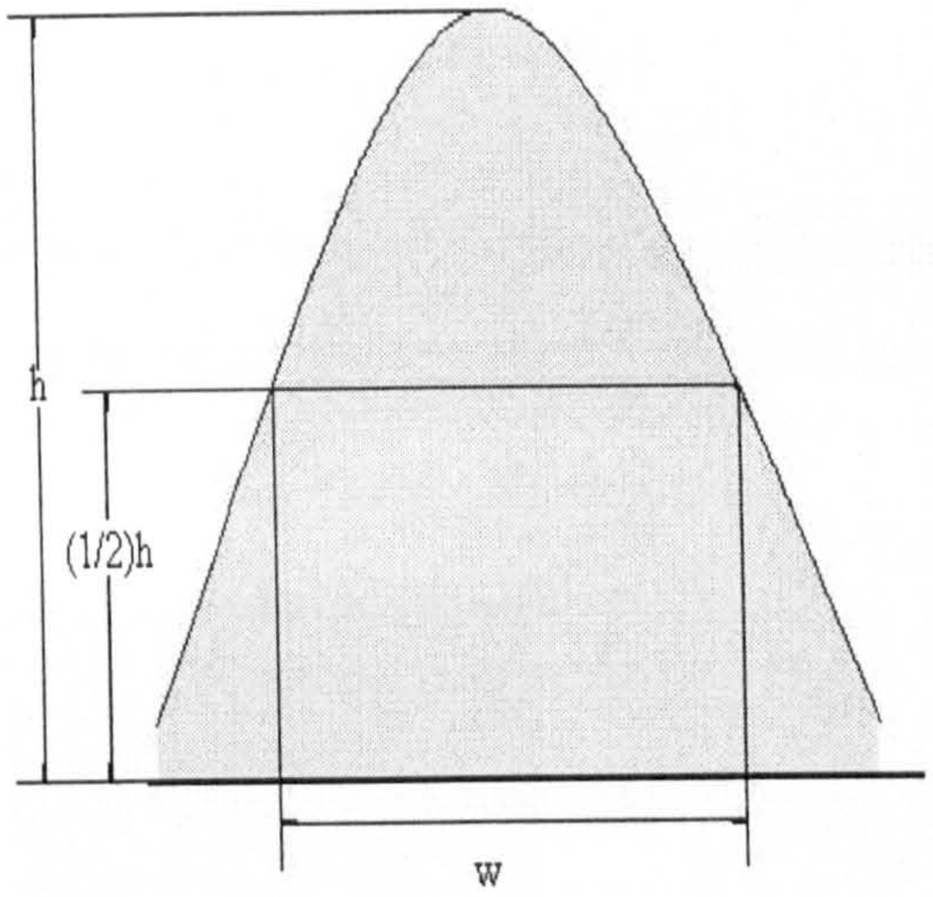

(a)

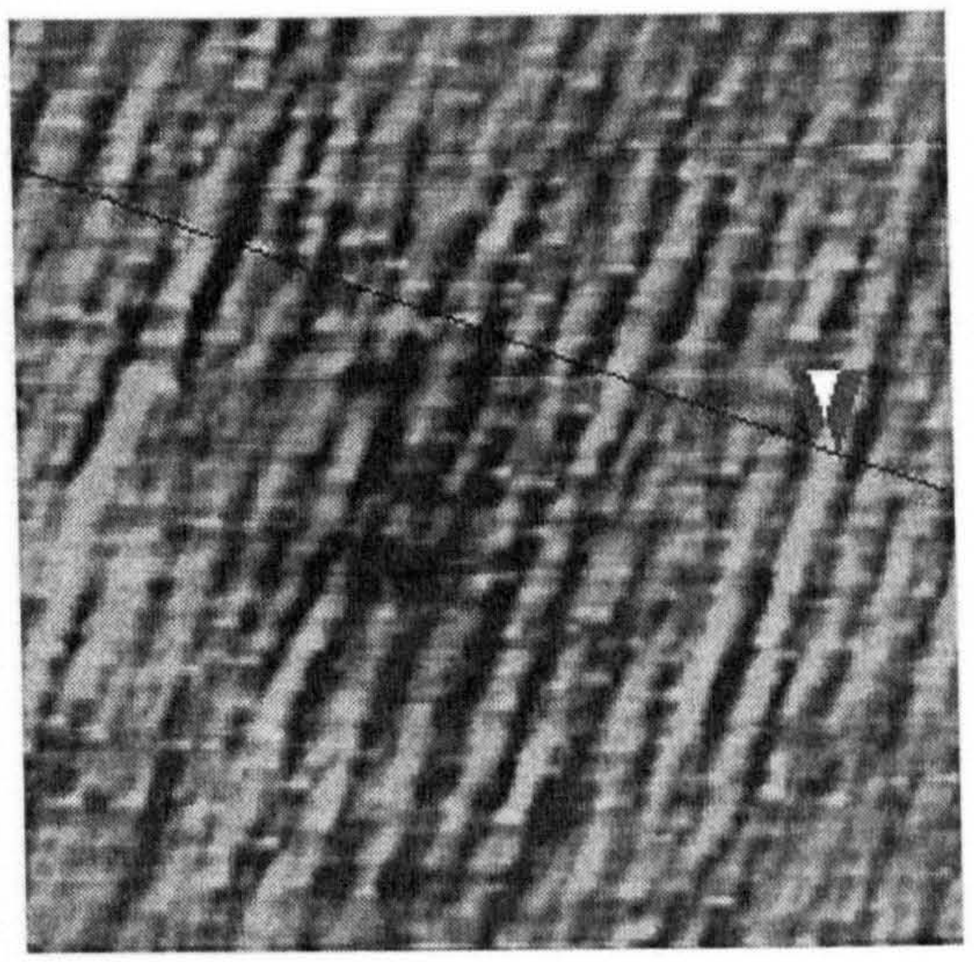

(b)

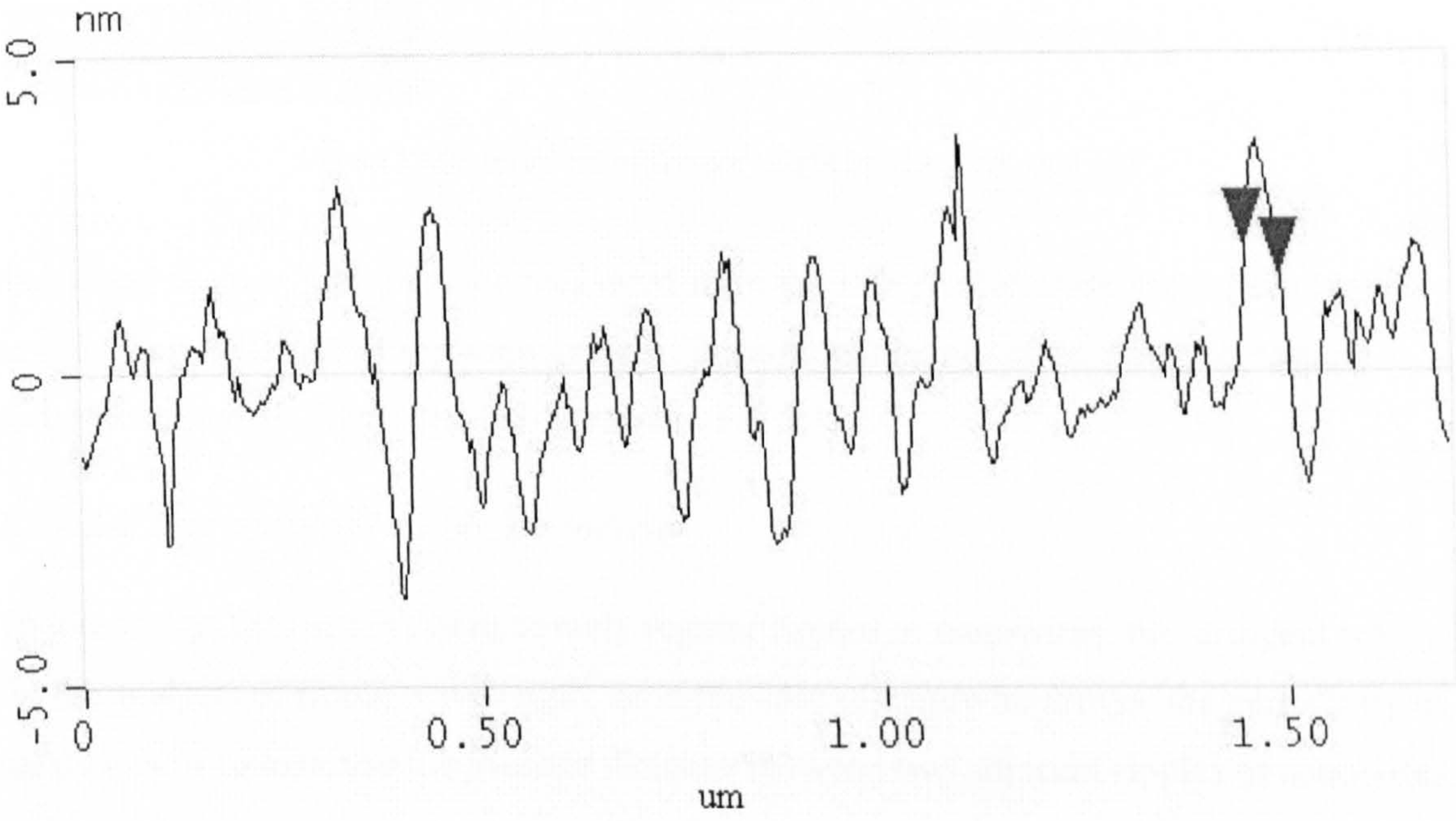

(c)

Fig 5.11 Cross-section analysis of wire width: (a) Definition of the width of nanowires with bell-shape cross-sections; (b) Cross-section analysis of wire width for the same image of Fig 5.11 (b); (c) Line- profile of the cross-section selected in Fig 5. 11 (b)

Ten measurements across different wires along one cross-section gives the average wire-width for that single cross-section, and the average of ten cross-sections at different locations gives the average wire-width of the entire image. The final average wire-width

for a sample is obtained from the average results of five to ten sets of images acquired at different locations on the sample.

In addition to the wire-width analysis, section-analysis offers a complementary tool for height analysis by using the "Average Grain Size" command. Fig 5.12 shows that

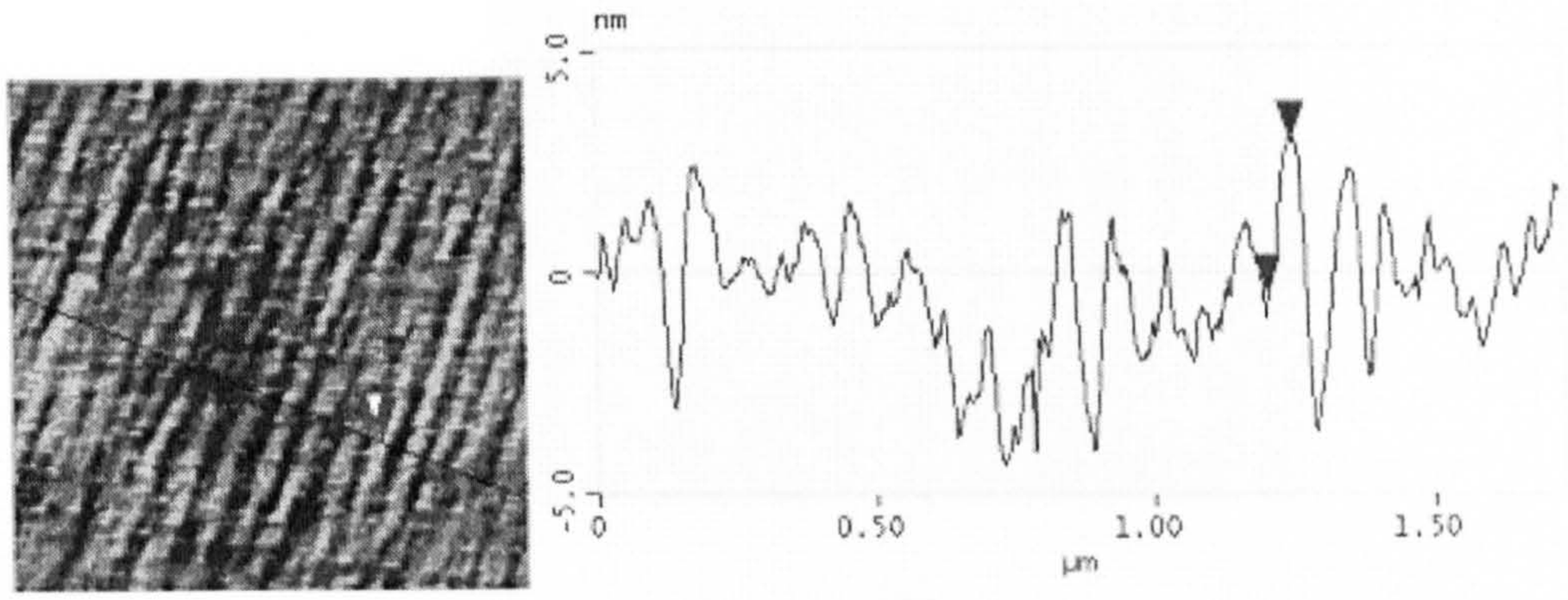

Fig 5.12 Measurement of feature height by "Section Analysis"

the typical feature height can be measured from the line profile cross-sectioned across any location on an AFM top-view image. Wire-height is measured from the vertical distance corresponding to the two arrows in Fig 5.12.

5.1.4.2.2.3 Analysis of Feature Periodicity

Theoretically, for features of extremely regular ripples or nanowires, the stringent way for the analysis of ripple wavelength, or in the case of nanowire arrays, the periodicity of nanowires, is to measure the average distance between two adjacent ripples or nanowires and take the average over the values measured along the entire image. However, in the case of this study, quasi-ripples and broken ripples were found in many AFM micrographs, and the theoretical method may generate results with primary wavelength hidden among the average. As a practical solution, the feature periodicity measurements were performed by using section analysis (Fig 5.13). A quotient of an overall distance of a number of parallel ripples or nanowires divided by their number gives the average periodicity of the features selected. The average of the results of ten measurements at different locations in one AFM image gives the average periodicity of the entire image.

The final average periodicity for a sample is obtained from the average results of five to ten sets of images acquired at different locations on the sample.

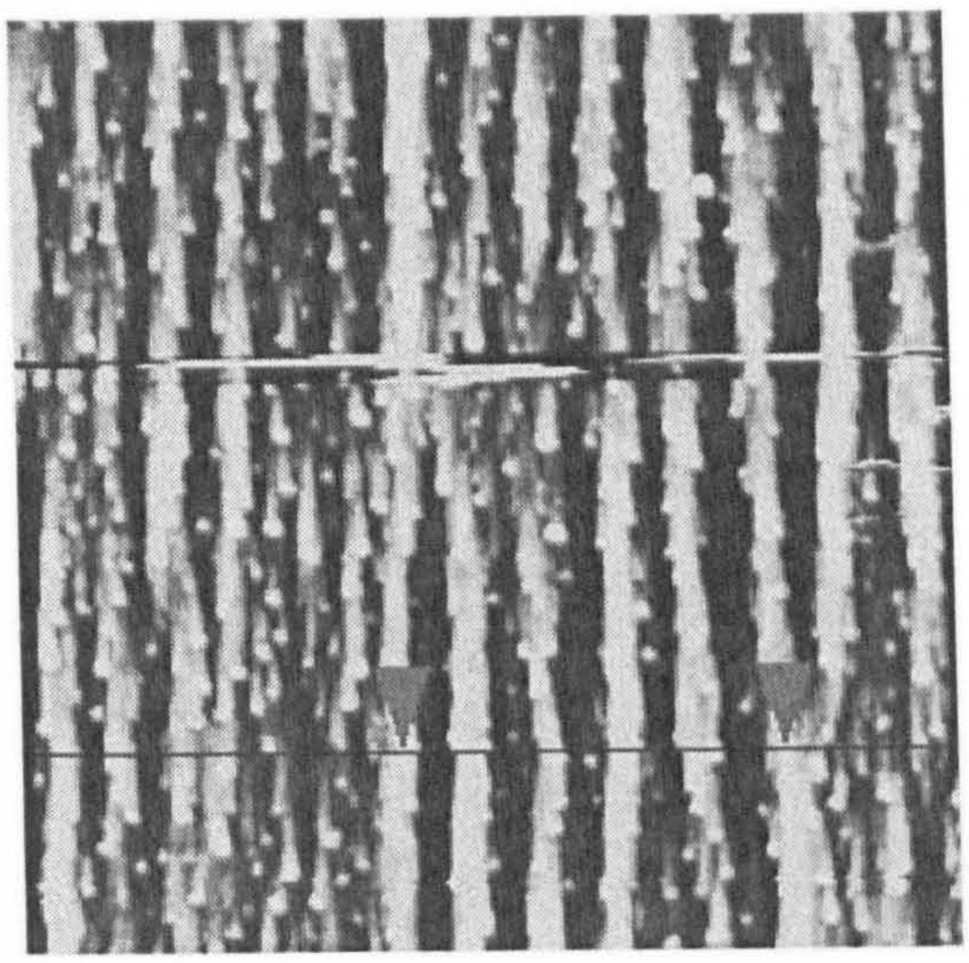

(a)

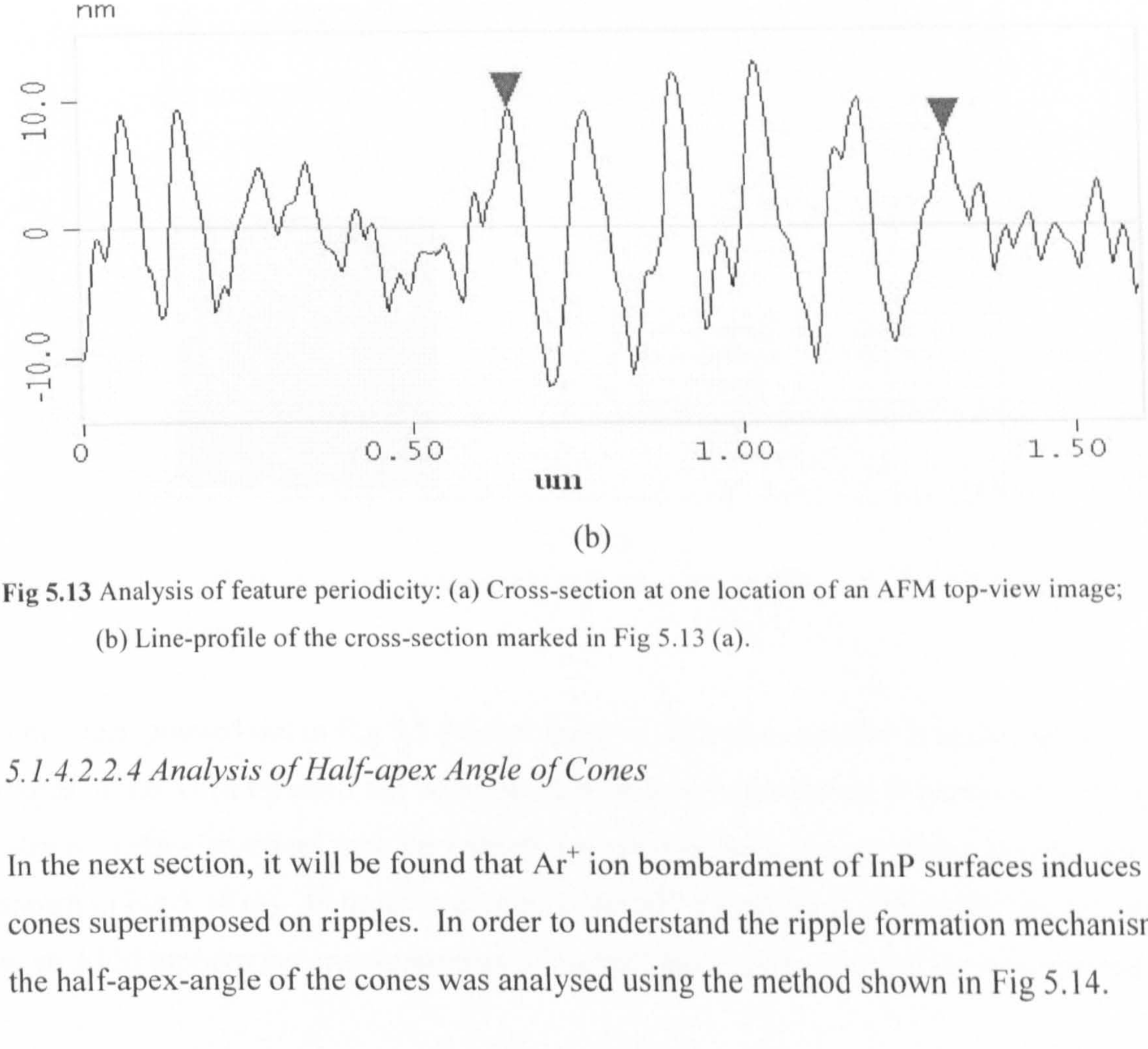

(b)

Fig 5.13 Analysis of feature periodicity: (a) Cross-section at one location of an AFM top-view image; (b) Line-profile of the cross-section marked in Fig 5.13 (a).

5.1.4.2.2.4 Analysis of Half-apex Angle of Cones

In the next section, it will be found that Ar^+ ion bombardment of InP surfaces induces cones superimposed on ripples. In order to understand the ripple formation mechanism, the half-apex-angle of the cones was analysed using the method shown in Fig 5.14.

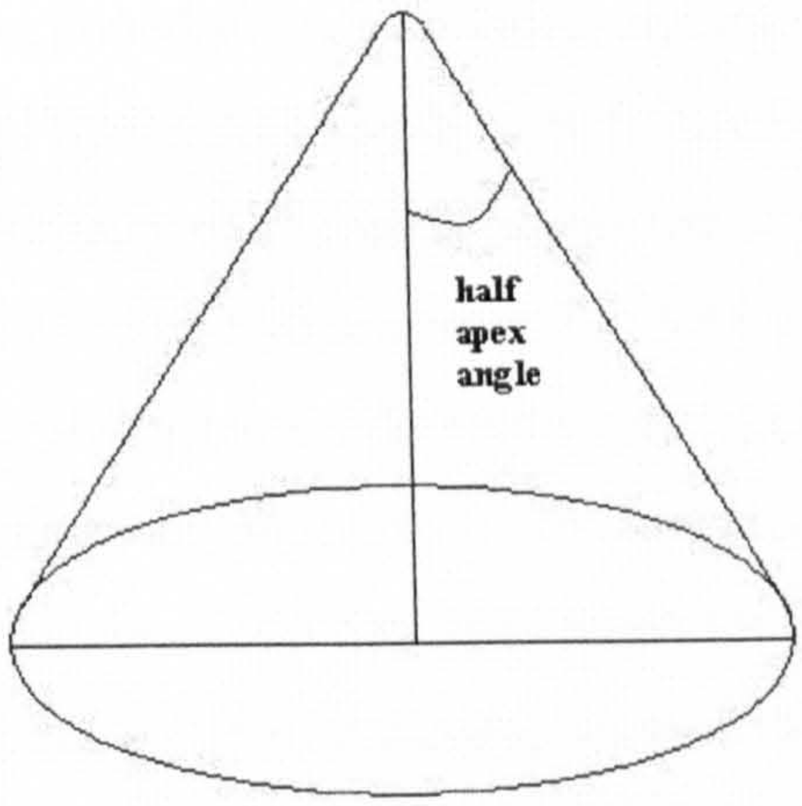

(a)

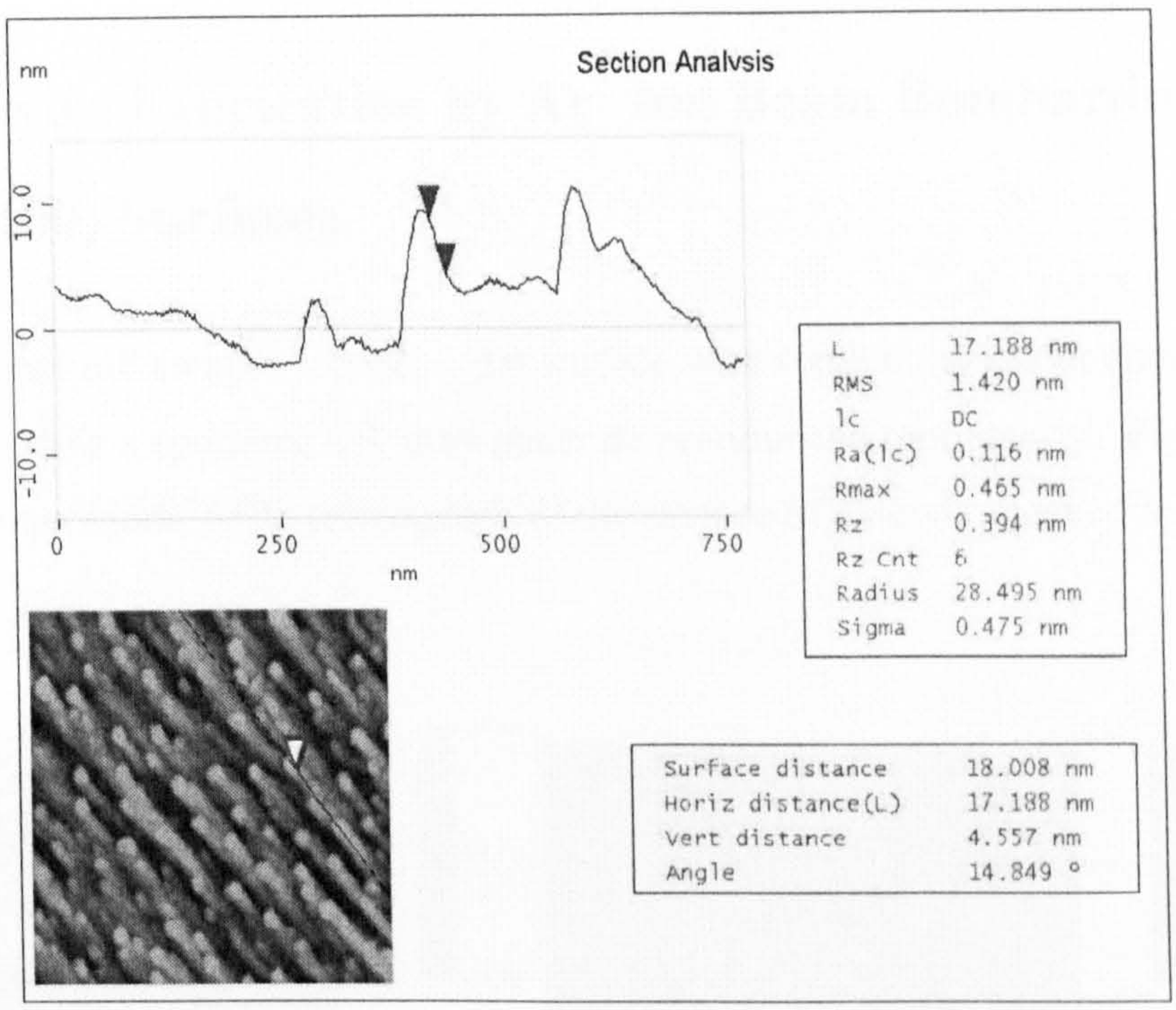

(b)

Fig 5.14 Analysis of half-apex-angle of cones: (a). Definition of half-apex-angle; (b). AFM analysis of half-apex-angle.

It has been pointed out in Fig 5.5 (c) that features with sizes smaller than the curvature radius of the AFM tips will not be resolved if they are sandwiched in between two bigger islands. Likewise, cones with very sharp tips may generate images with a rounded tip, as shown in Fig 5.14 (a). In order to eliminate the AFM tip convolution to the tips of cones in an AFM topography, measurements of the half apex angle of cones were performed at

two locations on the cross-sectioned surface of cones, and the values of half-apex angle were automatically generated by the AFM analysis software by trigonometry. The algorithm is based on the geometry of a triangle composed of three arms: one arm is defined by two locations (marked by two arrows in Fig 5.14 b) on the cross-sectioned surface of the cone; the other two arms are defined by the horizontal and vertical (parallel to the cone axis) coordinates corresponding to the two locations. Fig 5.14 (b) shows an example of an AFM section analysis of a half apex angle for a cone marked with two arrows. The upper arrow is off the tip of the cone, because the cone tip is rounded. The result is shown as "Angle" in the bottom right box in Fig 5.14 (b).

5.2 Nanowire Fabrication by Ar^+ Ion Beam Bombardment on InP (100) Surfaces

A non-sputtered InP sample renders a flat surface with some noise under an atomic force microscope, while a sputtered InP may generate pronounced topography. Fig 5.15 (a) is a typical contact mode AFM micrograph of the surface of a newly cleaved InP (100) sample.

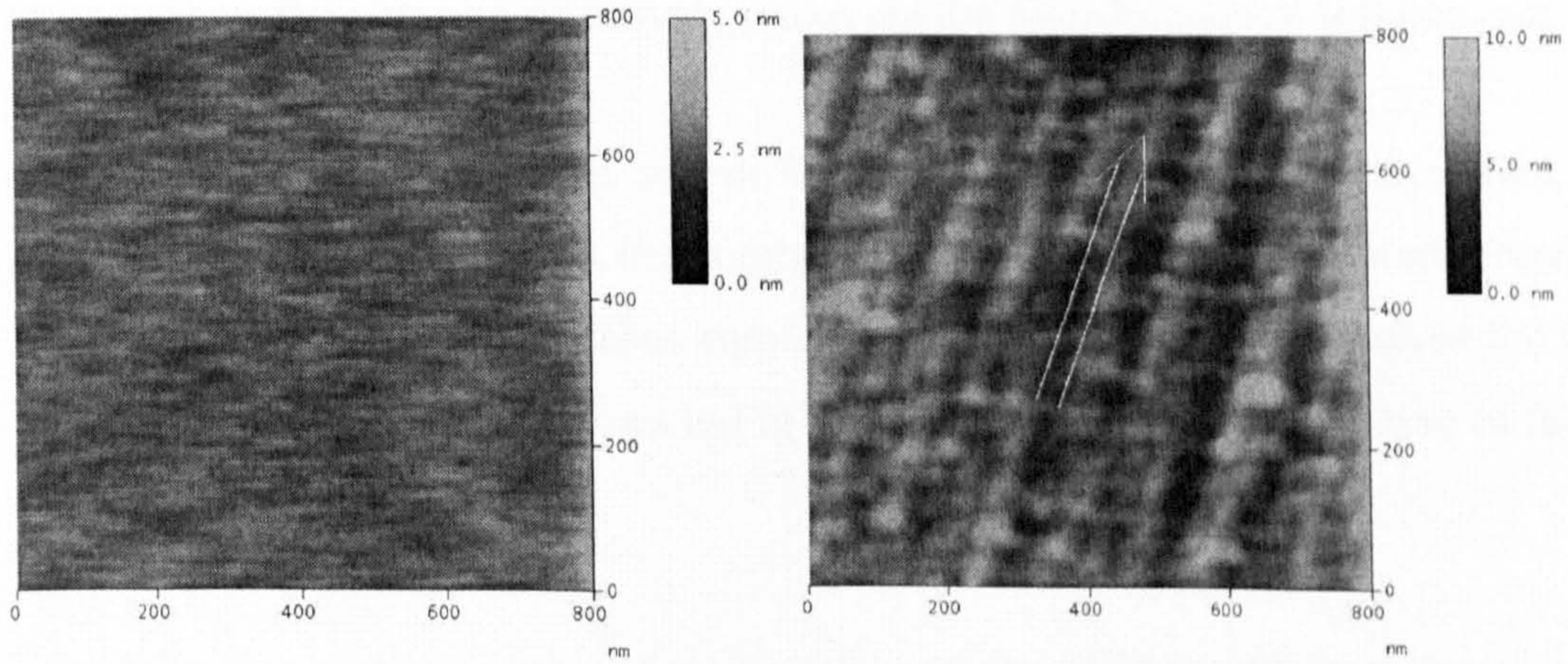

(a) (b)

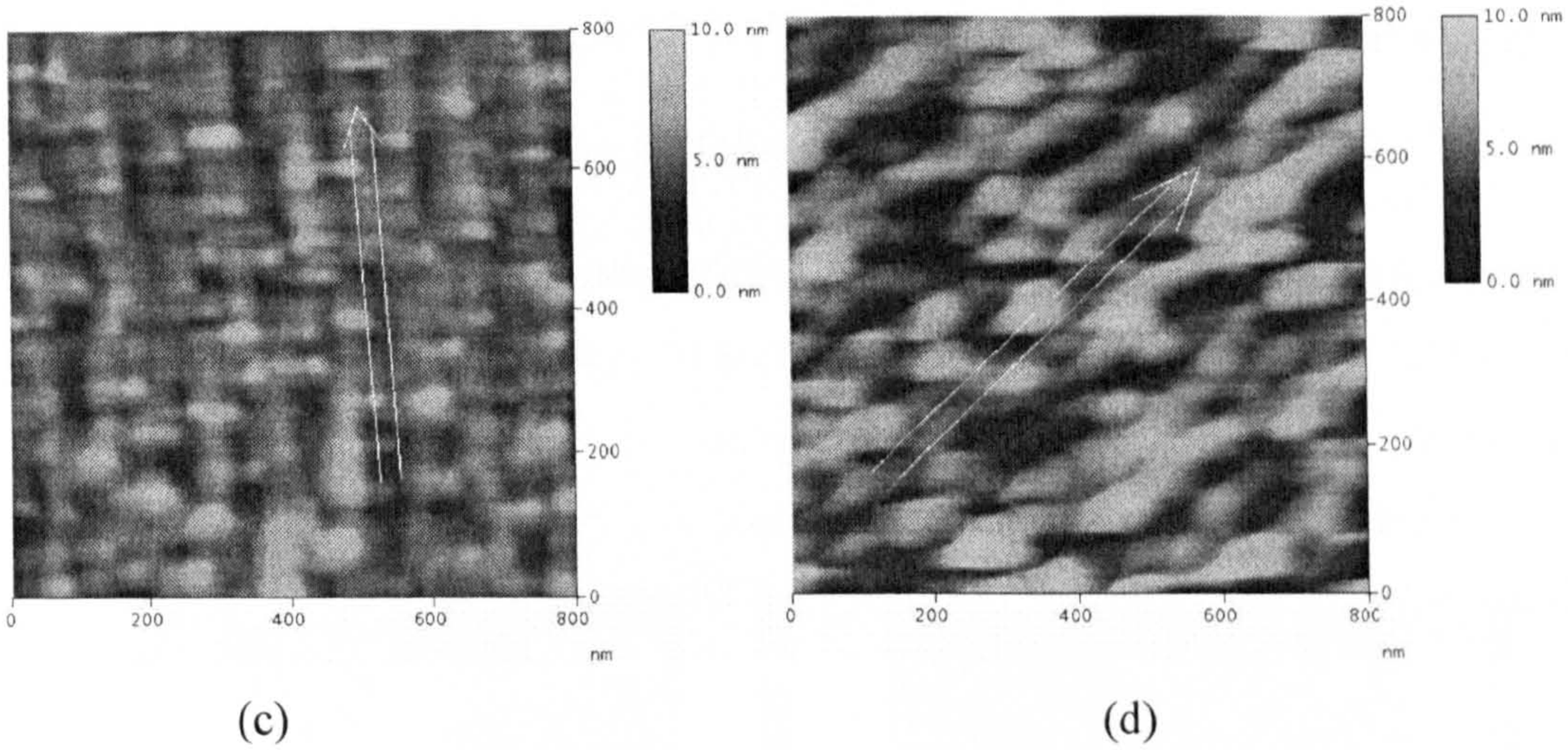

Fig 5.15 AFM micrograph of: (a) the surface of a newly cleaved InP (100) sample; (b) a sample irradiated along the direction [0,-1,-1]; (c) a sample irradiated along the direction perpendicular to the [0, -1, -1] direction; (d) a sample irradiated along the direction at 45° to [0, -1, -1]. Irradiation parameters: E =2 keV, $\theta = 72°$, Ds = 5.2×10^{16} cm^{-2}.

The image shows that the fine structure of the surface of a non-irradiated InP sample is actually flat. The quasi-wavy structure is actually high-frequency instrumental noise with average amplitude of 0.6 nanometers which is present in most of the AFM micrographs of this research. This noise can be filtered by applying two-dimensional Fourier Transform to the data and selectively removing the high-frequency components.

After Ar^+ ion beam irradiation with different ion energies, ion current densities, ion doses, and ion incident angles, the bombarded samples exhibited different morphologies as probed by AFM. In most cases, ripples were found along the azimuth of the ion beam direction, as shown by the arrows in Fig 5.15 (b), (c), and (d.), irrespective of the direction in the crystal plane.

The following sections of this chapter enumerate the AFM results from these series of experiments. These results are compared with the models described in Chapter 3, and a new model is proposed to account for the physical mechanism of the formation of these ripples and nanowires.

5.2.1 Morphology Changes of Ar^+ Ion Beam Irradiated InP (100) Surfaces with Different Irradiation Energy

According to the theory of sputtering introduced in Chapter 3, a minimum energy is needed to break the bond between In and P so that sputter induced topography can be initiated. As a tentative attempt to find out this crucial energy, various bombarding energies between 1 keV and 4.5 keV were tried. The samples were irradiated

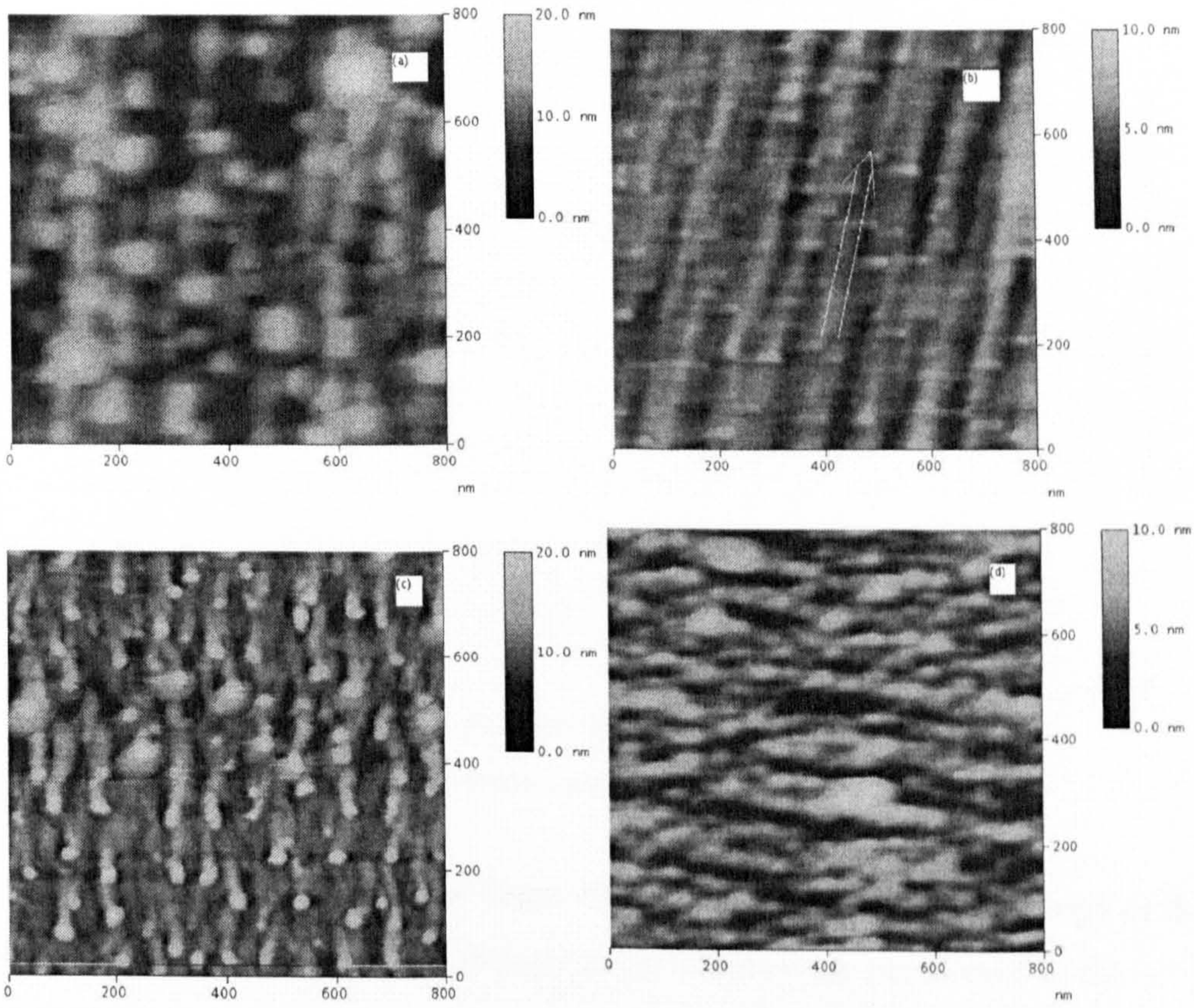

Fig 5.16 AFM micrographs of InP (100) surfaces irradiated by Ar^+ ion beam at 72° incident angle (to surface normal) at a dose of 5.2×10^{16} cm^{-2} with ion irradiation energies of (a) 1 keV, (b) 2 keV, (c) 3.5 keV, and (d) 4.5 keV.

at a fixed dose of 5.2×10^{16} cm^{-2} at 72° incident angle at room temperature. The morphology of the irradiated samples was examined by Digital Instruments' Multi-Mode SPM running in AFM contact mode in air. Fig 5.16 shows the results from this series of experiments.

Distinct ripples can be found from Fig 5.16 (b), and the corresponding energy of 2 keV was chosen as the irradiation energy for all experiments thereafter.

At this stage, it was rather difficult to decide whether the energy or the current density was the dominant factor in the generation of the observed topography. The irradiation current density was observed to increase with energy of the ion beams (Fig 5.17).

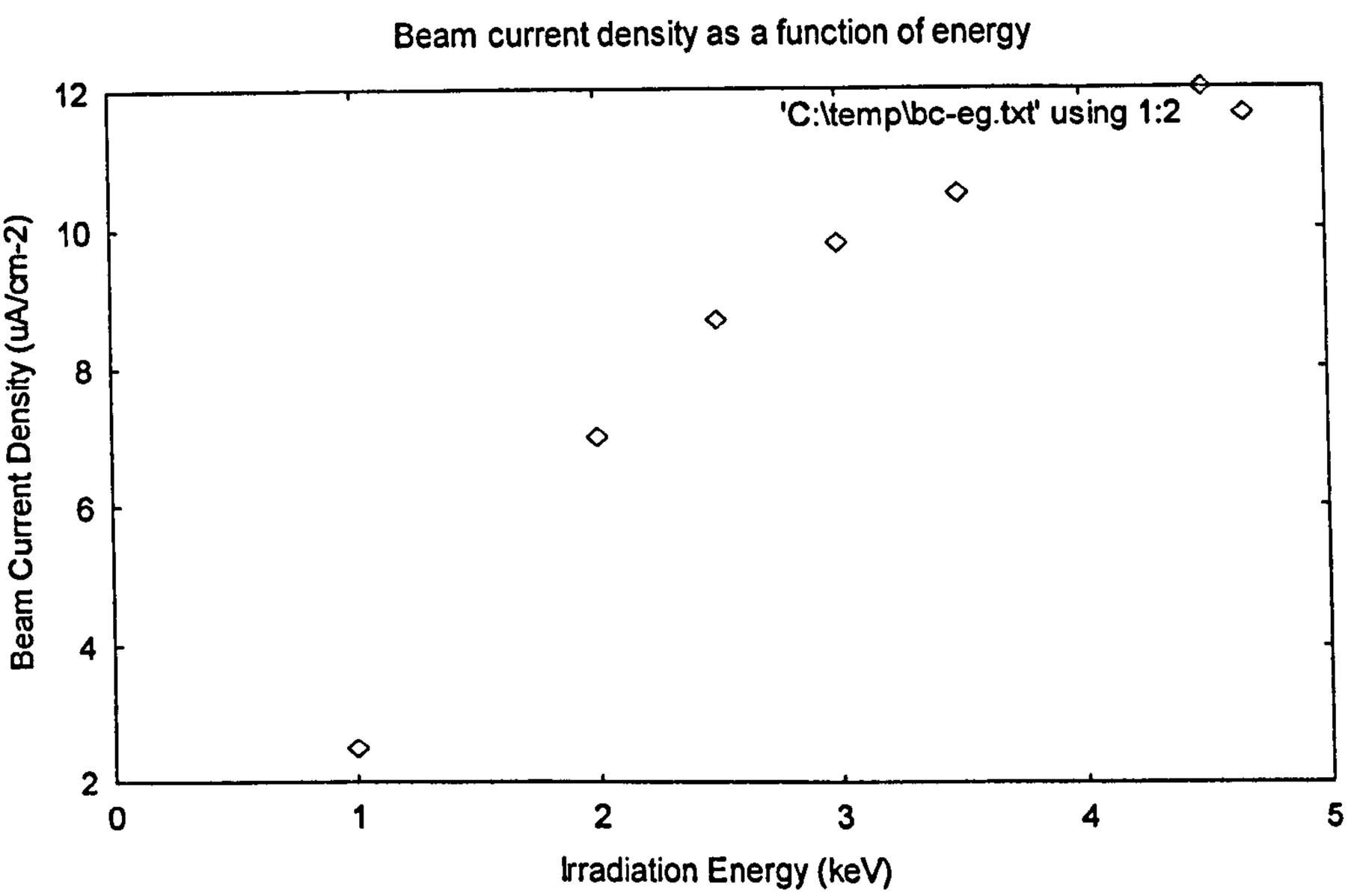

Fig 5.17 Dependence of ion beam current density upon irradiation energy

In order to investigate the effect of ion beam current density on the morphology of the Ar^+ irradiated InP (100) surfaces, subsequent experiments were performed in the following sections.

5.2.2 Morphology Changes with Different Irradiating Ion Current Density

After 2 keV Ar^+ ions bombardment at a grazing incident angle of 72° and with a fixed dose of 5.2×10^{16} cm^{-2} at different ion current densities, ripples were found along the azimuth of the ion beam direction, as marked with arrows in Fig 5.18. A height

distribution graph showing the profile of the feature along the straight line in Fig 5.18 (a) is presented in Fig 5.18 (g).

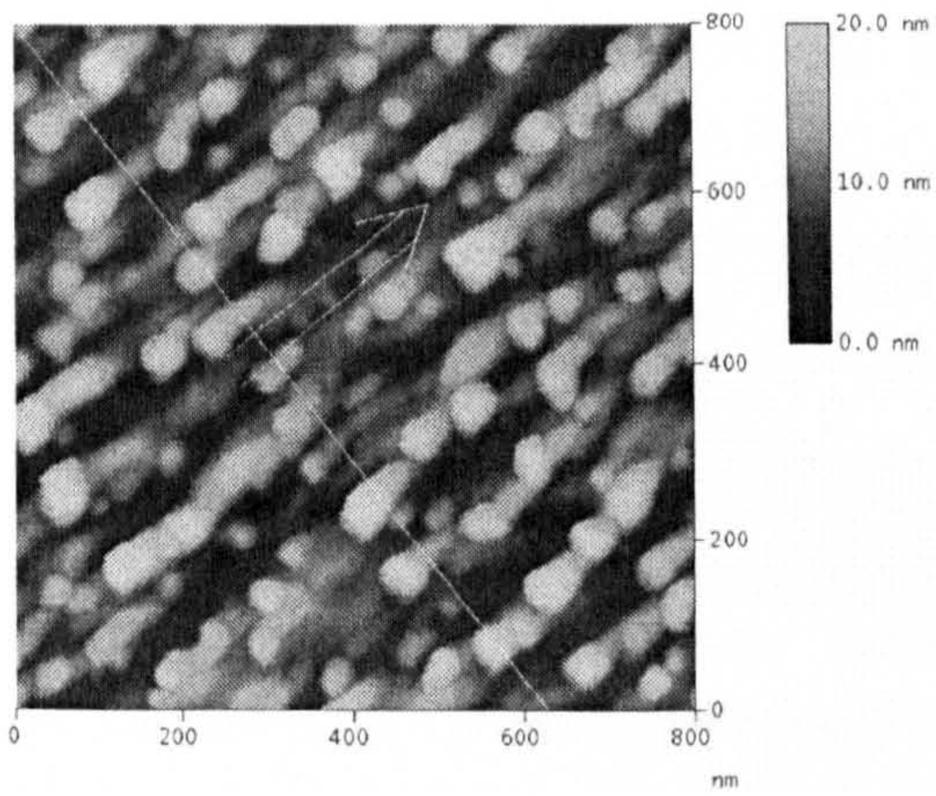

(a)

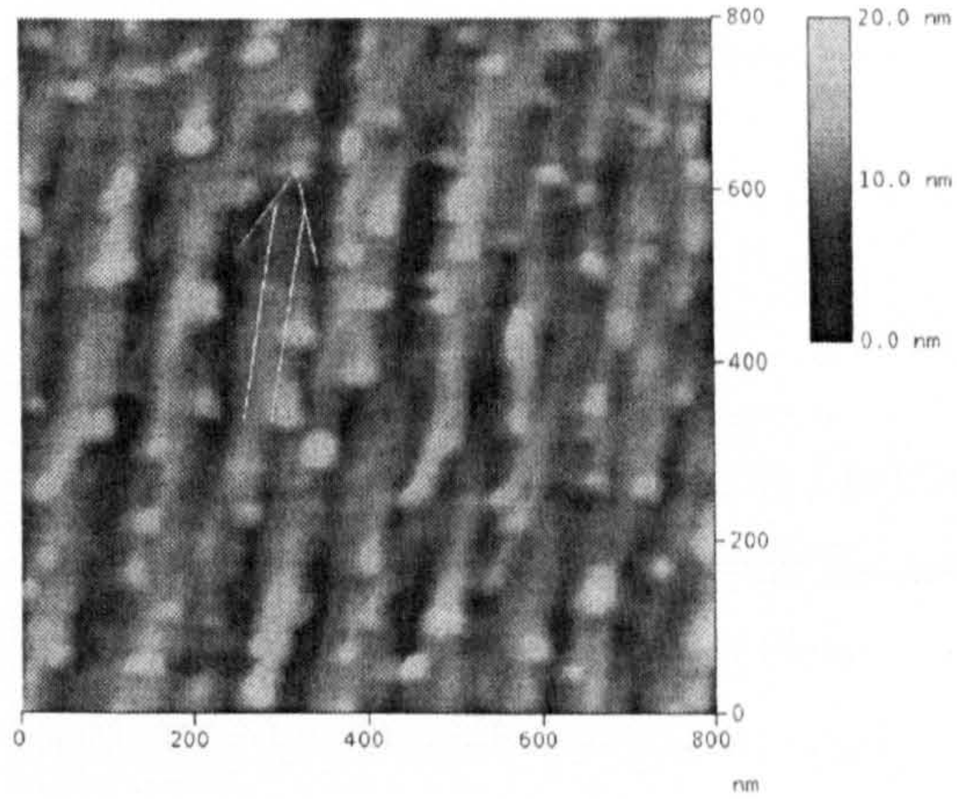

(b)

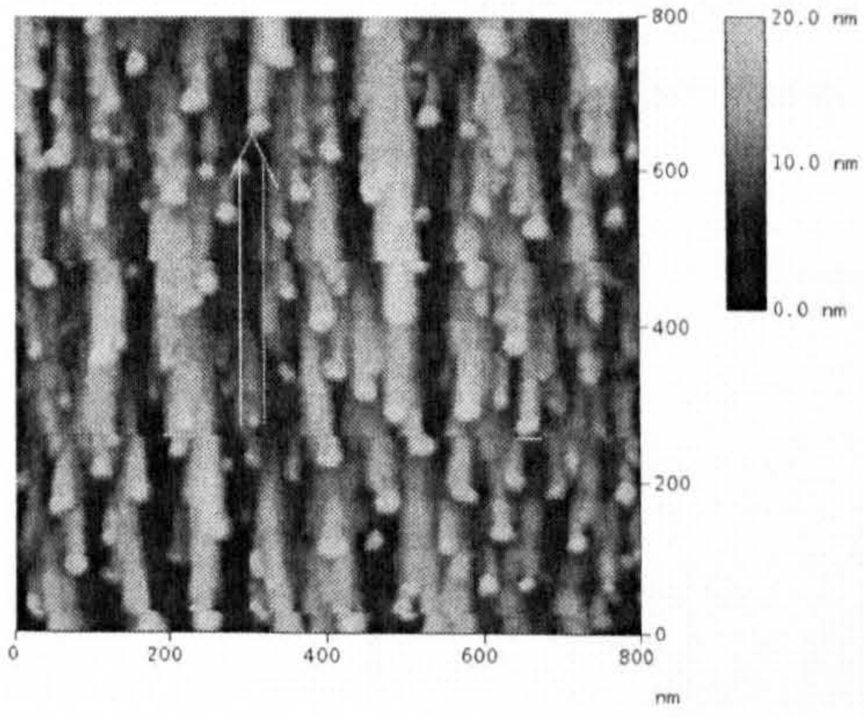

(c)

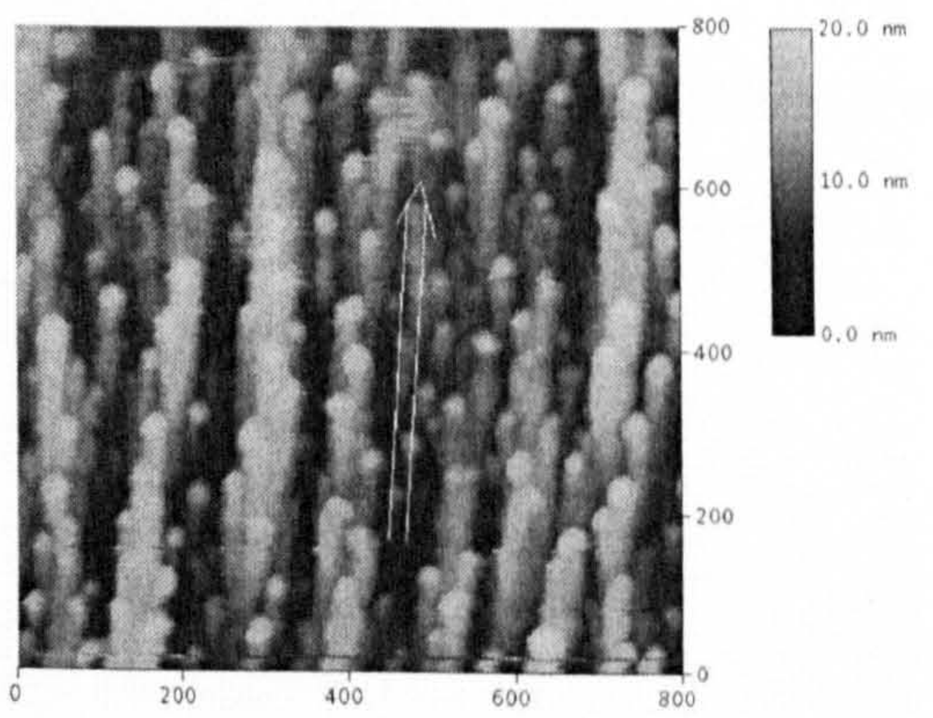

(d)

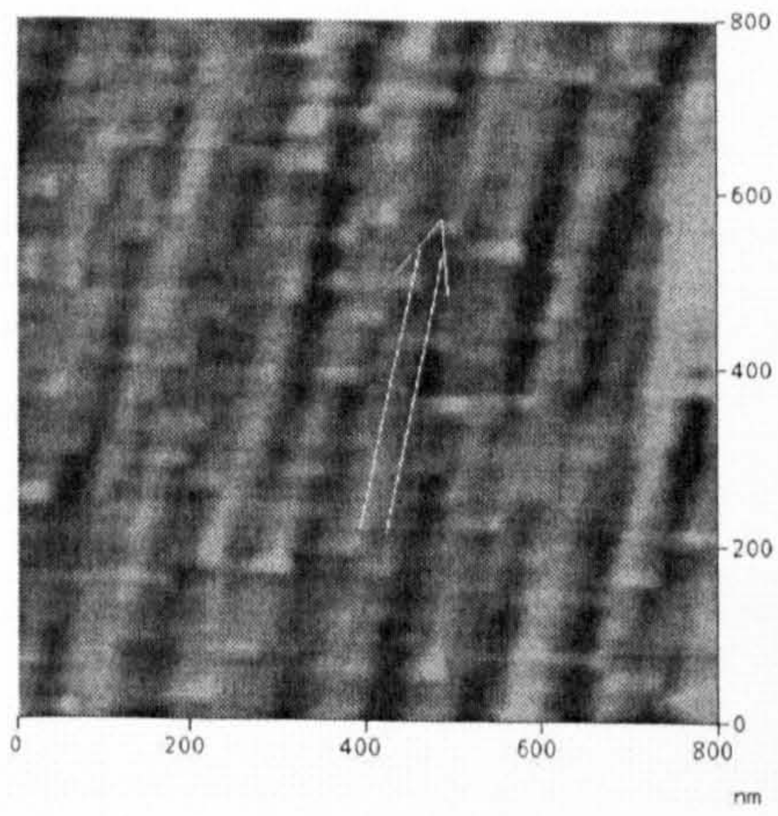

(e)

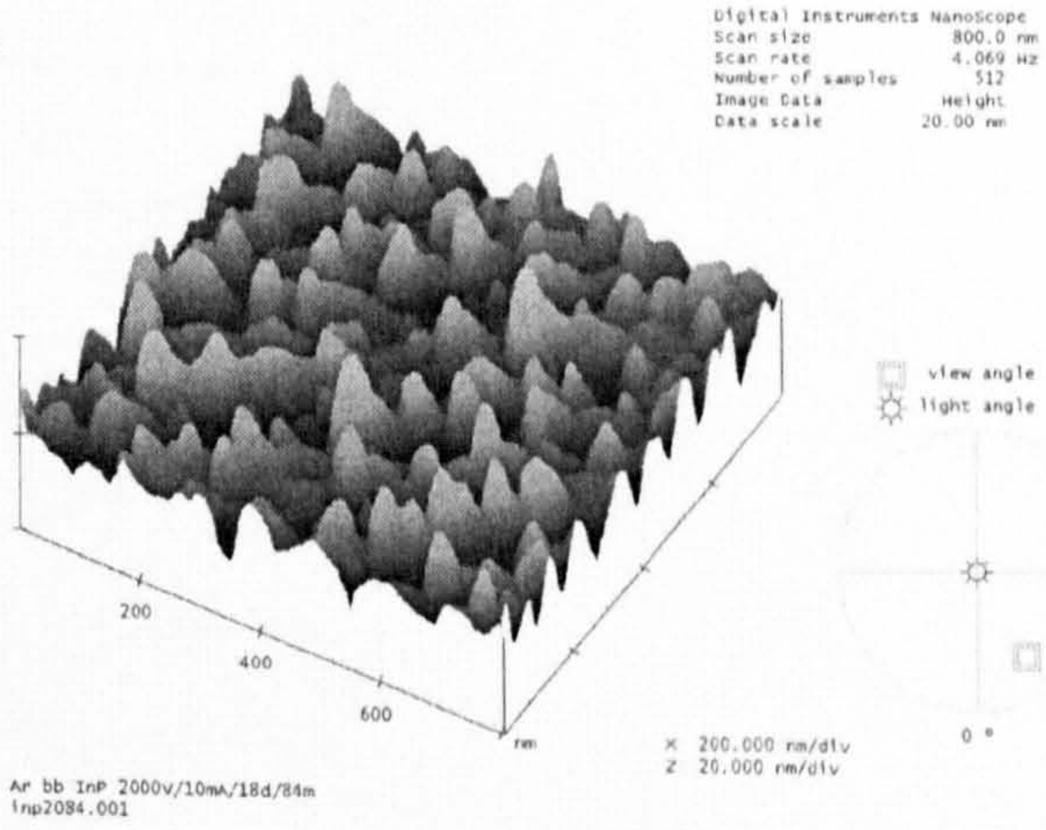

(f)

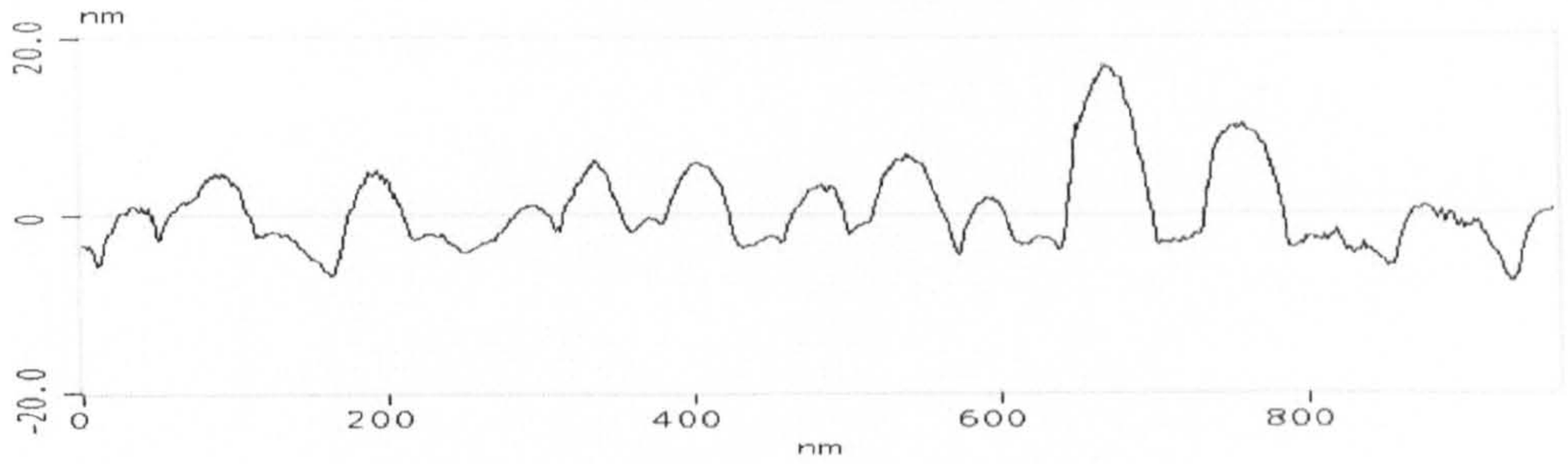

(g)

Fig 5.18 800 nm x 800 nm contact mode AFM micrographs of InP (100) surfaces irradiated by 2 keV Ar^+ ion beam at 72° incident angle (to surface normal) and at a dose of 5.2×10^{16} cm^{-2} with different ion current density: (a) 1.7 $\mu A/cm^2$; (b) 2.7 $\mu A/cm^2$; (c) 3.8 $\mu A/cm^2$; (d) 5.2 $\mu A/cm^2$; (e) 7.0 $\mu A/cm^2$; (f) Three-dimensional view of (a); (g) Line profile of the cross-section alone the line marked in (a).

Quantitative analysis of the data from Fig 5.18 gave rise to statistical results of ripple width, height and wavelength with respect to bombarding ion current density. These are shown in Fig 5.19.

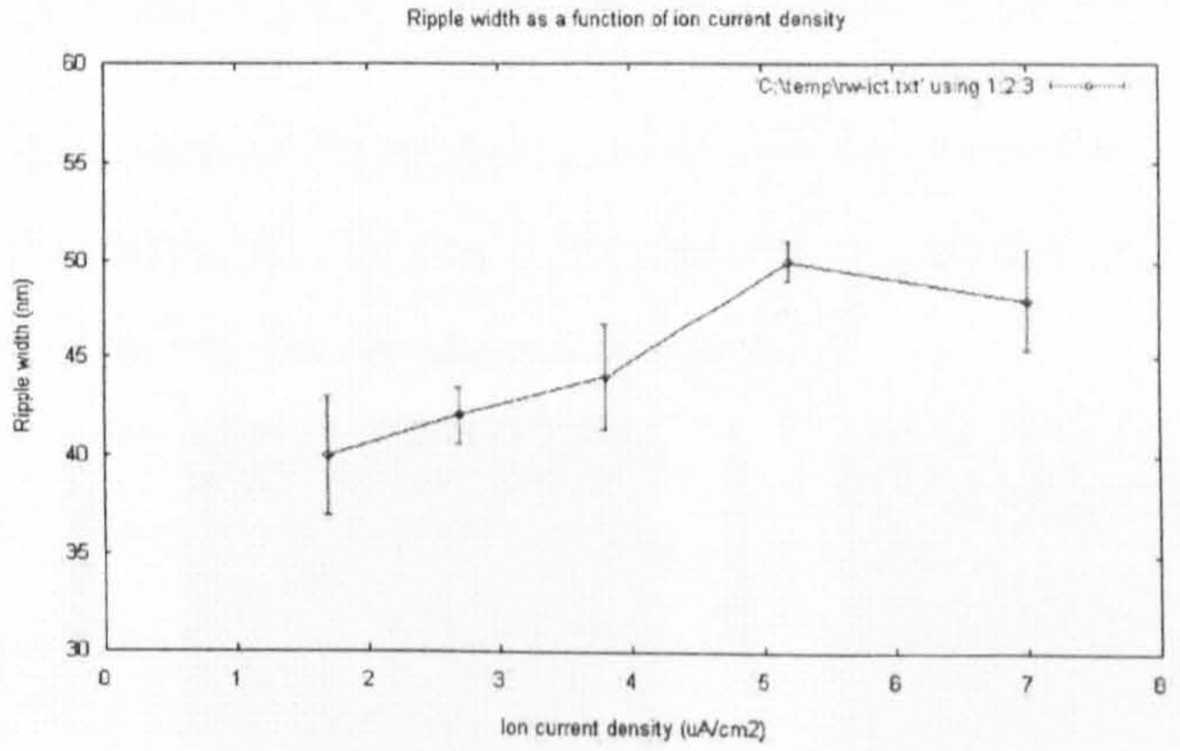

(a)

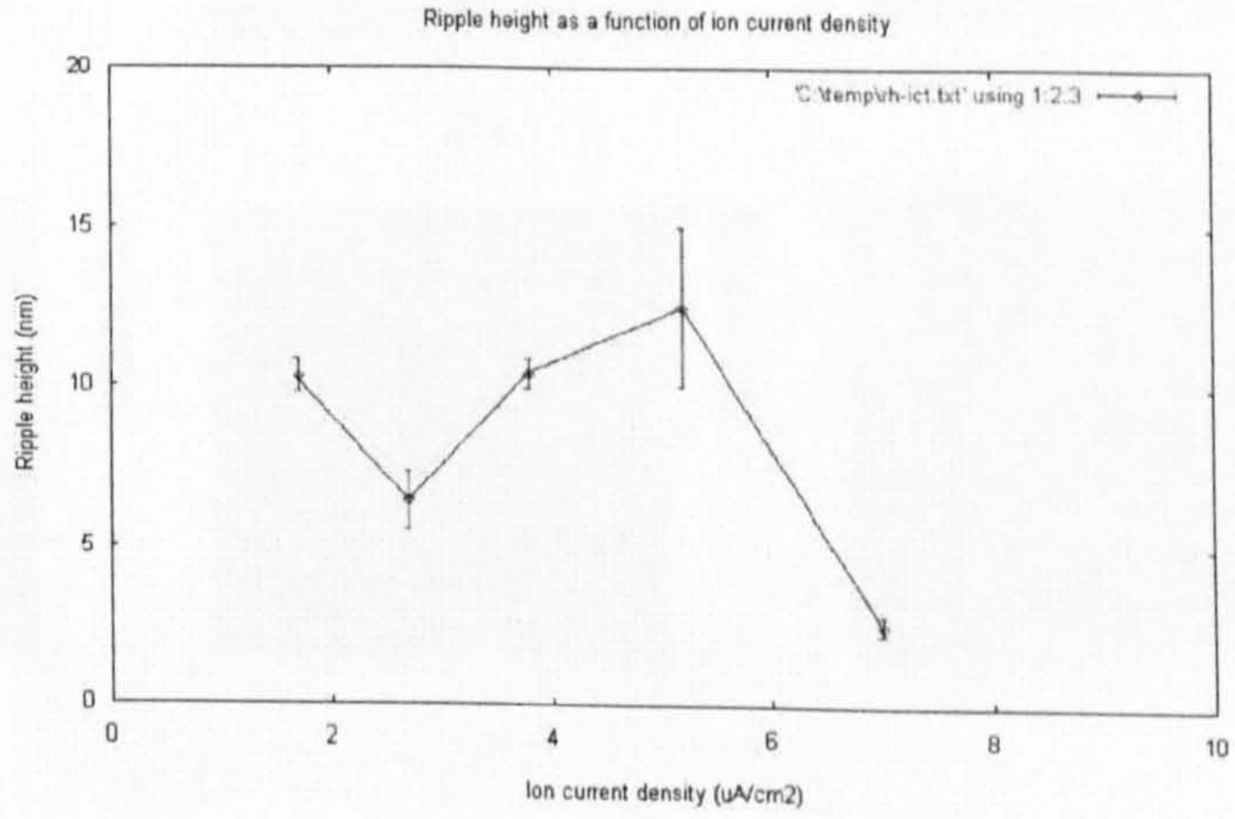

(b)

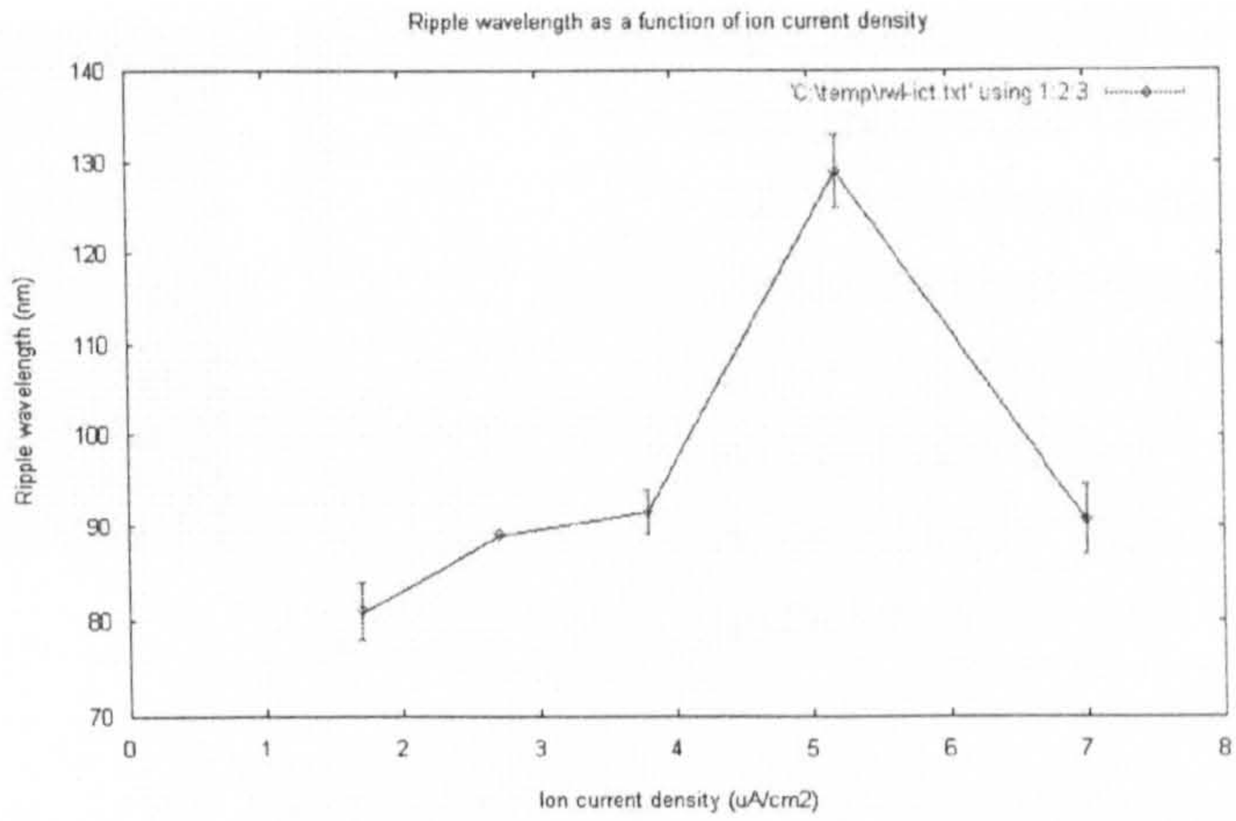

(c)

Fig 5.19 Dependence of ripple width (a), height (b) and wavelength (c) upon bombarding ion current density. Bombarding energy E = 2 keV, ion beam incident angle θ = 72° (to surface normal), ion dose = 5.2×10^{16} cm^{-2}.

The results will be analysed in section 5.3.

5.2.3 Morphology Changes with Different Irradiating Ion Dose

In order to observe the ion dose dependence of morphology change, Ar^+ ion bombardment of InP (100) surfaces was performed at a fixed energy and incident angle with different doses. The results are shown in Fig 5.20.

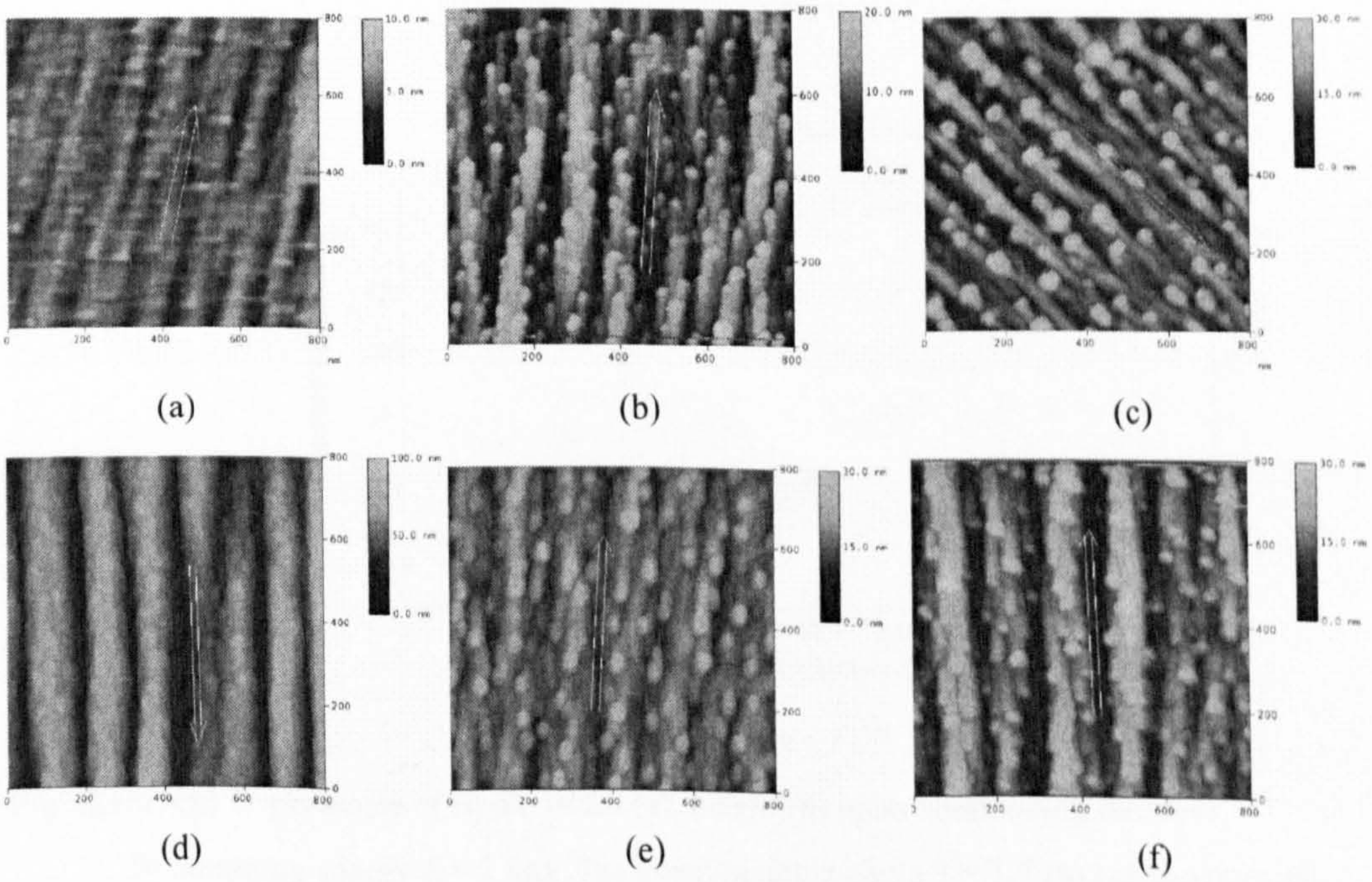

(a) (b) (c)

(d) (e) (f)

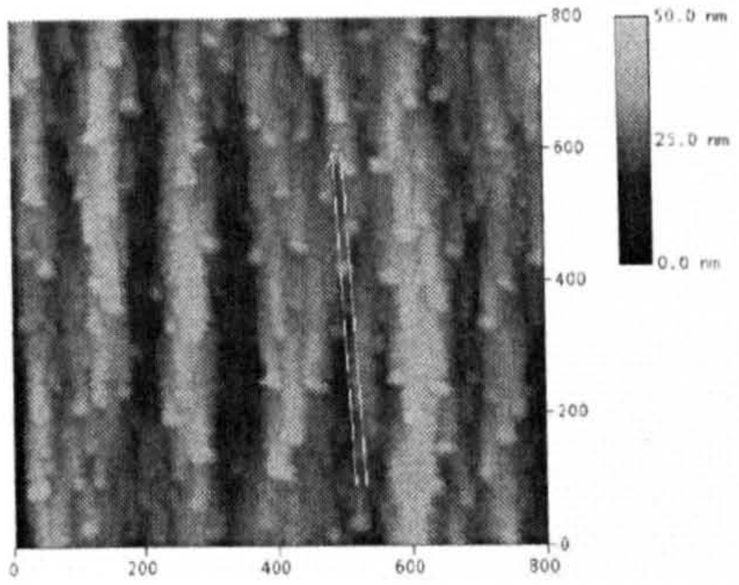

Fig 5.20 800 nm x 800 nm contact mode AFM micrographs of InP (100) surfaces irradiated with 2 keV Ar^+ ion beam under 72° incident angle (to surface normal) at different ion doses:
(a) Ds = 5.2 x 10^{16} cm^{-2}; (b) Ds = 1.5 x $10^{17}$$cm^{-2}$;
(c) Ds =1.75 x 10^{17} cm^{-2}; (d) Ds = 2.0 x 10^{17} cm^{-2};
(e) Ds = 2.8 x 10^{17} cm^{-2}; (f) Ds = 3.5 x 10^{17} cm^{-2};
(g) Ds = 5.1 x 10^{17} cm^{-2}.

(g)

Quantitative analysis of the data from Fig 5.20 gave rise to the dependence of ripple width, height, and wavelength upon ion dose as shown in Fig 5.21.

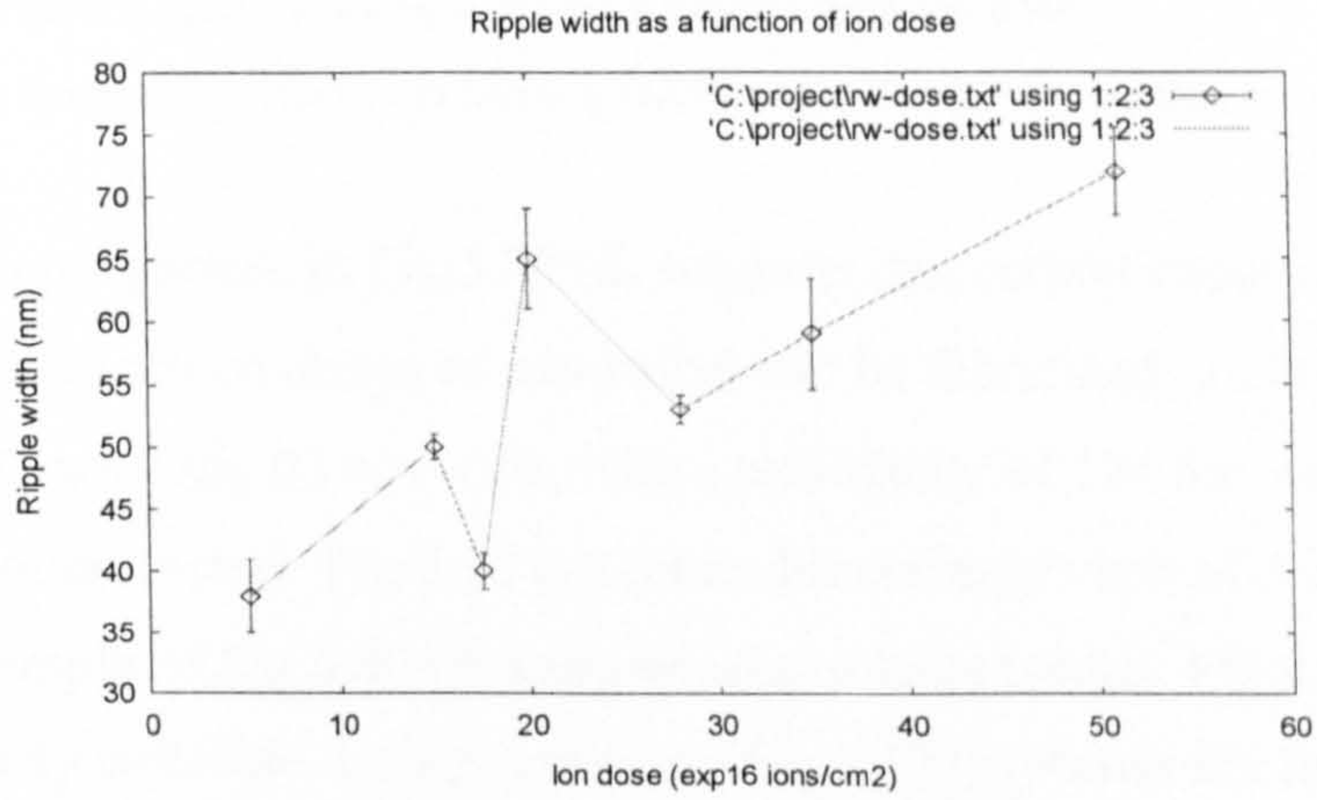

(a)

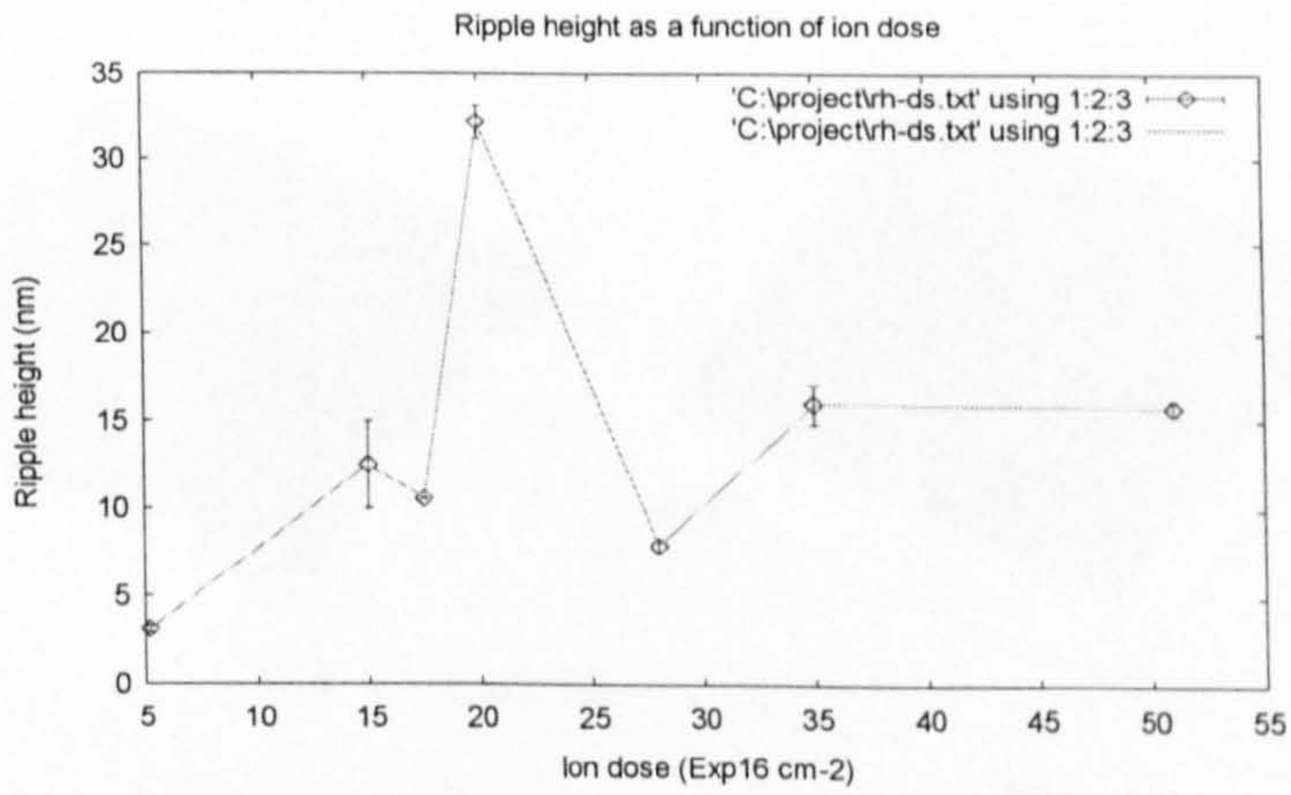

(b)

Fig 5.21(a)-(b) Dependence of ripple width (a), height (b) upon bombarding ion dose.
Bombarding energy E = 2 keV, ion beam incident angle θ = 72° (to surface normal).

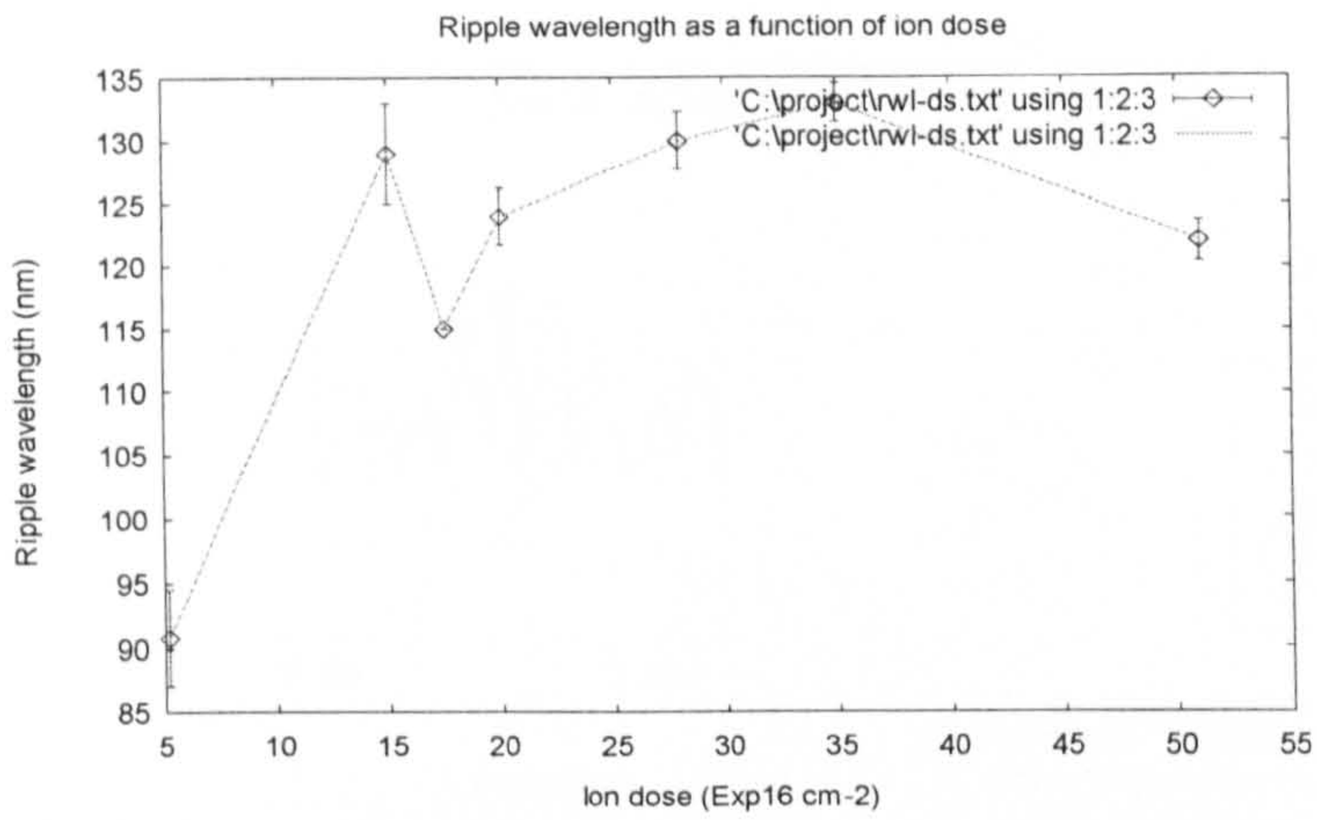

(c)

Fig 5.21(c) Dependence of ripple wavelength (c) upon bombarding ion dose.

Bombarding energy E = 2 keV, ion beam incident angle θ = 72° (to surface normal).

The spectacular ripple pattern in Fig 5.20 (d) suggests that certain experimental conditions exist under which arrays of nanowires can be fabricated. In this case, arrays of nanowires of 32 nm high, 65 nm wide, with a periodicity of 134 nm were found over a length of several micrometers. Fig 5.22 is a three-dimensional view of AFM micrographs obtained on the sample of Fig 5.20 (d) scanned over a larger scale. Fig 5.22 (a) and (b) were simultaneously collected during scanning. Fig 5.22 (c) shows the line profile of the cross-section along the straight line marked in the top-view image.

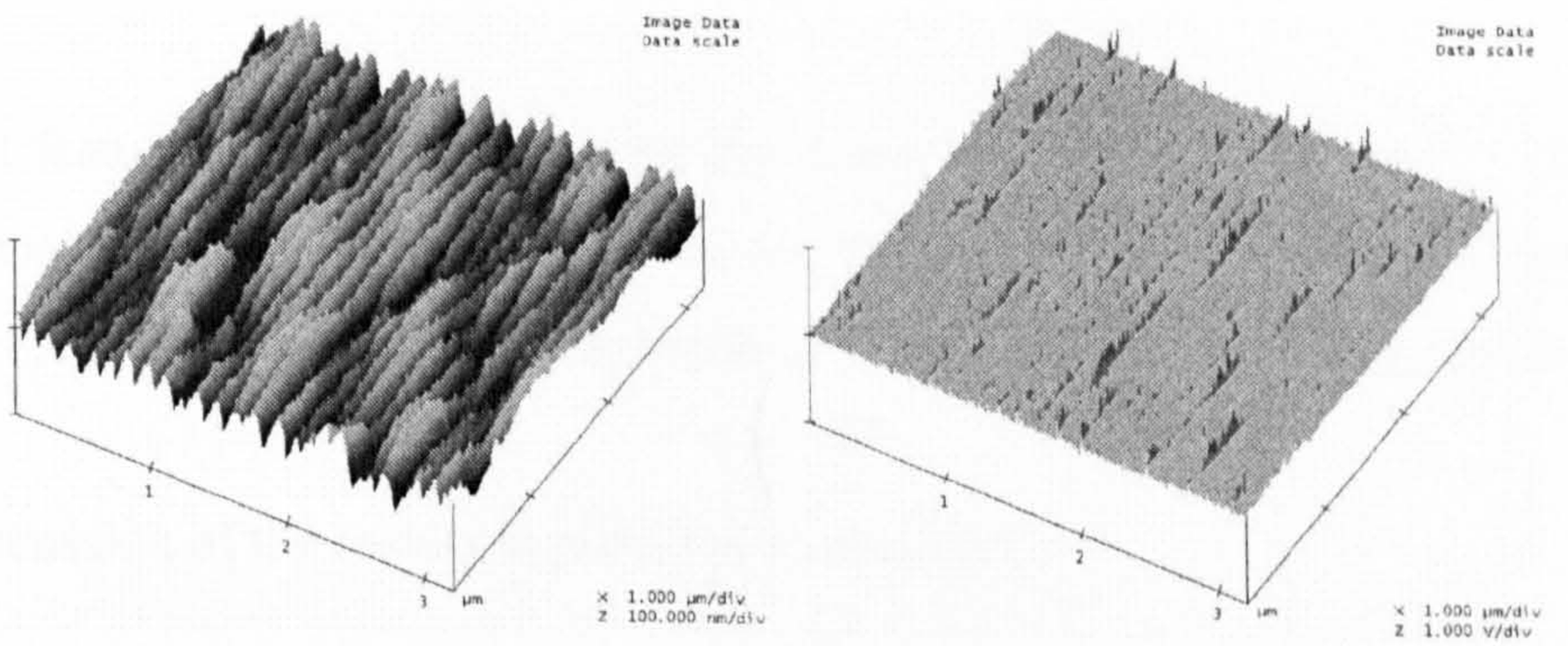

(a) (b)

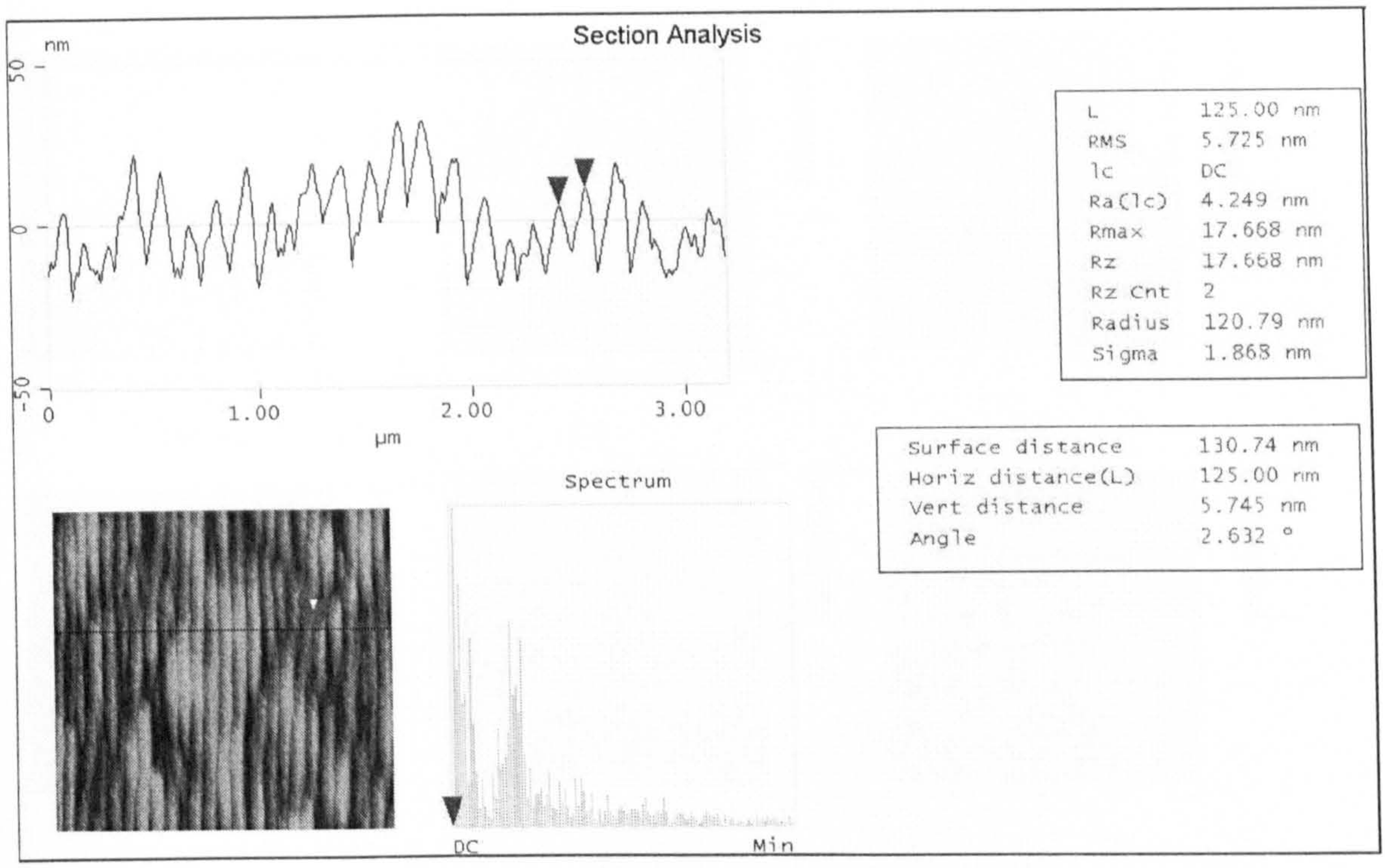

(c)

Fig 5.22 Three dimensional view (a, b) and section analysis (c) of nanowire arrays obtained by grazing incidence Ar^+ ion bombardment on InP (100) surface at a dose of 2×10^{17} cm^{-2} at room temperature. (a). Height plot, color scale 100 nm; (b) Friction plot, color scale 1 nm; (c). Line profile (upper left box) of the cross section along the straight line marked in the bottom left box (color scale 100 nm).

No distinct features were found with an ion doses below 5.2×10^{16} cm^{-2}. This implies that a critical ion dose is required to create the ripple pattern on InP (100) at room temperature, indicating substantial depletion of P from InP at this crucial ion dose.

Further discussion of the results is provided in section 5.3.

5.2.4 Morphology Changes with Different Ion Beam Incident Angles

Fig 5.23 is a collection of typical topographies of 2 keV Ar^+ ion bombarded InP (100) surfaces at room temperature at different beam incident angles. The experiment was performed at a fixed dose of 5.2×10^{16} cm^{-2}.

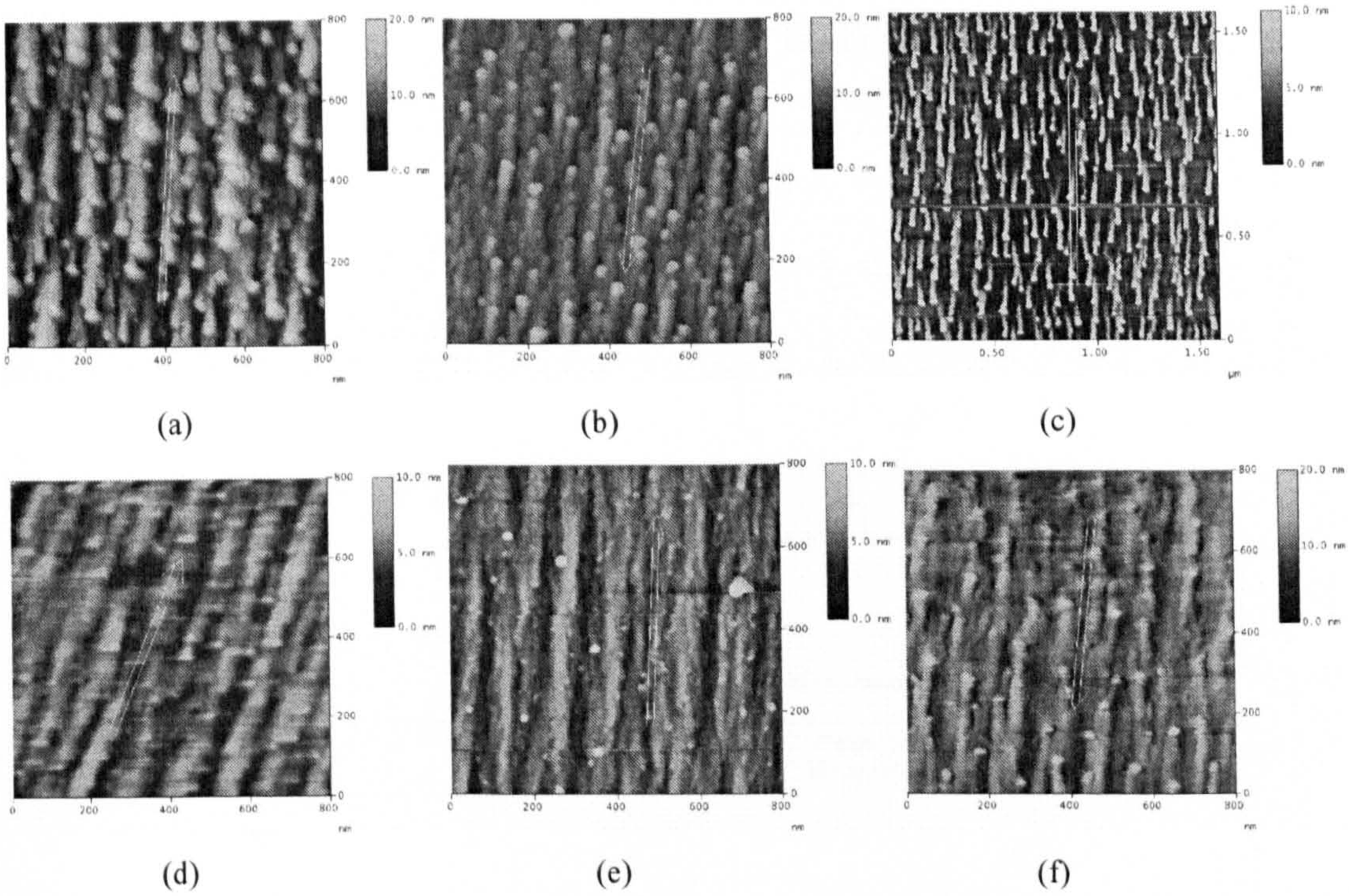

Fig 5.23. Contact mode AFM micrographs of InP (100) surfaces irradiated with 2 keV Ar^+ ion beam at a dose of 5.2×10^{16} cm^{-2} with different incident angle θ (to surface normal): (a) θ = 60°; (b) θ = 65°; (c) θ = 69°; (d) θ = 72°; (e) θ = 77°; (f) θ = 81°.

The effect of different ion beam incident angles on ripple wavelength was investigated by analysis of the dependence of ripple width, height, and wavelength upon ion incident angles. The results are shown in Fig 5.24.

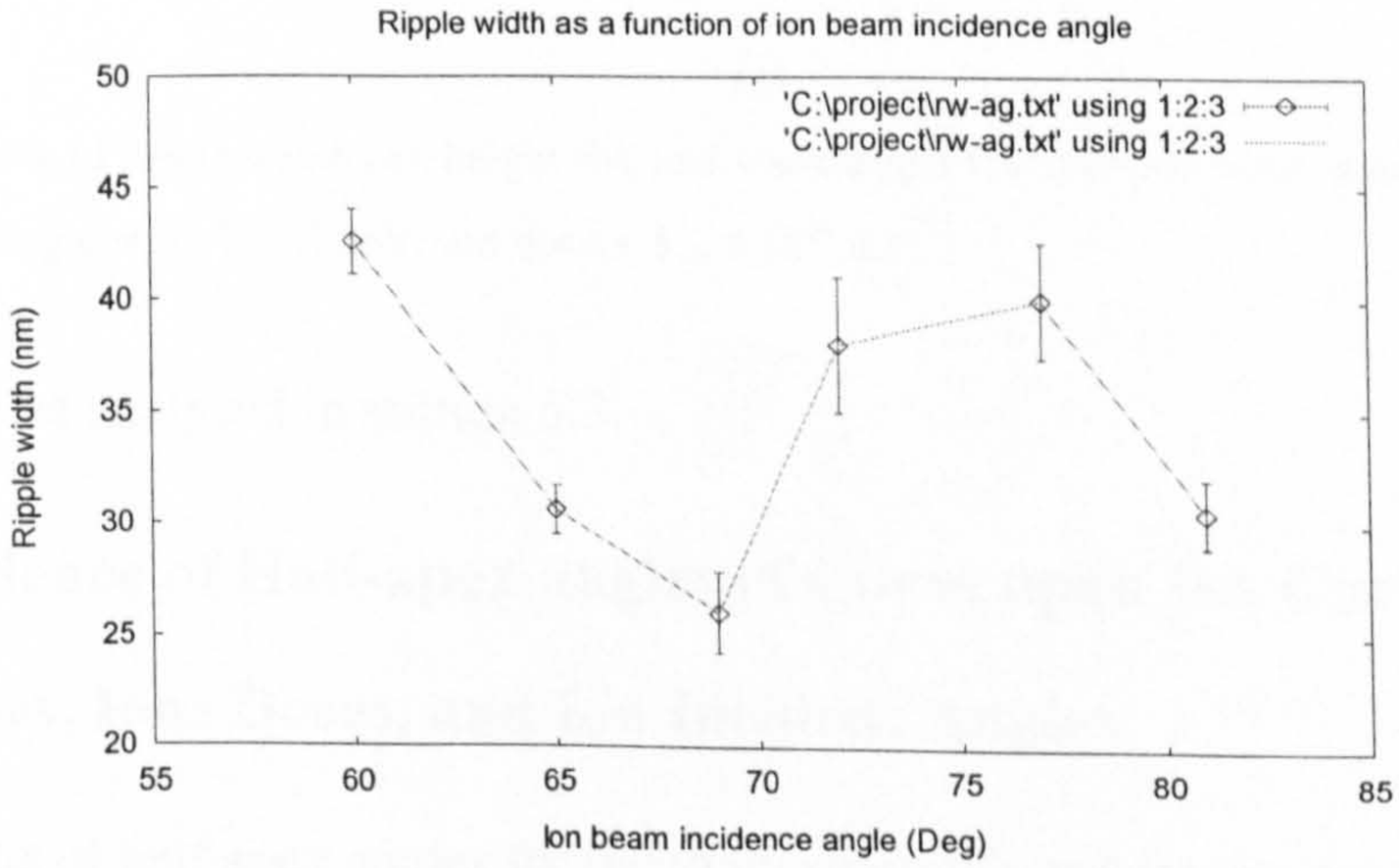

(a)

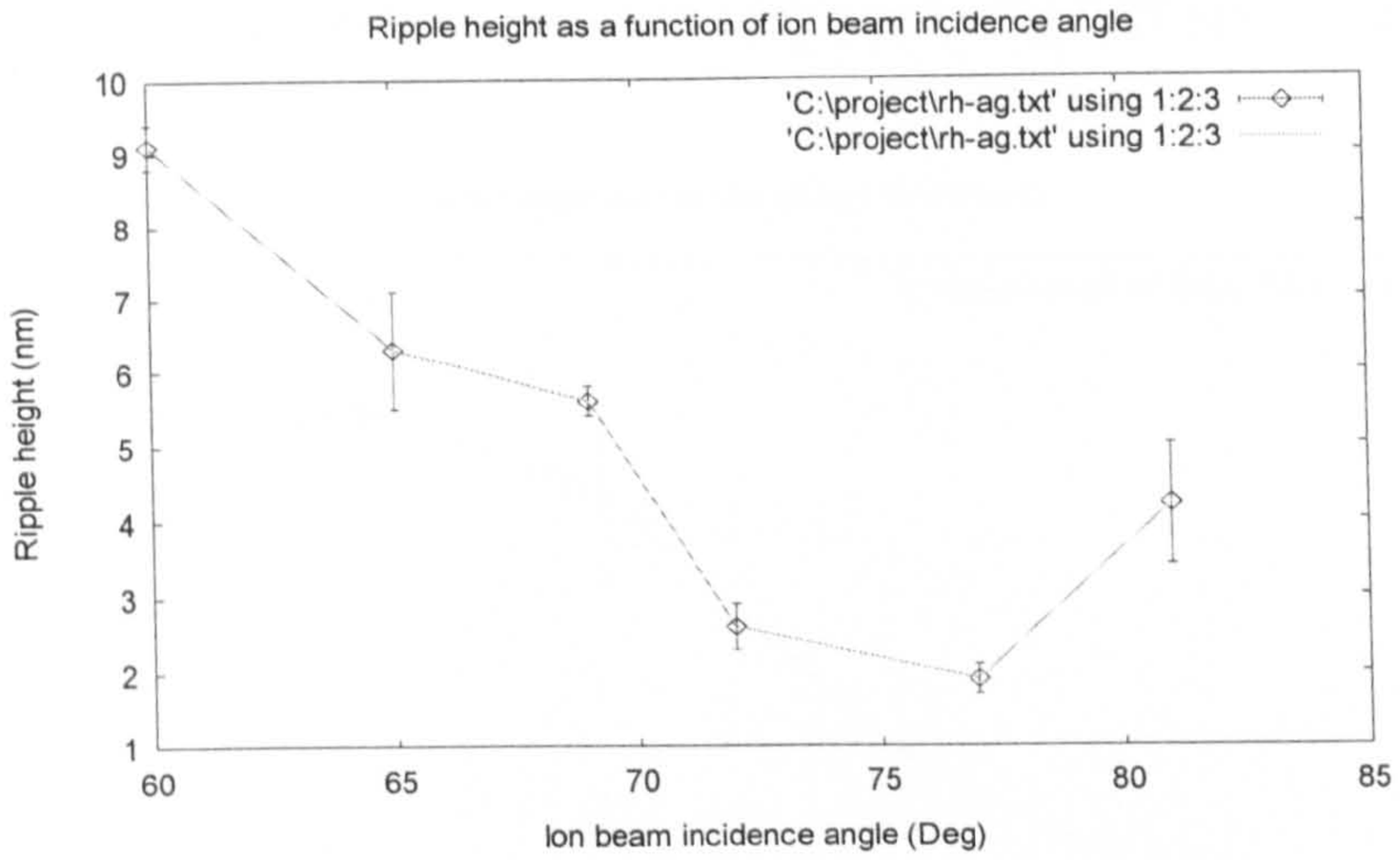

(b)

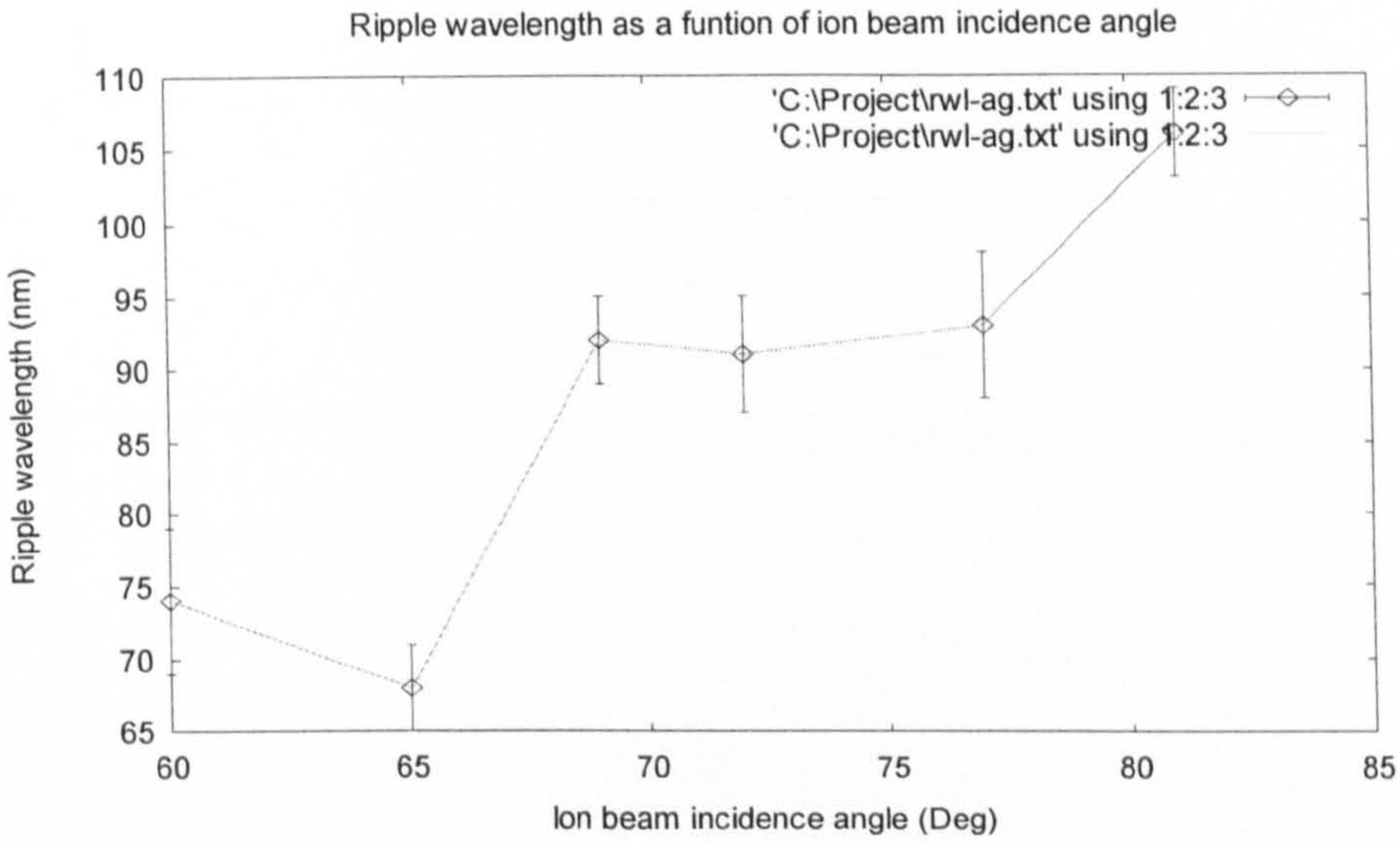

(c)

Fig 5.24 Dependence of ripple width (a), height (b), and wavelength (c) upon ion beam incident angle. Bombarding energy E = 2 keV, ion dose = 5.2×10^{16} cm^{-2}.

The results will be analysed in section 5.3.

5.2.5 Dependence of Half-apex-angles of Cones upon Ion Current Densities, Ions Doses, and Ion Incident Angles

Statistical results of half apex angles for the three series of experiments described in sections 5.2.2, 5.2.3, and 5.2.4 yield the half apex angle dependence on ion current

density, ion dose and ion beam incident angle as shown in Fig 5.25 (a), (b), and (c) respectively.

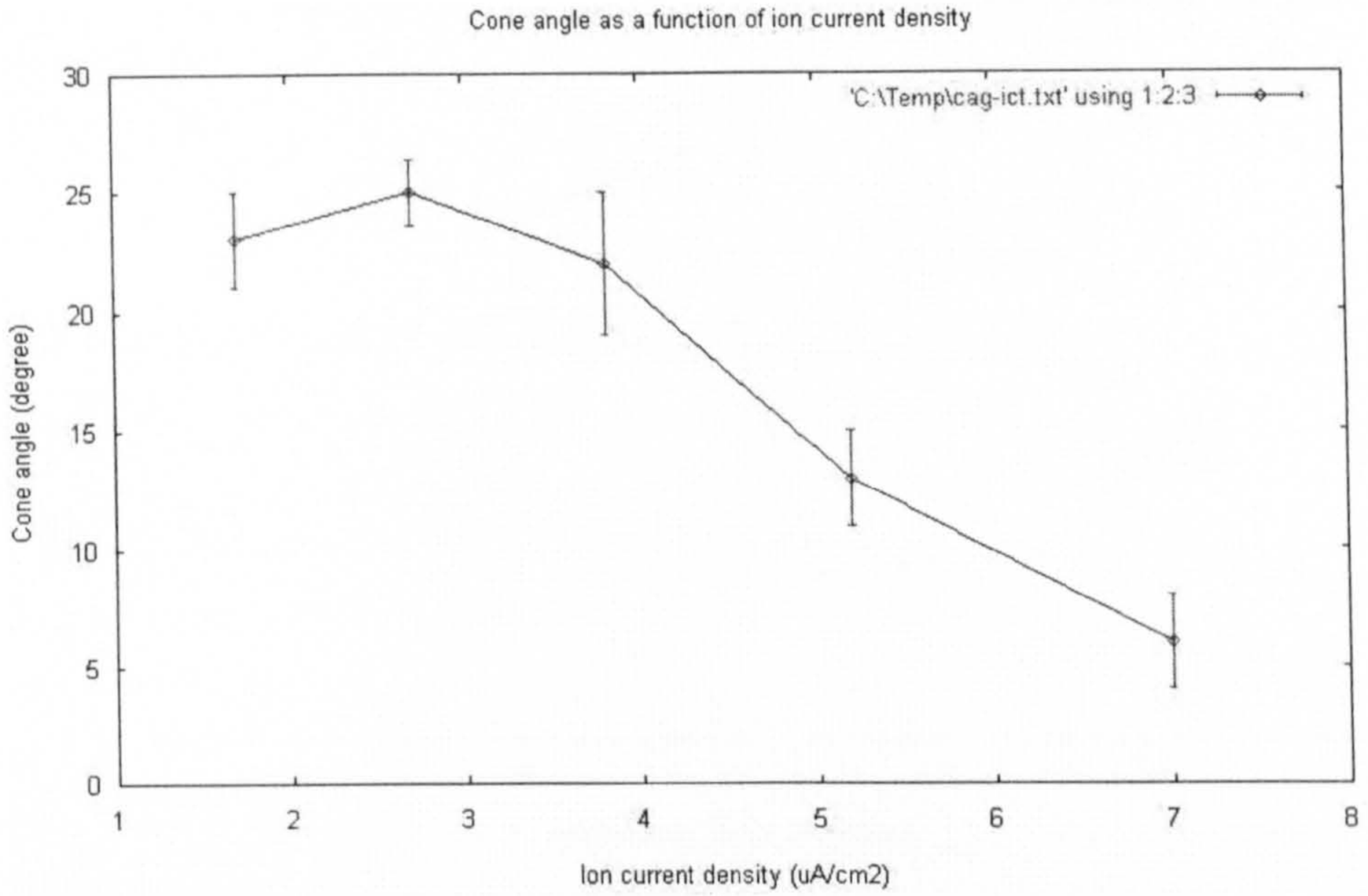

(a)

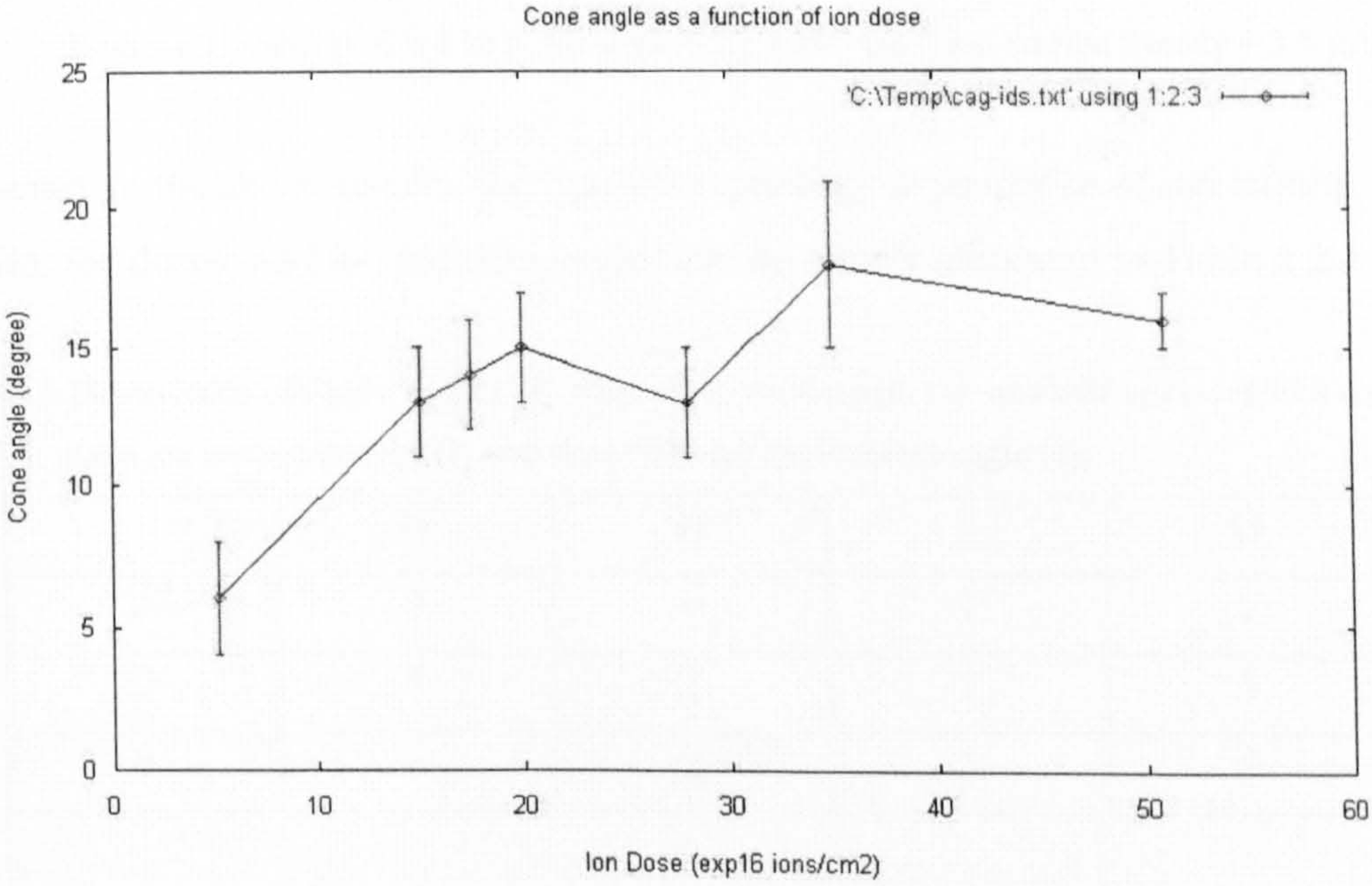

(b)

Fig 5.25 (a)-(b) Dependence of half apex angle upon ion current density (a), and ion dose (b). Parameters of ion bombardment: (a) Bombarding energy E = 2 keV, ion dose = 5.2×10^{16} cm^{-2}, ion incident angle $\theta = 72°$; (b) Bombarding energy E = 2 keV, ion incident angle $\theta = 72°$, ion current density = 3.8 $\mu A/cm^2$.

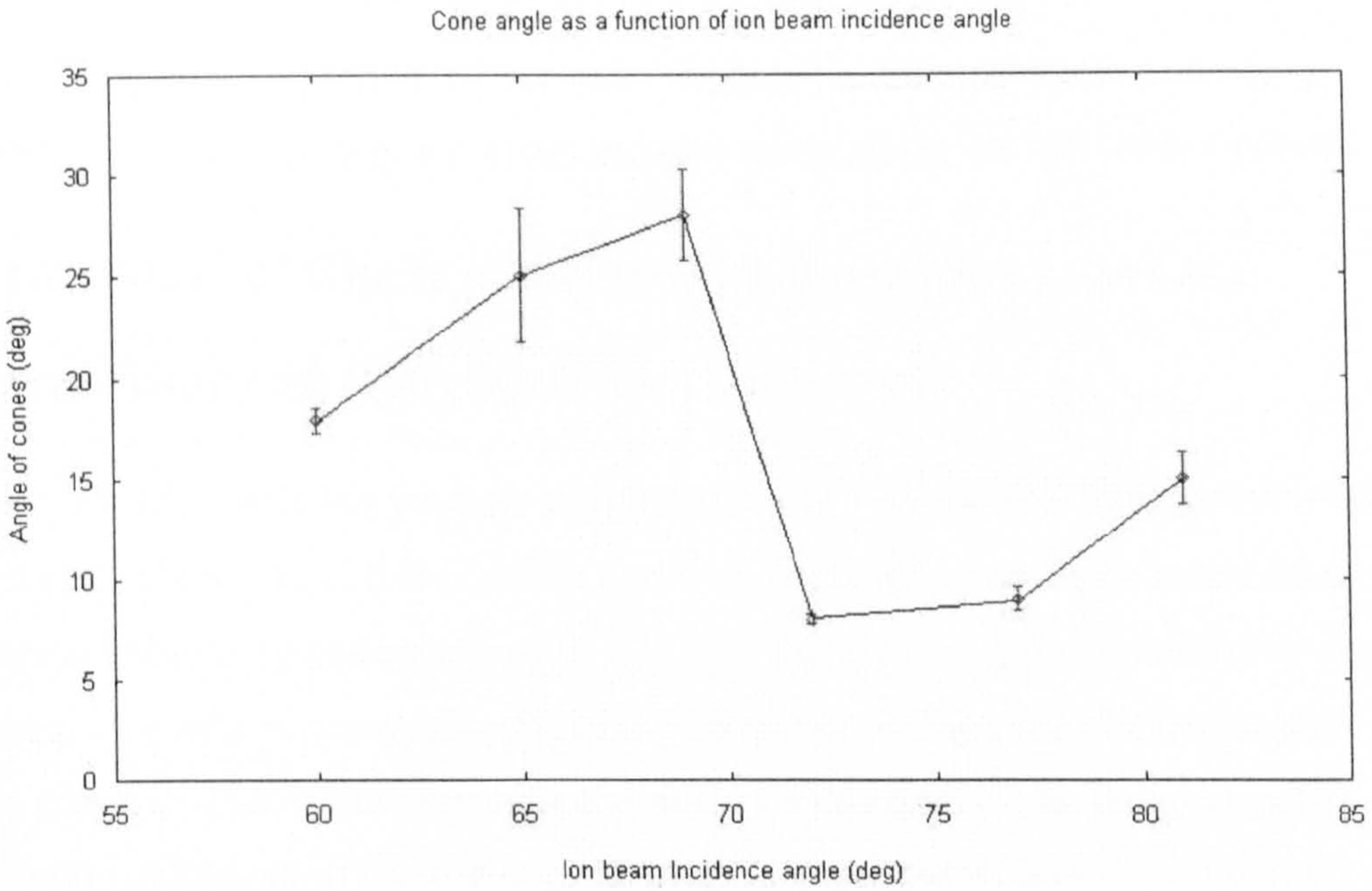

(c)

Fig 5.25 (c) Dependence of half apex angle upon ion beam incident angle. Parameters of ion bombardment: Bombarding energy E = 2 keV, ion dose = 5.2×10^{16} cm^{-2}, ion current density = 3.8 $\mu A/cm^2$.

In summary to the above results, the ripple morphology dependence of ion current densities, ion doses, and ion incident angles can be clearly tabulated in Table 5.2.1 below:

Table 5.2.1 Dependence of ripple width (W), height (H), wavelength (λ), and half-apex-angle of cones (Θ) upon ion current density (J), ion dose (D), and ion incident angle (θ)

	W	H	λ	Θ
J	↑	~	↑	↓
D	↑	↑	↑	↑
θ	~	↓	↑	↑

* Symbols in the table stand for: "↑"—an increasing relationship; "↓"—a decreasing relationship; "~"—an ambiguous relationship.

These results are analysed in detail in the following section.

5.3 Discussion of the Results

The results obtained in section 5.2 are to be analyzed in this section in order to understand the mechanism of ion beam induced morphology on InP (100) surfaces.

5.3.1 Discussion of Ripple and Nanowire Formation on Ar ion Irradiated InP (100) Surfaces

Although TRIM simulation predicts a high sputtering yield ratio of P/In (section 4.2) for ion energies below 1 keV, it is possible that with bombarding energies lower than 1 keV, the beam is liable to be reflected so that it is very difficult for ion penetration or erosion to happen. A useful measure, the effective penetration energy, may be responsible for the erosion process. This is the perpendicular energy equivalent of the perpendicular momentum component of the beam to the surface measured by eqn (5.3.1) below:

$$E_{eff} = E_0 \cos^2(\theta) \qquad (5.3.1)$$

Where E_{eff} is the effective penetration energy, E_0 is the ion energy, and θ is the angle of incidence of ion beam to the surface normal.

With $\theta = 72°$, we get $E_{eff} = 0.1\ E_0$. This means that at grazing incident conditions, the effective penetration energy is reduced to a factor of 10. In order to get enough energy for the erosion process, the bombarding energy E_0 must be sufficiently high. This is possibly the reason that no pronounced morphology was observed for the ion energies below 1 keV.

The independence of the surface topography upon ion beam azimuth angle shown in Fig 5.15 is in agreement with the results of Malherbe [52], who stated that amorphisation of the substrate under ion bombardment could minimise the effect of crystallographic orientated diffusion (or ion channelling) and energy barriers to interlayer surface diffusion. In the previous chapter (section 4.4.2), TRIM simulation of low-energy Ar^+ ion irradiation on InP surfaces predicted that the InP surfaces go amorphous with an ion dose of 5.2×10^{16} cm^{-2} if 1% f the vacancies introduced is assumed to remain in the target.

It was not possible to discern the origin of the dependence of ripple height on ion current density from Fig 5.19 (b) at that stage. But Fig 5.19(a) and (c) reveal a tendency for ripple width and wavelength to increase with bombarding ion current density, with a maxima at 5.2 $\mu A/cm^2$. It is reasonable to assume that the greater the ion current density, the greater the surface density of diffusing atoms σ, and hence a greater surface diffusion parameter B ($B = D_s \gamma \sigma / n^2 k_B T$, eqn (3.3.4)) induces ripples of longer wavelength. This is in qualitative agreement with the BH theory of ripple growth.

At this stage, one might argue that instead of an increasing ripple wavelength, eqn (3.3.8) predicts a decreasing wavelength upon increasing ion current density ($\lambda_C \sim J^{-1/2}$). Because the ion current density plays a role of ion flux J (the ion flux is proportional to the ion current density), as in opposition to the results in section 5.2.2. However, the density of diffusing atoms $\sigma\ (J,\ T)$ in eqn (3.3.8) is a function of ion flux J, and the increase in $\sigma\ (J,\ T)$ may be so significant that it overshadows the contribution of the increase in ion flux itself ($\lambda_C \sim \sigma(J,T)^{1/2}$). As a result, an increasing ripple wavelength is observed upon increasing the ion current density.

Fig 5.18 and 5.20 indicate a process of morphology development from tailed cones, joining of these cones, and periodic ripples from the joined cones. A prominent characteristic in Fig 5.18 and Fig 5.20 is that ripples are superimposed with cones as depicted in Fig 5.18 (f). The diameter of these cones is roughly the same as the ripple width, but the height is generally greater than their host ripples. Both Fig 5.19 and Fig 5.21 show that greater ion beam current and dose create ripples with greater width, height and wavelength.

Fig 5.21 (c) shows the unambiguous increase in ripple wavelength with increasing ion dose. This can be explained as a result of the significant increase in the concentration of mobile species ($\sigma\ (J,\ T)$ in eqn (3.3.8)) created by prolonged ion bombardment. These mobile species are generated from thermally activated diffusion [88] by the primary ions and knock-on atoms carrying a fraction of the initial momentum. The Krok group [88]

believes this to be the mechanism of wire-like structure formation. Based on this discussion, it can be said that the unusual development of ripples and wires due to the ion beam enhanced surface diffusion and the ion dose dependence of ripple wavelength on Ar^+ ion bombarded InP (100) surfaces at room temperature in Fig 5.19 (c) agrees with the prediction of the B-H theory.

It is observed that with the ion the beam incident angle approaching the grazing condition (see Fig 5.23 (a) to (f)), the structure evolves from tailed cones (with tails aligned along the ion beam direction) to ripples superimposed with cones. This suggests ripple development from large scale mergence of tailed cones at grazing incident angles. According to the results of TRIM simulation, the effect of preferential sputtering of P is reduced with increasing incident angle, and so less and less In ions are generated due to the reduction in preferential sputtering of P. However, the momentum transfer along the azimuth of the ion beam direction becomes stronger at grazing angle incidence. It is proposed that this momentum variation gradually assists the agglomeration and mergence of tailed cones so that ripples become finer and more distinguished under ion bombardment at grazing incidence (Fig 5.24 (a) and (b)). On the other hand, intense mergence of a ripple with its adjacent tailed cones and ripples makes ripple wavelength longer with ion beam approaching grazing incidence (Fig 5.24 c).

It can be found from Fig 5.21 that the development of bombardment-induced topography is directly proportional to the ion dose. An increasing feature wavelength with increasing ion dose on InP(100) agrees with the results from Dement *et al* [144] who reported the dependence of ripple wavelength upon ion dose in the form of $\lambda \sim J^{0.2}$. However, Dement *et al* excluded the seeding sputter erosion model by the fact that the RMS surface roughness was linearly proportional to the logarithm of the ion dose, rather than the ion dose itself. The dependence of ripple width and height upon ion dose was not dealt with in that report.

5.3.2 Ripple and Nanowire Formation from Mergence of Cones

Both previous results (ref. section 1.1.4) and TRIM simulations of low-energy Ar^+ ion sputtered InP surfaces have reported In enriched surfaces. Based on the discussion in the last section, it is reasonable to consider a cones mergence model for the ripple formation on Ar^+ ion bombarded InP surfaces at room temperature:

(a) Preferential sputtering [69] of P leaves an In enriched surface (Fig 5.26 a);

(b) Subseqnuent bombardment leads to diffusion of these In^+ ions. These ions could nucleate at some locations created by lattice mismatch between In and InP (the extent of lattice mismatch between In and InP crystals is 40%, calculated from the lattice parameters listed in Table 4.2). Prolonged bombardment leads to growth and agglomeration [100, 391] of these nucleated ensembles into cones (Fig 5.26 b);

(c) Further agglomeration of these cones by prolonged bombardment assists the cones to grow in height and diameter, and tails along the azimuth of the ion beam direction are attached to the cones because of the difference in growth rate between the direction facing towards and away from the bombarding ions (Fig 5.26 c);

(d) Small tailed cones agglomerate, merge [113], and eventually form ripples along the azimuth of the ion beam direction under prolonged ion bombardment. Large cones continue to grow and become superimposed on their host ripples (Fig 5.26 d).

(e) With increasing ion current and dose, ripples grow in amplitude and width (Fig 5.18 a, b, and Fig 5.21 e) due to the increase in growth rate of merged tailed cones and the mergence of a ripple with its adjacent cones upon greater bombarding ion current and prolonged ion bombardment.

(f) At some critical point, the two adjacent ripples merge into one so that a longer wavelength is observed (Fig 5.26 f) at greater ion current densities (Fig 5.19 c) and doses (Fig 5.21 c).

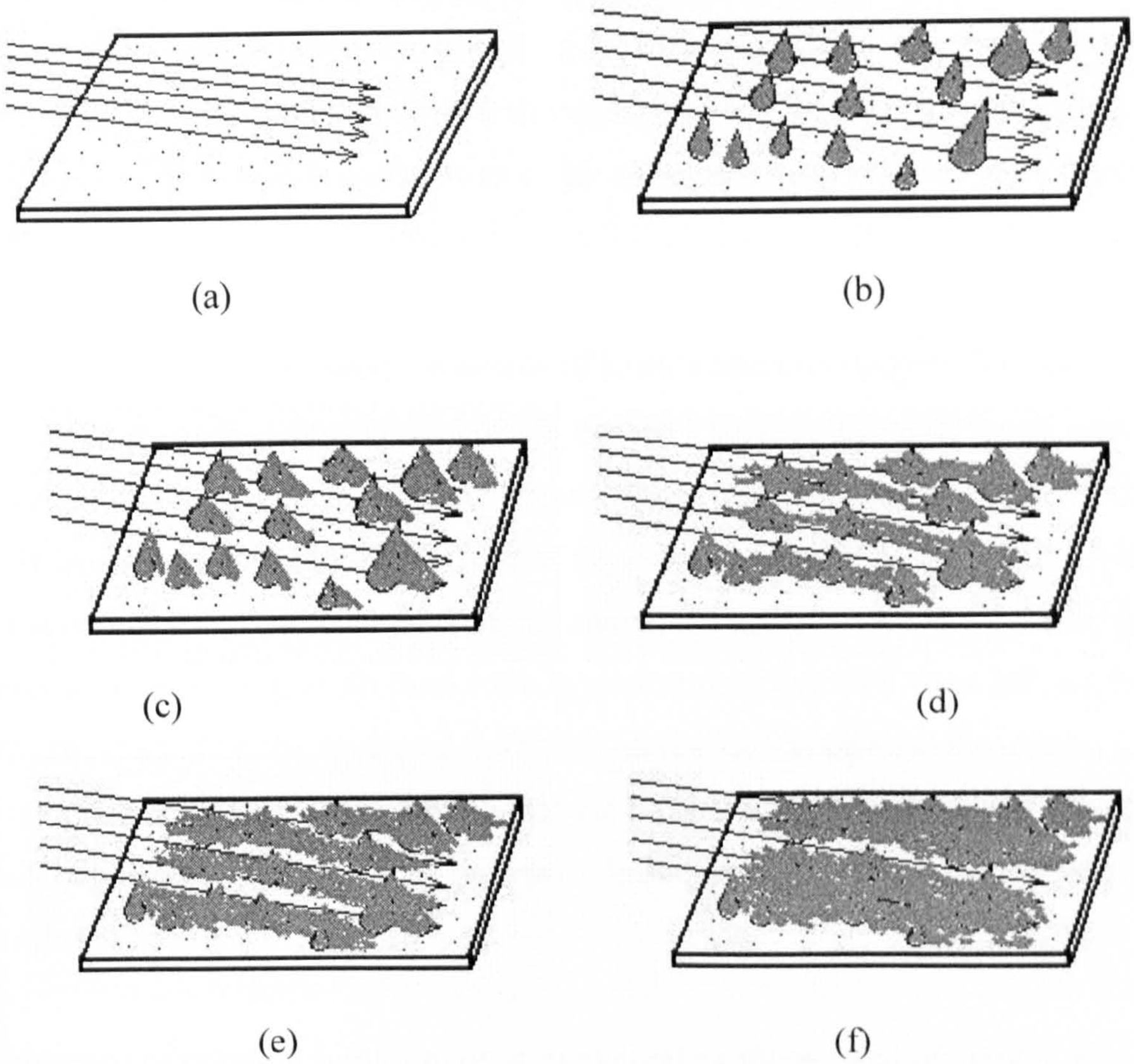

Fig 5.26 Schematic of cones mergence model

The formation of cones can be compared to the impurity seeding models [387, 389] described in section 3.3.7. In the case of this study, the In enriched regions act as seeding points instead of impurities within the metals. The initiation of the cones in Fig 5.19 is also in agreement with the prediction of the KS model described in section 3.3.4. The difference between the example there [385] and the present study is that, under grazing incidence, the system may become anisotropic in the *(x, y)* plane, and the cones formed after the characteristic time begin to agglomerate and merge along the surface component of the ion beam direction.

Tailing of cones in Fig 5.20 (and more clearly, in Fig 5.23 c) is similar to the results of 4 keV Ar^+ ion bombardment on InSb (001) surfaces reported by F. Krok *et al* [88]

(Fig1.13). They believe that the growth of wires was the result of elongation of the initial dots due to non-uniform sputtering loss from the different sides of the dots. However, in the Krok report, no periodicity of wires was claimed. Non-uniform sputtering around the cones gives rise to non-balanced growth of the cones resulting in tailed or elongated cones.

An apparent difference between the results of Krok's and this study is that the concentration or surface density of cones in the Krok report was much lower than these reported in this study. This is probably because the surface binding energy of Sb (1.324 eV, calculated from the sublimation heat of Sb given in Ref [405]) in InSb is much higher than that of P (0.61 eV, calculated from the same reference) in InP. As a result, the effect of preferential sputtering of Sb from InSb is weaker than that of P from InP, so that fewer In ions are retained on the sputtered InSb than on the InP surface for the same experimental condition. Or it could be that the diffusion of In on InSb surfaces is more difficult because of the mobility of In ions on InSb surfaces is much lower than that on InP surfaces.

The presence of periodic ripples may be explained by the stress-field model proposed by M Batzil *et a*l [7, 8]. The formation of stress fields is caused by energy minimisation of the system. The cone-cone interactions mediated by the substrate result in a repulsive force between cones [417, 418]. The lattice of the substrate (InP) surrounding coherently strained indium cones is compressed. If two cones get close together, the compressed lattice of the substrate surrounding both cones overlaps, resulting in a larger lattice distortion in the overlapped area and consequently an increase in the strain energy. This leads to the repulsive force between cones. Strain field mediated repulsive forces are relatively long range compared with the short range attractive forces between single In atoms or single In cones (metallic adhesion forces). The presence of a long range repulsive force and a short range attractive force may cause the ordering of systems into periodic structures so that the energy of the system may be significantly reduced. For the case of In cones on an InP substrate, the short range tensile stress leads to the mergence of adjacent cones, and long range compressive stress between two adjacent ripples leads to periodic

separation of ripples on the InP substrate. Following the continual growth of ripples in size, the energy of the system is increased continuously. This drives the system away from thermodynamic equilibrium. If the ripple-width reaches a value where the system can decrease its energy by joining two ripples together, mergence of ripples occurs so that a longer wavelength is observed at greater ion dose.

The ion dose dependence of half apex angle (Fig 5.25 b) is similar to that of ripple width and height in Fig 5.21 (a) and (b). A significant drop of half apex angle is found at 72° incident angle, indicating the onset of large scale mergence of cones at this threshold incident angle. Above this incident angle, more pronounced ripples are produced. As a matter of fact, the first three experimental points in Fig 5.25 (c) are statistical results of the half apex angles of individual cones without mergence, while the latter three points give the half apex angle of cones superimposed on their host ripples. An unambiguous trend of the half apex angle increasing with increasing ion beam incident angle in both the first three and the latter three points proves that kinetic momentum transfer from Ar^+ ions to the samples under grazing ion incident angle assists the growth and mergence of cones.

Fig 5.25 (a) shows that cones become sharper with increased ion beam current densities. This could indicate that bombarding time plays an important role in the growth of cones. In order to keep a fixed irradiation dose, lower ion current density requires more time compared with higher ion current density. With persistent ion irradiation above the threshold energy, the enriched In ions are diffused and nucleated at some lattice mismatched points, and gradually grow into cones. However, it is difficult for cone mergence to achieve at low ion current densities because of the insufficient surface diffusion, and the cones grow in height and diameter, rather than merge into ripples. As a result, the half apex angle becomes larger and larger. At high ion current densities, diffusion of In ions increases. The kinetic energy that one In ion could acquire from the cascades generated by incident ions would be much higher than that in the case of low ion current density. This would lead to the growth of larger cones and consequently larger cone apex angles are expected at higher ion current densities [78]. However, in the

present study, bombardment time is substantially reduced at high ion current density in order to keep the ion dose constant. The cascades produced in a short time could just be sufficient to diffuse some of the In ions to some nucleation sites for faster cone initiation, and others to assist cones to grow. These small cones would yield smaller half apex angles at higher ion current densities. This is in qualitative agreement with the trend of an increase in half apex angle upon decrease in the ion current density and is shown in Fig 5.25 (a). In addition, at high ion current density, the number of cones per unit area would be so big that some cones would begin to merge so that ripples appear with small amplitude. This gives an explanation for Fig 5.19 (b) in which a significant drop in ripple height is observed at high ion current density.

5.3.3 Relationship between the Cone Mergence Model and Other Ripple Models

It seems not clear to separate the cone mergence model from the stress- field self-organization of nanowires and the BH ripple model discussed in chapter 3. The formation of ripples on InP (100) surfaces has been explained by the BH ripple model to some extent, while the generation of periodicity has been related to the stress-field model. Nanowires formed on ion beam irradiated CaF_2 surfaces has been explained by stress-field induced self-assembly of Ca ions (chapter 1 and 3). Later in chapter 7, formation of structures on ion beam irradiated Si_3N_4 surfaces will be shown to observe the BH ripple model. At this stage, it is worth comparing some physical properties of InP with CaF_2 and Si_3N_4. It is known that the strength of an ionic bond is much weaker than that of a covalent bond, so that the height of the potential barrier (W, cf., section 3.3.1.2) for an atom to escape from its equilibrium position in an ionic bond is much lower than that in a covalent bond. This leads to a very high diffusion coefficient (D in eqn (3.3.2)) for CaF_2, and a very low D value for Si_3N_4. As a result, diffusion of Ca atoms on CaF_2 surfaces is much easier than that of Si atoms on Si_3N_4 surfaces. The high mobility of Ca atoms is favorable to the stress field created by the lattice mismatch between Ca and CaF_2, so that the stress-field model was successful in explaining the nanowire formation on low-energy

Ar^+ ion irradiated CaF_2 surfaces. In the case of Si_3N_4, it is extremely difficult for Si atoms to escape from their equilibrium positions because of the high potential barrier. This leads to a very weak diffusion of Si atoms on S_3N_4 surfaces, with physical sputtering dominates, so that the BH ripple model is more favorable in explaining ripples formation on the Ar^+ ion sputtered Si_3N_4 surfaces.

For InP, however, the potential barrier W lies between that of CaF_2 and Si_3N_4 (c.f. table 4.1). Due to the exponential dependence of D upon W (eqn 3.3.2), the diffusion of In atoms on InP surfaces is neither as easy as that of Ca atoms on CaF_2 surfaces, nor as difficult as that of Si atoms on Si_3N_4 surfaces. At the early stage of the irradiation, diffusion of In atoms initiate the formation of In enriched cones with tails; At some stage, weak stress field may be induced so that broken ripples form by mergence of tailed cones; at certain stage with sufficient ion dose, stress field becomes so strong that long ranged order is created, and the broken ripples merge to form non-broken ripples or nanowires. This suggests that neither the stress-field model nor the ripple model alone can explain the formation of ripples and nanowires on the Ar^+ ion irradiated InP surfaces. The cone mergence model described in this chapter can be regarded as a combination of the two models.

Chapter 6

Compositional Changes and Electronic Structure of Ar^+ Ion Beam Induced Nanowires on InP (100) Surfacs

As described in Chapter 2, XPS is an efficient tool for non-destructive analysis of the chemical composition of solid surfaces. Although it is poor in lateral resolution [334] (0.15-1 mm), the combination of XPS and Scanning Tunnelling Spectroscopy (STS) is able to probe the composition of single nanowires. In this chapter, XPS analysis is used to find changes in the chemical composition of the InP (100) surfaces after Ar^+ ion bombardment. Attempts with spatially resolved STS to measure tunnelling conductance of single nanowires is made in order to find further evidence of the cone mergence model.

6.1 X-ray Photoelectron Spectroscopy Characterization of Compositional Changes in Ar^+ Ion Beam Induced Nanowires on InP (100) Surfaces

Sputtering of a compound crystal often breaks the balance of the original chemical composition by depletion of one or more atomic components of the crystal. Formation of Ca nanowires on CaF_2 (111) surfaces by Ar^+ ion beam bombardment[6-8] presented a typical example of nanowire formation by preferential sputtering of the lighter atoms in ionic crystals. In order to prove that this phenomenon exists in the covalent crystal InP, XPS was performed on the Ar^+ ion beam bombarded InP samples.

Large discrepancies exist in various reports (Ref [115] and the other results quoted there) of chemical composition of Ar^+ ion sputtered InP surfaces. Among the results from 26 studies quoted in Ref [115], Ar^+ sputtering of InP (100) surfaces mostly reported enrichment of indium, while those on (110) and (111) surfaces mostly enrichment of phosphorus. Some studies on InP (111) and (110) surfaces [112, 115] exhibited decreased tendency of preferential sputtering of P upon ion beam incident angle. Before the presentation of

experimental results of this study, it is necessary to have a brief introduction of the theory of compositional change of ion beam bombarded solid surfaces.

6.1.1 Theory of Compositional Changes in Ion Beam Bombarded Surfaces of Compound Solids

In parallel with the research on ripple morphology, surface compositional changes due to low-energy ion bombardment on compound crystal surfaces have also been extensively investigated. *The surface stoichiometry may be influenced by sputtering parameters*[91] *such as ion species (e.g., Ar^+, He^+, Ne^+, Cs^+, and Xe^+), ion beam energy, incidence angle, ion dose, and substrate temperature, and the measurement method used such as AES (Auger Electron Spectroscopy)*[92, 419, 420]*, XPS(X-ray photoelectron spectroscopy*[91, 92, 421]*, RBS(Rutherford Backscattering Spectroscopy)*[123]*, and SIMS (Secondary Ion Mass Spectroscopy)*[91, 94]. Theory [361] predicted that the ratio of the equilibrium sputtered surface fractional composition C_i^s of a compound AB to the bulk fractional composition X_i^b is given by

$$\frac{C_b^s}{C_a^s} = \frac{C_b^b}{C_a^b}\frac{Y_a}{Y_b} \tag{6.1}$$

Where Y_i represents the component sputter yield. The ratio of the component sputtering yields can be approximated through Sigmund's sputtering theory in the linear cascade regime [361]

$$\frac{Y_a}{Y_b} = \left(\frac{M_b}{M_a}\right)^{2m}\left(\frac{U_b}{U_a}\right)^{1-2m} \tag{6.2}$$

where M_i and U_i denote the atomic mass and surface binding energy respectively. Substitution of equation (6.2) into (6.1) yields:

$$\frac{C_b^s}{C_a^s} = \frac{C_b^b}{C_a^b}\left(\frac{M_b}{M_a}\right)^{2m}\left(\frac{U_a}{U_b}\right)^{1-2m} \tag{6.3}$$

m is an energy dependent parameter originating from the particular form of the power cross-section that Sigmund used in his theory. For applications in low-energy sputtering,

the relevant value for *m* should be *2m = 0.33*. For InP, calculation by Malherbe[115] showed that $C_P^s/C_{In}^s = 0.72$, which predicted an indium-enriched sputtered surface. Based on the prediction of the theory and the analysis of many research results on the ion bombardment of InP, Malherbe concluded that *the mass difference between the In and P atoms is the major factor contributing to the preferential sputtering of InP. The effect of the surface binding energies of the two atomic species is of secondary importance.* Ar, being less efficient in transferring its energy to In atoms, augments preferential sputtering of P. The conclusion was further confirmed by other research groups [421].

Although earlier research in low-energy argon ion bombardment of III-V nitrides failed to find a nitrogen depleted surface[419], preferential sputtering of nitrogen has been recently displayed by quantitative AES analysis of compositional changes in GaN induced by low-energy Ar^+ ion bombardment under off-normal incidence[420].

Discrepancies with the theory of preferential sputtering which predicts an As enriched surface after low energy argon ion bombardment of GaAs exist in many documents [421-423](and references quoted) with the altered surface observed to be top layer As rich and subsurface regions As depleted. This was interpreted as arising from the higher mobility of Ga atoms over As in some specific temperature range (including room temperature), which overbalances the production of the ion-bombardment-induced defects. T. D. Bussing et al [424] attributed the phenomena of As depletion to bombardment induced surface Gibbsian segregation.

6.1.2 Compositional Changes on Ar^+ Ion Beam Bombarded InP (100) Surfaces

The bombarded sample of InP (100) from Fig 5.20 (d) was examined with XPS. All XPS analyses were carried out in a commercial spectrometer system (Kratos Axis Ultra, Fig 6.1), using a monochromatic Al Kα ($h\nu$ = 1486.6 eV) photon source. The system is also equipped with both a 165 mm Hemispherical Analyser (HAS) for the acquisition of spectra and a concentric Spherical Mirror Analyser (SMA) for XPS imaging. High

photoelectron collection efficiency and charge neutralisation are achieved using a magnetic immersion lens (Kratos Patent EP 0 243 060 B1), in conjunction with the Kratos "Axis" charge neutralisation system. The system specifications described above allows an energy resolution of ~ 0.45 eV, as determined from the FWHM of the Ag $3d_{3/2}$ feature and a spatial resolution of < 27 μm. The analyzer was operated in Fixed Analyzer Transmission (FAT) mode for the acquisition of all spectra although the pass energy was varied between 160 eV and 10 eV for survey and high-resolution scans of discrete core-levels, respectively. All spectra were obtained at normal emission and the base pressure of the analysis chamber during the experimental period was $\leq 8.0 \times 10^{-10}$ mbar. All samples were analyzed initially without prior preparation. Spectra were also obtained following Ar^+ ion bombardment at 4 kV and a 40° incident angle for 60 seconds. The choice of 4 keV was for the purpose of material removal. Typical sample drain currents of 5-7 μA were obtained during bombardment and the ion etching rate was determined to be ~ 3-4 $nm.min^{-1}$ as determined from depth profile analysis of a Ta_2O_5 thin film of known thickness. The energy scale of the spectrometer was calibrated in accordance with an internationally accepted procedure (ISO TC\201 SC7). Spectra analysis was performed using CasaXPS Demo version. Quantification of atomic concentration was carried out after automatic peak area definition and background (Tougaard) subtraction. Fitting of experimental spectra using synthetic components was carried out initially by subtracting an appropriate background (Tougaard) from spectra. Synthetic components were subsequently created using a product of Gaussian and Lorentzian line-shapes (ref. section 2.3). The height, position and full width at half maximum (FWHM) of the components associated with a particular peak were optimized iteratively using the chi-squared method.

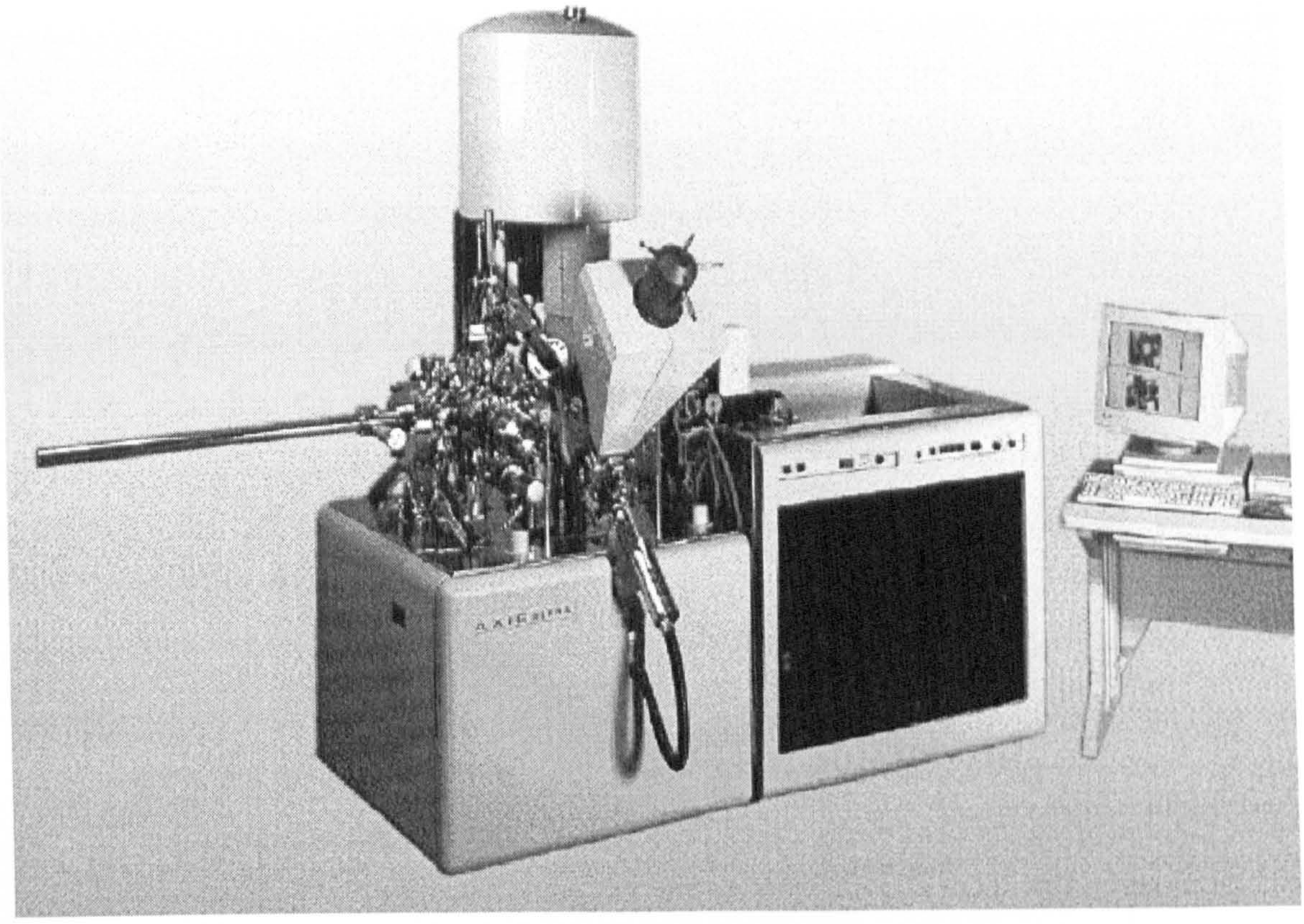

Fig 6.1 Photograph of Kratos Axis Ultra X-ray Photoelectron Spectrometer

6.1.2.1 Effect of Surface Cleaning of Ar^+ ion bombardment on InP (100)

An argument exists in all the results presented in Chapter 5 for the necessity of surface treatment before Ar^+ ion bombardment. Examples of sample treatment of III-V semiconductor surfaces can be found from a number of reports. F. Krok *et al*[78] reported ion cleaning treatment of InSb (100) surfaces with a 0.7 keV Ar^+ ion beam rastered at alternating angles (+60° and -60° off the normal) for 3 hrs at elevated temperature (700 K) following annealing to 750 K for a few hours. Using AFM and AES, Sung *et al* [425] found that a combination of 30 eV Ar^+ ion bombardment and annealing at about 300°C produced a clean defect free surface. Even earlier reports showed [131, 137] that Ar^+ ion bombardment alone is an efficient surface treatment technique for InP. Due to the lack of heating device in the UHV chamber (Fig 5.1), the results in Chapter 5 were collected on samples cut from an InP (100) wafer without further surface treatment before Ar^+ ion bombardment. In order to examine the extent of the cleaning effect of Ar^+ ion

bombardment on InP (100) surfaces, an air cleaved InP (100) sample was loaded into the XPS chamber followed by 4 keV Ar^+ ion bombardment under 40° incidence angle for 60 seconds. X-ray photoelectron spectra were collected *in situ* in UHV on the sample surface before and after Ar^+ ion bombardment as shown in Fig 6.2.

It can be clearly observed that native indium oxides and some contaminants like barium (probably from the tape initially used to dice the InP (100) wafer) have been eliminated after 60 seconds Ar^+ ion bombardment, and carbon contamination has been reduced to a negligible level. The bombardment dose to all the samples in Chapter 5 is well above this level. Hence, it is relatively safe to say that no surface treatment is required on the as received InP (100) samples used to investigate Ar^+ ion irradiation induced topography.

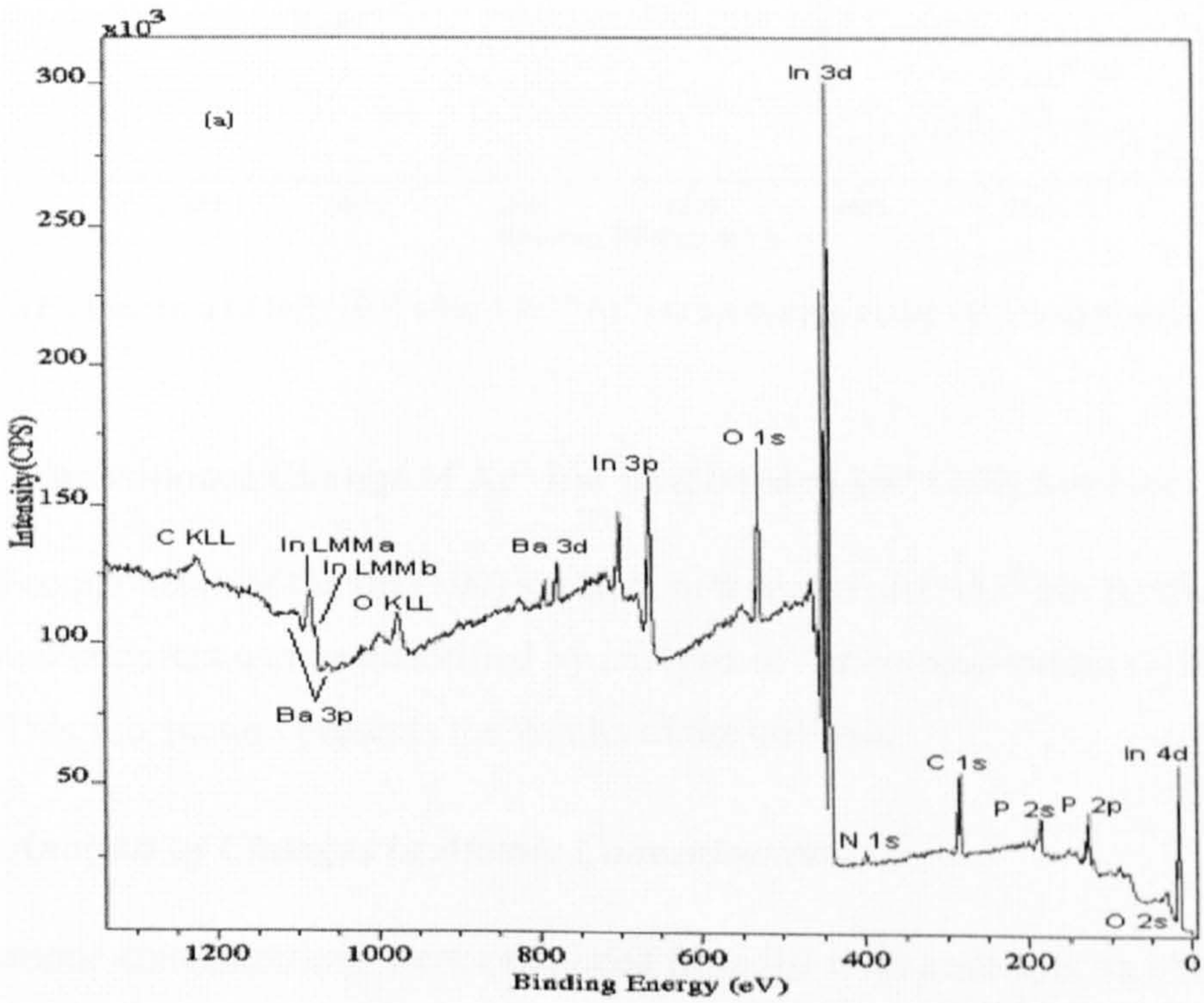

Fig 6.2 (a) XPS spectrum of InP (100) surface before ion sputtering

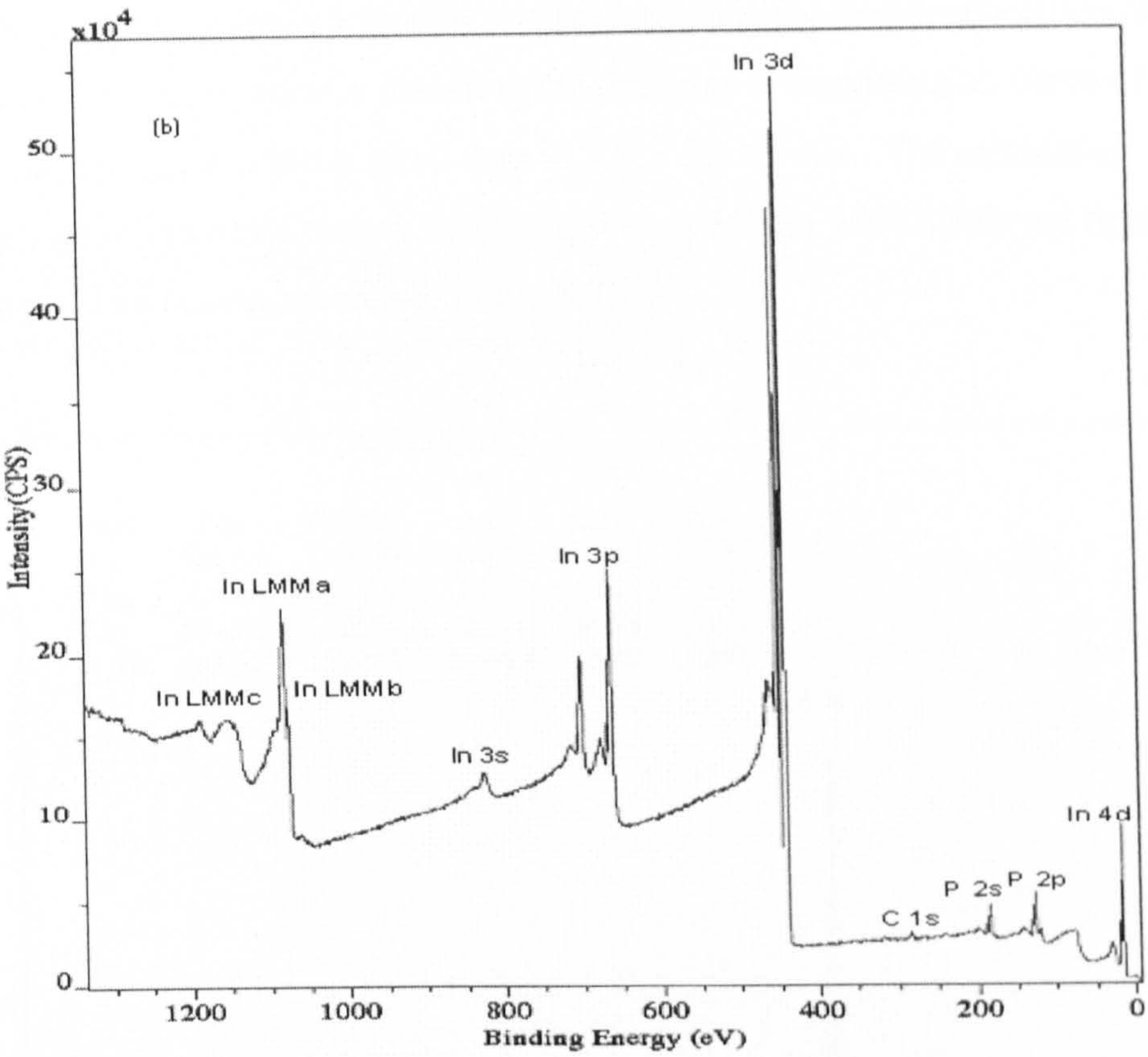

Fig 6.2 (b) XPS spectrum of InP (100) after 4 keV Ar^+ ion sputtering under 40° incident angle for 60s

6.1.2.2. Compositional Change of Ar^+ Ion Bombarded InP (100) Surface

Chemical components of the InP(100) surfaces before and after Ar^+ ion bombardment Ar^+ ion bombardment can be quantified by analysis of the corresponding wide scan spectra. This sub-section presents the results of the analysis.

6.1.2.2.1 Analysis of Changes in Atomic Concentrations

Surface atomic concentrations were calculated from the wide scan spectra obtained on surfaces of a non-sputtered and a sputtered sample. The analysis was carried out using CasaXPS demo version XPS analysis software choosing Tougaard background and Kratos element library. The software automatically defines regions of the peaks chosen for analysis. The area under each peak was corrected by its Relative Sensitivity Factor (RSFs) corresponding to the transition provided by the Kratos element library. The RSFs used in this study were 0.468, 7.265, 0.78, and 0.278 for P2p, In3d, O1s and C1s

respectively. Transmission correction was performed at the time a quantification table was computed by automatically detecting the presence of transmission curve of the spectrometer included in the original data in VMS file format. The calculated concentrations of elements chosen in a wide-scan spectrum were displayed together with the spectrum. The results are shown in Fig 6.3.

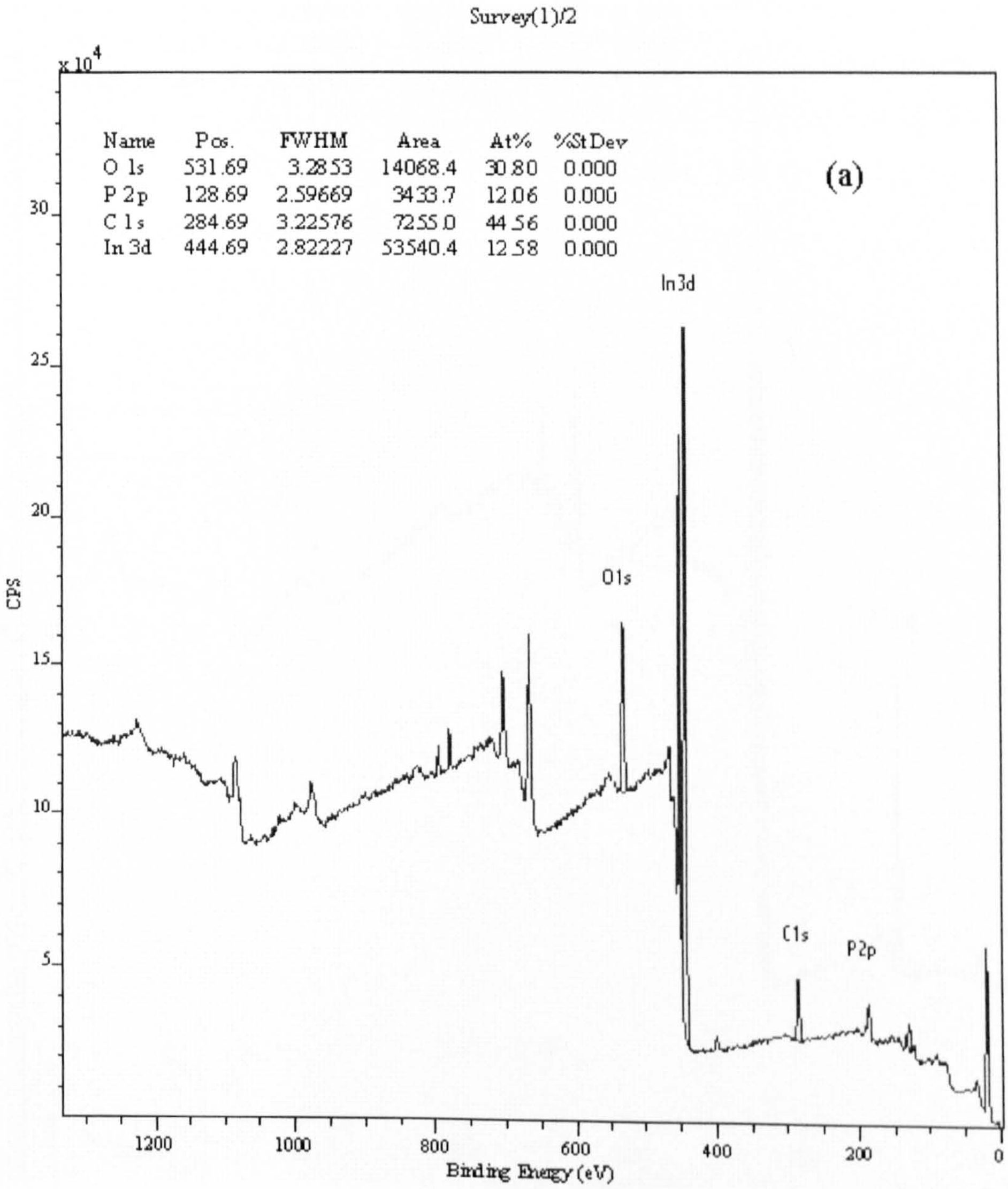

Fig 6.3 (a) Atomic concentration analysis of the non-sputtered InP (100) sample.

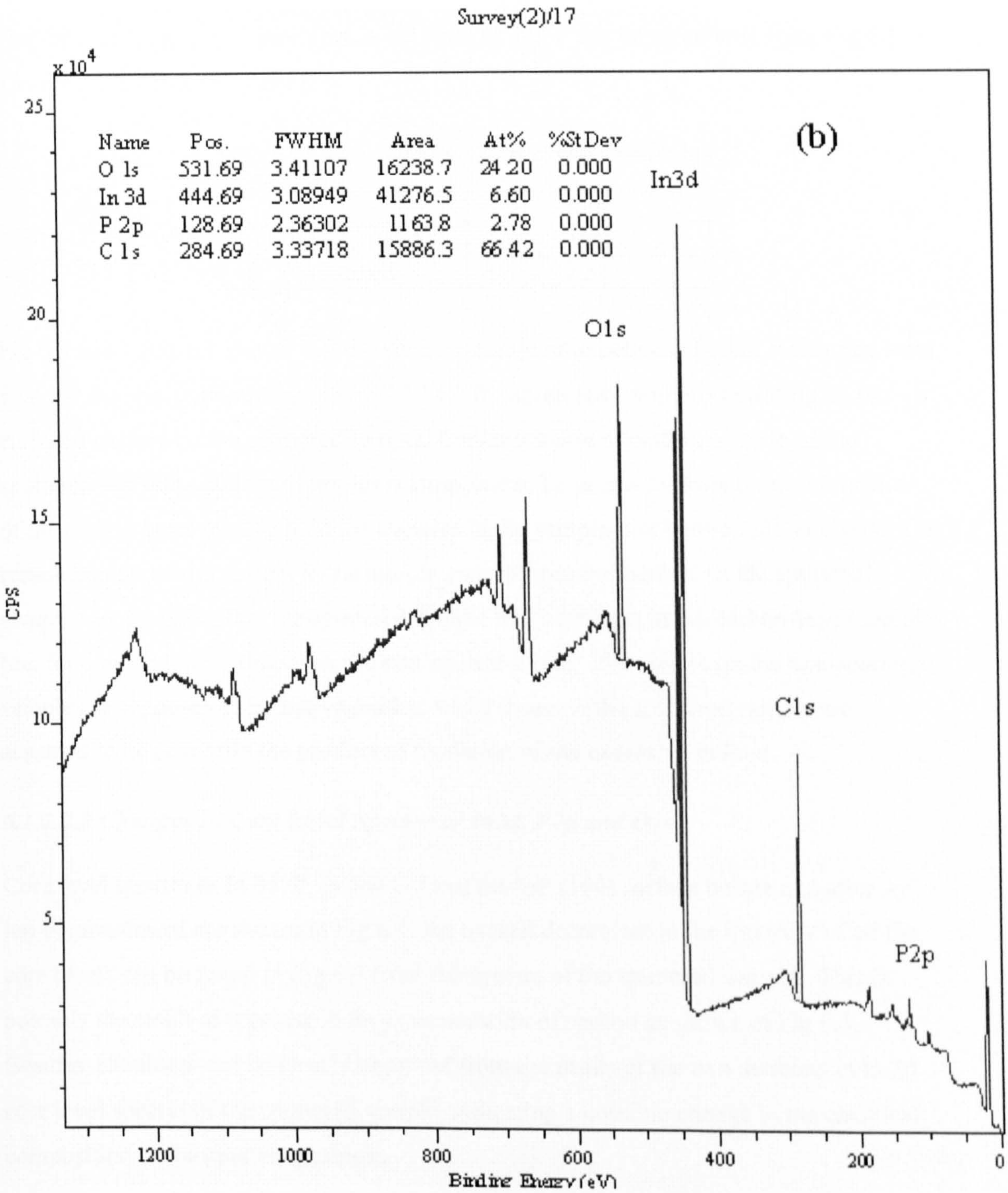

Fig 6.3 (b) Atomic concentration analysis of the sputtered (b) InP (100) sample. The sample had been kept in air for 12 months after sputtering by 2 keV Ar^+ ion beam at 72° incident angle and a dose of 1.75×10^{17} cm^{-2}

The ratio of the atomic concentration between In and P can be calculated from Fig 6.3. The results are listed in table 6.1.

Table 6.1 Calculated ratios of atomic concentrations In/P

	In/P
Non-sputtered	1.04
Sputtered	2.37

Fig 6.3 and Table 6.1 shows that the surface atomic ratio between In and P changed from 1.04 for the non-sputtered sample to 2.37 for the sputtered sample, suggesting an In enriched surface on the sputtered sample. Contamination of carbon on both of the sputtered and non-sputtered samples is supposed to be primarily from trace sublimation of the carbon tapes used to hold the samples in the sample-box before XPS analysis. The reason behind the increment in the atomic concentration of carbon on the sputtered sample was probably that the sputtered sample had been kept in the carbon-taped sample-box for a much longer time than the non-sputtered one. The oxides on the non-sputtered sample are supposed to be native oxides, while those on the sputtered sample are assumed to be primarily the product of oxidation of the excessive indium.

6.1.2.2.2 Changes in Core Level Spectra of In3d, P2p and O1s

Core level spectra of In 3d, P 2p and O 1s of the InP (100) surface before and after Ar^+ ion bombardment are shown in Fig 6.4. An overall decrement in the intensity of all the core levels can be found in Fig 6.4 from the spectra of the sputtered sample. This is possibly the result of increase in the concentration of carbon as shown in Fig 6.3. Besides, shoulders can be clearly observed from the peaks of the two doublets in In 3d core level spectra of the sputtered sample, indicating a possible change in the chemical composition of the sputtered sample.

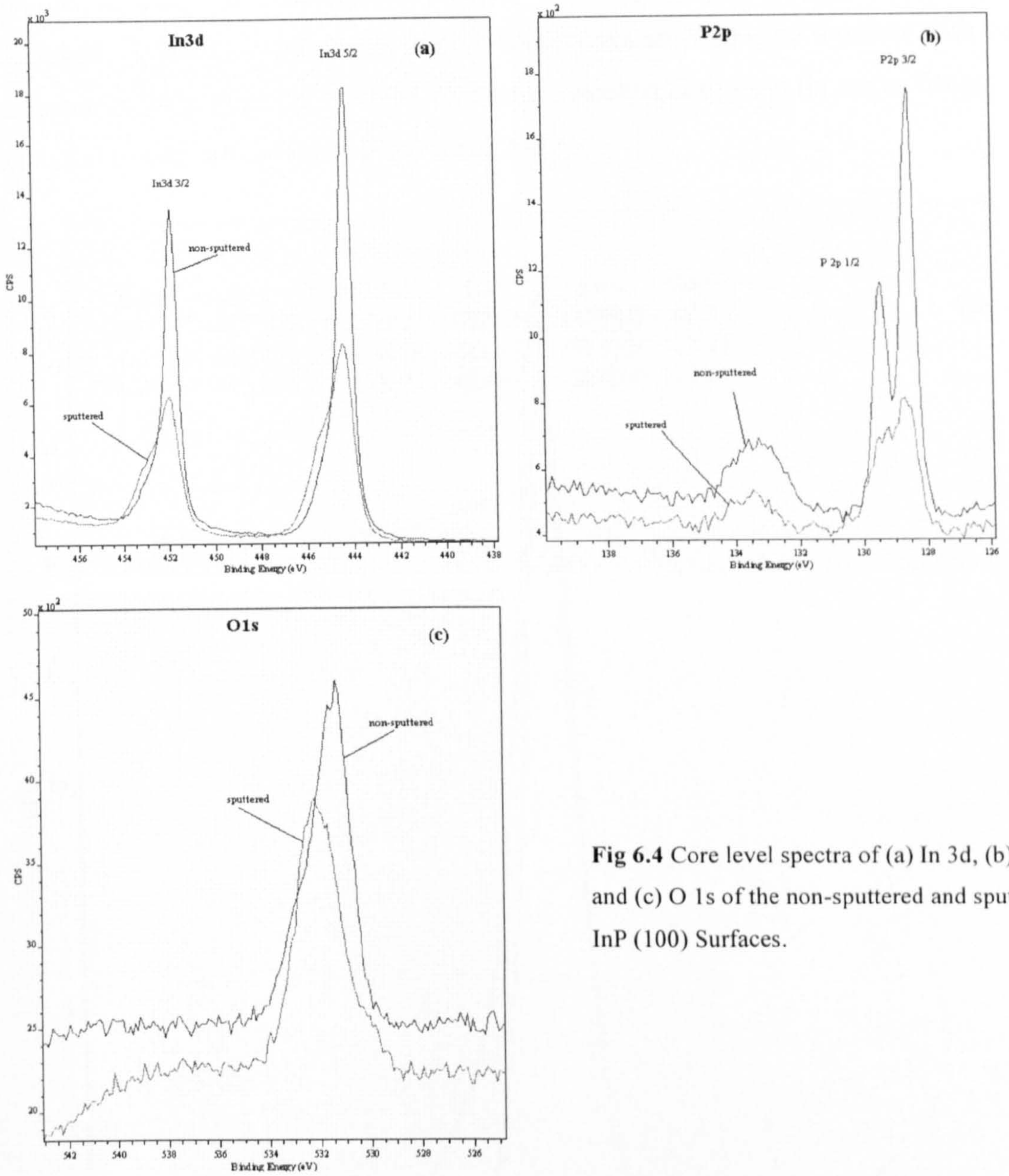

Fig 6.4 Core level spectra of (a) In 3d, (b) P 2p, and (c) O 1s of the non-sputtered and sputtered InP (100) Surfaces.

The sputtered sample had been kept in air for 12 months before XPS analysis. It is reasonable to assume that the dominant factor affecting the elemental composition on the surface of the sputtered sample is ambient oxidation. In order to find out the details of structural change on the surface of the sputtered sample, the core level spectra displayed in Fig 6.4 are decomposed to reveal possible components in these spectra. Curve fitting to the spectra in Fig 6.4 was carried out using GL (m) line-shape (a product of Gaussian and Lorenzian, with the mixing parameter $m = 30\text{--}90$, Ref. eqn. (2.14) in section 2.3.1.3)

with Tougaard background. The value of *m* may differ from fitting of one curve to another, as long as best fitting with physical meaning to the envelope curve can be achieved. Synthetic components of core level peaks are displayed together with the parameters (peak position, FWHM, and area concentration) used for curve fitting. The analysed results are shown in Fig 6.5 and Fig 6.6.

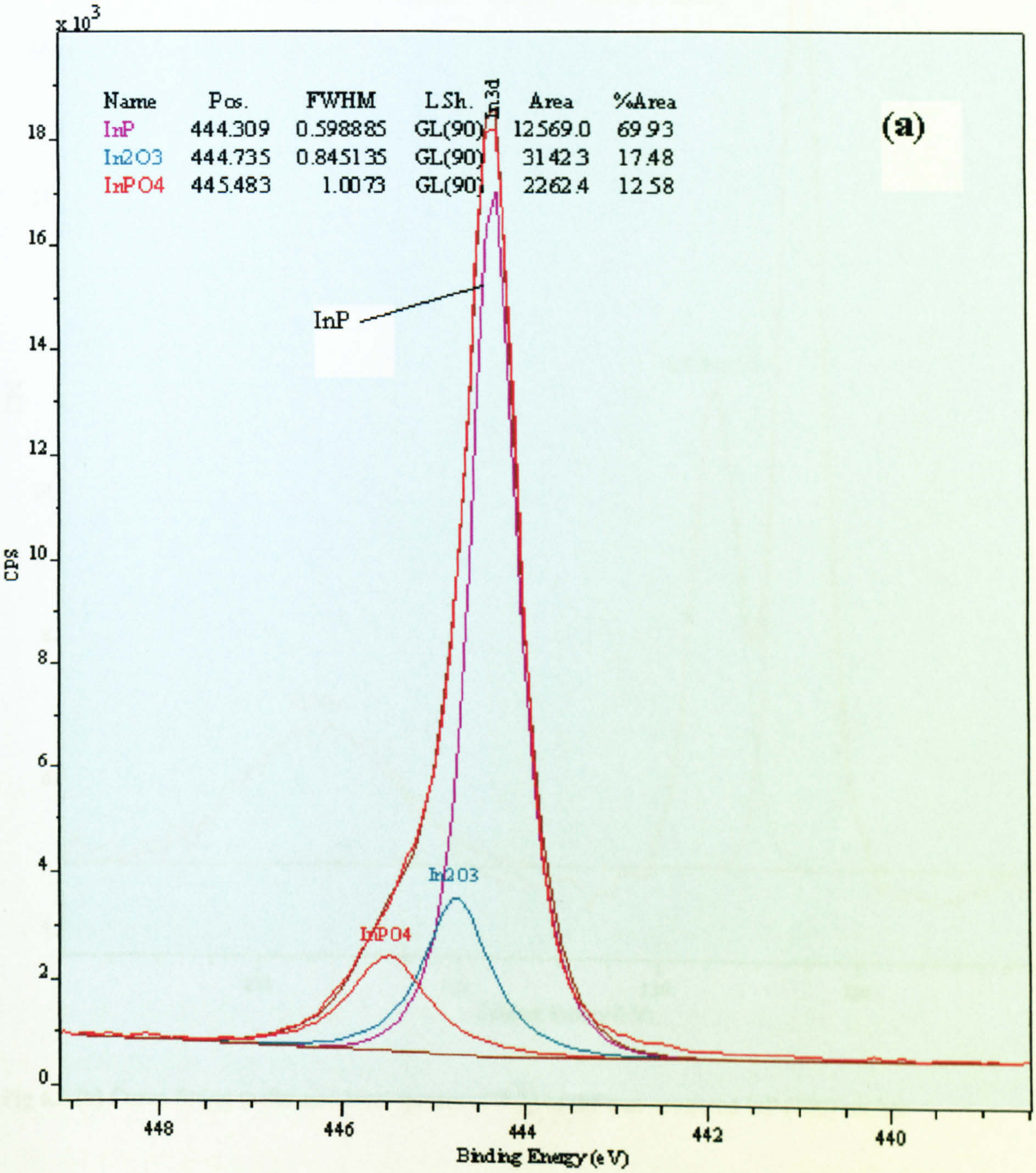

Fig 6.5 (a) Curve-fitting to the core level spectra of In $3d_{5/2}$ of the non-sputtered InP (100) surface

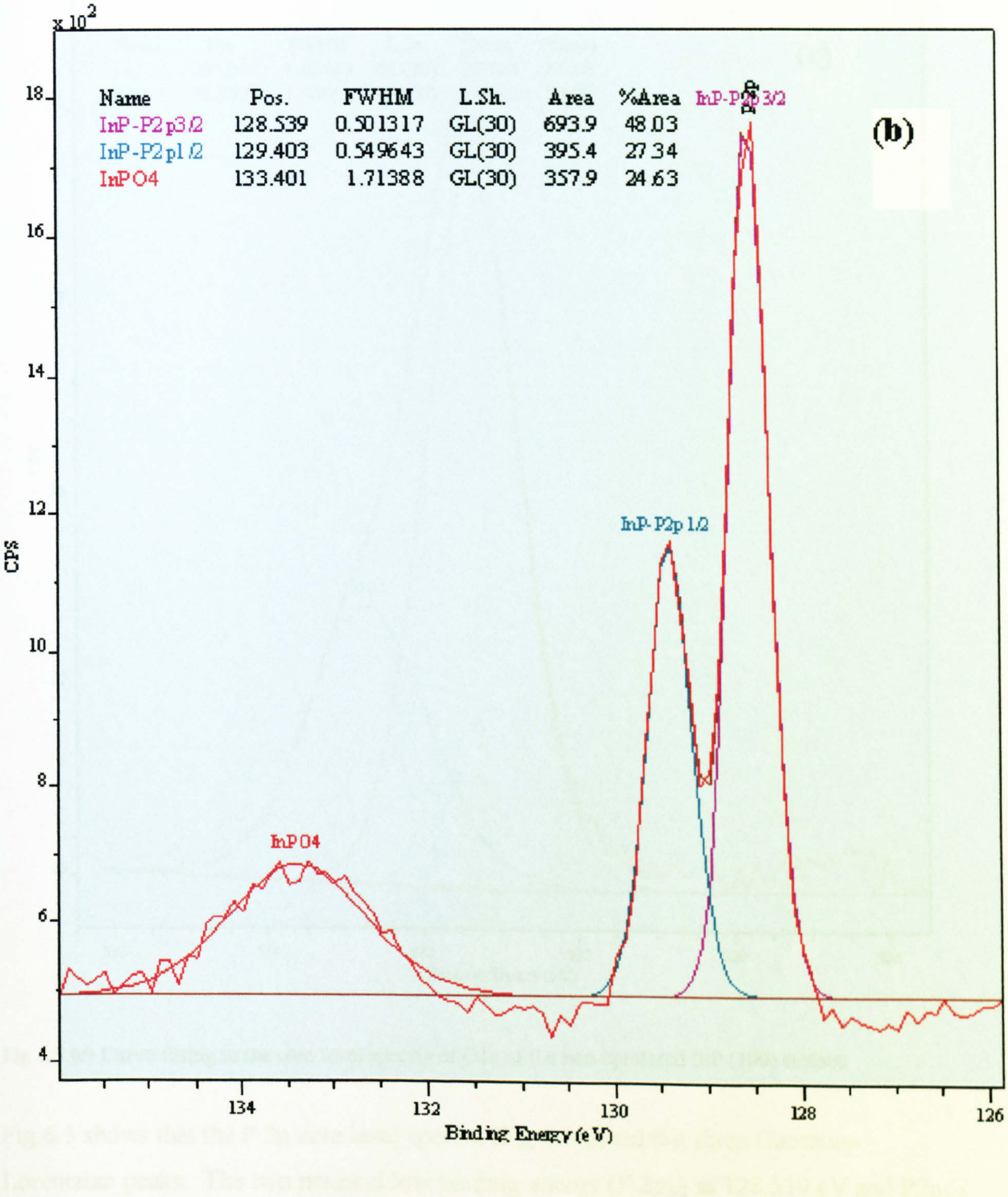

Fig 6.5 (b) Curve-fitting to the core level spectra of P 2p of the non-sputtered InP (100) surface

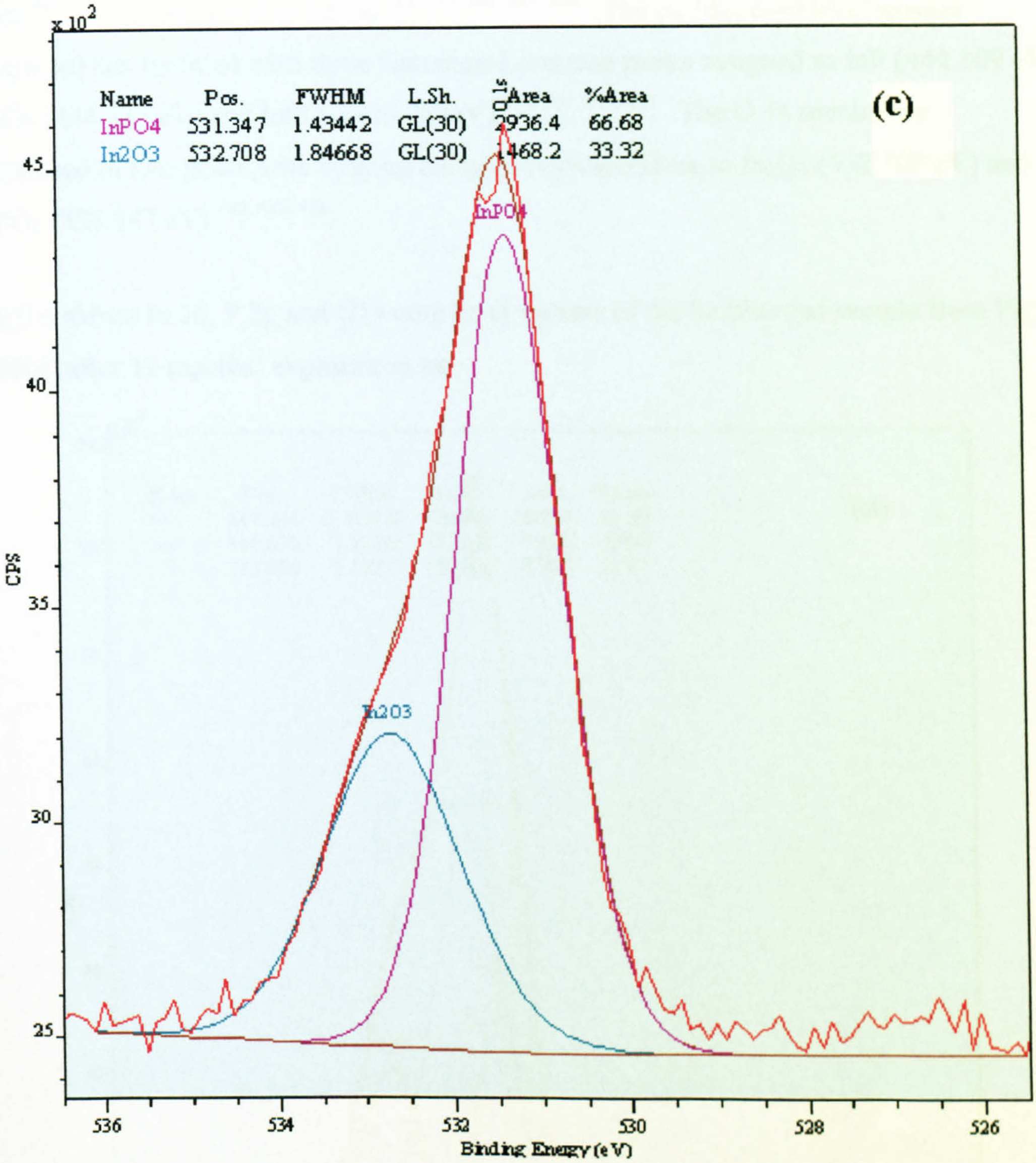

Fig 6.5 (c) Curve-fitting to the core level spectra of O1s of the non-sputtered InP (100) surface

Fig 6.5 shows that the P 2p core level spectra (Fig 6.5 b) exhibit three Gaussian-Lorentzian peaks. The two peaks at low binding energy (P $2p_{3/2}$ at 128.539 eV and $P2p_{1/2}$ at 129.403 eV) can be assigned to phosphorus in InP [113, 133, 426] due to spin-orbit splitting, whereas the peak at high binding energy (133.401 eV), which is 4.5 eV away from the centre of the two P2p doublet, indicative of phosphate formation consisting of PO_4

units [427], can be assigned to $InPO_4$ [113, 133, 145, 427, 428]. The In $3d_{5/2}$ core level spectra (Fig 6.5a) can be fitted with three Gaussian-Loretzian peaks assigned to InP (444.309 eV), In_2O_3 (444.735 eV) and $InPO_4$ (445.783eV) [113, 133, 145, 428]. The O 1s spectra are composed of two peaks with binding energies corresponding to In_2O_3 (532.708 eV) and $InPO_4$ (531.347 eV) [133, 427, 428].

Fig 6.6 shows In 3d, P 2p and O1s core level spectra of the bombarded sample from Fig 5.20(d) after 12 months' exposure in air.

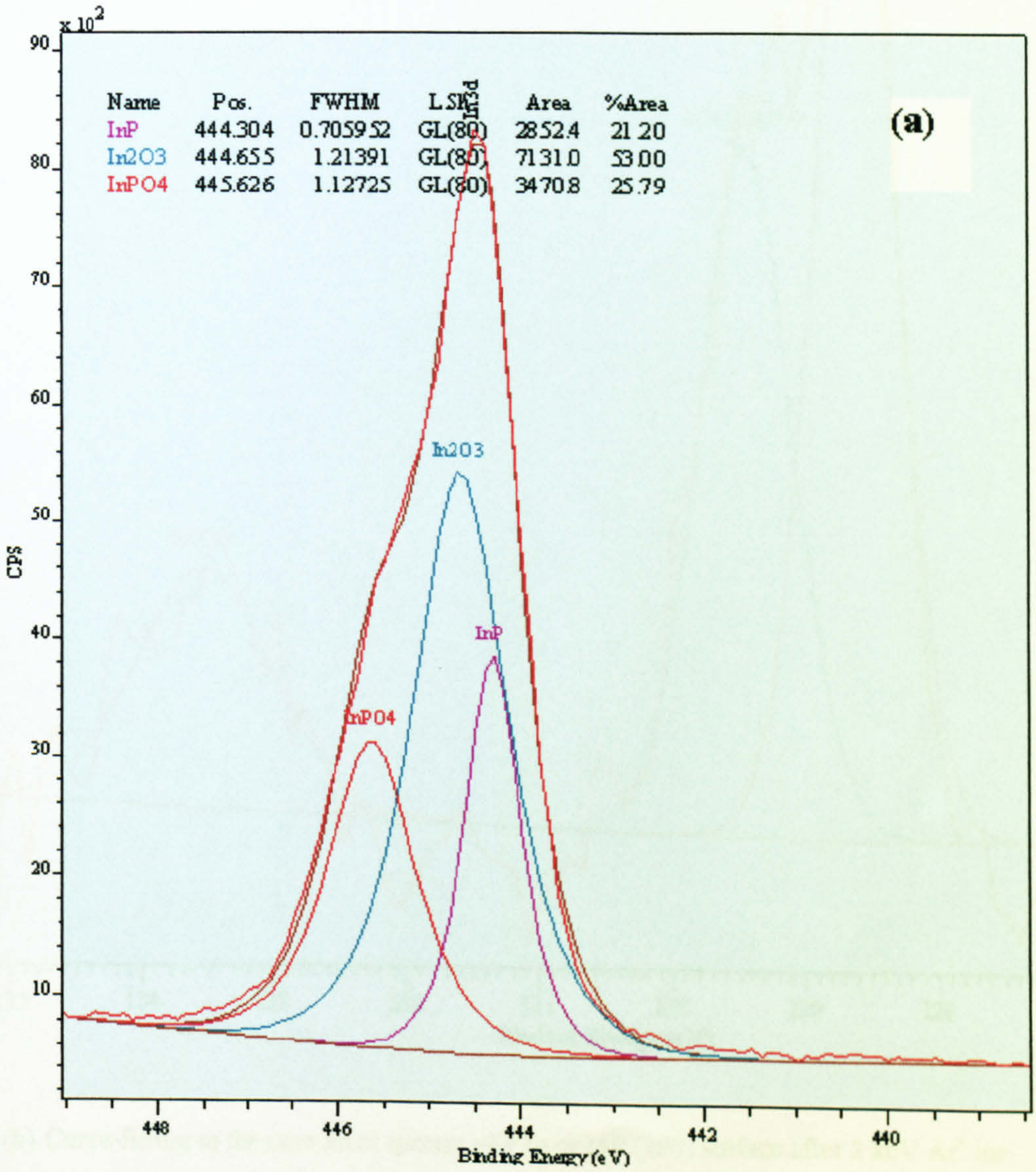

Fig 6.6 (a) Curve-fitting to the core level spectra of In $3d_{5/2}$ of InP (100) surface after 2 keV Ar^+ ion sputtering at 72° incident angle and a dose of 1.75×10^{17} cm^{-2}. The sputtered sample had been kept in air for 12 months before XPS analysis.

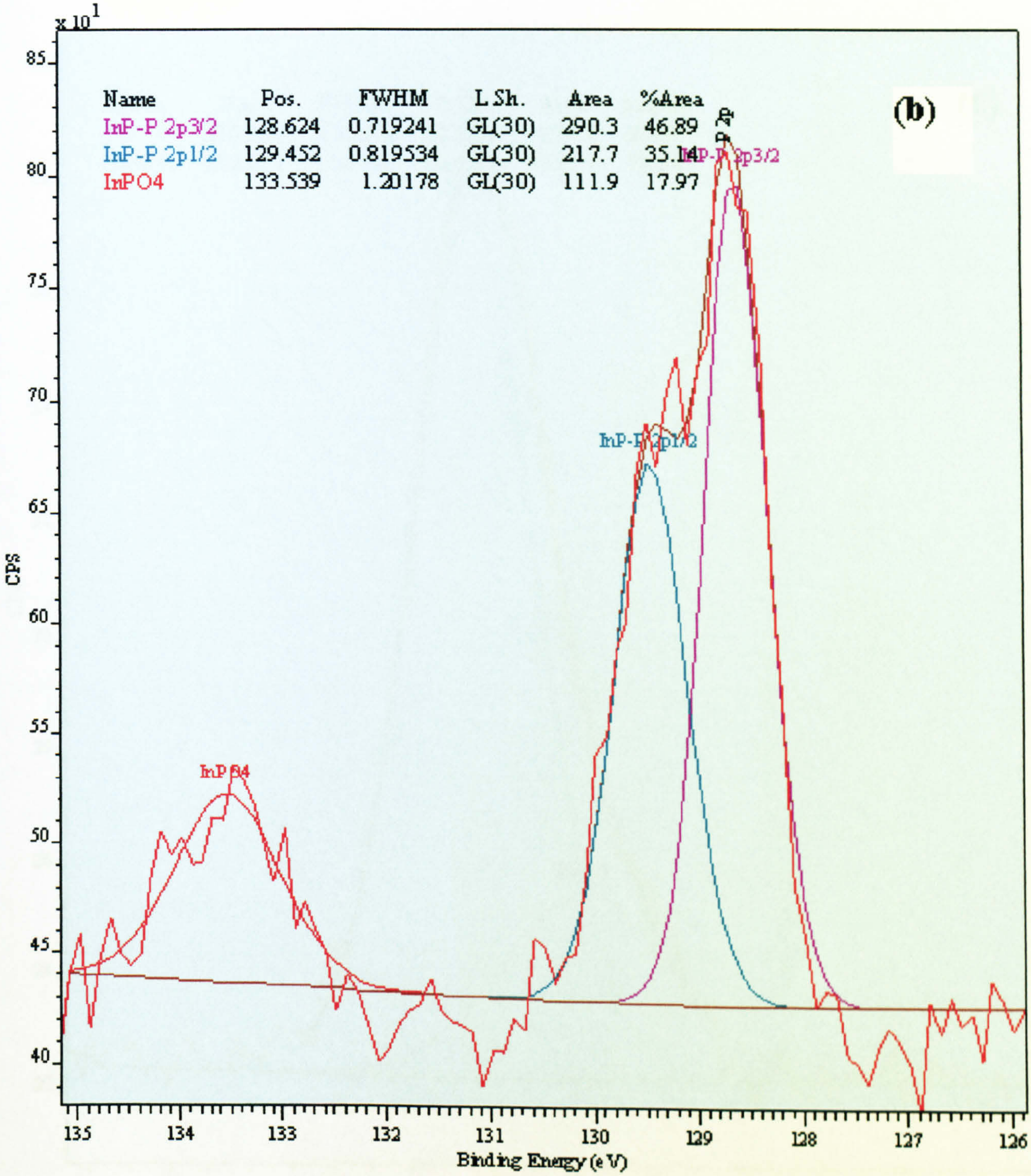

Fig 6.6 (b) Curve-fitting to the core level spectra of P2p of InP (100) surface after 2 keV Ar^+ ion sputtering at 72° incident angle and a dose of 1.75×10^{17} cm^{-2}. The sputtered sample had been kept in air for 12 months before XPS analysis.

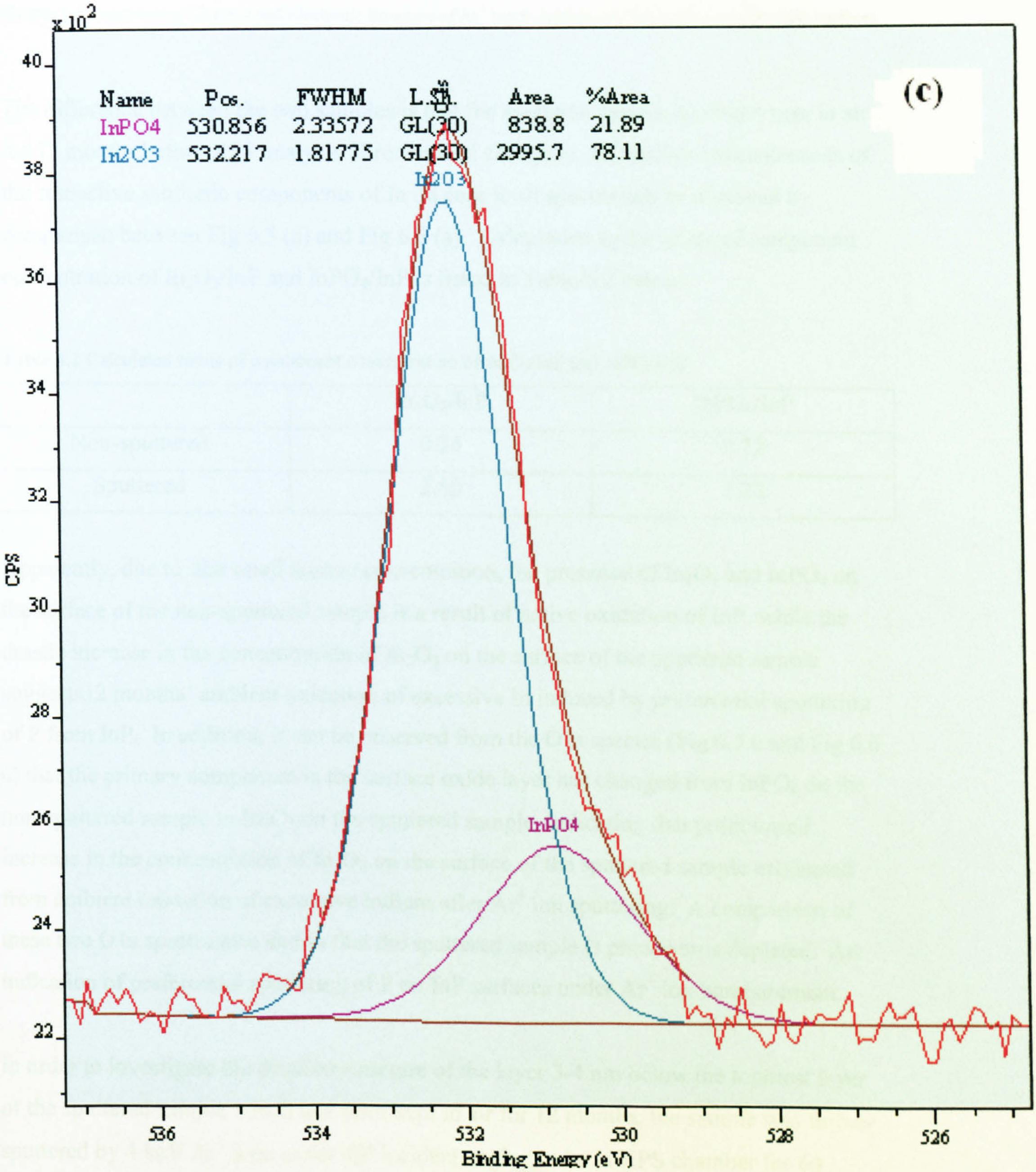

Fig 6.6 (c) Curve-fitting to the core level spectra of O1s of InP (100) surface after 2 keV Ar^+ ion sputtering at 72° incident angle and a dose of 1.75×10^{17} cm^{-2}. The sputtered sample had been kept in air for 12 months before XPS analysis.

The difference between the two samples is that the sputtered sample had been kept in air for 12 months before XPS analysis. Pronounced change in the relative concentrations of the respective synthetic components of In 3d core level spectra can be observed by comparison between Fig 6.5 (a) and Fig 6.6 (a). Calculation to the ratios of component concentration of In_2O_3/InP and $InPO_4$/InP is listed in Table 6.2 below:

Table 6.2 Calculated ratios of component concentration of In_2O_3/InP and $InPO_4$/InP

	In_3O_2/InP	$InPO_4$/InP
Non-sputtered	0.25	0.72
Sputtered	2.50	1.22

Apparently, due to the small atomic concentration, the presence of In_2O_3 and $InPO_4$ on the surface of the non-sputtered sample is a result of native oxidation of InP, while the drastic increase in the concentration of In_2O_3 on the surface of the sputtered sample suggests12 months' ambient oxidation of excessive In induced by preferential sputtering of P from InP. In addition, it can be observed from the O1s spectra (Fig 6.5 c and Fig 6.6 c) that the primary component in the surface oxide layer has changed from $InPO_4$ on the non-sputtered sample to In_2O_3 on the sputtered sample, indicating that pronounced increase in the concentration of In_2O_3 on the surface of the sputtered sample originated from ambient oxidation of excessive indium after Ar^+ ion sputtering. A comparison of these two O1s spectra also shows that the sputtered sample is phosphorus depleted. An indication of preferential sputtering of P on InP surfaces under Ar^+ ion bombardment.

In order to investigate the detailed structure of the layer 3-4 nm below the topmost layer of the sputtered sample which had been kept in air for 12 months, the sample was further sputtered by 4 keV Ar^+ ions under 40° incident angle *in-situ* in XPS chamber for 60 seconds after acquisition of the narrow scan spectra shown in Fig 6.6. In $3d_{5/2}$, P 2p and O1s core level spectra core level spectra collected after this stage is shown in Fig 6.7.

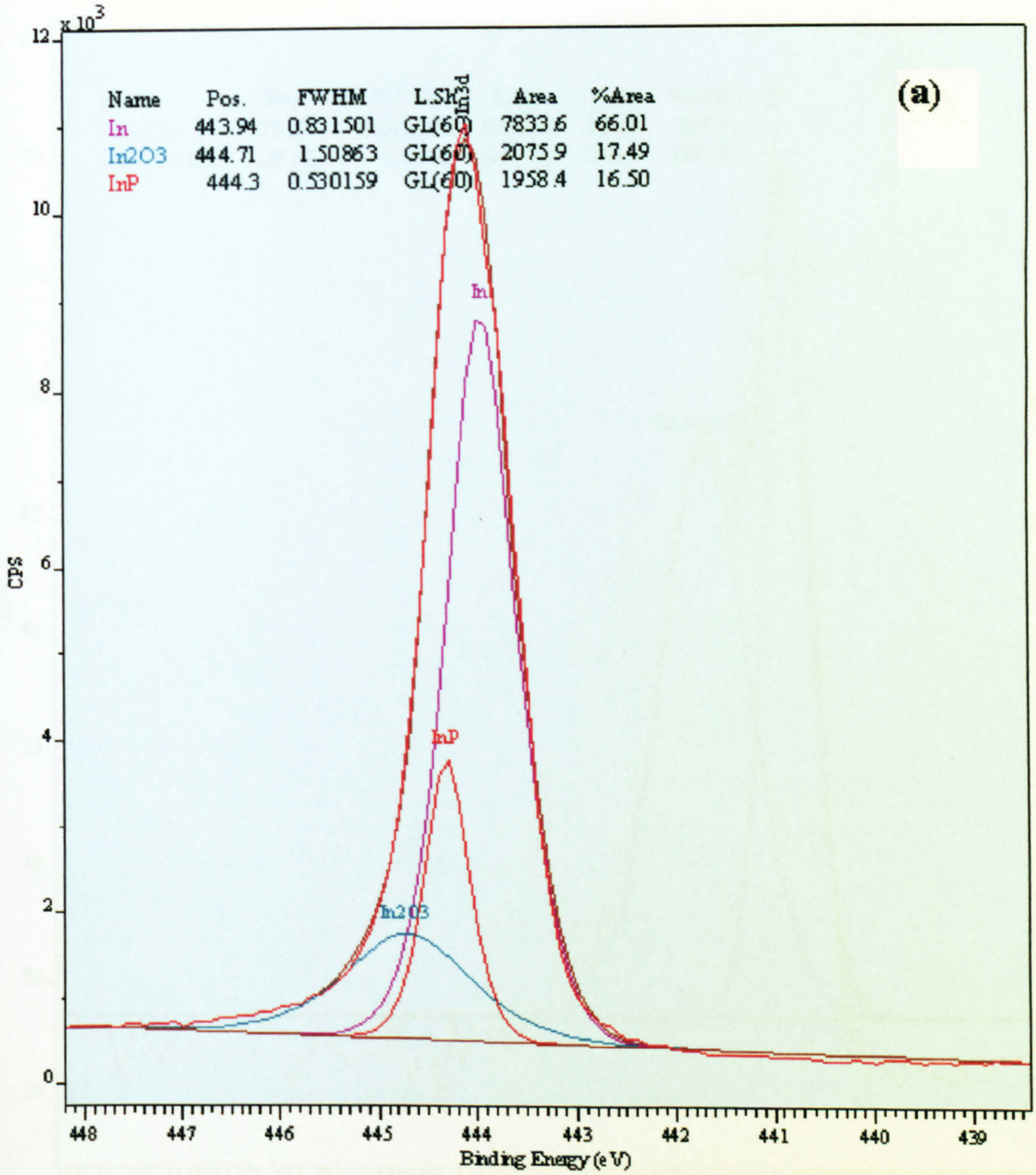

Fig 6.7 (a) Core level spectra of In $3d_{5/2}$ of the InP (100) surface after 2 keV Ar^+ ion sputtering at 72° incident angle and a dose of 1.75×10^{17} cm^{-2}. The sample had been kept in air for 12 months following further 4 keV Ar^+ ion sputtering under 40° incidence for 60 seconds in the XPS chamber before XPS analysis.

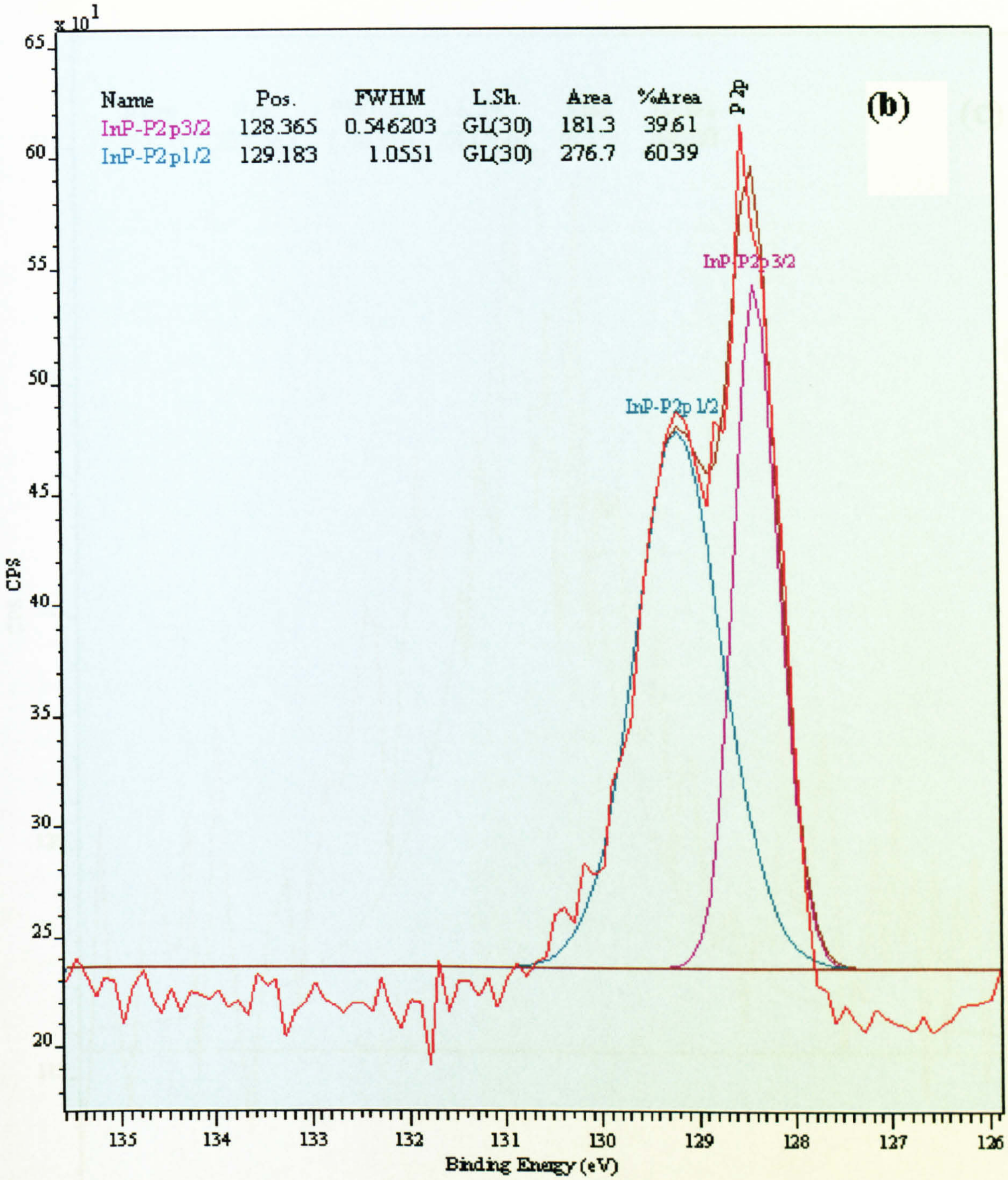

Fig 6.7 (b) Core level spectra of P2p of the InP (100) surface after 2 keV Ar^+ ion sputtering at 72° incident angle and a dose of 1.75×10^{17} cm^{-2}. The sample had been kept in air for 12 months following further 4 keV Ar^+ ion sputtering under 40° incidence for 60 seconds in the XPS chamber before XPS analysis.

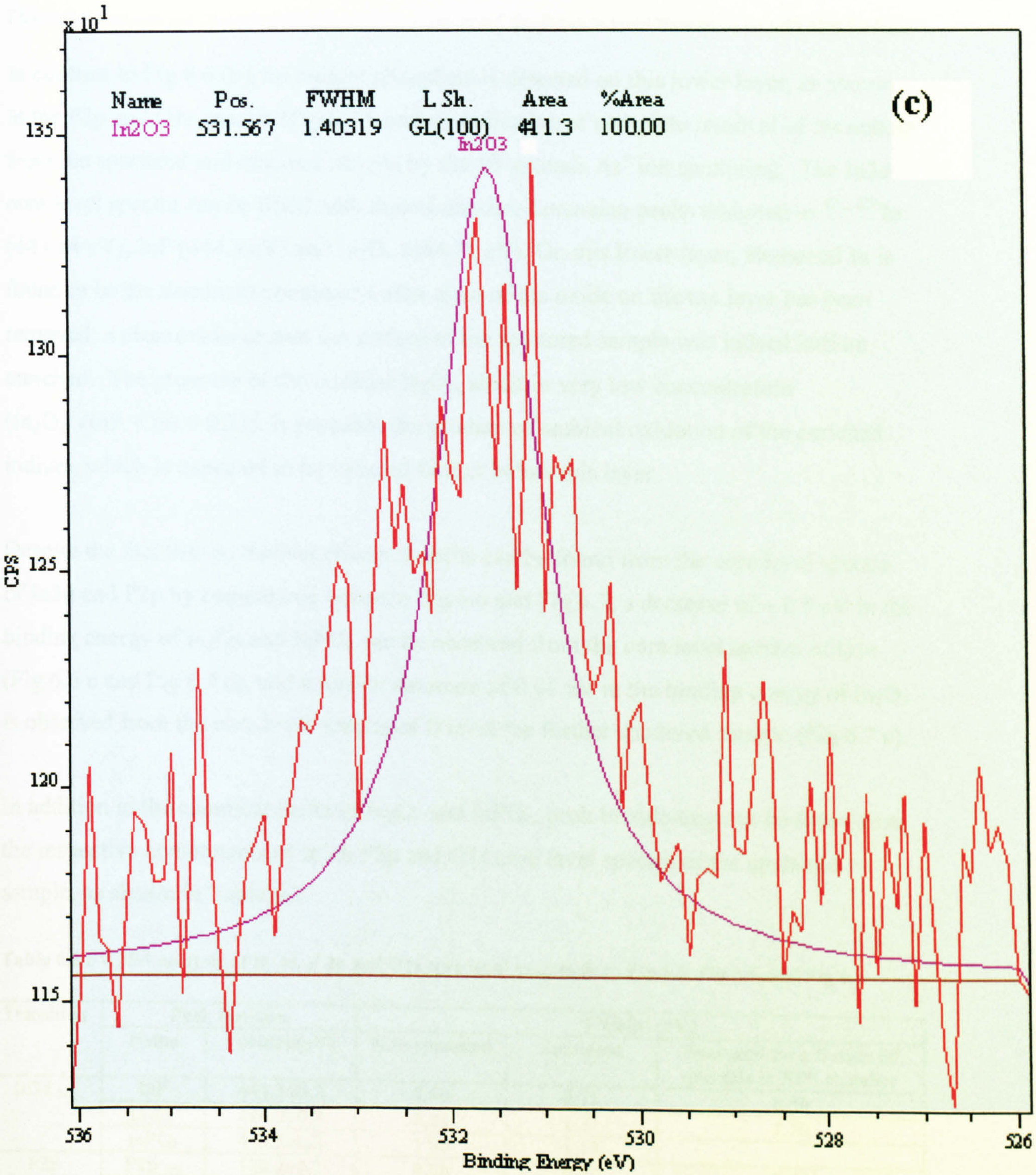

Fig 6.7 (c) Core level spectra of O1s of the InP (100) surface after 2 keV Ar^+ ion sputtering at 72° incident angle and a dose of 1.75×10^{17} cm^{-2}. The sample had been kept in air for 12 months following further 4 keV Ar^+ ion sputtering under 40° incidence for 60 seconds in the XPS chamber before XPS analysis.

In contrast to Fig 6.6 (b), no indium phosphate is detected on this lower layer, as shown in the P2p and O1s spectra (Fig 6.7 b and c), indicative of complete removal of phosphate from the sputtered and oxidised sample by the 60 seconds Ar^+ ion sputtering. The In3d core level spectra can be fitted with three Gaussian-Lorenzian peaks assigned to [421, 428]In (443.94 eV), InP (444.3 eV) and In_2O_3 (444.71 eV). On this lower layer, elemental In is found to be the dominant component after most of the oxide on the top layer has been removed, a clear evidence that the surface of the sputtered sample was indeed indium enriched. The presence of the residual In_2O_3, albeit in very low concentration (In_2O_3/ (InP + In) = 0.21), is probably the product of ambient oxidation of the enriched indium, which is expected to be reduced further below this layer.

Despite the fact that no distinct chemical shifts can be found from the core level spectra of In3d and P2p by comparison between Fig 6.6 and Fig 6.7, a decrease of ~ 0.5 eV in the binding energy of In_2O_3 and $InPO_4$ can be observed from the core level spectra of O1s (Fig 6.6 c and Fig 6.7 c), and a further decrease of 0.65 eV in the binding energy of In_2O_3 is observed from the core level spectra of O1s on the further sputtered sample (Fig 6.7 c).

In addition to the chemical shifts of In_2O_3 and $InPO_4$, peak broadening can be found from the respective components of In3d, P2p and O1s core level spectra of the sputtered sample, as shown in Table 6.3

Table 6.3 FWHM analysis of In 3d, P 2p and O1s core level spectra from Fig 6.5, Fig 6.6, and Fig 6.7

Transition	Peak Position		FWHM (eV)		
	Name	Position(eV)	Non-sputtered	Sputtered	Sputtered for a further 60 seconds in XPS chamber
$In3d_{5/2}$	InP	444.3±0.2	0.60	0.71	0.50
	In_2O_3	444.7±0.2	0.84	1.21	1.50
	$InPO_4$	445.5±0.2	1.00	1.13	
P2p	$P2p_{3/2}$	128.8±0.2	0.50	0.72	0.55
	$P2p_{1/2}$	129.4±0.2	0.55	0.82	1.06
	InPO4	133.4±0.2	1.71	1.20	
O1s	In_2O_3	532.7±0.5	1.85	1.82	1.40
	$InPO_4$	531.3±0.5	1.43	2.34	

Comparing the FWHM of the sputtered and the non-sputtered sample, peak broadening can also be found from the two peaks of P2p and the synthetic component associated with

In in InP on the sputtered sample. A possible explanation to the peak broadening is that the depletion of phosphorus from InP creates some defects and changes the chemical bonding between In and P. The enriched In could replace those lattice sites previously occupied by P, or be jammed as interstitials after ion sputtering, leading to contraction of lattice spacing [429]. It is pointed out [429] that In interstitials produced upon ion bombardment at room temperature can migrate over long distances leaving behind immobile vacancies as point defects. Introduction of a point defect in a crystalline matrix induces displacement of neighboring atoms. The relaxation of vacancy-type defects causes inward displacement of surrounding atoms resulting in lattice expansion, i.e., positive strain; interstitial atoms produce an outward displacement of surrounding atoms resulting in a negative strain. The latter is greater than that of single vacancies and relieves the exact cancellation of simple defect stress fields leading to lattice contraction. As a result, a disorder is created on the surface of the sputtered sample. Generation of surface disorder would induce a perturbation of the chemical environment of In and P in InP and consequently create a number of closely spaced peaks non-resolvable by curve fitting [430].

The great increase in the In/P ratio (2.37) upon further sputtering of the sputtered and oxidised InP (100) sample proves that XPS depth profiling by *in situ* Ar^+ ion sputtering is not a good choice for in depth analysis of multi component samples with an intense preferential sputtering effect like InP.

6.2 Electronic Structure of Ar^+ Ion Irradiated InP (100) Surfaces

Scanning Tunnelling Spectroscopy is a spectroscopic analysis technique which uses a scanning tunnelling microscope with the aim of analysing tunnelling conductance and band structure of surface features at nanometre or atomic scale.

The principle of Scanning Tunnelling Spectroscopy has been described in section 2.1.2. This section presents the experimental results of STS on the Ar^+ ion irradiated InP (100) surfaces. The objective of these measurements is to extract some spatially resolved information of the chemical composition on surfaces of the Ar^+ ion irradiated samples in nanometre scale. If the ripples and nanowires fabricated in Chapter 5 can be found indium enriched by STS, the theory of preferential sputtering and the model of nanowire formation by cone-mergence can be justified further.

STM/STS/CITS experiments were performed at room temperature with a commercial VT-STM system under UHV condition (Omicron GmbH, Germany). During the measurements the base pressure was kept at 2×10^{-10} mbar. The tips used were prepared by mechanical cutting from 90%Pt-10%Ir alloy wires and characterized by successful acquisition of correct image of steps and terraces with atomic resolution on good quality Au (111) substrates or highly orientated pyrolytic graphite (HOPG) surfaces. In spectroscopic mode, *I/V* curves were recorded simultaneously with a constant current image by the interrupted-feed-back-loop technique. Based on these measurements the first derivative of the tunneling current with respect to voltage *(dI/dV)* was calculated. The *dI/dV* spectra were normalized using the method proposed by Feenstra [282] where the differential conductance is divided by the total conductance - *(dI/dV)/(I/V)*. The *(dI/dV)/(I/V)* quantity is a measure of the local density of states of the surface - LDOS. The divergence problem in the case of *(dI/dV)/(I/V)* was overcome by applying some amount of broadening *(ΔV)* to the I/V values. In all cases $\Delta V = 1V$ value was chosen.

The typical *I/V* curve recorded on a non-sputtered InP surface is presented in Fig 6.8 (a). In all cases the bias voltage values were chosen to correspond to the energy of the state relative to the Fermi level of the sample. It is clearly observed that the *I/V* curve shows the asymmetric shape, the tunneling current being higher for the negative polarization of the sample than that for the positive voltage of the same value. This type of asymmetry is typical for p-type semiconductor materials. The normalized *(dI/dV)/(I/V)* spectrum calculated from the I/V curve is presented in Fig 6.8 (b). It is clearly observed that the normalized *(dI/dV)/(I/V)* curve shows asymmetric shape with the energy gap. The width

of the gap measured as a region with *(dI/dV)/(I/V) = 0* is about 1 eV. The energy gap is mainly located above the Fermi level, which is typical for p-type semiconductor materials. The band-gap measured this way is 0.34 eV smaller than that listed in Table 4.1. This difference depicts the effect of native oxides (as has been found by XPS analysis in section 6.1.2.2) on the tunneling conductance.

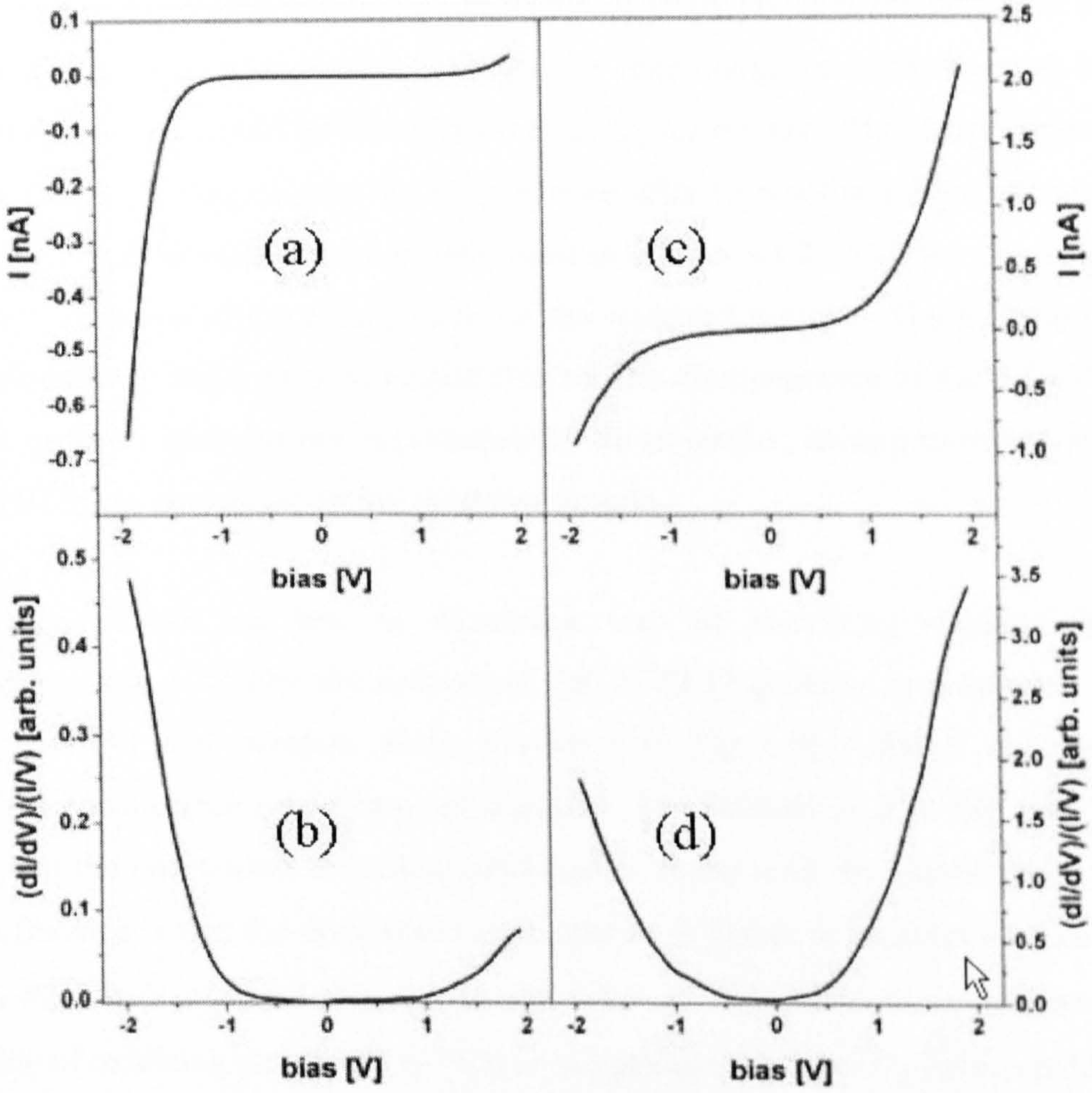

Fig 6.8 (a, b): The *I/V* curve and its normalized form *(dI/dV)/(I/V)* recorded on the non-sputtered InP (100) surface. **Fig 6.8 (c, d):** The I/V curve and its normalized form *(dI/dV)/(I/V)* recorded on the sputtered InP (100) surface.

The typical *I/V* curve recorded on the sputtered InP surface is presented in Fig 6.8 (c). It is clearly observed that the *I/V* curve shows a nearly symmetric shape with high tunneling current for both negative and positive bias voltage. This type of I/V curve is rather typical

for semi-metallic or even metallic materials. The normalized *(dI/dV)/(I/V)* spectrum calculated from the *I/V* curve is presented in Fig 6.8 (d). It is observed that the normalized *(dI/dV)/(I/V)* curve shows lack of the energy gap which is typical for metals.

The metal-like conductance behavior on the sputtered sample implies that the sample is either covered with In or conducting In_2O_3 (c.f. Chapter 4) after 12 months exposure in air. Because of the strong aptitude of oxidation of In by O_2, it is reasonable to assume that almost all the indium nanowires formed from cone-mergence on the topmost layer of the sputtered sample would be transformed to In_2O_3 nanowires. The disappearance of a band-gap of 3.6 eV suggests that the In_2O_3 formed after 12 months' ambient oxidation is not in its non-stoichiometric form as mentioned in section 4.1.2. This may be a result of incomplete oxidation of the excessive In on the sputtered sample. The inclusion of the non-oxidized In in In_2O_3 may be responsible for the disappearance of the 3.6 eV band-gap. In order to give further explanation to these results, measurement of spatially resolved STS was performed on the sputtered sample.

It has been pointed out that an illustrative way of presenting spatially resolved spectroscopic data is to plot the normalized *(dI/dV)/(I/V)* quantity as a function of bias voltage (energy) and position along the surface. Fig 6.9(c) shows the tunneling normalized conductance map measured along the line denoted as α in Fig 6.9(b). It is evident that the normalized tunneling conductance varies with the spatial position. The major difference is that the normalized conductance is higher at location #1 than that at location #2. It is reported that the conductivity of In_2O_3 thin films decreases with adsorption of oxidizing gases such as NO_2 or oxygen as O^{2-}, O^- or O_2^- which reduces the number of free electrons in the material[431]. Ionised oxygen on the surface of an In_2O_3 film works as a dopant that compensates free electrons, as opposed to the case of semiconductors such as silicon where doping is used to create free carriers. Considering only oxygen adsorption, the results in Fig 6.9 indicate that the area at location #2 adsorbs more oxygen than that at location #1.

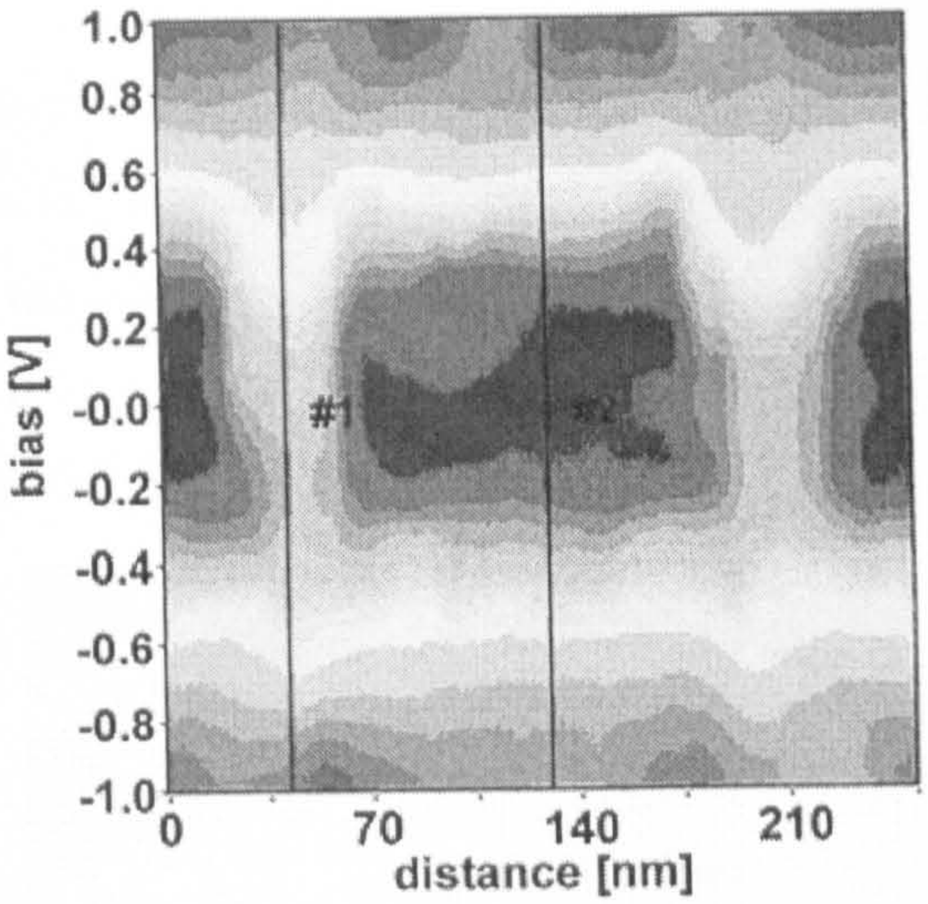

(a)

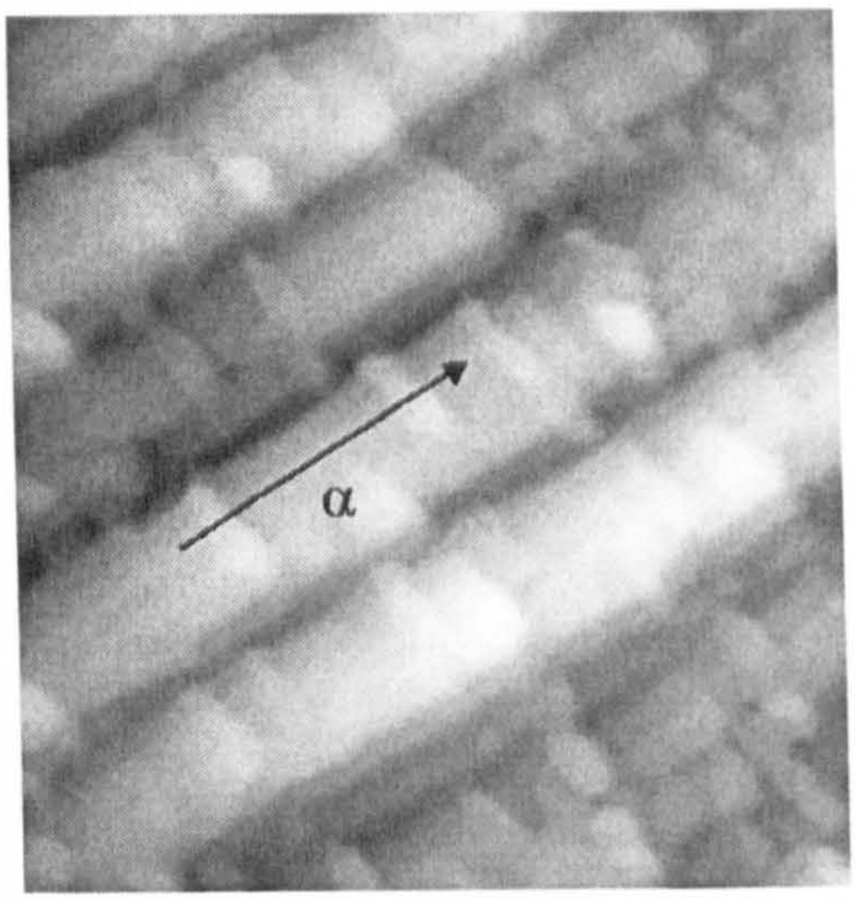

(b)

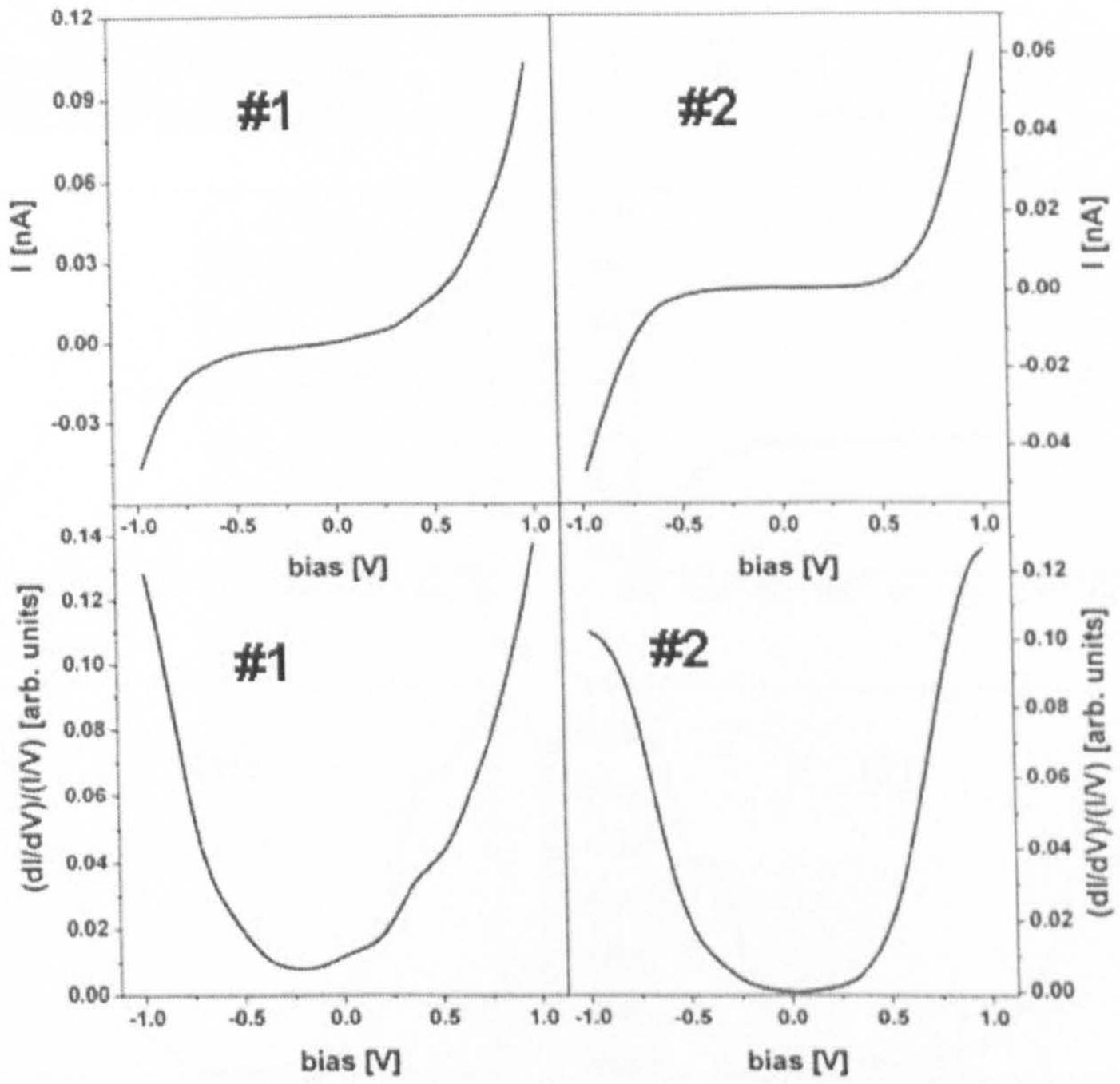

(c)

Fig 6.9 Spatially resolved scanning tunneling spectroscopy measurements on the surface of the sputtered sample: (a) Normalized tunneling conductance map measured as a function of bias voltage and position; (b) STM image of the sputtered InP surface; (c) The *I/V* and *(dI/dV)/(I/V)* curves selected at different spatial positions (#1 - #2). The # positions are shown in Fig 6.9 (a).

Further STS measurement was performed in an attempt to find any difference in tunneling conductance between the areas occupied by nanowires (bright rows in Fig 6.9 b) and the areas in between the nanowires (dark areas between the two bright rows in Fig 6.9 b) on Ar^+ ion bombarded InP (100) surfaces. The results are shown in Fig 6.10, with a region marked with α to analyze tunneling conductance at different locations.

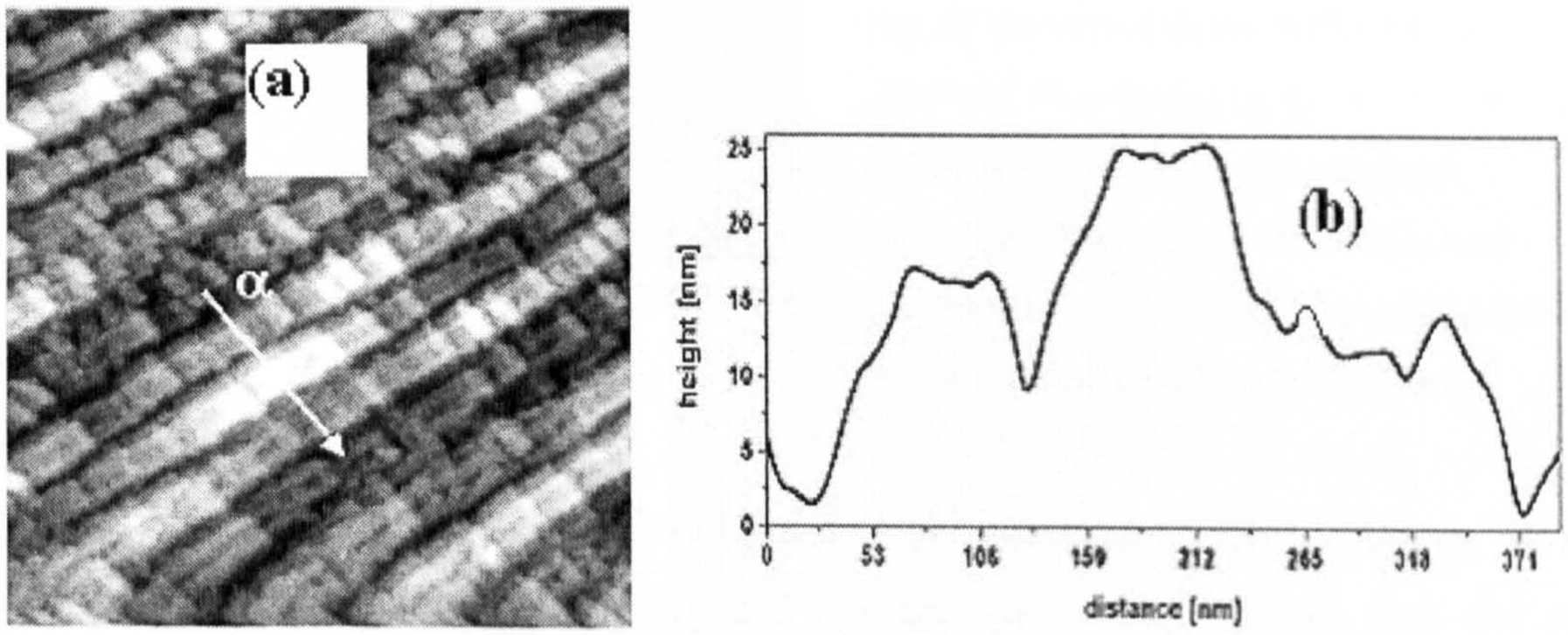

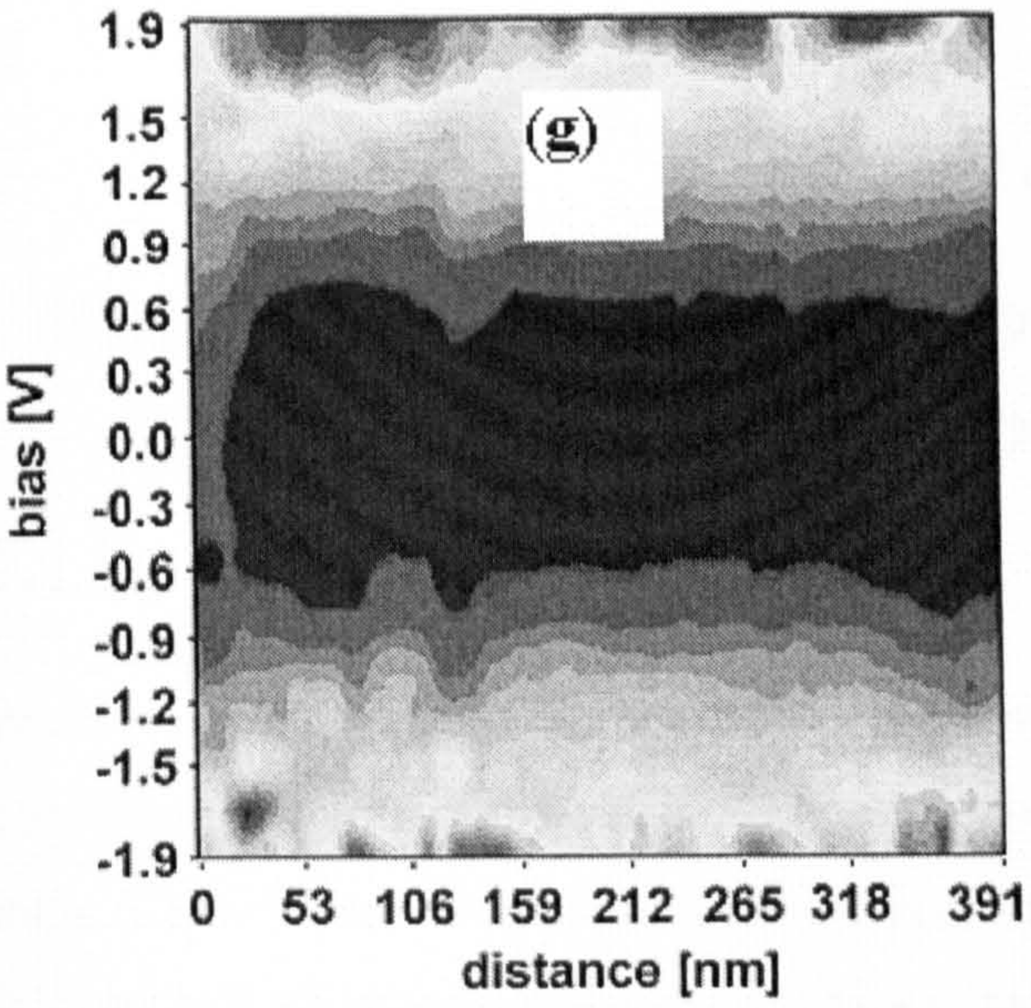

Fig 6.10 Comparison of scanning tunneling conductance between the areas on the bright rows and those in between the bright rows: (a) 1200 nm x 1200 nm STM image (bias = + 2V, tunneling current set point = 1 nA) on the surface of the sputtered InP (100) sample; (b) Cross section measured along the α line in (a); (c—f) The *I/V* curve and its normalized form *(dI/dV)/(I/V)* recorded on the bright rows (c,d) and between the bright rows (e,f); (g) Normalized tunneling conductance map measured as a function of bias voltage and position along the α line marked in (a).

No substantial differences in the *I/V* and *(dI/dV)/(I/V)* curves in Fig 6.10 can be found compared to those in Fig 6.9, and Fig 6.8 (c) and (d), which shows that the region selected with α line in Fig 6.10 (a) is probably composed of conducting In_2O_3. Subtle difference can be found in the normalized tunnelling conductance with *(dI/dV)/(I/V)* values lower in the region on the bright rows, indicative of stronger oxygen adsorption in these areas.

Fig 6.9 suggests that because of the conductive characteristics of In_2O_3, it is literally impossible to resolve the difference in the conductance at the two locations underneath the In_2O_3 layer defined in Fig 6.10 (a). A possible solution to probe distinct differences in the tunnelling conductance between the areas occupied by the nanowires and those in between the nanowires in Fig 6.10 (a) is to perform both ion bombardment and STS measurement *in situ* in UHV so that the effect of surface oxidation can be avoided.

It is thus clear that all the results of *I-V* curves and tunnelling spectroscopy presented in this section actually depict respective results of the oxide layer on top of the bombarded sample surface. On the other hand, the oxide layer stabilizes the features of the bombarded surface and protects the bombardment induced patterns from deterioration.

Chapter 7

Morphology and Monte-Carlo Simulations of Ar^+ Ion Beam Irradiated Si_3N_4 (100) Surfaces

7.1 Introduction

Preferential sputtering of the lighter component of a multi-component crystal has been confirmed experimentally as an established model in the fabrication of nanowires on both ionic (CaF_2) [6, 8] and covalent (InP) crystals (Chapter 5 and Chapter 6). The generality of this mechanism was briefly explored by Ar^+ ion irradiation on Si_3N_4 surfaces. As an important passivation material in the semiconductor industry, Si_3N_4 has not been reported up to now as a material to produce periodic structure by low energy ion beam bombardment. Conducting or semiconducting silicon nanowires on insulating Si_3N_4 substrate, if these can be fabricated by ion irradiation, offer enticing applications in silicon nanoelectronics. It is worth exploring the possibility of preferential sputtering of nitrogen under Ar^+ ion bombardment to fabricate Si nanowires on covalent Si_3N_4 surfaces.

The ratio of equilibrium sputtered surface fractional composition can be calculated according to eqn. (6.3) as:

$$\frac{C_N^{\ s}}{C_{Si}^{\ s}} = \frac{C_N^{\ b}}{C_{Si}^{\ b}} \left(\frac{M_N}{M_{Si}}\right)^{2m} \left(\frac{U_N}{U_{Si}}\right)^{1-2m} \tag{7.1}$$

For an assessment of the value of (C_N^s/C_{Si}^s), substituting $(C_N^b/C_{Si}^b) = 4/3$, the atomic mass of silicon and nitrogen $M_{si} = 28.086$, $M_N = 14.007$, the surface binding energy [365] $U_{si} = 4.7\ eV$, $U_N = 2\ eV$, and $2m = 0.33$ [115], into eqn (7.1), the ratio of equilibrium sputtered surface fractional composition is calculated to be $C_N^s/C_{Si}^s = 0.6$.

Alternatively, the equilibrium fractional composition can be assessed by TRIM simulation in conjunction with eqn (6.1). Therefore, eqn (7.1) gives the value of equilibrium fractional composition as follows:

$$\frac{C_N^{\ s}}{C_{Si}^{\ s}} = \frac{C_N^{\ b}}{C_{Si}^{\ b}} \frac{Y_{Si}}{Y_N} = \frac{4}{3} x \frac{7}{15} = 0.62 \qquad (7.2)$$

This value is in line with the value (0.6) calculated by eqn. (6.1). Thus, it is safe to say that the value *2m=0.33* used by Malherbe[115] for the calculation of equilibrium sputtered surface fractional composition of low energy Ar^+ sputtered InP also applies to Si_3N_4. The value of C_N^s/C_{Si}^s ~0.6 indicates that N is expected to be preferentially sputtered from Si_3N_4, leaving a Si enriched surface.

This chapter enumerates some typical results from the Ar^+ ion irradiated Si_3N_4 (100) surfaces, followed by some analysis of the growth model of the features.

7.2 Method of Experiment

Ar^+ ion beam sputtering of LPCVD (Low Pressure Chemical Vapor Deposition) Si_3N_4 (143 nm thick, supplied by University of Southampton) under glancing incidence angle (72°) was performed with a series of irradiation doses at room temperature. Considering the possible space charge during ion bombardment because of the insulating nature of Si_3N_4, the sample side opposite to the ion beam was grounded with silver paint before introduction of the sample to the load-lock. The irradiated samples were terminated by deposition of 1 nm of Ag *in situ* after ion beam irradiation in the UHV chamber used in Chapter 5 in order to protect the irradiated samples from oxidation. The topography of the irradiated samples was examined by contact mode AFM in air. Distinct features were not found until the irradiation energy was raised to 4.5 keV.

7.3 Results and Discussion

Fig 7.1 shows the AFM topography of the surfaces of the Si_3N_4 samples irradiated with different ion doses. Fig 7.1 (a) shows that the non-irradiated sample has a flat surface with a population of some particles (of density 16 per square centimeter, possibly drops formed in the process of LPCVD deposition) of size 30 nm in diameter and 4 nm in height.

Fig 7.1 (b) suggests a hint of ripple initiation upon Ar^+ ion beam irradiation. Figs 7.1 (c) to (f) show the Ar^+ ion irradiated ripples from initiation, growth, breakage, and disappearance upon prolonged ion irradiation. Fig 7.1 (c) shows that the minimum ion dose in initiating ripple growth is 1.0×10^{17} cm^{-2}. Fig 7.1 (d) presents distinct ripple growth at a dose of 1.2×10^{17} cm^{-2}. Fig 7.1 (e) reveals breakage of ripples at a dose of 1.6×10^{17} cm^{-2}. Ripples disappear at dose 2.5×10^{17} cm^{-2} (Fig 7.1 f). The reason for the breakage and disappearance is possibly that the Si_3N_4 layer (173 nm thick) has been completely removed by prolonged sputtering of Ar^+ ions. This will be assessed by TRIM simulation in the next section.

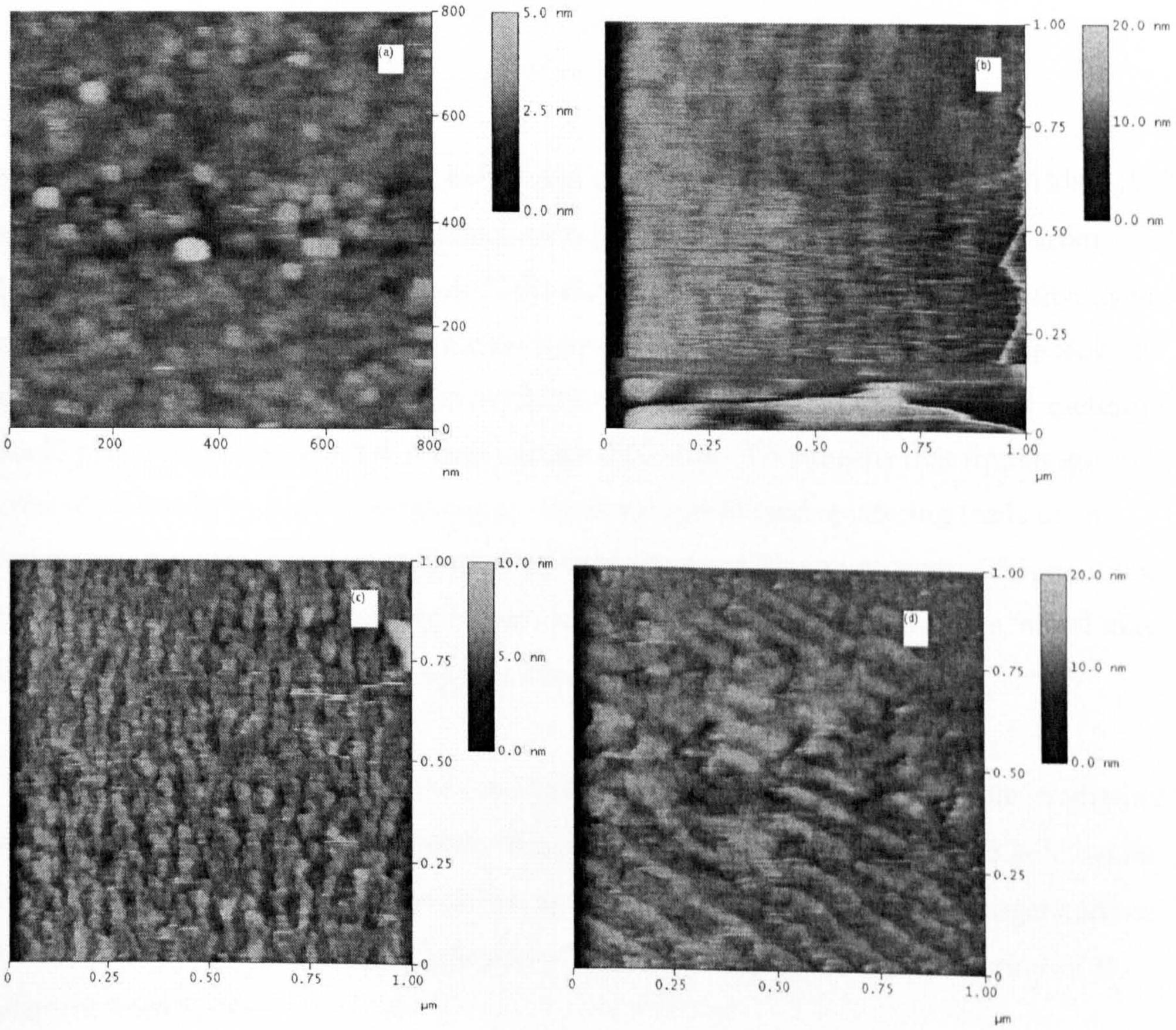

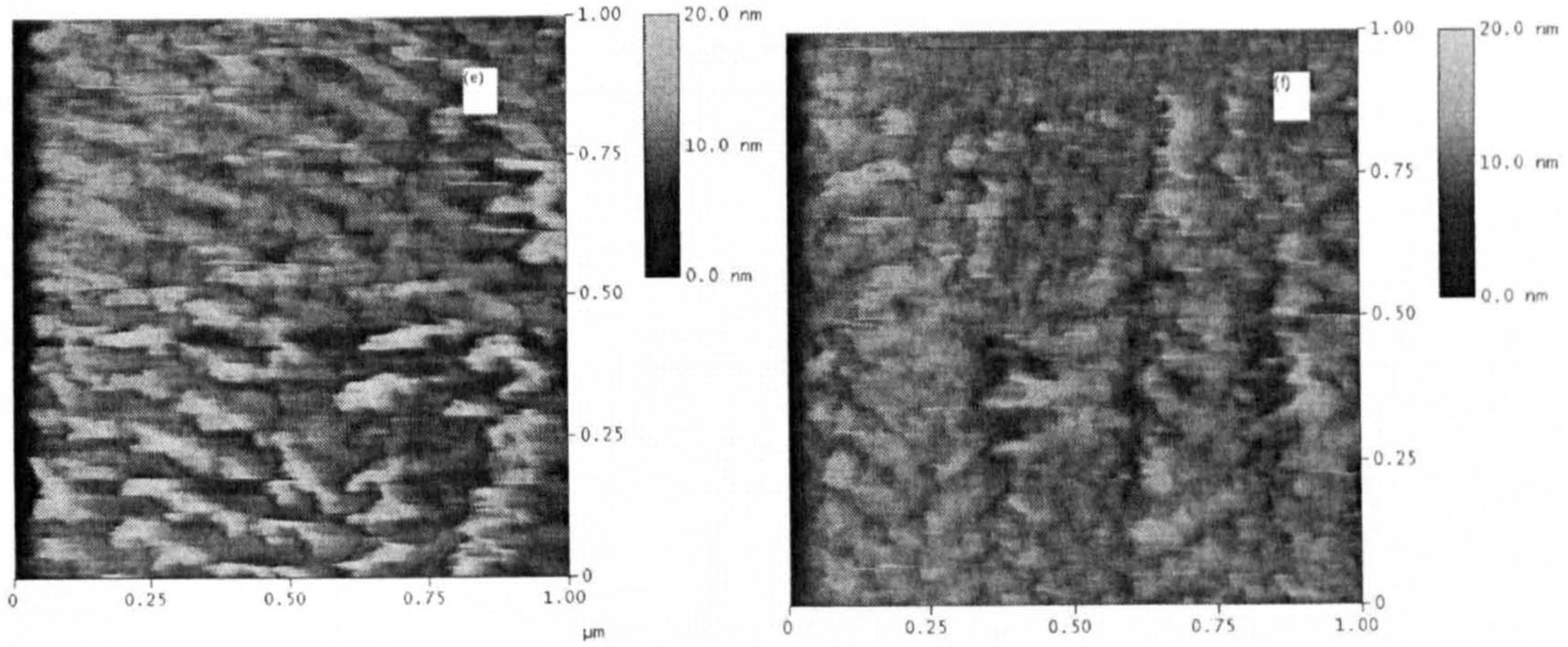

Fig 7.1 Contact mode AFM micrographs of LPCVD Si_3N_4 (100) surfaces irradiated with a 4.5 keV Ar^+ ion beam at72° incident angle (to surface normal) and different ion dose:
(a) $D_s = 0$ (Un-irradiated); (b) $D_s = 8.4 \times 10^{16}$ cm^{-2}; (c) $D_s = 1.0 \times 10^{17}$ cm^{-2};
(d) $D_s = 1.2 \times 10^{17}$ cm^{-2}; (e) $D_s = 1.6 \times 10^{17}$ cm^{-2}; (f) $D_s = 2.5 \times 10^{17}$ cm^{-2}.

Statistical results for ripple width, height and wavelength is shown in Fig 7.2. Although similar dependence of these parameters upon irradiating ion dose can be found from Fig 7.2 compared to those in chapter 5, the mechanism of dynamic ripple growth may be different from the cone-mergence model proposed in Chapter 5. Because of the lack of mobility (ref. section 5.3.3) of Si on surfaces of Si_3N_4, the curvature dependent sputtering could play a more important role than surface diffusion. This means that ripples are created primarily by kinetic roughening. However, prolonged sputtering leads to an increase in the concentration of Si ions involving in the diffusion process. This could be the reason of increasing wavelength upon ion dose. Therefore, the BH ripple model may be appropriate in explaining the ripples structures shown in Fig 7.1.

The biggest difference between the ion irradiated InP and the Si_3N_4 lies in the irradiating energy in ripple initiation parameters. Ripples were initiated on Si_3N_4 at 4.5 keV, while initiation of ripples on InP can be as low as 2 keV. This means that the stronger surface binding energy in Si_3N_4 exerts a substantial barrier to the preferential sputtering of N element from Si_3N_4.

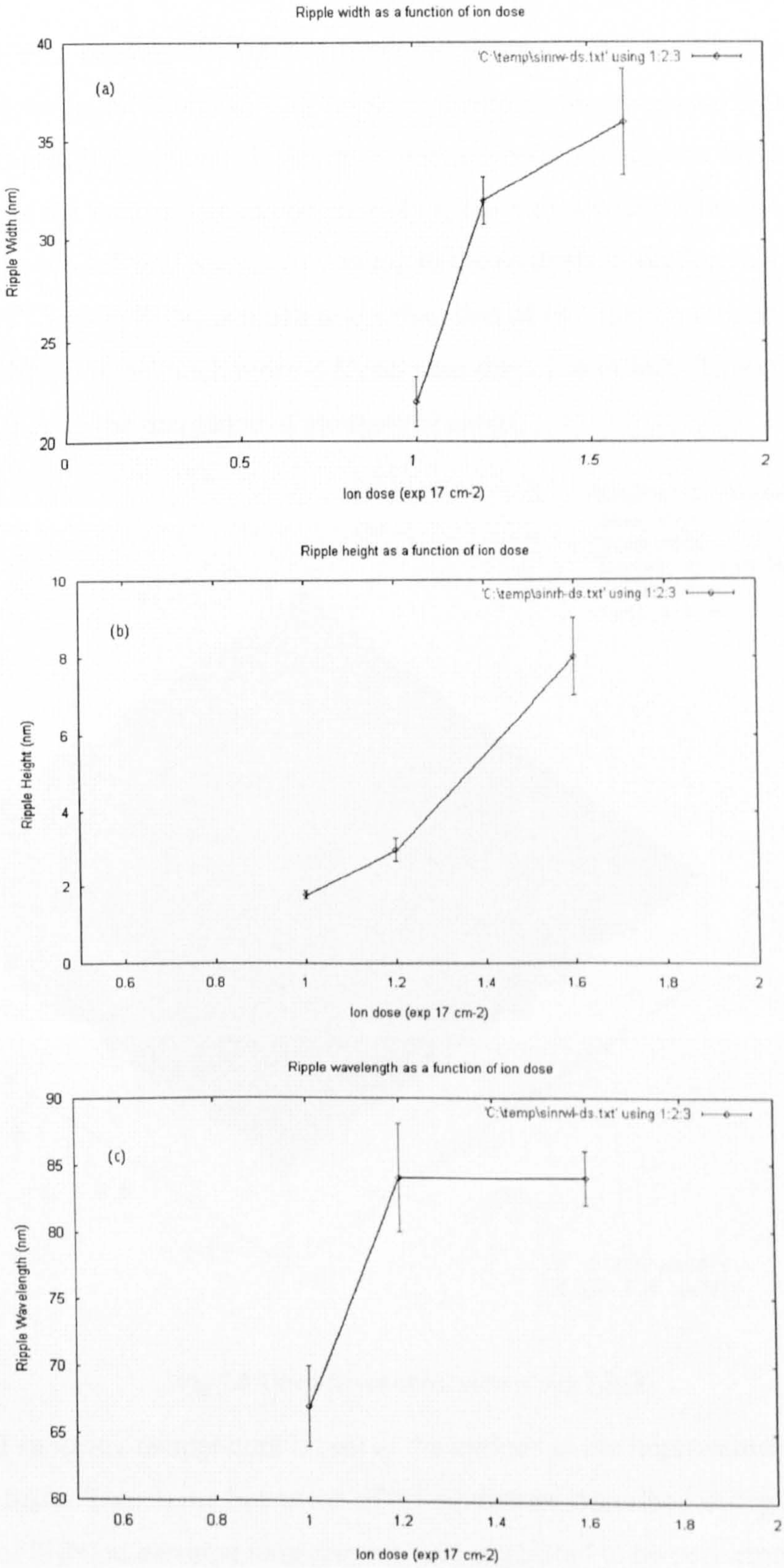

Fig 7.2 Dependence of ripple width (a), height (b), and wavelength (c) upon irradiation ion dose.

Another difference between the ripple growth mechanism of Ar^+ ion irradiated Si_3N_4 and that of InP can be found from Fig 7.3. In place of ripples superimposed by tailed cones from ion irradiated InP, elongated islands comprise ripples induced on Si_3N_4 as shown in Fig 7.3. One of the factors that can be possibly taken into account is the mobility difference between InP and Si_3N_4. According to the analysis in section 5.3.3, the mobility of Si^{4+} ions in Si_3N_4 is much lower than that of In^{3+} ions in InP, and diffusion of Si atoms in Si_3N_4 will be much more difficult than that of In in InP. This could generate a great resistance to the mergence of elongated islands.

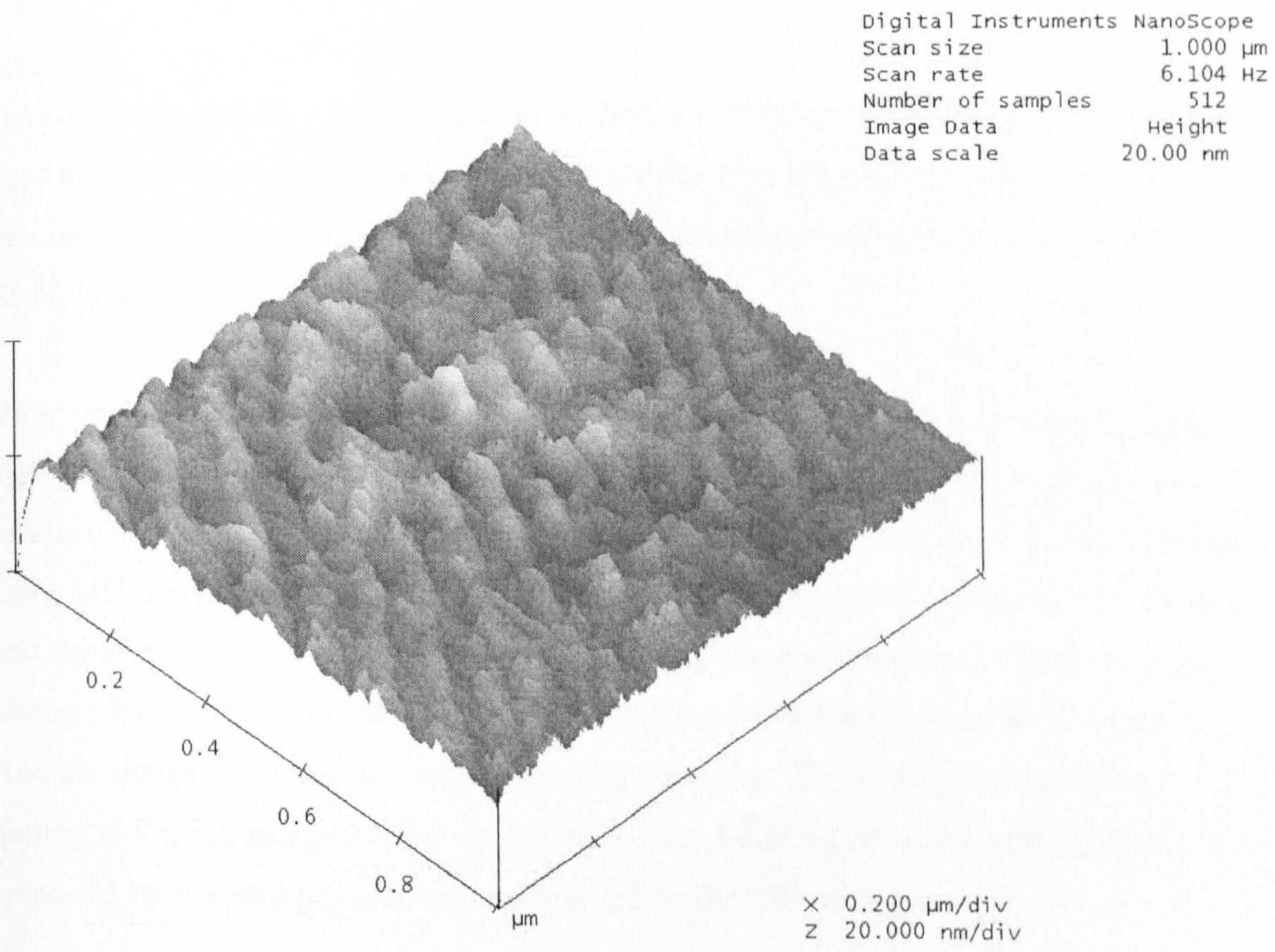

Fig 7.3 Three-dimensional view of Fig 7.1 (d)

Elevation of substrate temperature is one of the options in the improvement of the mobility of Si_3N_4. Due to the limitation of the equipment described in Fig 5.1, Ar^+ ion irradiation of Si_3N_4 at elevated temperatures was suggested to be performed in an UHV system integrating a variable temperature STM and an ion gun at Genova University in

Italy. Exploratory experiments were performed there in an ECR (Electron Cyclotron Resonance) chamber with variable temperature stage. The experiments were carried out with a series of different experimental parameters (varying temperature, energy, ion beam incidence angle, and ion dose) but failed to generate ripple-like structures. One of the reasons for this failure is that the irradiating energy (maximum 2 keV) is not as high as the system in Newcastle. Another reason is that the ECR beam is a broad beam, so that during the irradiation process, the local ion current density is much lower than that produced by the focused beam. The suggested *in situ* ion bombardment of Si_3N_4 and STM characterization failed to be arranged because of the unavailability of the system during the short period available for that study visit.

An alternative option in the fabrication of ripples and nanowires on Si_3N_4 (100) surfaces is to use LPCVD Si_3N_4 samples with much greater thickness of Si_3N_4 layer on a Si wafer so that irradiation at higher doses can be easily performed before the total removal of the Si_3N_4 layer.

Problems may exist in the acquisition of AFM images on Ar^+ sputtered Si_3N_4 surfaces with a contact mode AFM silicon tip. A silicon tip carrying native SiO_2 will probably produce high adhesion and friction if the tip is brought into contact with Si_3N_4. Because some SiO_2 may be present in Si_3N_4, which will form a SiO_2/SiO_2 contact between the tip and the sample, and a contact between two parts of the same material is liable to yield strong adhesion and friction. This poses a serious problem to tip-force minimization. And the tip may be worn very quickly during scanning. The relatively poor image quality in Fig 7.1 may be indicative of insufficient 1 nm Ag coverage of SiO_2 on the sputtered sample and possible tip wear caused by the SiO_2 contact.

7.4 Monte-Carlo Simulation of Ar^+ ion Bombardment on Si_3N_4 (100) surfaces

In order to understand further the results presented in the previous section, the effect of Ar ion irradiation of Si_3N_4 surfaces is analyzed by TRIM simulation in this section.

Consider a Si_3N_4 surface irradiated by 4.5 keV Ar^+ ions under 72° incident angle to a depth of 143 Ångstrom. Before starting TRIM simulation, the three material input parameters for Si_3N_4 have to be decided. The lattice displacement energy was chosen as 15 eV and 28 eV for Si and N respectively, which is suggested by the TRIM table; the lattice binding energy was selected to be 2 eV and 3 eV for Si and N; and the surface binding energy 4.7 eV and 2 eV for Si and N.

7.4.1 Dynamic Plot of Collision Cascades

The dynamic plot of collision cascades, Depth vs. Y-Axis plot, is shown in Fig 7.4. Fig 7.4 is the plot collected after a bombardment of 246 ions. The dark dots represent collisions between the ion (Ar^+) and target atoms (Si and N), in which the target atoms are knocked from their lattice sites. The gray dots are collisions between recoiling target atom, silicon, nitrogen, and other target atoms. The recoiling target atoms cause collision cascades which dominates the damage process. The dot is only plotted if the energy transfer is large enough to displace the atom from its lattice site.

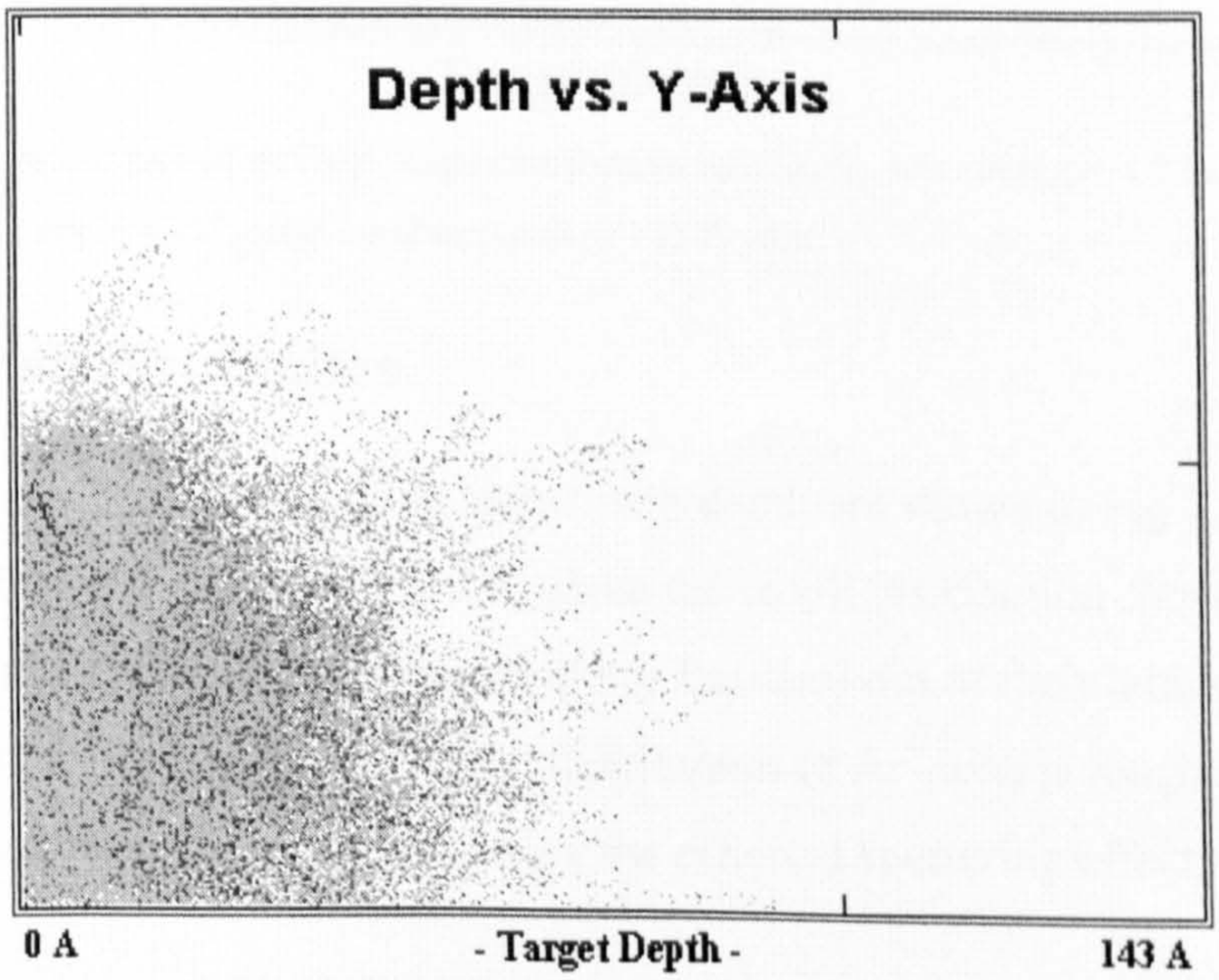

Fig 7.4 TRIM simulation plot of the collision cascade of Ar^+ ion bombardment on Si_3N_4 surface. Ion energy = 4.5 keV, ion incident angle = 72°.

7.4.2 Ion-Range Distribution

The ion-range distribution showing the ion distribution and its four statistical moments for all ions stopped within the target (Moments = range, straggle, skewness, and kurtosis). Fig 7.5 shows that the build-up of Ar^+ ions in Si_3N_4 is in the depth of 23 Å.

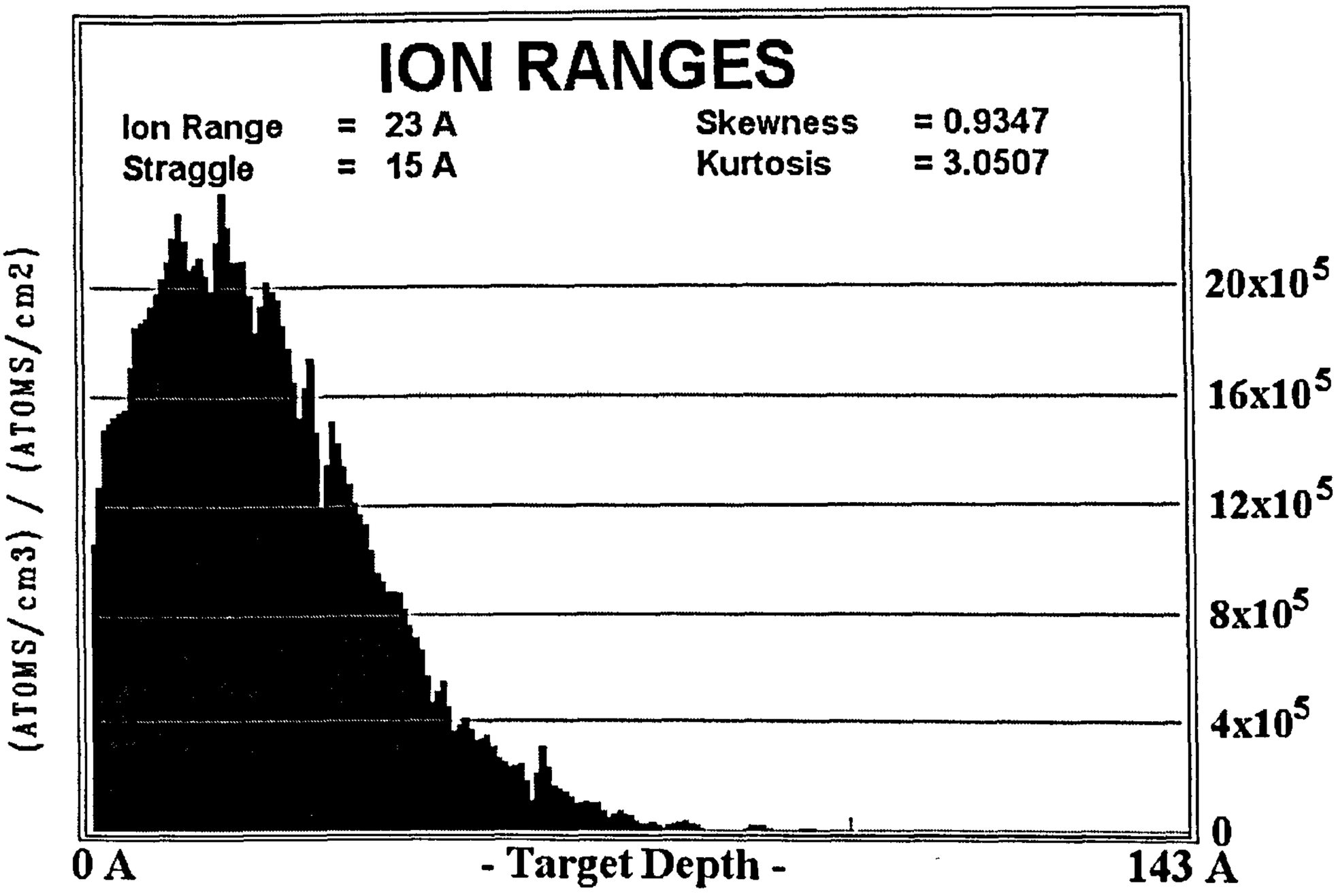

Fig 7.5 TRIM simulation plot of Ar^+ ion-range distribution into Si_3N_4. Ion energy = 4.5 keV, ion incident angle = 72°, after bombardment of 13500 ions.

7.4.3 Ion/Recoil Distribution

The distributions of ions and recoiled atoms with depth are shown in Fig 7.6. The ion distribution is the same as that in Fig 7.5, while the recoil distribution shows the distribution of all the silicon and nitrogen atoms knocked out of their lattice sites, creating vacancies. Fig 7.6 shows that the distribution of Ar^+ ions is roughly the same as vacancies of silicon and nitrogen, indicating the efficient sputtering effect of Ar^+ ions at this energy.

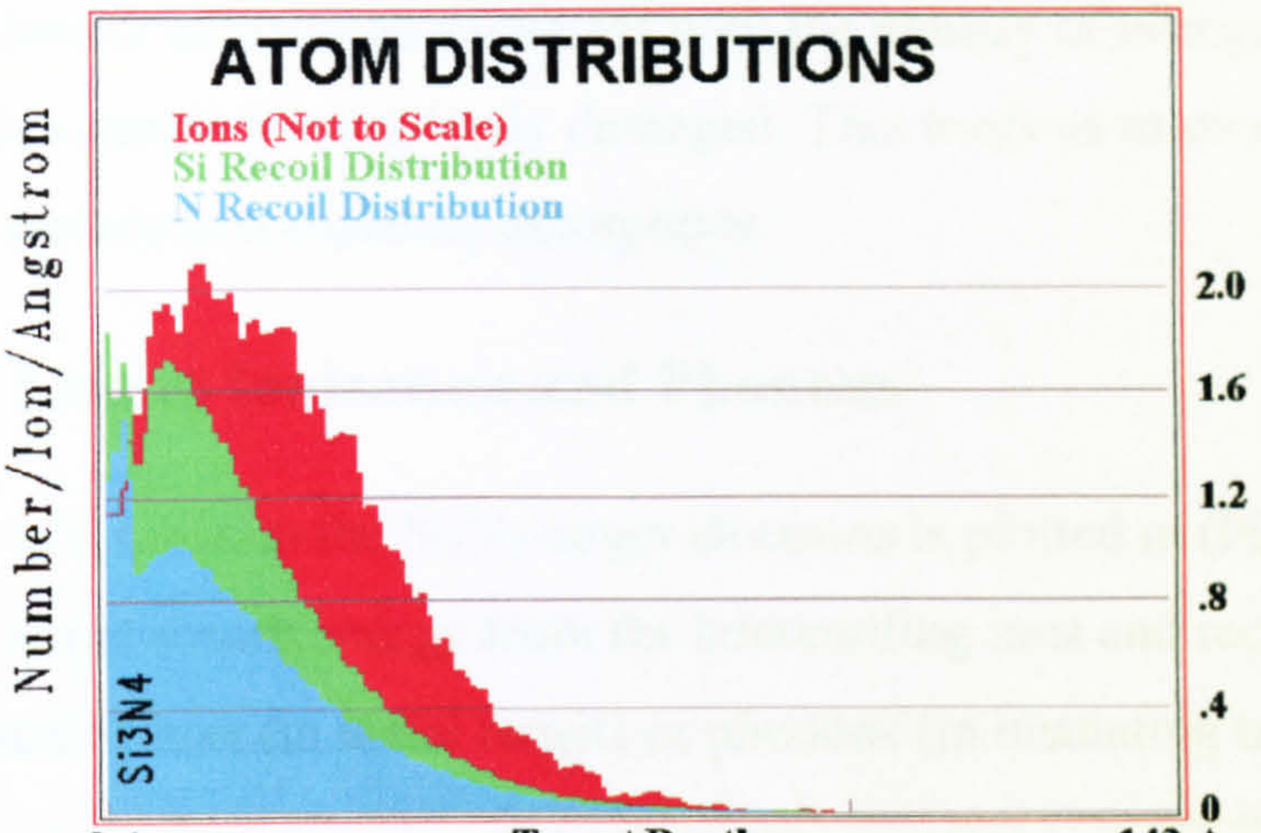

Fig 7.6 TRIM simulation plot of Ion/Recoil distribution on a Si_3N_4 target irradiated by 4.5 keV Ar^+ ions at an incident angle of 72°, after bombardment of 13500 ions.

The structure of the Si_3N_4 surface under ion irradiation can be evaluated by the ion/recoil distribution plot. Suppose 99 % of the damage self anneals, leaving only 1 % to contribute to the amorphous phase, the Si_3N_4 surface irradiated by 4.5 keV Ar^+ ions at 72° incident angles and a dose of 5×10^{16} cm^{-2} can be assessed as follows.

Rewriting eqn (4.2.1), the number of vacancies created by ion irradiation of dose $D_s = 5 \times 10^{16}$ cm^{-2} can be calculated as

$$N_v = R_v D_s \tag{7.3}$$

R_v can be found from Fig 7.6 to be 1.5 per ion per Å for nitrogen (the peak rate). Considering 1 Å = 10^{-8} cm, $R_v = 1.5 \times 10^8$ cm^{-1}. With $D_s = 5 \times 10^{16}$ cm^{-2}, eqn (7.3) gives the number of nitrogen vacancies as $N_v = 7.5 \times 10^{24}$ cm^{-3}. With the assumption that only 1 % of the vacancies remains in the target, the final density of nitrogen vacancies will be $N_{v(f)} = 7.5 \times 10^{22}$ cm^{-3}.

The number (N) of nitrogen atoms per cubic centimeter in the target can be calculated as (considering 4 nitrogen atoms in one Si_3N_4 molecule):

$$N = 4\frac{d}{m}N_A = 4x\frac{3.44}{140.478}x6.0224x10^{23} = 5.90x10^{22}\ (cm^{-3}) \tag{7.4}$$

Comparing the density of nitrogen vacancies with the density of nitrogen atoms, it can be found that the Si_3N_4 target is completely damaged. This leads us to conclude that the irradiated Si_3N_4 surface is completely amorphous.

7.4.4 Energy Loss to Ionization and Phonons

The energy loss of Ar ions to the Si_3N_4 target electrons is plotted in (Fig 7.7) shows. The electrons of the target absorb energy from the bombarding ions and recoil atoms, and release it afterward as heat (in metal target) or phonons (in insulating target).

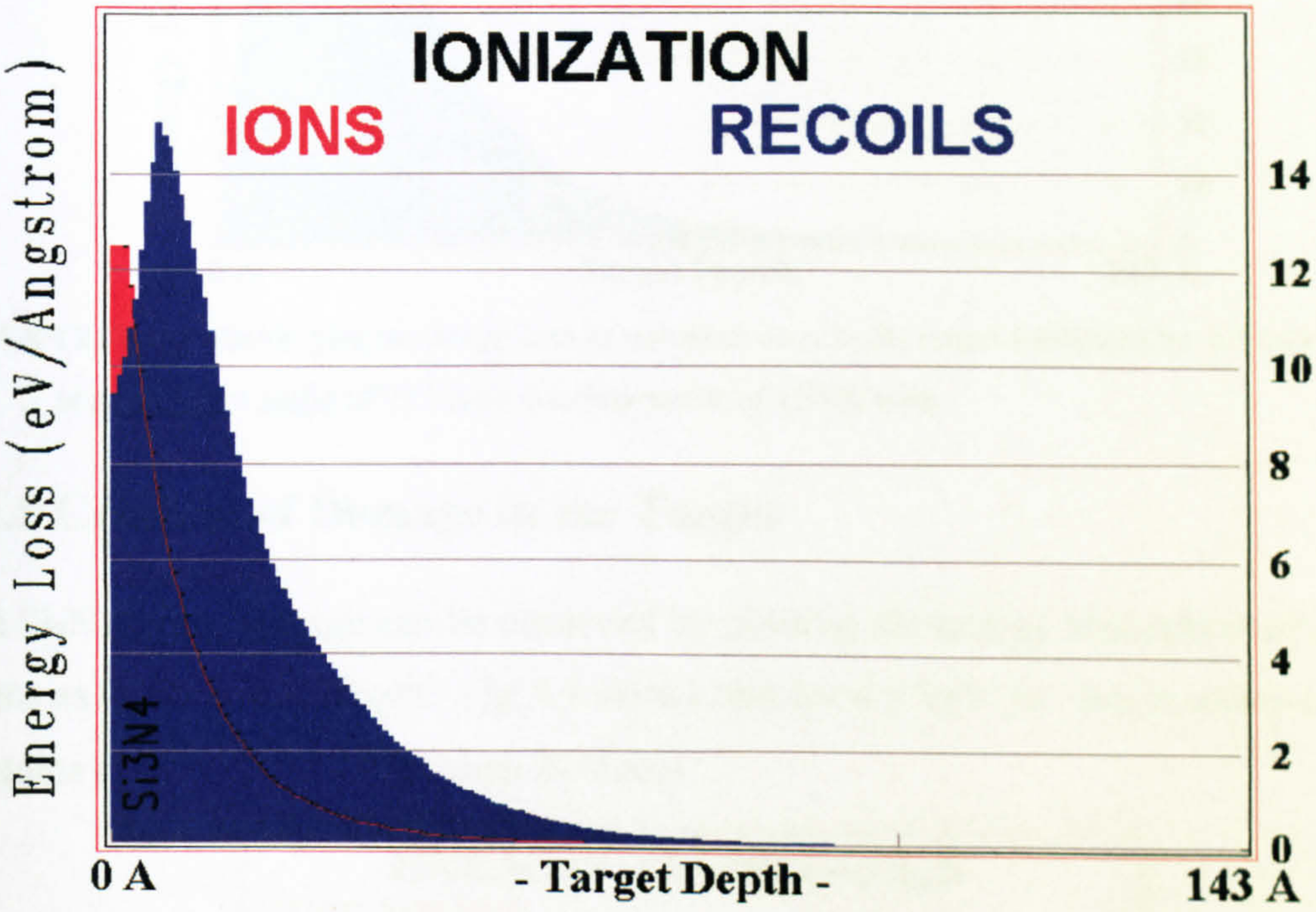

Fig 7.7 TRIM simulation plot of energy loss to ionization on a Si_3N_4 target irradiated by 4.5 keV Ar^+ ions at an incident angle of 72°, after bombardment of 13500 ions.

It can be observed from Fig 7.7 that for 4.5 keV Ar^+ ion irradiation of Si_3N_4, most of the ion energy loss occurs to the electrons of recoil atoms, i.e., Si or N. Only a small portion of the ion energy contributes to ionization of the target.

The energy loss to phonons is shown in Fig 7.8. Similar to Fig 7.7, it can be found that most of the phonons are generated by the recoiling target atoms. Statistics in a sub-

window of the TRIM interface shows that the energy loss to phonons is 4% from ions, and 75% from the recoil atoms.

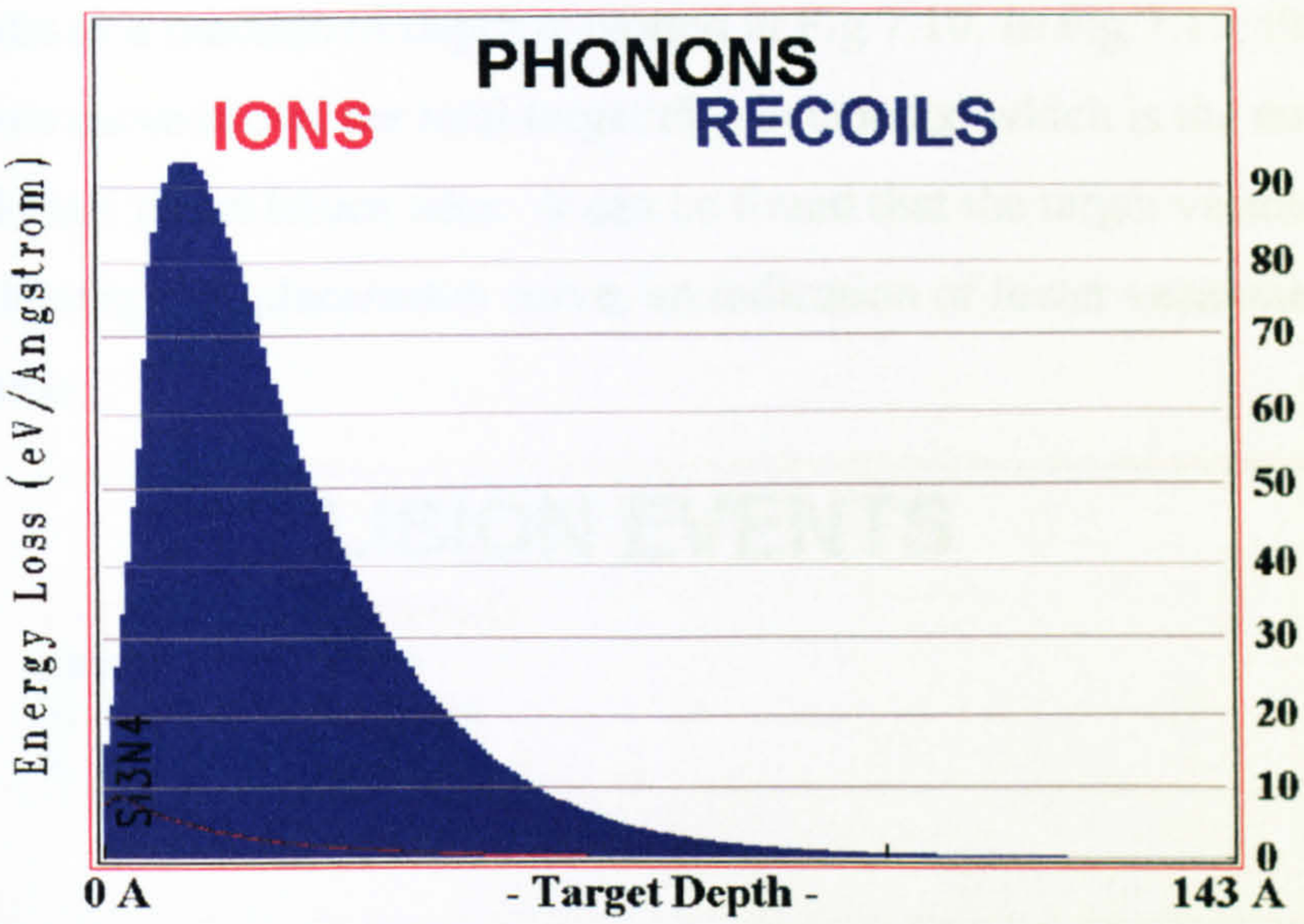

Fig 7.8 TRIM simulation plot of energy loss to phonons on a Si_3N_4 target irradiated by 4.5 keV Ar^+ ions at an incident angle of 72°, after bombardment of 13500 ions.

7.4.5 Creation of Damage in the Target

The Si_3N_4 target damage can be observed by plotting the energy absorption by the target atoms as a function of depth. Fig 7.9 shows that for 4.5 keV Ar^+ ion irradiation of Si_3N_4, N atoms absorb more energy than Si atoms.

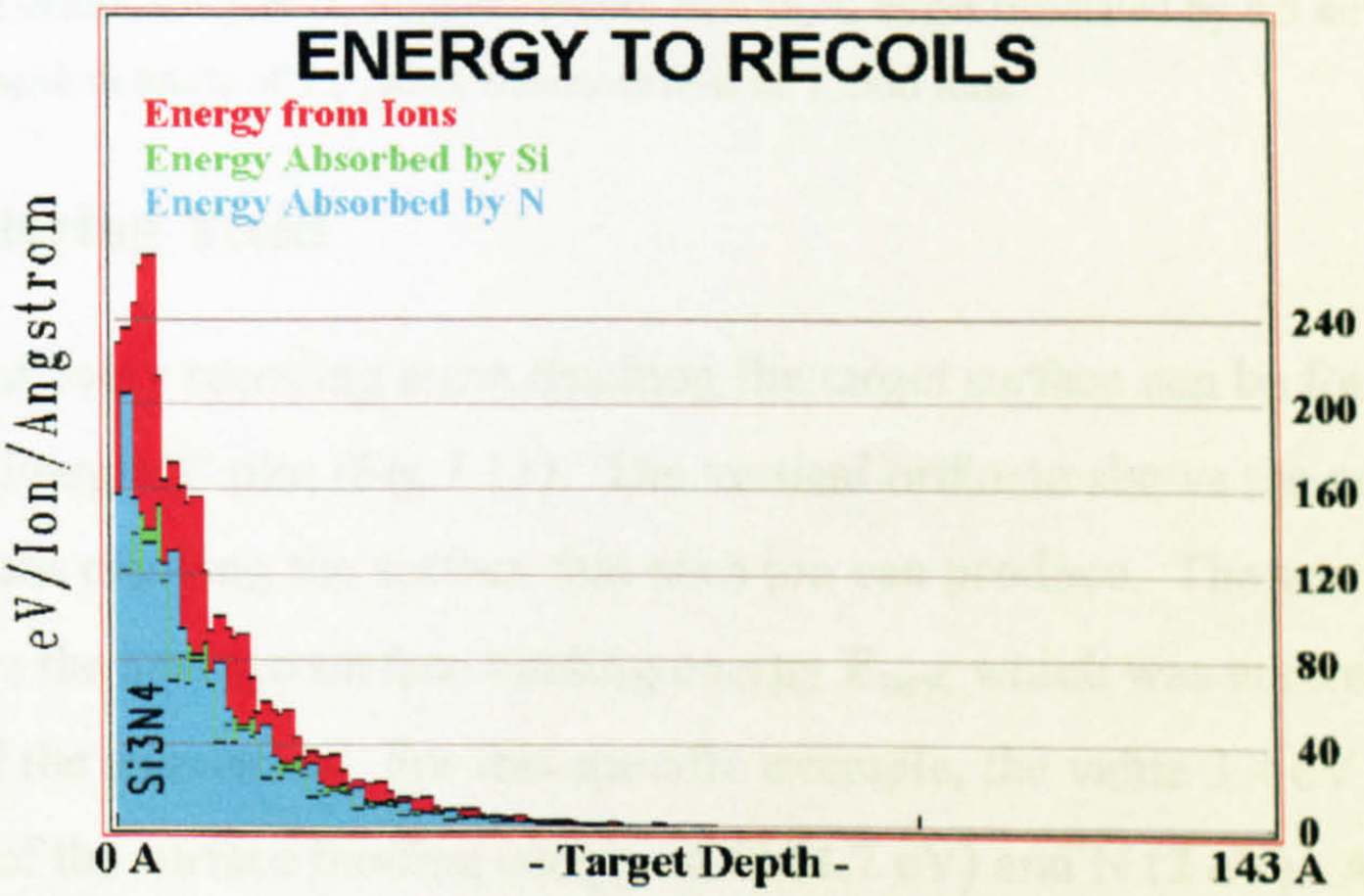

Fig 7.9 TRIM simulation plot of energy absorption on a Si_3N_4 target irradiated by 4.5 keV Ar^+ ions at an incident angle of 72°, after bombardment of 13500 ions.

In order to observe the target damage more directly, a distribution of target vacancies and displacements as a function of depth is plotted in Fig 7.10. In Fig 7.10, the target displacements curve shows the total target displacements, which is the number of atoms knocked off their target lattice sites. It can be found that the target vacancies curve is lower that the target displacements curve, an indication of fewer vacancies than the displacements.

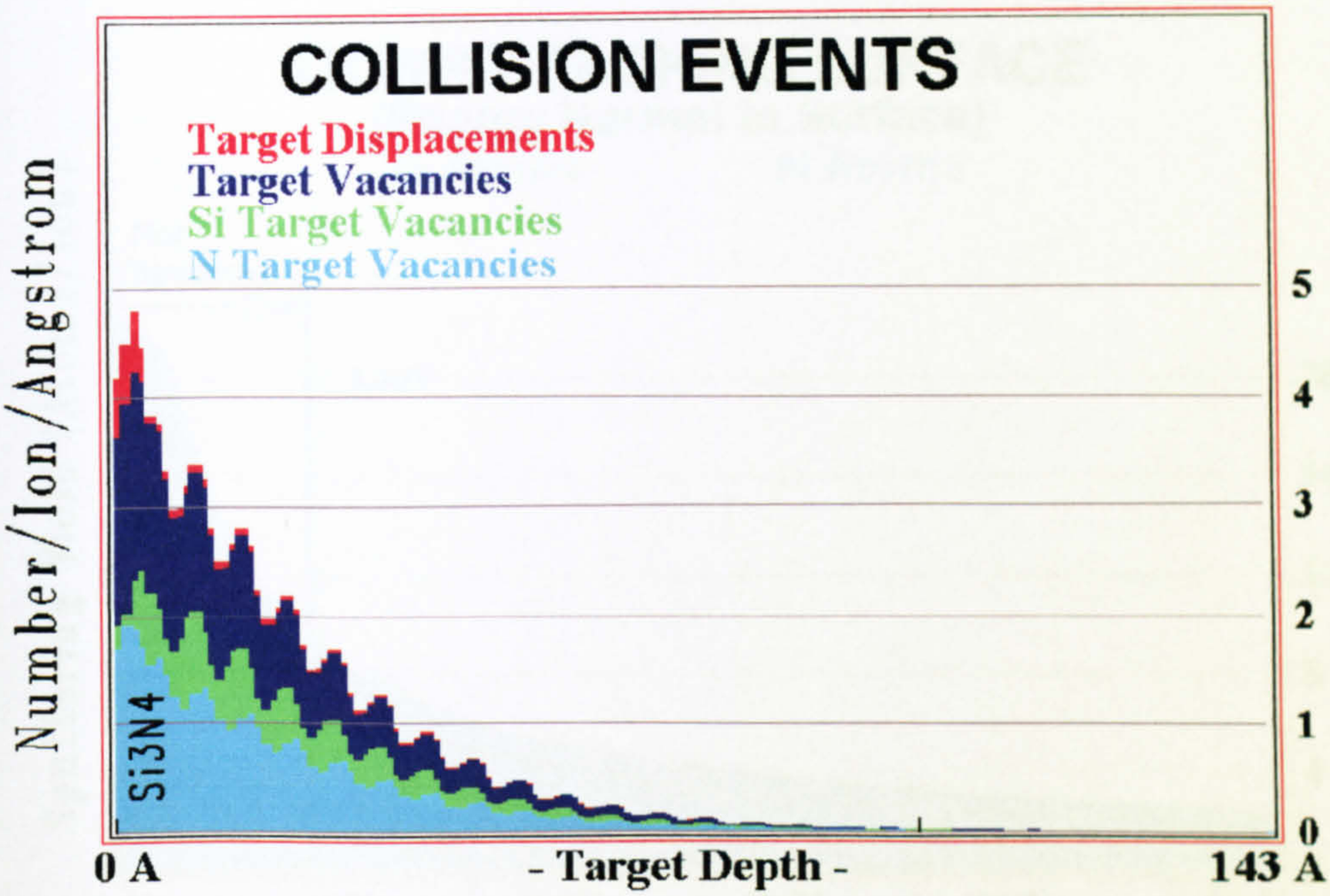

Fig 7.10 TRIM simulation plot of collision events on a Si_3N_4 target irradiated by 4.5 keV Ar^+ ions at an incident angle of 72°, after bombardment of 13500 ions.

7.4.6 Sputtering Yield

The energy of every recoiling atom reaching the target surface can be found from the "sputtering (integral)" plot (Fig 7.11). The vertical ordinate shows the number of recoiling atoms reaching the surface that each ion can produce. The vertical bar marked 3.4 eV shows the average surface binding energy E_{surf}, which was entered at the beginning of the simulation. For this specific example, the value 3.4 eV is obtained from the average of the surface binding energy of Si (4.7 eV) and N (2 eV). A recoiled atom must have a minimum energy of this value to be sputtered. At 3.4 eV, the number of atoms which reached the surface with more than this energy can be found from Fig 7.11

to be 9.4 and 7.6 for N and Si respectively. This gives the results of sputtering yield of 9.4 atoms/ion and 7.6 atoms/ion for N and Si respectively. Accurately, the sputtering yields for N and Si have to be calculated from their own surface binding energy individually. One can find from Fig 7.11 that the actual sputtering yield for N and Si is 15 atoms/ion and 7 atoms/ion respectively, with their surface binding energy 2 eV and 4.7 eV. This agrees with the number shown in the "Sputtering Yield" table on the TRIM interface (not shown in Fig 7.11).

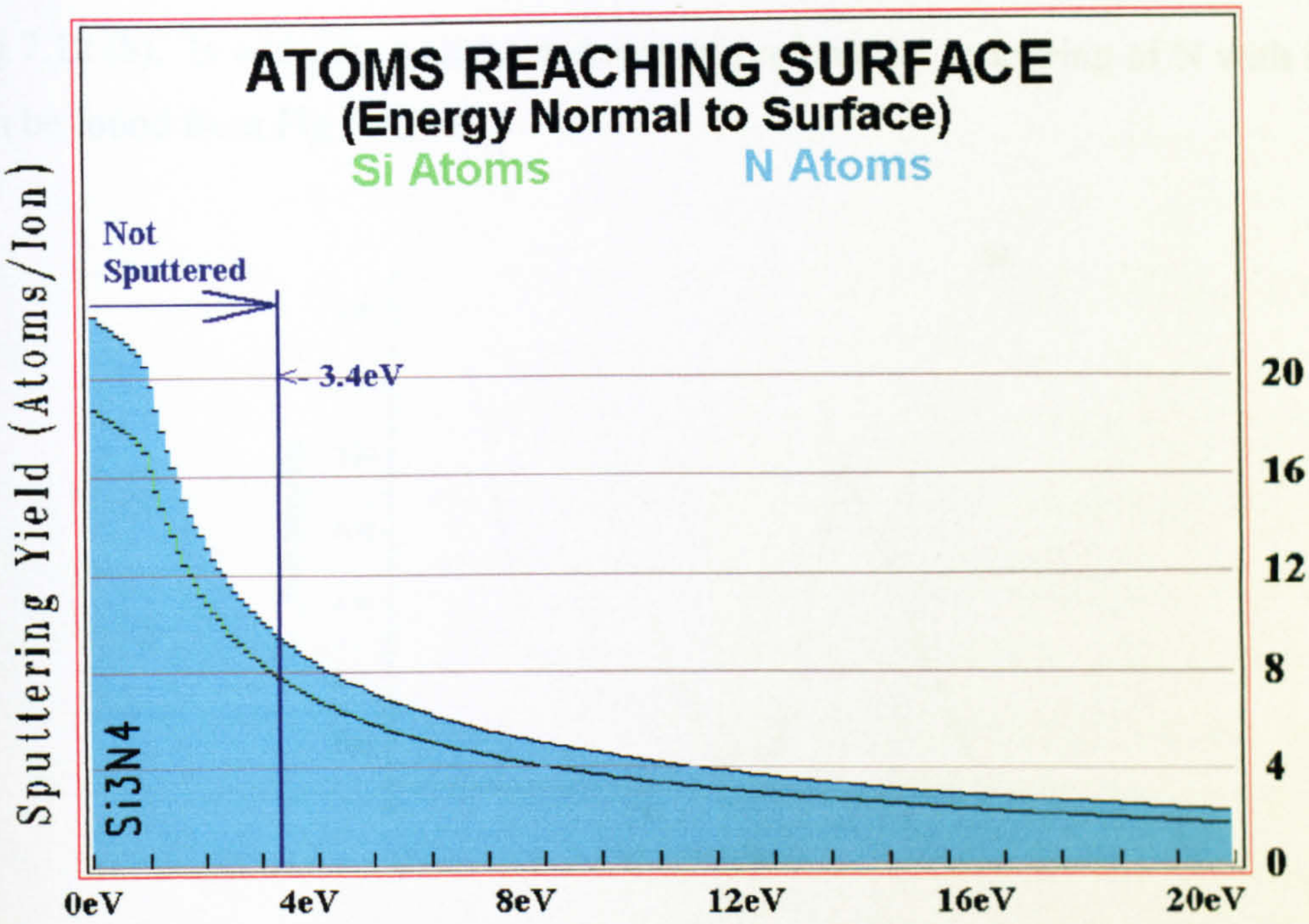

Fig 7.11 TRIM simulation plot of Sputtering (Integral) on a Si_3N_4 target irradiated by 4.5 keV Ar^+ ions at an incident angle of 72°, after bombardment of 13500 ions.

The above analysis of sputtering yield of N and Si shows that sputtering yield is very sensitive to the surface binding energy. In addition, the sputtering yield calculated with this method underestimates some effects, e.g., surface roughening, due to ion sputtering, because the surface binding energy may change on the surface of a damaged target. A rough and damaged target tends to have a reduced surface binding energy. As a result, the sputtering yield will be higher than the simulated result on a damaged target. Generally, the plots of sputtering yield to surface binding energy are accurate to about 30% [365].

The number of atoms sputtered from the surface can be evaluated by the simulated sputtering yield. Calculation of TRIM showed a ratio of sputtering yield N /Si to be around 2:1 for Ar^+ ion energies ranging from 0.5 keV to 4.5 keV, with ion incident angle 72° to surface normal, indicative of preferential sputtering of N in this energy range (Fig 7.12a). Simulation of higher energy (5 keV –100 MeV) bombardment generates a stable N/Si ratio of 2.1 with subtle fluctuations of ± 0.02, which is not drawn in Fig 7.12 (b). In addition, a slight decrease of preferential sputtering of N with ion energy can be found from Fig 7.12 (a).

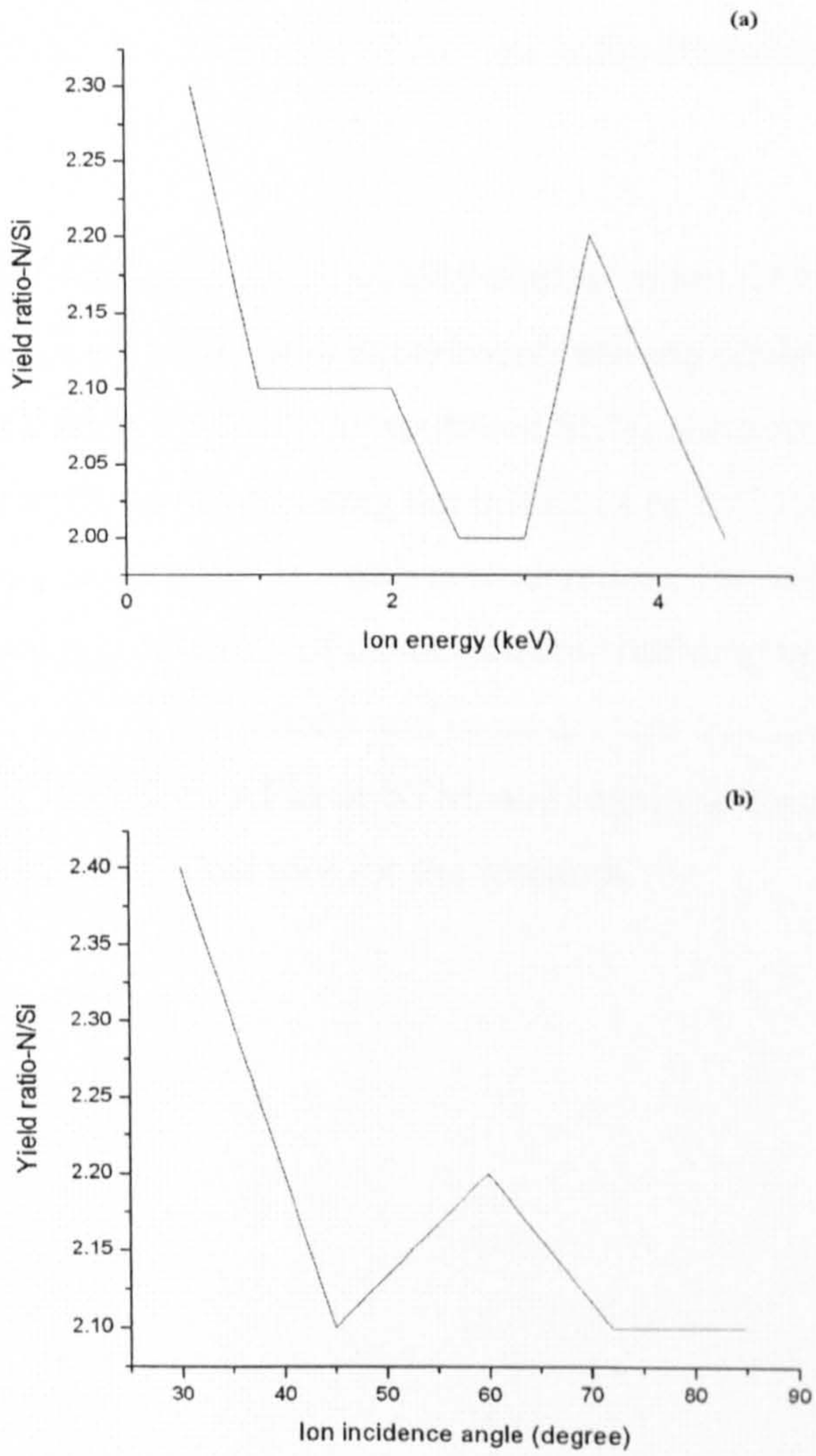

Fig 7.12 TRIM simulation of the ratio of sputtering yield Y_N/Y_{Si} dependence of:

(a) ion energy (ion incident angle = 72°); and (b) ion incident angle (ion energy = 4.5 keV).

Similarly, insignificant decrease in the effect of preferential sputtering of N with increasing ion incidence angle can be found from Fig 7.12 (b). With ion projection approaching grazing incidence condition, the effect of preferential sputtering of N becomes weaker.

7.5 Tentative Conclusion and Future Work

Ripples of 32 nm wide, 3 nm high, with a period of 84 nm were fabricated by low energy Ar^+ ion irradiation of Si_3N_4 (100) at room temperature at a dose of 1.2×10^{17} cm^{-2}. The experiment suggests that the formation of Ar^+ ion induced ripples on Si_3N_4 (100) surfaces is in agreement with the BH ripple model.

Due to the difficulty in collecting high quality contact mode AFM images on Ar^+ ion bombarded Si_3N_4 surfaces, substantial experiments are required to understand the details of the interaction of silicon tips with the sputtered Si_3N_4 surfaces. Tips with gold coating would be a possible option in eliminating the influence of SiO_2/SiO_2 contact. Image acquisition in tapping mode AFM is worth consideration. The ultimate goal of the research would be mass production of nanoelectronic building blocks with arrays of silicon nanowires of regular periodicity and cross-section on insulating Si_3N_4 substrate. A system integrating ion beam, AFM or STM, and high resolution XPS, in the same UHV chamber, would be an ideal tool for the research.

Chapter 8 Summary

Recent techniques in nanowire fabrication and characterization are reviewed in this thesis. Fabrication of nanowires can be divided into two groups, the top-down and the bottom-up techniques. The top-down approach is primarily realized by nanolithography, SPM nanostructuring, soft lithography, and energetic particles, while the bottom-up approach can be realized by adoption of vapour phase synthesis, templated growth, electrodeposion, and molecular beam epitaxy. Sometimes a combination of the two techniques is used.

Characterization of nanowires mainly involves morphology, chemical composition, electron transport properties, mechanical properties, and photonic properties. Techniques of morphology characterization involve Scanning/Transmission Electron Microscope and Scanning Probe Microscope (Scanning Tunnelling Microscope, Atomic Force Microscope, and Scanning Near-field Optical Microscope). Techniques of non-destructive analysis of chemical composition of nanowires include X-ray Photoelectron Spectroscopy, Auger Electron Spectroscopy, and Ion Scattering. Electron transport properties of nanowires are mainly investigated by the four-probe approach. Inspection of mechanical properties like Young's Modulus, adhesion, lubrication and wear, etc., is normally carried out using an Atomic Force Microscope. Observation of photonic properties is usually detected by Scanning Near-field Optical Microscope.

Following a brief introduction of the physics of ion-beam interactions with solid surfaces, several models of ion beam induced topography on solid surfaces are reviewed in Chapter 3. Theoretical simulation of Ar^+ ion beam interaction with InP surfaces is introduced in chapter 4. The TRIM simulation suggests preferential sputtering of the lighter element (P) in covalently bound solid (InP) surfaces under ion beam bombardment.

The experiments focused on Ar^+ ion beam directed self-assembly of nanowire arrays on InP (100) surfaces. In an attempt to create nanowire arrays on InP (100) surfaces by Ar^+ ion bombardment, the experiments were carried out to investigate morphology of Ar^+ ion beam bombarded InP (100) surfaces under four series of different experimental

parameters: (i) Bombardment with different ion energy; (ii) Bombardment with different ion current density; (iii) Bombardment with different ion dose; (iv) Bombardment at different ion beam incident angle. Ripple topography was mostly observed, with nanowires formed from mergence of tailed cones at some crucial experimental condition. On the basis of AFM analysis of these ripples and nanowires, a cones-mergence model is proposed to account for the formation of nanowires on Ar^+ ion bombarded InP (100) surfaces. It is proposed that because of the moderate mobility of In ions on InP surfaces, the cone-mergence model represents a combination of the model of stress-field induced self-assembly and the BH ripple model: Preferential sputtering of P from InP initiates tailed cones with tails aligned toward the ion beam direction and these cones agglomerate and merge into ripples or wires with prolonged ion bombardment. Nanowires with regular periodicity form under some crucial dose and ion beam incident angle. The drive to the formation of periodic nanowires is referenced to stress-field induced self-assembly of cone structures produced by ion bombardment. The low mobility, however, leads to less regular structures than those observed earlier on CaF_2 surfaces.

In order to justify the proposed cones mergence model, XPS and STS were performed to inspect the difference of composition and electronic structure between the non-sputtered and the sputtered InP (100) surfaces. XPS core level spectra of In 3d, P 2p and O1s revealed peak broadening of some peaks in the spectra on surfaces 5 nm below the topmost layer on the bombarded sample. Curve fitting to these broadened peaks resolved some new peaks characteristic of In atoms, a direct evidence of In enriched surfaces on the sputtered samples. STS analysis found that the normalized conductance *(dI/dV)/(I/V)* curve of the bombarded sample showed a lack of an energy gap which is typical for metals. But the STS results failed to show substantial difference of conductance between the areas populated by In enriched nanowires and those areas occupied by intrinsic InP. A possible explanation of this inability is that both of the areas selected were enveloped by conducting native indium oxides.

An ideal system for efficient investigation of nanowire fabrication and characterization by Ar^+ ion bombardment on InP (100) surfaces could be a comprehensive one integrating

ion beam, multi probe STM, and AES or XPS in one UHV chamber, with variable temperature sample holders, so that characterization could be performed *in situ* with fabrication, eliminating the influence of atmospheric gases.

In order to explore applications of Ar^+ ion induced nanowires in nanoelectronics device fabrication and photonic functionalization, further investigation is needed to fabricate nanowires of smaller periodicity, higher area density and rectangular cross section, on InP (100) surfaces by Ar^+ ion bombardment. Electronic conductance measurement of single nanowires with two probes placed across two ends of a wire, and examination of potential photonic properties, like lasing action, remain to be explored. Termination and isolation of the fabricated nanowires will be a great challenge to the application of these wires.

Fabrication of nanowire arrays was also explored by Ar^+ ion irradiation on LPCVD Si_3N_4 (100) surfaces (Chapter 7). TRIM simulation predicted a silicon enriched surface. Substantial elevation of irradiation energy in initiating ripple growth on the Si_3N_4 surfaces reveals the stronger effect of crystal surface binding energy of Si_3N_4 compared with InP. The lack of mobility of Si on Si_3N_4 surfaces is not ideal for the fabrication of regular structures. The interaction of AFM silicon tips with Si_3N_4 surfaces is worth further investigation so that the effect of native silicon oxides on the tip-wear is well understood.

This research suggests that selection of useful systems with sufficient surface mobility at a viable substrate processing temperature is vital for the fabrication of high quality periodic nanowires by Ar^+ ion irradiation. For systems with very high surface mobility (e.g. CaF_2), excellent long range order can be easily achieved by self-organized stress field. This long range order favours the formation of nanowire arrays of regular cross-section and periodicity on the irradiated surfaces, because the highly mobile ions can be easily assembled by the long range stress field. For systems with very low surface mobility (e. g. Si_3N_4), long range order is extremely difficult to achieve, and the dominant process is kinetic roughening. The surface morphology is explained by the BH ripple

model. For systems with moderate mobility (e.g. InP), the surface morphology is defined by a combination of the BH mechanism and the self-organized stress field. At the early stage of the irradiation, the surface is dominated by the BH mechanism, so that tailed cones and broken ripples are observed; at certain stage of the irradiation, the stress field with long ranged order is created, and the tailed cones and broken ripples merge to form non-broken ripples and nanowires. The influence of the surface cation mobilities to the morphology models is summerised in table 8.1.

Table 8.1 Relationship between ion beam induced morphology models and surface cation mobilities

Cation mobility\model	Stress-field model	Cone-mergence model	BH ripple model
Low			✓
Medium		✓	
High	✓		

References

1 G. Binning, H. Rohrer, Ch. Gerber, and E. Weibel, Phys. Rev Lett. **49**, 57-60 (1982).

2 H. Grabert and M. H. Devaret, *Single Charge Tunneling: Coulomb Blockade Phenomena in Nanostructures* (Springer, New York, 1992).

3 D. M. Pooley, H. Ahmed, H. Mizuta, and K. Nakazato, Appl. Phys. Lett **74**, 2191-2193 (1999).

4 Y. Zhang, T. Ichihashi, E. Landree, F. Nihey, and S. Iijima, Science **285**, 1719-1722 (1999).

5 Jiangtao Hu, Ouyang Min, Peidong Yang, and Charles M. Leiber, Nature **399**, 48-51 (1999).

6 Matthias Batzill, in *Fabrication and Characterization of Nanostructures on CaF_2* (Department of Physics, University of Newcastle upon Tyne, 1999).

7 M. Batzill, F. Bardou, and K. J. Snowdon, *Physical Review B-Condensed Matter* **63**, 233408 (2001).

8 M. Batzill, F. Bardou, and K. J. Snowdon, Journal of Vacuum Science and Technology A **19**, 1829 (2001).

9 Intel Corporation, http://www.intel.com/technology/silicon/65nm_technology.htm (2006).

10 M. M. Alkaisi, R. J. Blaikie, and S. J. McNab, Adv. Mater. **13**, 877-887 (2001).

11 M. M. Alkaisi, R. J. Blaikie, S. J. McNab, R. Cheung, and D. R. S. Cumming, Appl. Phys. Lett. **75**, 3560-3562 (1999).

12 R. J. Blaikie, M. M. Alkaisi, S. J. McNab, D. R. S. Cumming, R. Cheung, and D. G. Hasko, Microelectron. Eng. **46**, 85-88 (1999).

13 M. K. Herndon, R. T. Collins, R. E. Hollingsworth, P. R. Larson, and M. B. Johnson, Appl. Phys. Lett **74**, 141-143 (1999).

14 X. B. Yin, N. Fang, X. Zhang, I. B. Martini, and B. J. Schwartz, Appl. Phys. Lett. **81**, 3663-3665 (2002).

15 M. T. Li, L. Chen, and S. Y. Chou, Appl. Phys. Lett. **78**, 3322-3324 (2001).

16 S. Y. Chou, P. R. Krauss, W. Zhang, L. J. Guo, and L. Zhuang, J. Vac. Sci. Tech. B **15**, 2897-2904 (1997).

17 D.-Y. Khang, H. Yoon, and H. H. Lee, Adv. Mater. **13**, 749-752 (2001).

18 Stephen Y. Chou, Peter R. Krauss, and Preston J. Renstrom, Science **272**, 85-87 (1996).

19 M. Batzill, M. Sarstedt, and K. J. Snowdon, Nanotechnology **9**, 20-29 (1998).

20 L. L. Sohn and R. L. Willett, Appl. Phys. Lett. **67**, 1552-1554 (1995).

21 B. Klehn and U. Kunze, J. Appl. Phys. **85**, 3897-3903 (1999).

22 U. Kunze and B. Klehn, Adv. Mater. **11**, 1473-1475 (1999).

23 M. Heyde, K. Rademann, B. Cappella, M. Geuss, H. Sturm, T. Spangenberg, and H. Niehus, Rev. Sci. Instrum. **72**, 136-141 (2001).

24 H. Iwasaki, T. Yoshinobu, and K. Sudoh, Nanotechnology **14**, R55-R62 (2003).

25 K. Sattler, Jpn. J. Appl. Phys. Part 1 - Regul. Pap. Short Notes Rev. Pap. **42**, 4825-4829 (2003).

26 H. L. Zhang, H. L. Li, and Z. F. Liu, Microelectron. Eng. **63**, 381-389 (2002).

References

[27] P. Berenz, X. Y. Xiao, and H. Baltruschat, J. Phys. Chem. B **106**, 3673-3680 (2002).

[28] X. D. Hu, J. Yu, J. P. Chen, and X. T. Hu, Appl. Surf. Sci. **187**, 173-178 (2002).

[29] H. Qiu, Y. F. Lu, and Z. H. Mai, Jpn. J. Appl. Phys. Part 1 - Regul. Pap. Short Notes Rev. Pap. **40**, 290-294 (2001).

[30] K. Wilder, C. F. Quate, D. Adderton, R. Bernstein, and V. Elings, Appl. Phys. Lett. **73**, 2527-2529 (1998).

[31] U. Ramsperger, T. Uchihashi, and H. Neijoh, Appl. Phys. Lett. **78**, 85-87 (2001).

[32] M. Wendel, B. Irmer, J. Cortes, R. Kaiser, H. Lorenz, J. P. Kotthaus, A. Lorke, and E. Williams, **20**, 349-356 (1996).

[33] Chan Kyeong Hyon, Seng Chul Choi, Sung Woo Hwang, Doyeol Ahn, Yong Kim, and Eun Kyu Kim, Jpn. J. Appl. Phys. **38**, 7257-7259 (1999).

[34] M. Su, X. G. Liu, S. Y. Li, V. P. Dravid, and C. A. Mirkin, Journal of the American Chemical Society **124**, 1560-1561 (2002).

[35] M. Zhang, D. Bullen, S. W. Chung, S. Hong, K. S. Ryu, Z. F. Fan, C. A. Mirkin, and C. Liu, Nanotechnology **13**, 212-217 (2002).

[36] S. H. Hong, J. Zhu, and C. A. Mirkin, Science **286**, 523-525 (1999).

[37] S. H. Hang and C. A. Mirkin, Science **288**, 1808-1811 (2000).

[38] A. Ivanisevic and C. A. Mirkin, Journal of the American Chemical Society **123**, 7887-7889 (2001).

[39] J. Zou, D. Bullen, X. F. Wang, C. Liu, and C. A. Mirkin, Appl. Phys. Lett. **83**, 581-583 (2003).

[40] D. Bullen, S. W. Chung, X. F. Wang, J. Zou, C. A. Mirkin, and C. Liu, Appl. Phys. Lett. **84**, 789-791 (2004).

[41] H. Zhang, K. B. Lee, Z. Li, and C. A. Mirkin, Nanotechnology **14**, 1113-1117 (2003).

[42] Richard D. Piner, Jin Zhu, Feng Xu, Seunghun Hong, and Chad A. Mirkin, Science **283**, 661 (1999).

[43] Chad A. Mirkin, Seunghun Hong, and Linette Demers, ChemPhysChem, 37-39 (2001).

[44] M. Brehmer, L. Conrad, and L. Funk, Journal of Dispersion Science and Technology **24**, 291-304 (2003).

[45] B. D. Gates and G. M. Whitesides, Journal of the American Chemical Society **125**, 14986-14987 (2003).

[46] Younan Xia, John A Rogers, Kateri E. Paul, and George M. Whitesides, Chem. Rev. **99**, 1823-1848 (1999).

[47] M. Geissler, H. Wolf, R. Stutz, E. Delamarche, U. W. Grummt, B. Michel, and A. Bietsch, **19**, 6301-6311 (2003).

[48] Y. N. Xia, J. J. McClelland, R. Gupta, D. Qin, X. M. Zhao, L. L. Sohn, R. J. Celotta, and G. M. Whitesides, Advanced Materials **9**, 147-149 (1997).

[49] S. H. Chio, K. L. Wang, M. S. Leung, G. W. Stupian, N. Presser, B. A. Morgan, R. E. Robertson, M. Abraham, S. W. Chung, J. R. Heath, S. L. Cho, and J. B. Ketterson, J. Vac. Sci. Tech. A **18**, 1326-1328 (2000).

[50] S. Matsui, Proc. IEEE **85**, 629-643 (1997).

[51] M. Wibing, M. Batzill, and K. J. Snowdon, Nanotechnology **8**, 40-45 (1997).

[52] Johan B. Malherbe, Nuclear Instruments and Methods in Physics Research B **212**, 258 (2003).

[53] Daiichiro Sekiba, Stefania Bertero, Renato Buzio, Francesco Buatier de Moneot, Corrado Boragno, and Ugo Valbusa, Applied Physics Letters **81**, 2632 (2002).

[54] Eun-Hee Cirlin, John J. Vajo, Robert E. Doty, and T. C. Hasenberg, Journal of Vacuum Science and Technology A **9**, 1395 (1991).

[55] Jonah D. Erlebacher and Micheal J. Aziz, MRS Proceedings 1996 (1996).

[56] Maxim A. Makeev, Rodofo Cuerno, and Albert-Laszlo Barabasi, Nuclear Instruments and Methods in Physics Research B **197**, 185-227 (2002).

[57] S. Habenicht, W. Bolse, and K. P. Leib, Phys. Rev. B **60**, R2200 (1999).

[58] R. Gago, L. Vazquez, R. Cuerno, M Varela, C. Ballesteros, and J. M. Albella, Nanotechnology **13**, 304 (2002).

[59] Jonah D. Erlebacher, Michael J. Aziz, Eric Chason, Michael B. Sinclair, and Jerrold A. Floro, Journal of Vacuum Science and Technology A **18**, 115 (2000).

[60] Ivor Brodie and Julius J Muray, *The Physics of Micro/Nano-Fabrication* (Plenum Press, New York and London, 1992).

[61] S. Rusponi, C. Boragon, and U. Valbusa, Physical Review Letters **78**, 2795 (1997).

[62] S. Rusponi, C. Boragon, and U. Valbusa, Physics of Low-Dimensional Sturctures **12**, 55 (1998).

[63] S. Habenicht, W. Bolse, H. Fieldmann, U. Geyer, H. Hofsass, K. P. Leib, and F. and Roccaforte, Europhysics Letters **50**, 209 (2000).

[64] S. Rusponi, G. Costantini, C. Boragon, and U. Valbusa, Physical Review Letters **81**, 2735 (1998).

[65] G. Carter and V. Vishnyakov, Physical Review B **54**, 17647-17653 (1996).

[66] Eric Chason, T. M. Mayer, B. K. Kellerman, D. T. Mcllory, and A. J. Howard, Physical Review Letters **72**, 3040 (1994).

[67] Alexandre Cuenat and Aziz Micheal J., Material Research Society Symposium Proceedings **696**, N2.8.1 (2002).

[68] Jonah Erlebacher, Michael J. Aziz, Eric Chason, Michael B. Sinclair, and Jerrold A. Floro, Physical Review Letters **82**, 2330 (1999).

[69] J. B. Malherbe, Critical Reviews in Solid State and Materials Sciences **19**, 129-195 (1994).

[70] R. Mark Bradley and James M. Harper, Journal of Vacuum Science and Technology A **6**, 2390-2395 (1988).

[71] J Sone, J Fujita, Y Ochiai, S Manako, S Matsui, E Nomura, T Baba, H Kawaura, T Sakamoto, C D Chen, Y Nakamura, and J S Tsai, Nanotechnology **10**, 135-141 (1999).

[72] M. Batzill and K J Snowdon, Appl. Phys. Lett. **77**, 1 (2000).

[73] M. G. Rosenfield, M. G. R. Thomson, P. J. Coane, K.T. Kwietniak, J. Keller, D. P. Klaus, R. P. Volant, C. R. Blair, K. S. Tremaine, T. H. Newman, and F. J. Hohn, J. Vac. Sci, Tech. B **11**, 2615-2620 (1993).

[74] J. Fujita, T. Kishimoto, M. Morinaga, S. Mitake, and F. Shimizu, NEC Research & Development **40**, 401-404 (1999).

[75] J. Fujita, T. Kisimoto, M. Morinaga, S. Matsui, and F. Shimizu, Journal of Vacuum Science & Technology B **16**, 3855-3858 (1998).

76 J. Fujita, M. Morinaga, T. Kishimoto, M. Yasuda, S. Matsui, and F. Shimizu, Nature **380**, 691-694 (1996).

77 B Ziberi, F Frost, and B Rauschenbach, Appl. Phys. Lett **87**, 033113 (2005).

78 F Krok, J. J. Kolodziej, B. Such, P. Piatkowski, and M. Szymonski, Nuclear Instruments & Methods in Physics Research Section B- Beam Interactions with Materials and Atoms **212**, 264-269 (2003).

79 Yoshihiko Yuba, Sumiaki Hazamaa, and Kenji Gamo, Nuclear Instruments & Methods in Physics Research Section B- Beam Interactions with Materials and Atoms **206**, 648-652 (2003).

80 C. M. Demanet, K. Vijaya Sankar, J. B. Malherbe, N. G. van der Berg, and R. Q. Odendaal, Surface and Interface Analysis **24**, 497-502 (1996).

81 F Frost, B Ziberi, T Hoche, and B Rauschenbach, Nuclear Instruments & Methods in Physics Research Section B- Beam Interactions with Materials and Atoms **216**, 9-19 (2004).

82 S Facsko, H Kurz, and T Dekorsy, Phys. Rev. B **63**, 165329 (2001).

83 M. Batzill, F. Bardou, and K J Snowdon, Phys. Rev Lett. **85**, 780 (2000).

84 Eric Chason, Jonah Erlebacher, Michael J. Aziz, J. A. Floro, and M. B. Sinclair, Nuclear Instruments and Methods in Physics Research B **178**, 55 (2001).

85 S. Rusponi, G. Costanini, C. Boragon, and U Valbusa, Physics of Low-Dimensional Sturctures **5-6**, 95 (1999).

86 S. Rusponi, G. Costantini, C. Boragno, and U. Valbusa, Physical Review Letters **81**, 4184 (1998).

87 S. Rusponi, G. Costantini, F. Buatier de Mongeot, C. Boragon, and U Valbusa, Applied Physics Letters **75**, 3318 (1999).

88 M Szymonski, F Krok, P Struskia, J Kolodzieja, and B Sucha, Progress in Surface Science **74**, 331-341 (2003).

89 Yongqi Fu, Ngoi Kok Ann Bryan, and Wei Zhou, Opt. Express **12**, 1803-1809 (2004).

90 Yongqi Fu, Opt. Express **12**, 227-233 (2004).

91 K. Elst, A. Adriaens, and F. Adams, International Journal of Mass Spectrometry and Ion Processes **171**, 191 (1997).

92 S. W. MacLaren, J. E. Barker, N. L. Finnegan, and C. M. Loxton, Journal of Vacuum Science and Technology A **10**, 468 (1992).

93 S. Facsko, T. Dekorsy, C. Koerdt, C. Trappe, H. Kurz, A. Vogt, and H. L. Hartnagel, Science **Vol. 285.**, 1551 - 1553 (1999).

94 F. A. Stevie, P. M. Kahora, D. S. Simons, and P. Chi, Journal of Vacuum Science and Technology A **6**, 76 (1988).

95 S Duncan, R Smith, DE Sykes, and JM Walls, Vacuum **34**, 145-151 (1984).

96 A Karen, K Okuno, F Soeda, and A Ishitani, J. Vac. Sci, Tech. A **9**, 2247-2252 (1991).

97 F Frost, A. Schindler, and F Bigl, Phys. Rev Lett. **85**, 4116-4120 (2000).

98 S. Facsko, T. Bobek, H. Kurz, T. Dekorsy, S. Kyrsta, and R. Cremer, Appl. Phys. Lett **80**, 130-132 (2002).

99 F. Frost and B. Rauschenbach, J. Appl. Phys. A **77**, 1-9 (2003).

100 J. Kato, M. Nozu, Y. Fujimoto, M. Tanemura, and F. Okuyama, Journal of Vacuum Science and Technology A **13**, 207-215 (1995).

101 M. P. Seah, S. J. Spencer, P. J. Cumpson, and J. E. Johnstone, Surface and interface analysis **29**, 782-790 (2000).

102 J.B. Malherbe and N. G. van der Berg, Surface and Interface Analysis **22**, 538-542 (1994).

103 W. H. Gries, Surface and Interface Analysis **14**, 611-618 (1989).

104 W. H. Gries and K Miethe, Mikrochimica acta **1**, 169 (1987).

105 N. L. DeMeo, J. P. Donnelly, F. J. O'Donnell, M. W. Geis, and K. J. O'Connor, Nuclear Instruments & Methods in Physics Research Section B- Beam Interactions with Materials and Atoms **7-8**, 814-819 (1985).

106 Jorg Linders, Heinz Niedrig, Thomas Sebald, and Martin Sternberg, Nuclear Instruments & Methods in Physics Research Section B- Beam Interactions with Materials and Atoms **13**, 374-376 (1986).

107 N. Bouadma, P. Devoldere, and P. Ossart, Appl. Phys. Lett **48**, 1285-1287 (1986).

108 R. F. C. Farrow, Thin Solid Films **80**, 197-211 (1981).

109 Z. L. Liau and H. J. Zeiger, J. Appl. Phys **67**, 2434-2440 (1990).

110 D.C. Peacock, Vacuum **33**, 601 (1983).

111 Osamu Wada, J. Phys. D **17**, 2429-2437 (1984).

112 X. Hou, M. Yu, and X. Wang, Chinese Physics Letters **2**, 31 (1985).

113 J. S. Pan, S. T. Tay, C. H. A. Huan, and A. T. S. Wee, Surface and Interface Analysis **26**, 930-938 (1998).

114 Osamu Wada, J. Electrochem. Soc. **131**, 2373 (1984).

115 J. B. Malherbe and W. O. Barnard, Surface Sciences **255**, 309 (1991).

116 C. R. Bayliss and D. L. Kirk, Thin Solid Films **29**, 97-106 (1975).

117 M. G. Dowsett, R. M. King, and E. H. C. Parker, Appl. Phys. Lett **31**, 529-531 (1977).

118 C J Jones and D. L. Kirk, Journal of Physics D-Applied Physics **12**, 837 (1979).

119 J. C. Tsang, Kahn A., and P. Mark, Surf. Sci. **97**, 119-127 (1980).

120 Kathleen A. Stair and Yip-Wah Chung, Appl. Surf. Sci. **26**, 381-391 (1986).

121 D. K. Skinner, J. Elctron. Mater. **9**, 67 (1980).

122 D. T. Clark, T. Fok, G. G. Roberts, and R. W. Sykes, Thin Solid Films **70**, 261-283 (1980).

123 R. Stanley Williams, Solid State Communications **41**, 153-156 (1982).

124 C. W. Tu and A. R. Schlier, Appl. Surf. Sci. **11/12**, 355 (1982).

125 D. K. Skinner, J. G. Swanson, and C. V. Hayness, Surface and Interface Snalysis **5**, 38 (1983).

126 Y. Shapira, L. J. Brillson, and A. Heller, j. Vac. Sci, Tech. A **1**, 766-770 (1983).

127 B. Gruzza, B. Achard, and C. Pariset, Surf. Sci. **162**, 202-208 (1985).

128 B. Gruzza and C. Pariset, Surf. Sci. **247**, 408-416 (1991).

129 B. Gruzza, C. Pariset, and S. Abdellaoui, Surface and interface analysis **16**, 54 (1990).

130 B. Gruzza, A Porte, L Bideux, C Jardin, and J Miloua, Acta Physica Polonica A **81**, 223 (1992).

131 B. Achard, B. Gruzza, and C. Pariset, Surf. Sci. **160**, L519-L523 (1985).

132 R. N. S. Sodhi, W. M. Lau, and S.L.J. Ingrey, Surface and Interface Analysis **12**, 321 (1988).

133 W. M. Lau, R. N. S. Sodhi, B. J. Flinn, TanK. H., and G. M. Bancroft, Appl. Phys. Lett **51**, 177-179 (1987).

134 C. Jardin, D. Robert, B. Achard, B. Gruzza, and C. Pariset, Surface and interface analysis **10**, 301 (1987).

135 Xun Wang, Appl. Surf. Sci. **33/34**, 88-98 (1988).

136 S. J. Pearton, U. K. Chakrabarti, A. P. Perley, and K. S. Jones, J. Appl. Phys **68** (1990).

137 S. Abdellaoui, B. Gruzza, C. Pariset, M. Bouslama, C. Jardin, and D. Robert, Surf. Sci. **208**, L21-L28 (1989).

138 S. Valeri, M. Lolli, and P. Sberveglieri, Surface and Interface Analysis **16**, 59 (1990).

139 S. Valeri, M. Lolli, and P. Sberveglieri, Surf. Sci. **238**, 2 May 1990 (1990).

140 J. B. Malherbe, H. Lakner, and W. H. Gries, Surface and Interface Analysis **17**, 719 - 725 (1991).

141 J. B. Malherbe, Appl. Surf. Sci. **70/71**, 322-326 (1993).

142 J. Morais, T. A. Fanzan, and R. Landers, Phys. Status Solidi **141**, K19 (1994).

143 F. Okuyama and J. Kato, J. Vac. Sci, Tech. B **12**, 3054-3056 (1994).

144 C. M. Demanet, J. B. Malherbe, N. G. vander Berg, and Vijaya Sankar, Surface and Interface Analysis **23**, 433-439 (1995).

145 W. Yu, J. L. Sullivan, SaiedS. O., and G. A. C. Jones, Nuclear Instruments & Methods in Physics Research Section B- Beam Interactions with Materials and Atoms **135**, 250-255 (1998).

146 B. Ziberi, F. Frost, M. Tartz, H. Neumann, and B. Rauschenbach, Thin Solid Films **459**, 106-110 (2004).

147 Wen-Sheng Shi, Hong-Ying Peng, Yu-Feng Zheng, Ning Wang, Nai-Gui Shang, Zhen-Wei Pan, Chun-Sing Lee, and Shuit-Tong Lee, Adv. Mater. **12**, 1343-1345 (2000).

148 S. T. Lee, Y. F. Zhang, N. Wang, Y. H. Tang, I. Bello, C. S. Lee, and Y. W. Chung, J. Mater. Res. **14**, 4503-4507 (1999).

149 Chia-Chun Chen and Chun-Chia Yeh, Adv. Mater. **12**, 738-741 (2000).

150 Xiangfeng Duan and Charles M. Leiber, Adv. Mater. **12**, 298-302 (2000).

151 Xiangfeng Duan and Charles M. Lieber, J. Am. Chem. Soc. **122**, 188-189 (2000).

152 Mark S. Gudiksen, Jianfang Wang, and Charles M Lieber, J. Phys. Chem. B **105**, 4062-4064 (2001).

153 Xiangfeng Duan, Jianfang Wang, and Charles M Lieber, Appl. Phys. Lett **76**, 1116-1118 (2000).

154 C. Li, D. Zhang, S. Han, X. Liu, T. Tang, B. Lei, Z. Liu, and C. Zhou, in *Molecular Electronics Iii* (New York Acad Sciences, New York, 2003), Vol. 1006, p. 104-121.

155 Young Churl Choi, Won Seok Kim, Young Soo Park, Seung Mi Lee, Dong Jae Bae, Young Hee Lee, Gyeong-Su Park, Won Bong Choi, Nae Sung Lee, and Jong Min Kim, Adv. Mater. **12**, 746-749 (2000).

156 Y. Zhou, S. H. Yu, X. P. Cui, C. Y. Wang, and Z. Y. Chen, Chem. Mater. **11**, 545-546 (1999).

157 D. Zhang, D. N. Mcilroy, Y. Geng, and M. G. Norton, J. Mater. Sci. Lett. **18**, 349-351 (1999).

158 T. I. Kamins, R. Stanley Williams, D. P. Basile, T. Hesjedal, and J. S. Harris, J. Appl. Phys. **89**, 1008-1016 (2001).

159 Z. Q. Liu, W. Y. Zhou, L. F. Sun, D. S. Tang, X. P. Zou, Y. B. Li, C. Y. Wang, G. Wang, and S. S. Xie, Chem. Phys. Lett. **341**, 523-528 (2001).

160 M. Lu, M. K. Li, L. B. Kong, X. Y. Guo, and H. L. Li, Composites Part B-Engineering **35**, 179-184 (2004).

161 K. K. Lew and J. M. Redwing, Journal of Crystal Growth **254**, 14-22 (2003).

162 Y. J. Xing, D. P. Yu, Z. H. Xi, and Z. Q. Xue, Chinese Physics **11**, 1047-1050 (2002).

163 Yiying Wu and Peidong Yang, Chem. Mater. **12**, 605-607 (2000).

164 Yiying Wu and Peidong Yang, Appl. Phys. Lett **77**, 43-45 (2000).

165 L. M. Cao, J. Liu, C. X. Gao, Y. C. Li, X. D. Li, Y. Q. Wang, Z. Zhang, Q. L. Cui, G. T. Zou, L. L. Sun, and W. K. Wang, Journal of Physics-Condensed Matter **14**, 11017-11021 (2002).

166 K. Saulig-Wenger, D. Cornu, F. Chassagneux, T. Epicier, and P. Miele, Journal of Materials Chemistry **13**, 3058-3061 (2003).

167 P. A. Hu, Y. Q. Liu, and X. B. Wang, Applied Physics A-Materials Science & Processing **77**, 743-745 (2003).

168 Z. J. Li, H. J. Li, X. L. Chen, A. L. Meng, K. Z. Li, Y. P. Xu, and L. Dai, Applied Physics A-Materials Science & Processing **76**, 637-640 (2003).

169 D. H. Feng, T. Q. Jia, X. Li, Z. Z. Xu, J. Chen, S. Z. Deng, Z. S. Wu, and N. S. Xu, Solid State Communications **128**, 295-297 (2003).

170 S. Z. Deng, Z. S. Wu, J. Zhou, N. S. Xu, R. Chen, and J. Chen, Chemical Physics Letters **356**, 511-514 (2002).

171 H. Y. Kim, J. Park, and H. Yang, Chemical Communications, 256-257 (2003).

172 H. Y. Kim, J. Park, and H. Yang, Chemical Physics Letters **372**, 269-274 (2003).

173 Michael H. Huang, Yiying Wu, Henning Feick, Ngan Tran, Eicke Weber, and Peidong Yang, Adv. Mater. **13**, 113-116 (2001).

174 D. F. Liu, D. S. Tang, L. J. Ci, X. Q. Yan, X. Y. Liang, Z. P. Zhou, H. J. Yuan, W. Y. Zhou, and G. Wang, Chinese Physics Letters **20**, 928-931 (2003).

175 Y. Zhang, H. B. Jia, X. H. Luo, X. H. Chen, D. P. Yu, and R. M. Wang, Journal of Physical Chemistry B **107**, 8289-8293 (2003).

176 J. Zhou, N. S. Xu, S. Z. Deng, J. Chen, and J. C. She, Chemical Physics Letters **382**, 443-446 (2003).

177 Jun. Zhou, S. Z. Deng, N. S. Xu, Jun. Chen, and J. C. She, Applied Physics Letters **83**, 2653-2655 (2003).

178 X. C. Jiang, T. Herricks, and Y. N. Xia, Nano Letters **2**, 1333-1338 (2002).

179 Xiaolong Chen, Jianye Li, Yongge Cao, Yucheng Lan, Hui Li, Meng He, Chaoying Wang, Ze Zhang, and Zhiyu Qiao, Ad. Mater. **12**, 1432-1434 (2000).

180 C. C. Tang, S. S. Fan, H. Y. Dang, P. Li, and Y. M. Liu, Appl. Phys. Lett. **77**, 1961-1963 (2000).

181 Maoqi He, Indira Minus, Piezhen Zhou, S. Noor Mohammed, Joshua B. Halpern, Randy Jacobs, Wendy L. Samey, Lourdes Salamanca-Riba, and R. D. Vispute, Appl. Phys. Lett. **77**, 3731-3733 (2000).

182 H. W. Seo, S. Y. Bae, J. Park, H. Yang, and B. Kim, Journal of Physical Chemistry B **107**, 6739-6742 (2003).

183 C. H. Liang, L. C. Chen, J. S. Hwang, K. H. Chen, Y. T. Hung, and Y. F. Chen, Applied Physics Letters **81**, 22-24 (2002).

184 J. Q. Hu, Q. Li, X. M. Meng, C. S. Lee, and S. T. Lee, Journal of Physical Chemistry B **106**, 9536-9539 (2002).

185 T. Ohgai, X. Hoffer, A. Fabian, L. Gravier, and J. P. Ansermet, Journal of Materials Chemistry **13**, 2530-2534 (2003).

186 T. Li, S. G. Yang, L. S. Huang, B. X. Gu, and Y. W. Du, Chinese Physics Letters **21**, 729-732 (2004).

187 K. J. Ziegler, B. Polyakov, J. S. Kulkarni, T. A. Crowley, K. M. Ryan, M. A. Morris, D. Erts, and J. D. Holmes, Journal of Materials Chemistry **14**, 585-589 (2004).

188 K. S. Shankar, S. Kar, A. K. Raychaudhuri, and G. N. Subbanna, Applied Physics Letters **84**, 993-995 (2004).

189 T. Ohgai, L. Gravier, X. Hoffer, M. Lindeberg, K. Hjort, R. Spohr, and J. P. Ansermet, Journal of Physics D-Applied Physics **36**, 3109-3114 (2003).

190 J. Oh, Y. Tak, and Y. Lee, Electrochemical and Solid State Letters **7**, C27-C30 (2004).

191 Yan Li, Dongsheng Xu, Qingming Zhang, Daping Chen, Fuzhi Huang, Yajie Xu, Guolin Guo, and Zhennan Gu, Chem. Mater. **11**, 3433-3435 (1999).

192 Y. Z. Piao and H. Kim, Chemical Communications, 2898-2899 (2003).

193 X. J. Liang, J. L. Li, X. Liu, J. Z. Wang, H. Liu, Q. K. Xue, and J. F. Jia, Surface and Interface Analysis **36**, 100-103 (2004).

194 M. Lu, M. K. Li, L. B. Kong, X. Y. Guo, and H. L. Li, Chemical Physics Letters **374**, 542-547 (2003).

195 Zhibao Zhang, Dmitry Gekhtman, Mildred S. Dresselhaus, and Jackie Y. Ying, Chem. Mater. **11**, 1659-1665 (1999).

196 Huaqiang Cao, Zheng Xu, Hai Sang, Dong Sheng, and Chenyang Tie, Adv. Mater. **13**, 121-123 (2001).

197 S. Dudois, A. Michel, J. P. Eymery, J. L. Duvail, and L. Piraux, J. Mater. Res. **14**, 665-671 (1999).

198 K. Miki, J. H. G Owen, D. R. Bowler, G. A. D. Briggs, and Sakamoto K., Surf. Sci. **421**, 397 (1999).

199 K. Miki, J. H. G. Owen, D. R. Bowler, G. A. D. Briggs, and K. Sakamoto, Phys. Rev. B **59**, 14868-14871 (1999).

200 Kyung-Bok Lee, Sang-Min Lee, and Jinwoo Cheon, Adv. Mater. **13**, 517-520 (2001).

201 Zhengwei Pan, Hau-Ling Lai, Frederik C. K. Au, Xiaofeng Duan, Weiya Zhou, Wensheng Shi, Ning Wang, Chun-Sing Lee, Ning-Biu Wong, Shuit-Tong Lee, and Sishen Xie, Adv. Mater. **12**, 1186-1190 (2000).

202 H. Q. Wu, X. W. Wei, M. W. Shao, and J. S. Gu, Journal of Crystal Growth **265**, 184-189 (2004).

203 A. Govindaraj, B. C. Satishkumar, Manashi Nath, and C.N. R. Rao, Chem. Mater. **12**, 202-205 (2000).

204 Y. Zhang and Hongjie Dai, Appl. Phys. Lett **77**, 3015-3017 (2000).

205 Jan Richter, Micheal Nerting, Wolfganf Pompe, Ingolf Monch, and Hans K. Schackert, Appl. Phys. Lett. **78**, 536-538 (2001).

206 Jermiah K. N. Mbindyo, Brian D. Resiss, Benjamin R. Martin, Charistine D. Keating, Nicheal J. Natan, and Thomas E. Mallouk, Adv. Mater. **13**, 249-254 (2001).

207 H. J. Liu, D. K. Biegelsen, N. M. Johnson, F. A. Ponce, and R. F. W. Pease, J. vac. Sci, Tech. B **11**, 2532 (1993).

208 W.K. Hsu, S. Trasobares, H. Terrones, M. Terrones, N. Grobert, Y. Q. Zhu, W.Z. Li, R. Escudero, J. P. Hare, H. W. Kroto, and D. R. M. Waiton, Chem. Mater. **11**, 1747-1751 (1999).

209 S. Bhattacharyya , S. K. Saha, and D. Chakravorty, Appl. Phys. Lett. **77**, 3770-3772 (2000).

210 S. Bhattacharrya, *S.K. Saha, and D.* Chakravorty, Appl. Phys. Lett. **76**, 3896-3898 (2000).

211 M. E. Toimil Molares, V. Buschmann, D. Dobrev, R. Neumann, R. Scholz, R. Schuchert, and J. Vetter, Ad. Mater. **13**, 62-65 (2001).

212 X. F. Wang, J. Zhang, H. Z. Shi, Y. W. Wang, G. W. Meng, X. S. Peng, L. D. Zhang, and J. Fang, J. Appl. Phys. **89**, 3847-3851 (2001).

213 Y. W. Wang, G. W. Meng, C. H. Liang, Wang G. Z., and L. D. Zhang, Chem. Phys. Lett. **339**, 174-178 (2001).

214 G. B. Ji, W. Chen, S. L. Tang, B. X. Gu, Z. Li, and Y. W. Du, Solid State Communications **130**, 541-545 (2004).

215 J. X. Xu, X. M. Huang, G. Z. Xie, Y. H. Fang, and D. Z. Liu, Materials Research Bulletin **39**, 811-818 (2004).

216 K. R. Pirota, D. Navas, M. Hernandez-Velez, K. Nielsch, and M. Vazquez, Journal of Alloys and Compounds **369**, 18-26 (2004).

217 A. K. Bentley, J. S. Trethewey, A. B. Ellis, and W. C. Crone, Nano Letters **4**, 487-490 (2004).

218 X. Y. Yuan, G. S. Wu, T. Xie, Y. Lin, and L. D. Zhang, Nanotechnology **15**, 59-61 (2004).

219 J. B. Ding, D. H. Qin, Y. Huang, L. Cao, and H. L. Li, Journal of Materials Engineering and Performance **12**, 584-588 (2003).

220 C. G. Jin, W. F. Liu, C. Jia, X. Q. Xiang, W. L. Cai, L. Z. Yao, and X. G. Li, Journal of Crystal Growth **258**, 337-341 (2003).

221 X. Y. Zhang, G. H. Wen, Y. F. Chan, R. K. Zheng, X. X. Zhang, and N. Wang, Applied Physics Letters **83**, 3341-3343 (2003).

222 K. H. Lee, Y. J. Kim, and W. Y. Jeung, in *Advanced Materials Processing Ii* (Trans Tech Publications Ltd, Zurich-Uetikon, 2003), Vol. 437-4, p. 45-48.

223 L. Li, Y. Zhang, G. H. Li, and L. D. Zhang, Chemical Physics Letters **378**, 244-249 (2003).

224 Y. T. Pang, G. W. Meng, L. D. Zhang, W. J. Shan, C. Zhang, X. Y. Gao, and A. W. Zhao, Solid State Sciences **5**, 1063-1067 (2003).

225 L. A. Bauer, D. H. Reich, and G. J. Meyer, Langmuir **19**, 7043-7048 (2003).

226 Y. G. Guo, C. J. Li, L. J. Wan, D. M. Chen, C. R. Wang, C. L. Bai, and Y. G. Wang, Advanced Functional Materials **13**, 626-630 (2003).

227 Y. T. Pang, G. W. Meng, W. J. Shan, L. D. Zhang, X. Y. Gao, A. W. Zhao, and Y. Q. Mao, Applied Physics a-Materials Science & Processing **77**, 717-720 (2003).

228 Z. H. Zhang, K. Sumitomo, H. Omi, T. Ogino, and X. Zhu, Surface and Interface Analysis **36**, 114-118 (2004).

229 C. W. Tu, Journal of Vacuum Science & Technology A **21**, S160-S166 (2003).

230 T. Sato, I. Tamai, C. Jiang, and H. Hasegawa, in *Compound Semiconductors 2001* (Iop Publishing Ltd, Bristol, 2002), p. 325-330.

231 Faustion Martelli, (Laboratorio Nazionale TASC, INFM, Trieste, 2006), Vol. 2006.

232 Hanxuan Li, Ju Wu, Zhangguo Wang, and Theda Daniels-Race, Appl. Phys. Lett **75**, 1173-1175 (1999).

233 L. Gonzalez, J. M. Carcia, R. Garcia, F. Briones, J. Martinez-Pastor, and C. Balleeseros, Appl. Phys. Lett **76**, 1104-1106 (2000).

234 Mandar M. Deshmukh, D. C. Ralph, M. Thomas, and Silcox, Appl. Phys. Lett. **75**, 1631-1633 (1999).

235 T. Yasuda, S. Yamasaki, and S. Gwo, Appl. Phys. Lett. **77**, 3917-3919 (2000).

236 Takeyoshi Sugaya, Mutsuo Ogura, Yoshinobu Sugiyama, Kazuyuki Matsumoto, Kenji Yonei, and Takashi SekiGuchi, Appl. Phys. Lett. **78**, 76-78 (2001).

237 Sung-Wook Chung, Jae-Young Yu, and James R. Heath, Appl. Phys. Lett. **76**, 2068-2070 (2000).

238 Xiang Feng Duan, Yu Huang, Jianfang Wang, and Charles M. Lieber, Nature **409**, 66-69 (2001).

239 Z. H. Zhong, F. Qian, D. L. Wang, and C. M. Lieber, Nano Lett. **3**, 343-346 (2003).

240 Y. Huang, X. F. Duan, Y. Cui, and C. M. Lieber, Nano Lett. **2**, 101-104 (2002).

241 Daihua Zhang, Chao Li, Song Han, Xiaolei Liu, Tao Tang, Wu Jin, and Chongwu Zhou, Appl. Phys. Lett **82**, 112-114 (2003).

242 Michael S. Arnold, Phaedon Avouris, Zheng Wei Pan, and Zhong L Wang, J. Phys. Chem. B **107**, 659 -663 (2003).

243 Yu Huan, Xiang Feng Duan, Yi Cui, Lincoln J Lauhon, Kyoung-Ha Kim, and Charles M Lieber, Science **294**, 1313-1317 (2001).

244 Y. Cui and C. M. Lieber, Science **291**, 851-853 (2001).

245 Xiangfeng Duan, Yu Huang, and Charles M. Lieber, Nano Letters **2**, 487-490 (2002).

246 Yi Cui, Xiangfeng Duan, Jinagtao Hu, and Charles M. Lieber, J. Phys. Chem. **104**, 5213-5216 (2000).

247 Y. Cui, Z. H. Zhong, D. L. Wang, W. U. Wang, and C. M. Lieber, Nano Letters **3**, 149-152 (2003).

248 G. S. Cheng, A. Kolmakov, Y. X. Zhang, M. Moskovits, R. Munden, M. A. Reed, G. M. Wang, D. Moses, and J. P. Zhang, Appl. Phys. Lett. **83**, 1578-1580 (2003).

249 N. I. Kovtyukhova, B. R. Martin, J. K. N. Mbindyo, P. A. Smith, B. Razavi, T. S. Mayer, and T. E. Mallouk, J. Phys. Chem. B **105**, 8762-8769 (2001).

250 Yiying Wu and Peidong Yang, Adv. Mater. **13**, 520 (2001).

251 M. S. Gudiksen, L. J. Lauhon, J. Wang, D. C. Smith, and C. M. Lieber, Nature **415**, 617-620 (2002).

252 M. Law, D. Sirbuly, J. Johnson, J. Goldberger, R. Saykally, and P. Yang, Science **305**, 1269 (2004).

253 X. F. Duan, Y. Huang, R. Agarwal, and C. M. Lieber, Nature **421**, 241-245 (2003).

254 Hannes Kind, Yan Haoquan, Benjamin Messer, Law Matthew, and Peidong Yang, Ad. Mater. **14**, 158-160 (2002).

255 A. Kolmakov and M. Moskovits, Ann. Rev. Mater. Res. **34**, 151-180 (2004).

256 F. Favier, E. C. Walter, M. P. Zach, T. Benter, and R. M. Penner, Science **293**, 2227-2231 (2001).

257 C. Z. Li, H. X. He, A. Bogozi, J. S. Bunch, and N. J. Tao, Appl. Phys. Lett. **76**, 1333-1335 (2000).

258 E. C. Walter, R. M. Penner, H. Liu, K. H. Ng, M. P. Zach, and F. Favier, Surf. Interface Anal. **34**, 409-412 (2002).

259 E. Comini, G. Faglia, G. Sberveglieri, Z. W. Pan, and Z. L. Wang, **81**, 1869-1871 (2002).

260 Q. H. Li, Y. X. Liang, Q. Wan, and T. H. Wang, Appl. Phys. Lett. **85**, 6389-6391 (2004).

261 Q. Wan, Q. H. Li, Y. J. Chen, T. H. Wang, X. L. He, J. P. Li, and C. L. Lin, Appl. Phys. Lett. **84**, 3654-3656 (2004).

262 C. Li, D. H. Zhang, X. L. Liu, S. Han, T. Tang, J. Han, and C. W. Zhou, Appl. Phys. Lett. **82**, 1613-1615 (2003).

263 A. Kolmakov, Y. Zhang, G. Cheng, and M. Moskovits, Ad. Mater. **15**, 997-1000 (2003).

264 O. K. Varghese, D. W. Gong, M. Paulose, K. G. Ong, E. C. Dickey, and C. A. Grimes, Adv. Mater. **15**, 624-627 (2003).

265 H. Q. Liu, J. Kameoka, D. A. Czaplewski, and H. G. Craighead, Nano Lett. **4**, 671-675 (2004).

266 Xiangfeng Duan, Chunming Niu, Vijendra Sahi, Jian Chen, J. Wallace Parce, Stephen Empedocles, and Jayl Goldman, Nature **425**, 274-278 (2003).

267 Zhaoning Yu, Steven J. Schablitsky, and S. Y. Chou, Appl. Phys. Lett. **74**, 2381-2383 (1999).

268 H. W. Schumacher, U. F. Keyser, U. Zeitler, R. J. Huang, and K. Eberl, Appl. Phys. Lett. **75**, 1107-1109 (1999).

269 D. H. Reich, M. Tanase, A. Hultgren, L. A. Bauer, C. S. Chen, and G. J. Meyer, J. Appl. Phys. **93**, 7275-7280 (2003).

270 M. Tanase, D. M. Silevitch, A. Hultgren, L. A. Bauer, P. C. Searson, G. J. Meyer, and D. H. Reich, J. Appl. Phys. **91**, 8549-8551 (2002).

271 Joseph I. Goldstein, *Scanning electron microscopy and X-ray microanalysis : a text for biologists, materials scientists, and geologists* (Plenum Press, New York, 1992).

272 David B. Williams and C. Barry Carter, *Transmission electron microscopy : a textbook for materials science* (Plenum Press, New York, 1996).

273 Flemming Besenbacher, Reports on Progress in Physics **59**, 1737 (1996).

274 Dawn A. Bonnell, *Scanning Probe Microscopy and Spectroscopy:Theory, Techniques, and Applications* (Wiley-VCH, New York, 2001).

275 R. Wiesendanger, *Scanning Probe Microscopy* (Springer-Verlag, Berlin, 1998).

276 Yi Zhu and Cungui Zhang, *Principle and Application of Electron Microscope (in Chinese)* (Beijing University Press, Beijing, 1983).

277 Zurich ETH, Zurich, 2005), Vol. 2005.

278 Josh Klesel, edited by How the SEM Works (http://mse.iastate.edu/microscopy/path2.html) (Material Science and Engineering Department at Iowa State University, Iowa, 2004).

279 e-Museum Nobel, edited by The Nobel Foundation (http://www.nobel.se/physics/educational/microscopes/scanning/) (The Nobel Foundation, Stockholm, 2004).

280 A. Bryant, D. P. E. Smith, and C. F. Quate, Appl. Phys. Lett **48**, 832-834 (1986).

281 Jerry Tersoff, in *Scanning Probe Microscopy and Spectroscopy*, edited by Dawn A. Bonnell (John Wiley & Sons, Inc., Publication, New York, 2001), p. 59-107.

282 R. M. Feenstra, Joseph A. Stroscio, and A. P. Fein, Surf. Sci. **181**, 295-306 (1987).

283 B. Bhushan, Wear **229**, 465-492 (1999).

284 Dawn A. Bonnell and D. Huey Bryan, in *Scanning Probe Microscopy and Spectroscopy*, edited by Dawn A. Bonnell (John Willey & Sons., Inc., Publication, New York, 2001), p. 15.

285 Digital Instruments, 2001), p. 11-11.

286 Nancy Burnham and Richard J. Colton, J. Vac. Sci, Tech. A **7**, 2906-2913 (1989).

287 U. Landman, W.D. Luedtke, N.A. Burnham, and R.J. Colton, Science **248**, 454 (1990).

288 F. Oulevey, G. Gremaud, A. Semoroz, A. J. Kulik, N. A. Burnham, E. Dupas, and D. Gourdon, Review of Scientific Instruments **69**, 2085-2094 (1998).

289 Bin Wu, Andreas Heidelberg, and John J. Boland, Nature Materials **4**, 525-529 (2005).

290 Jeong-Won Kang and Ho-Jung Hwang, J. Korean Phys. Soc. **38**, 695 (2001).

291 Hideyuki Ikeda, Yue Qi, Tahir Cagin, Konrad Samwer, William L. Johnson, and William A. Goddard, Phys. Rev Lett. **82**, 290072903 (1999).

292 Paulo S. Branicio and Jose-Pedro Rino, Phys. Rev B **62**, 16950?16955 (2000).

293 Binquan Luan and Mark O. Robbins, Nature **435**, 929-932 (2005).

294 Ernst Meyer and Roland Luthi, in *Handbook of Nanostructured Materials and Nanotechnology*, edited by H. S. Nalwa (Academic Press, San Diego, 2000), Vol. 2:Spectroscopy and Theory, p. 346.

295 R. W. Carpick, J. Vac. Sci, Tech. B **14**, 1289-1295 (1996).

296 A. Socoliuc, R. Bennewitz, E. Gnecco, and Ernst Meyer, Phys. Rev. Lett. **92**, 134301 (2004).

297 Martin Dienwiebel, Gertjan S. Verhoeven, Namboodiri Pradeep, Joost W. M. Frenken, Jennifer A. Heimberg, and Henny W. Zandbergen, Phys. Rev. Lett. **92**, 126101 (2004).

298 P. Poncharal, Z. L. Wang, D. Ugarte, and W. A. de Heer, Science **283**, 1513-1516 (1999).

299 Z. L. Wang, P. Poncharal, and W. A. de Heer, J. Phys. Chem. Solids **61**, 1025 (2000).

300 Zhong L. Wang, Adv. Mater. **12**, 1295 (2000).

301 Sergei V. Kalinin and Dawn A. Bonnell, in *Scanning Probe Microscopy and Spectroscopy*, edited by Dawn A. Bonnell (John Wiley & Sons Inc. Publication, New York, 2001), p. 216.

302 J. Ruzyllo, in *http://www.semiconductorglossary.com/default.asp?searchterm=ballistic+transport*, 2005).

303 Zhibao Zhang, Xiangzhou Sun, M. S. Dresselhaus, Ying Jackie Y., and I. Heremans, Phys. Rev. B **61**, 4850-4861 (2000).

304 Yu-Ming Lin, Stephen B. Cronin, Jackie Y. Ying, M. S. Dresselhaus, and Joseph P. Heremans, Appl. Phys. Lett. **76**, 3944-3946 (2000).

305 Y. L. Wang, X. C. Jiang, T. Herricks, and Y. N. Xia, Journal of Physical Chemistry B **108**, 8631-8640 (2004).

306 M. L. Tian, J. G. Wang, J. Snyder, J. Kurtz, Y. Liu, P. Schiffer, T. E. Mallouk, and M. H. W. Chan, Applied Physics Letters **83**, 1620-1622 (2003).

307 J. J. Zhao, C. L. Buia, J. Han, and J. P. Lu, Nanotechnology **14**, 501-504 (2003).

308 V. Rodrigues and D. Ugarte, Materials Science and Engineering B-Solid State Materials for Advanced Technology **96**, 188-192 (2002).

309 V. Rodrigues and D. Ugarte, Nanotechnology **13**, 404-408 (2002).

310 I. P. Batra, P. Sen, and S. Ciraci, Journal of Vacuum Science & Technology B **20**, 812-817 (2002).

311 V. Rodrigues and D. Ugarte, Physica Status Solidi B-Basic Research **230**, 475-480 (2002).

312 C. A. Stafford, Physica Status Solidi B-Basic Research **230**, 481-489 (2002).

313 Shigeru Tsukamoto and Kikuji Hirose, ArXiv: Cond-Mat **1** (2004).

314 Baolin Wang, Shuangye Yin, Guanghou Wang, and Jijun Zhao, J. Phys.: Condens. Matter **13**, L403-L408 (2001).

315 Frederick C. K. Au, K. W. Wong, Y. H. Tang, Y. F. Zhang, I. Bello, and S. T. Lee, Appl. Phys. Lett. **75**, 1700-1702 (1999).

316 Young-Jo Ko, Mincheol Shin, Seongjae Lee, and Kyong Wan Park, J. Appl. Phys. **89**, 374-379 (2001).

317 Q. H. Li, Q. Wan, Y. X. Liang, and T. H. Wang, Appl. Phys. Lett **84**, 4556-4558 (2004).

318 J. R. Kim, H. M. So, J. W. Park, J. J. Kim, J. Kim, C. J. Lee, and S. C. Lyu, Applied Physics Letters **80**, 3548-3550 (2002).

319 L. Zhang, T. Sakai, N. Sakuma, T. Ono, and K. Nakayama, Appl. Phys. Lett **75**, 3527-3529 (1999).

320 Yu-Ming Lin, S. B. Cronin, O. Rabin, Jackie Y. Ying, and M. S. Dresselhaus, Appl. Phys. Lett **79**, 677-679 (2001).

321 M. Magoga and C. Joachim, Physical Review B **59**, 16011-16021 (1999).

322 H. Ruda and A. Shik, J. Appl. Phys. **86**, 5103-5108 (1999).

323 David K Ferry and Stephen M. Goodnick, *Transport in Nanostructures* (Cambridge University Press, Cambridge, 1997).

324 Yoshimasa Murayama, *Mesoscopic Systems: Fundamentals and Applications* (Wiley-VCH, Niigata, 2001).

325 D. W. Wang, J. G. Lu, C. J. Otten, and W. E. Buhro, Appl. Phys. Lett. **83**, 5280-5282 (2003).

326 H. K. Seong, H. J. Choi, S. K. Lee, J. I. Lee, and D. J. Choi, Appl. Phys. Lett. **85**, 1256-1258 (2004).

327 G. D. Marzi, D. Iacopino, A. J. Quinn, and G. Redmond, J. Appl. Phys. **96**, 3458-3462 (2004).

328 Y. J. Ma, F. Zhou, L. Lu, and Z. Zhang, Solid State Commun. **130**, 313-316 (2004).

329 Philip Kim and Charles M. Lieber, Science **286**, 2148-2150 (1999).

330 E Giovine, A Notargiacomo, L Di Daspare, E Palange, F Evangelisti, R Leoni, G Castellano, G Torrioli, and V Foglietti, Nanotechnology **12**, 132-135 (2001).

331 Hideo Fujii, Seigo Kanemaru, Takashi Matsukawa, and Junji Itoh, Jpn. J. Appl. Phys. **38**, 7237-7240 (1999).

332 Hideo Fujii, Seigo Kanemaru, Takashi MAatsukawa, and Junji Itoh, Appl. Phys. Lett. **75**, 3986-3988 (1999).

333 Makoto Kanagawa, Electronics and Communications in Japan, Part 2 **84**, 285-293 (2001).

334 M Geva, in *Indium Phophide and Related Materials: Processing, Technology, and Devices*, edited by Avishay Katz (Artech House, Boston; London, 1992), p. 46.

335 Ian W. Drummond, in *Surface Analysis by Auger and X-ray Photoelectron Spectroscopy*, edited by D Briggs and John T. Grant (IM Publications and SurfaceSpectra Limited, Manchester, 2003), p. 117.

336 D. Briggs and M. P. Seah, *Practical Surface Analysis* (John Wiler & Sons, Chichester, 1990).

337 David Briggs and John T. Grant, *Surface Analysis by Auger and X-ray Photoelectron Spectroscopy* (IM Publications and SurfaceSpectra Limited, Chichester, 2003).

338 Sven Tougarrd, in *Surface Analysis by Auger and X-ray Photoelectron Spectroscopy*, edited by D Briggs and John T. Grant (IN Publications and SurfaceSpectra Limited, Chichester, 2003), p. 296.

339 Neal Fairley, in *Surface Analysis bt Auger and X-ray Photoelectron Spectroscopy*, edited by D Briggs and John T. Grant (IN Publications and Surface Spectra Limited, Devon, 2003), p. 401.

340 M. P. Seah, in *Surface Analysis by Auger and X-rar Photoelectron Spectroscopy*, edited by D Briggs and John T. Grant (IM Publications and SurfaceSpectra Limited, Chichester, 2003), p. 346.

341 John T. Grant, in *Surface Analysis by Auger and X-ray Photoelectron Spectroscopy*, edited by D Briggs and John T. Grant (IM Publications and SurfaceSpectra Limited, Chichester, 2003), p. 83.

342 William F. Stickle, in *Surface Analysis by Auger and X-ray Photoelectron Spectroscory*, edited by D Briggs and John T. Grant (IM Oublications and SuefaceSpectra Limited, Chichester, 2003), p. 382.

343 P.M.A Sherwood, in *Practical Sueface Analysis-Volume 1-Auger and X-Ray Photoelectron Spectroscopy*, edited by D Briggs and M. P. Seah (John Wiley & Sons Ltd, Chichester, 1990), Vol. 1, p. 572.

344 D Briggs, in *Surface Analysis by Auger and X-ray Photoelectron Spectroscopy*, edited by D Briggs and John T. Grant (IM publications abs Surface Spectra Limited, Chichester, 2003), p. 44.

345 University Northern Arizona, in *http://www.google.co.uk/search?q=cache:UdW86Nb0PskJ:www.physics.nau.edu/~porter/AES.ppt+Auger+Electron+Spectroscopy&hl=en* (Department of Physics & Astronomy, Northern Arizona University, Flagstaff, Vol. 2004.

346 Inc Material Interface, in *http://www.materialinterface.com/surface2.html*, Sussex, 2004).

347 for the University of Aarhus and Aalborg University Nanoscience Center, in *http://www.inano.dk/sw269.asp* (Interdisciplinary Nanoscience Center (iNANO), Aarhus, 2004), Vol. 2004.

348 Ugo Bardi, edited by The Basic Principle of LEIS (http://www.unifi.it/unifi/surfchem/solid/leis/) (Dipartimento di Chimica Universita' di Firenze, 1998).

349 V. I. Klimov, A. A. Mikhailovsky, S. Xu, A. Malko, J. A. Hollingsworth, C. A. Leatherdale, H. J. Eisler, and M. G. Bawendi, Science **290**, 314-317 (2000).

350 J. C. Johnson, H. Q. Yan, R. D. Schaller, L. H. Haber, R. J. Saykally, and P. D. Yang, Journal of Physical Chemistry B **105**, 11387-11390 (2001).

351 H. (Ed.) Fujita, *Micromachines as Tools for Nanotechnology* (Springer, Tokyo, 2003).

352 Andy Round, in *http://spm.phy.bris.ac.uk/techniques/SNOM/* (IRC NANOSCALE CHARACTERISATION AND BIOLOGICAL NANOSCIENCE WORKSHOP, Bristol, 2004), Vol. 2004.

353 M. Sakurai, *Nanoscale Spectroscopy and its Applications to Semiconductor Research* (Springer, Tokyo, 2001).

354 Makoto Sakurai, Carsten Thirstrup, and Masakazu and Aono, RIKEN Review **38**, 18 (2001).

355 S. J. Bull, Newcastle upon Tyne, 2005).

356 Brian D. Wirth, edited by Ion-surface interactions (http://iron.nuc.berkeley.edu/~bdwirth/Public/NE220/documents/Lecture40_040503.pdf) (University of California, Berkeley, Berkeley, 2004).

357 W. Eckstein, *Computer Simulation of Ion-Solid Interactions* (Springer-Verlag, New York, 1991).

358 L.I. Maissel and R. Glang, *Handbook of Thin Film Technology, chapter 3.* (McGraw-Hill, New York, 1970).

359 J. P. Biersack, Nucl. Instrum. Methods Phys. Res. Sect. B-Beam Interact. Mater. Atoms **27**, 21-36 (1987).

360 J.F. Ziegler, J.P. Biersack, and U. Littmark., *The Stopping and Range of Ions in Solids* (Pergamond Press, New York, 1985).

361 Peter Sigmund, *Sputtering by Particle Bombardment I: Physical Sputtering of Single-Element Solids* (Springer-Verlag, New York, 1981).

362 R. R. Olson, M. E. King, and G.K. Wehner, J. Appl. Phys **50**, 3677-3683 (1979).

363 W. Eckstein, C. Garciarosales, J. Roth, and J. Laszlo, Nucl. Instrum. Methods Phys. Res. Sect. B-Beam Interact. Mater. Atoms **83**, 95-109 (1993).

364 G.K. Wehner and D. Rosenberg, J. Appl. Phys **31**, 177 (1960).

365 J.F. Ziegler, in *(http://www.srim.org/index.htm)* (Ziegler, J.F., 2005), Vol. 2005.

366 Nix Roger, edited by 1. Structure of Metallic Surfaces (Queen Mary, University of London., London, 2003).

367 M. Purtton, *Introduction to Surface Physics* (Oxford University Press, York, 1994).

368 I. Finnie and Y. H. Kabil, **Wear 8**, 60 (1965).

369 Peter Sigmund, Physical Review **184**, 383 (1969).

370 Peter Sigmund, Journal of Materials Science **8**, 1545 (1973).

371 I. Koponen, M. Hautala, and O. P. Sievanen, Physical Review Letters **78**, 2612 (1997).

372 K. Elst, W. Vandervorst, J. Alay, J. Snauwaert, and L. Hellemans, Journal of Vacuum Science and Technology B **11**, 1968 (1993).

373 Z. X. Jiang and P. F. A. Alkemade, Applied Physics Letters **73**, 315 (1998).

374 John J. Vajo, Robert E. Doty, and Eun-Hee Cirlin, Journal of Vacuum Science and Technology A **14**, 2709 (1996).

375 K. Elst and W. Vandervorst, Journal of Vacuum Science and Technology A **12**, 3205 (1994).

376 T. M. Mayer, E. Chason, and A. J. Howard, Journal of Applied Physics **76**, 1633 (1994).

377 Rodololfo Cuerno, Hernan A. Makse, Silvina Tomassone, Stephen T. Harrington, and H. Eugene Stanley, Physical Review Letters **75**, 4464 (1995).

378 S. Park, B Kahng, H. Jeong, and A. L. Barabasi, Physical Review Letters **83**, 3486 (1999).

379 Elliott A. Eklund, R. Bruinsma, J. Rundnik, and R. Stanley Williams, Physical Review Letters **67**, 1759 (1991).

380 H. N. Yang, G. C. Wamg, and T. M. Lu, Physical Review B **50**, 7635 (1994).

381 M. Kardar, G. Parisi, and Y. C. Zhang, Phys. Rev. Lett. **56**, 889-892 (1986).

382 J. Kim, B. Kahng, and A. L. Barabasi, Appl. Phys. Lett **81**, 3654-3656 (2002).

383 M. A. Makeev and A. L. Barabasi, Appl. Phys. Lett. **71**, 2800-2802 (1997).

384 R. Cuerno and A. L. Barabasi, Phys. Rev. Lett. **74**, 4746-4749 (1995).

385 B. Kahng, H. Jeong, and A.-L. Barabasi, Appl. Phys. Lett **78**, 805-807 (2001).

386 G. Carter, in *Erosion and Growth of Solids stimulated by atom and ion beams*, edited by G. Carter G. KiriaKidis, and J. L. Whitton (Advanced study Institute, 1986), p. 70.

387 G Carter, B Navinsek, and J. L. Whitton, *Sputtering by Particle Bombardment II* (Springer-Verlag, Birlin, 1983).

388 G. K. Wehner and D. J. Hajicek, J. Appl. Phys **42**, 1145-1149 (1971).

389 G.K. Wehner, J. Vac. Sci, Tech. A **3**, 1821-1835 (1985).

390 M. M. Nindi, D. C. Stulik, C. B. Millham, and T. J. Larson, Nuclear Instruments & Methods in Physics Research Section B- Beam Interactions with Materials and Atoms **44**, 1-124 (1989).

391 S. M. Rossnagel and R. S. Robinson, J. vac. Sci, Tech. **20**, 195-198 (1982).

392 D.W. Palmer, edited by InAs The Semiconductors-Information Web-Site (http://www.semiconductors.co.uk/propiiiv5653.htm#InP, InSb) (Palmer Semiconductor Associates, Devon, 2004).

393 The Institution of Electrical Engineers, *Properties of Indium Phospide* (INSPEC, London; New York, 1991).

394 V. Swaminathan, in *Indium Phosphide and Related Materials: Processing, Technology, and Devices*, edited by Avisshay Katz (Artech House, Boston; London, 1992), p. 3,11.

395 Silicon FarEast, http://www.siliconfareast.com/sio2si3n4.htm (2006).

396 H Toraya, Journal of Applied Crystallography **33**, 95-102 (2000).

397 Material Interface Inc, http://www.almazoptics.com/CaF2.htm (2006).

398 B. Goldstein, Phys. Rev. **121**, 1305 (1961).

399 Hj. Matzke, Journal of Materials Science **5**, 831 (1970).

400 H. Schmidt, U. Geckle, and M. Bruns, Phys. Rev B **74**, 045203 (2006).

401 Bart Van Zeghbroeck, edited by http://ece-www.colorado.edu/~bart/book/book/chapter2/ch2_2.htm (Bart Van Zeghbroeck, Colorado, 2004).

402 I. R. Grant, in *Chemistry of Aluminium, Gallium, Indium and Tallium*, edited by A. J. Downs (Blackie Academic & Professional, London, 1993), p. 318.

403 R. B Martin, in *Chemistry of Aluminium, Gallium, Indium and Thallium*, edited by A. J. Downs (Blackie Academic & Professional, London, 1993), p. 499.

404 I. J. Polmear, in *Chemistry of Aluminium, Gallium Indium and Thallium*, edited by A. J. Downs (Blackie Academic & Professional, London, 1993), p. 82.

405 G. V. Samsonov, *Handbook of Physicochemical Properties of Elements* (Oldbourne Book Co., Ltd, London, 1968).

406 K. A. Evans, in *Chemistry of Aluminium, Gallium, Indium and Thallium*, edited by A. J. Downs (Blackie Academic & Professional, London, 1993), p. 286.

407 M. J. Taylor and P. J. Brothers, in *Chemistry of Aluminium, Gallium, Indium and Tantallium*, edited by A. J. Downs (Blackie Academic & Professional, London, 1993), p. 140.

408 Masatoshi Higuchi, Shinichiro Uekusa, Ryotaro Nakano, and Kazuhiko Yokogawa, J. Appl. Phys **74**, 6710-6713 (1993).

409 Yuzo Shigesato and David C. Paine, Appl. Phys. Lett **74**, 1268 (1993).

410 Radhouane Bel Hadj Tahar, Takayuki Ban, Yutaka Ohya, and Yasutaka Takahashi, J. Appl. Phys **83**, 2631-2645 (1998).

411 Chao Li, Daihua Zhang, Song Han, Xiaolei Liu, Tao Tang, and Chongwu Zhou, Adv. Mater. **15**, 143-146 (2003).

412 Do-Young Kim, Suk-Won Choi, and Junsin Yi, Journal of the Korean Physical Society **35**, 440-443 (1999).

413 M. Wissing, M. Holzwarth, D. S. Simeonova, and K J Snowdon, Review of Scientific Instruments **Volume 67**, pp. 4314-4320 (1996).

414 GmbH SPECS, edited by Ion Source IQE 12/38 (http://www.specs.de/products/ESCA/sources/ion-sources/iqe1238/iqe1238.htm) (SPECS GmbH, Birlin, 2004).

415 SPECS GmbH, *Operating Instruction-Ion Source IQE 12/38*, Berlin, 1986).

416 Instruments Veeco, edited by MultiMode Scanning Probe Microscope (http://www.veeco.com/html/product_bymarket_proddetail.asp?productID=177&MarketID=4&Title=AFM%2F%20SPMs%2F%20NSOM#) (Veeco Metrology Group, Chadds Ford, 2004).

417 R. Kern and P. Muller, Surface Science **392**, 103-133 (1997).

418 J. M. Rickman and D. J. Srolovitz, Surface Science **284**, 211-221 (1993).

419 S. J. Pearton, C. R. Abernathy, F. Ren, and J.R. Lothian, Journal of Applied Physics **76**, 1210 (1994).

420 J. Kovac and A. Zalar, Surface and Interface Analysis **34**, 253-256 (2002).

421 J. S. Pan, A. T. S. Wee, C. H. A. Huan, H. S. Tan, and K. L. Tan, Journal of Applied Physics **80**, 6655 (1996).

422 I. L. Singer, J. S. Murday, and L. R. Cooper, Journal of Vacuum Science and Technology **15**, 725 (1978).

423 H. Gnaser, B. Heinz, W. Bock, and H. Oechsner, Physical Review B **52**, 14086 (1995).

424 T. D. Bussing, P. H. Holloway, Y. X. Wang, J. F. Moulder, and J. S. Hammond, Journal of Vacuum Science and Technology B **6**, 1514-1518 (1988).

425 M. M. Sung, S. H. Lee, S. M. Lee, D. Marton, S. S. Perry, and J. W. Rabalais, Surf. Sci. **382**, 147-153 (1997).

426 Y. Chao, K. Svensson, D. Radosavkic, V. R. Dhanak, L. Siller, and M. R. C. Hunt, Phys. Rev B **64**, 235331 (2001).

427 G. Hughes and R. Ludeke, Journal of vacuum Science & Technology B **4**, 1109-1114 (1986).

428 G. Hollinger, E. Bergignat, J. Joseph, and Y. Robach, J. Vac. Sci. Technol. A-Vac. Surf. Films **3**, 2082-2088 (1985).

429 F. Eichhorn, J. Gaca, V. Heera, N. Schell, A. Turos, H. Weishart, and M. Wojcik, Vacuum **78**, 303-309 (2005).

430 Michael Hunt, Joint Report of Examiners (2005).

431 Martin Liess, Thin Solid Films **410**, 183-187 (2002).